Renat Yulmetov

Observations and Numerical Simulation of Icebergs in Broken Ice

Renat Yulmetov

Doctoral thesis

NTNU
Norges teknisk-naturvitenskapelige universitet
Thesis for the Degree of
Philosophiae Doctor
Faculty of Engineering Science and Technology
SFI Sustainable Arctic Marine
and Coastal Technology

NTNU
Norwegian University of
Science and Technology

NTNU
Norwegian University of
Science and Technology

UNIS
The University Centre in Svalbard

NTNU

Renat Yulmetov

Observations and Numerical Simulation of Icebergs in Broken Ice

Thesis for the Degree of Philosophiae Doctor

Trondheim, January 2017

Norwegian University of Science and Technology
Faculty of Engineering Science and Technology
SFI Sustainable Arctic Marine and Coastal Technology

NTNU
Norwegian University of
Science and Technology

UNIS
The University Centre in Svalbard

To my family

Abstract

Sea ice and icebergs are the major challenges for offshore activities in the Arctic. Design loads for Arctic offshore structures may be significantly reduced if the drift of sea ice and icebergs is possible to forecast accurately and perform physical ice management when required. So far, this has been successfully done solely for sea ice or solely for icebergs drifting in open water. There is a lack of knowledge about icebergs drifting together with broken ice, and there is no operational experience of deflecting an iceberg in broken ice.

An iceberg moving relatively sea ice should experience additional resistance force, which in general grows as the ice thickness, relative velocity or the ice concentration increase. It complicates the drift forecasting and potentially threatens iceberg towing operations in sea ice. This resistance force is hard to estimate: there are only a few analytical equations, and there is only one model-scale experiment of iceberg towing in ice. Published information about full-scale trials of towing is almost absent. However, numerical methods, that have been used to model floaters and ships in broken ice, are possible to utilize for the modelling of icebergs in broken ice.

This thesis covers observations, tracking and forecasting of icebergs and sea ice in the Greenland Sea and in the Barents Sea, and numerical modelling of iceberg towing in broken ice. The tracking has been performed using GPS that provided high temporal and spatial resolution of the drift trajectories. Statistical data on drift velocities, spectra, trajectory curvatures are derived. In addition, the relative drift velocity between the sea ice and icebergs is obtained. Characteristic values and observations are used for the numerical modelling part. Finally, for the first time, the yawing of real icebergs is measured and simulated. These data can be used for the design of offshore structures or when planning offshore operations, especially the ice management.

The numerical modelling of iceberg towing in ice is performed using the non-smooth discrete element method. A number of important knowledge gaps in material description and in the numerical method are filled. First of all, it is demonstrated that the collisions of floating ice floes are almost inelastic, resulting in restitution coefficient

values close to zero. Second, the characteristic feature of the method is a solution calculated in the form of contact impulses between the bodies, which makes it hard to estimate the contact forces. A conversion method between the contact impulses and the contact forces is proposed based on the experiments on a wide range of scales. Also, a potential flow is introduced in the vicinity of the simulated iceberg leading to better ice flow representation. Finally, an algorithm generating broken ice fields for the simulations is developed. The algorithm produces numerical ice fields having natural ice floe size distribution and target ice concentration.

In the situation when available relevant data are extremely limited, a validation study is performed on a model-scale experiment in broken ice. The numerical model reproduces the average towing force magnitude measured in the experiment and the motion of ice when the ice concentration is below 80%. In addition, the ice resistance obtained numerically is compared to existing analytical estimates of ice resistance to drifting icebergs. The estimates appear to give much lower ice resistance mainly due to no mechanical confinement during the drift.

The numerical model can be further developed in a number of ways: ice floe failure in different modes might be introduced, the model of iceberg in ice can be coupled with a ship model, validation against full-scale trials can be performed after they happen, etc. On the current stage, the model can be used as a numerical towing tank or as an aid for planning the first towing operations in the broken ice.

Table of contents

List of figures

Preface

This thesis is submitted to the Norwegian University of Science and Technology (NTNU) for partial fulfilment of the requirements for the degree of *philosophiae doctor*.

This doctoral work has been performed at the Department of Arctic Technology of the University Centre in Svalbard (UNIS) and the Department of Civil and Transport Engineering, NTNU, Trondheim with professor Aleksey Marchenko as main supervisor and with co-supervisors professor Sveinung Løset and associate professor Raed Lubbad.

x

Acknowledgments

During the past five years I was lucky to be surrounded by many great people. I enjoyed my life and work largely because of them.

First of all, I would like to express my gratitude to professor Aleksey Marchenko. In 2009 he invited me for a study semester on Spitsbergen and introduced me to ice physics and oceanography that turned out to be infinitely interesting. He was always open for scientific discussions and ready to answer my questions, especially in the field of mathematics. I enjoyed learning from him and working with him when we were out with RV Lance.

During these five years I experienced strong support from professor Sveinung Løset. In addition to the Arctic offshore engineering, I've learned from him how to organize work and received valuable scientific and engineering advice. His ability to motivate people is extraordinary, and I hope that many more generations of students will be intellectually ignited by him.

Closely familiar to the numerical methods that were used in this work, Raed Lubbad was a great adviser and internal reviewer. In addition to my supervisors I would like to mention professor Knut Høyland, from whom I learned about ice ridges and mechanical testing of ice.

Two of my friends who I have known for more than 11 years contributed to this thesis intellectually and morally — Sergey Kulyakhtin and Anton Kulyakhtin were a great advice on numerical methods, hydrodynamics and common sense.

Despite so many different research topics the Arctic Technology department at UNIS is an example of a friendly, fruitful and comfortable working environment. My great thanks go to my department colleagues for sharing their experience and ideas. I am grateful to the rest of UNIS friends, colleagues and administration. UNIS will always be like a second home for me and I wish it to continue being one big family no matter how large it grows.

I have never returned from Trondheim to Svalbard without a bunch of new ideas, fresh

Nomenclature and abbreviations

Nomenclature[1]

Symbol	Meaning	Symbol	Meaning
$\vec{U}$	drift velocity	Re_f	Reynolds number in full scale
U	drift speed	Re_m	Reynolds number in model scale
$\langle U \rangle$	mean drift speed	ν	kinematic viscosity
$\sigma(U)$	standard deviation of U	$\vec{F}_w^{IB}$	water drag acting on an iceberg
U_{max}	maximum drift speed	$\vec{F}_a^{IB}$	air drag acting on an iceberg
R	trajectory curvature radius	$\vec{F}_w^{IF}$	water drag acting on an ice floe
θ, ϕ	latitude and longitude	$\vec{F}_a^{IF}$	air drag acting on an ice floe
M	mass	C_w^{IB}, C_a^{IB}	iceberg drag coefficients
$\vec{F}_w$	water drag force	C_w^{IF}, C_a^{IF}	ice floe drag coefficients
$\vec{F}_a$	air drag force	A_{keel}, A_{sail}	keel and sail vertical cross-section areas
$\vec{F}_h$	hydrodynamic force	A	horizontal surface area of ice floe
$\vec{F}_C$	Coriolis force	ρ_w, ρ_a	densities of water and air
$\vec{F}_{wave}$	wave force	$\vec{V}_w, \vec{V}_a$	velocities of water and air
$\vec{F}_{ss}$	sea slope force	m	added mass
$\vec{F}_{tow}$	towing force	f	Coriolis frequency
$\vec{F}_{cont}$	contact force	Ω_{Earth}	angular velocity of the Earth
ρ_{IB}, ρ_{IF}	densities of glacial and saline ice	$\vec{k}$	outer normal to the Earth's surface
(ξ, η)	axes of the comoving system	g	gravity acceleration
(u, v)	velocity projections in the comoving system	$\nabla \zeta$	sea surface gradient
m_{11}, m_{22}	added masses for the principle axes	C_{wave}	wave force coefficient
m_{66}	added moment of inertia	l	waterline length
I	moment of inertia	a	wave amplitude

[1]might be different in the attached papers

Symbol	Meaning	Symbol	Meaning
ω	angular velocity	Δt	time step
F_ξ, F_η	external forces projections on the comoving system	w	normal projection of the contact velocity
M_ζ	external torque	D	mean caliper diameter
M_{cont}	contact torque	μ	friction coefficient
N_b, N_c	numbers of bodies and contacts	F_D	cumulative distribution function
$\mathbf{n}, \tau$	contact normal and tangent	f_D	probability density function
δ	contact separation distance	D_{min}, D_{max}	truncation limits for D
$\mathbf{x}$	positions of bodies	A_{ice}	area covered by ice floes
$\mathbf{U}$	velocities of bodies	A_{total}	domain area
$\mathbf{J}$	Jacobian	N_v	number of polygon vertices
$\mathbf{b}$	bias vector	r	roundness
$\mathbf{F}_{ext}$	continuous forces vector	N	number of ice floes
$\mathbf{w}$	normal contact velocities	h	ice thickness
λ	normal contact impulse	H	iceberg total height
F_{cont}^n	normal projection of the contact force	β	exponent in the floe size distribution
$\mathbf{A}, \mathbf{B}$	matrices for the Linear Complementarity Problem	L, W	length and width of the HSVA ice basin
λ_0	momentum before the impact	c	ice concentration
F_l	the most-likely collision peak force value	c_{crit}	highest-density packing concentration
$\lambda_{crushing}$	crushing constraint impulse	$\vec{F}_{si}$	sea ice force
l_{cont}	contact length	P	pressure in ice
λ_{ve}	visco-elastic constraint impulse	K, γ	contact stiffness and damping coefficient
P_S	pressure threshold value	P^*	empirical pressure constant
E	kinetic energy of a body		

Abbreviations

IM	ice management	DP	dynamic positioning
IB	icebreaker	RV	research vessel
DEM	discrete element method	FEM	finite element method
PERD	Program of Energy Research and Development	LCP	linear complementarity problem
HSVA	Hamburg Ship Model Basin	GPS	global positioning system
ACEX	Arctic Coring EXpedition	PGS	projected Gauss-Seidel
PIC	particle-in-cell	ENU	East, North, Up
CFD	computational fluid dynamics	SALM	single articulated leg mooring
SPH	smoothed particle hydrodynamics		

List of publications

Primary publications

JP1 Yulmetov, R., R. Lubbad, and S. Løset. 2016a. "Planar Multi-Body Model of Iceberg Free Drift and Towing in Broken Ice". *Cold Regions Science and Technology* 121:154–166. doi:10.1016/j.coldregions.2015.08.011
Writing and modelling were performed by the first author.

JP2 Yulmetov, R., and S. Løset. 2017. "Validation of Numerical Model of Iceberg Towing in Broken Ice (under review)". *Cold Regions Science and Technology*
Writing and modelling were performed by the first author.

JP3 Yulmetov, R., A. Marchenko, and S. Løset. 2016b. "Iceberg and Sea Ice Drift Tracking and Analysis off North-East Greenland". *Ocean Engineering* 123:223–237. doi:10.1016/j.oceaneng.2016.07.012
Data processing, modelling and writing were performed by the first author. The model of rotation was proposed by the second author. The trackers were deployed by the third author.

CP1 Skarbø, R., R. Yulmetov, and S. Løset. 2016. "Modelling Drift of Icebergs in Pack Ice off the North-East Greenland". In *Proceedings of the 23rd IAHR International Symposium On Ice, Ann Arbor, MI, USA, May 31–June 3, 2016*
Modelling and simulations were performed by Yulmetov. The paper was written by the first author.

CP2 Yulmetov, R., A. Marchenko, and S. Løset. 2012. "Characteristics of Sea Ice and Iceberg Drift Simulations in the Northwestern Barents Sea". In *Proceedings of the 21st IAHR International Symposium on Ice, Dalian, China, June 11–15, 2012*, 639–650. Dalian University of Technology Press
The paper was written by the first author. All authors participated in the fieldwork.

CP3 Yulmetov, R., A. Marchenko, and S. Løset. 2013b. "Ice Drift and Sea Current Analysis in the Northwestern Barents Sea". In *Proceedings of the 22nd International Conference on Port and Ocean Engineering under Arctic Conditions, Espoo, Finland, June 9–13, 2013*

The paper was written by the first author. All authors participated in the fieldwork.

Secondary publications

CP4 Yulmetov, R., and S. Løset. 2014. "Kinematic Characteristics of Sea Ice and Iceberg Drift in the Greenland Sea". In *Proceedings of the 22nd IAHR International Symposium on Ice, Singapore, August 11–14, 2014*, 727–734. doi:10.3850/978-981-09-0750-11208

Data processing and writing are done by the first author. The authors participated in the fieldwork.

CP5 Yulmetov, R., S. Løset, and K. Eik. 2013a. "Analysis of Drift of Sea Ice and Icebergs in the Greenland Sea". In *Proceedings of the 22nd International Conference on Port and Ocean Engineering under Arctic Conditions, Espoo, Finland, June 9–13, 2013*

Data processing and writing are done by the first author. The authors participated in the fieldwork.

CP6 Yulmetov, R., S. Løset, and R. Lubbad. 2014. "An Effective Numerical Method for Generation of Broken Ice Fields, Consisting of a Large Number of Polygon-Shaped Distinct Floes". In *Proceedings of the 22nd IAHR International Symposium on Ice, Singapore, August 11–14, 2014*, 829–836. doi:10.3850/978-981-09-0750-11207

The first author developed the method and wrote the whole paper.

CP7 Sinitsyn, A., D. Wrangborg, R. Yulmetov, A.T. Sund, and A. Marchenko. 2012. "Measurements of Deformations and Displacements of Stationary Quays in Svalbard with 3D Laser Scanner Riegl VZ-1000". In *Proceedings of the 21st IAHR International Symposium on Ice, Dalian, China, June 11–15, 2012*, 875–884. Dalian University of Technology Press

Yulmetov participated in the fieldwork and created some of the figures for the paper.

1 Introduction

1.1 Problem outline

Sea ice and icebergs are the major challenges for offshore structures in the Arctic. It is difficult to predict the drift of sea ice and icebergs, estimate ice loads on a structure during impacts, and deflect an iceberg to avoid collision. Continuous hydrocarbon production, structure integrity, the environment and human lives might be at risk.

There are a number of actions that can be taken to reduce this risk. Ice Management (IM) is defined as "*a sum of all activities where the objective is to reduce or avoid actions from any kind of ice features*" (Eik 2008). IM includes the following:

- Detection, tracking and forecasting of the ice features
- Threat evaluation
- Physical ice management such as ice breaking and iceberg towing
- Decision taking on disconnection of a structure and disconnection procedures

According to ISO 19906:2010(E), IM consists of "*active processes used to alter the ice environment with the intent of reducing the frequency, severity or uncertainty of ice actions*". However, this definition is related more to physical ice management and does not mention associated detection, tracking, forecasting and threat evaluation.

Incorporating the IM philosophy into the design of Arctic offshore structures and operations results in lower global design loads (Figure 1) and, therefore, lower costs and lower risks. IM has been performed successfully in relation to sea ice and icebergs in open water but non-simultaneously. For example, the effective floe size and, therefore, loads on Vidar Viking in Dynamic Positioning (DP) were reduced with the help of the icebreakers Oden and Sovetsky Soyuz during the Arctic Coring EXpedition
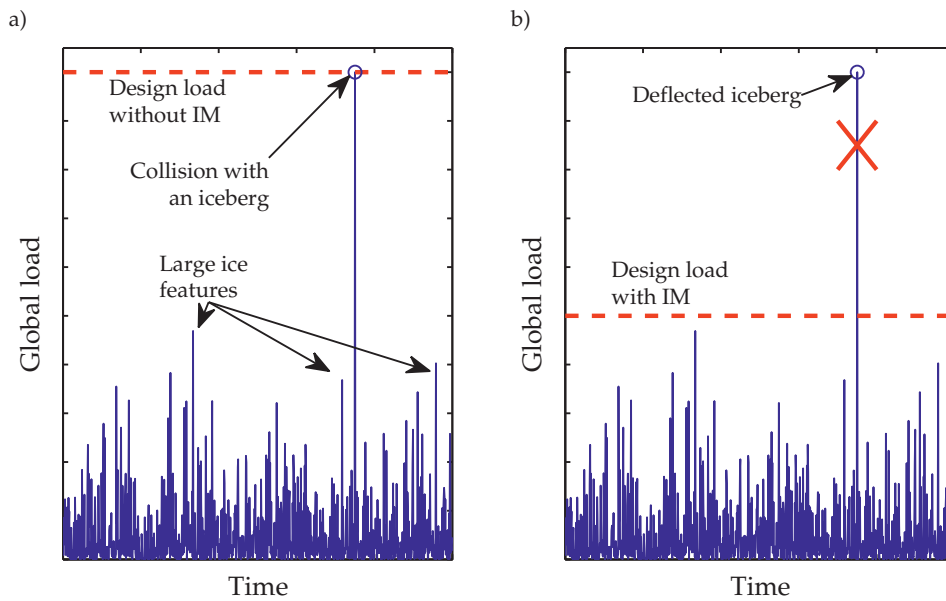
Figure 1: The concept of IM design philosophy. The design load can be significantly reduced when potential collisions with icebergs can be avoided using IM.

(Hamilton et al. 2011). In addition, every season, tens of icebergs are towed away from the offshore structures on the Grand Banks. Iceberg towing in open water has been successful in 85.5% of cases, as reported by Rudkin et al. (2005). However, iceberg drift forecasting and towing in the presence of ice appears to be challenging.

It is well-known that sea ice and icebergs drift under the action of air, water, sea ice and gravity. The action of the water is associated with the drag force caused by turbulent flow, hydrodynamic force due to a slowly varying current and wave-induced force; the gravity force is associated with sea surface gradients. Drift forecasting in open water can be performed by integrating the equations of motion. Given accurate metocean input data, the forecasting error can be reduced to less than 3 km in 48 h (see, for example, Kubat et al. (2005)). However, discontinuity and contact problems have to be considered for the coupled drift of ice and icebergs on a tactical scale. For physical IM in ice, to date, **there has been no information published on the towing of icebergs in sea ice to protect an offshore structure**. Only one model-scale experiment on iceberg towing in ice (Eik and Marchenko 2010) has been performed, which is obviously not sufficient. An attempt can be made to numerically model iceberg motion through broken ice.

Naturally broken and managed sea ice have been successfully modelled in relation

to various scientific and engineering problems using the Discrete Element Methods (DEM), both smooth and non-smooth. The DEM may be applied to calculate ice resistance to an iceberg drifting or being towed in broken ice. Certain challenges exist in relation to contact force calculations, the generation of broken ice fields, and numerical algorithms. Addressing these challenges would help to improve the accuracy of the model.

In addition to the engineering applications, icebergs and sea ice may be of interest to an oceanographers. Drifting icebergs are a source of fresh-water masses in polar regions (Hunke and Comeau 2011). Fresh meltwater and the cooling flux facilitate the formation of sea ice (Jongma et al. 2009). Coupling the drift of sea ice and icebergs in a relatively small-scale model might help to improve the accuracy of current global-scale climate models.

1.2 Research structure and scope

There is substantial interest in the feasibility of iceberg management in broken ice. Let us consider an iceberg drifting in broken ice of a certain thickness, concentration, and floe size distribution and in certain ocean currents, winds, etc. The following questions can be raised:

- How do these conditions affect the motion of iceberg?
- What level of towing forces should be expected depending on these parameters?
- Is it feasible to tow the iceberg to protect an offshore structure?

To answer these questions, one must understand what physical processes are actually occurring when the iceberg moves through the broken ice and model them. The problem can be called multiphysical because it involves complex flows around the iceberg and ice, surface waves, mechanical contacts between bodies, possibly (but not probably) ice failure in different modes, etc. A range of problems are identified and shown in Figure 2.

Hydrodynamics plays a tremendous role; however, it has usually been modelled only using the Rayleigh quadratic drag and by a simplified form of the added mass effect. The drag coefficient and the added mass coefficients for an arbitrarily shaped iceberg are highly variable tuning parameters in the forecasting models. Unfortunately, accurate Computational Fluid Dynamics (CFD) methods are hardly applicable when iceberg shape is uncertain, the Reynolds number is very high, and the
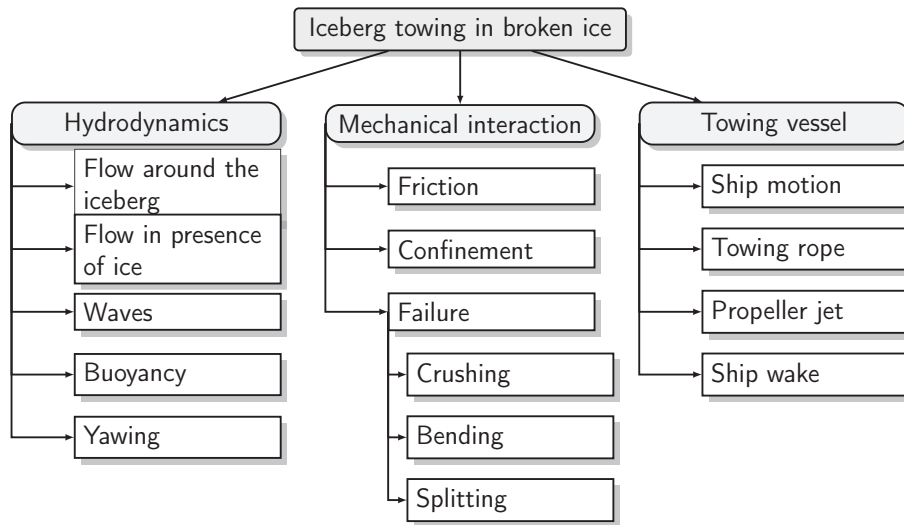
Figure 2: The motion of an iceberg through broken ice consists of many physical phenomena that must be considered. Some of the problems have already been studied.

flow characteristics are undetermined. For example, for an iceberg having a diameter of 50 m, the Reynolds number is on the order of 10^6–10^7. The complex hydrodynamics affects the broken ice motion around the iceberg. The hydrodynamic effects in the vicinity of a floater have been studied by Tsarau and Løset (2015). It has been found that in the flow induced by a large floating object, ice floes may loose more than 20% of their relative velocity when approaching the object.

The flow of broken ice itself around the iceberg causes large loads, especially when the ice concentration is high. When the ice pressure on the iceberg is too high, the ice floes start to crush or fail in bending or splitting depending on the size, relative velocity, thickness, confinement, etc. It is assumed, that, during free drift or towing, the failure of ice is not likely to occur, because the relative velocities, characteristic floe size and ice concentration are low; in other words, the confinement is not sufficient (JP1). Some local crushing occurs, but this does not significantly change the shapes of the ice floes.

According to Bigg et al. (1997), the wave radiation force generally contributes less than 5% of the total force. In addition, the ocean waves attenuate in broken ice within a few nautical miles from the ice edge (Frankenstein et al. 2001). Finally, towing operations are not likely to be performed in high sea states.

Rolling stability and rotational stability around the vertical axis are extremely important during towing operations. A towing operation is impossible without ensuring that the iceberg will not roll, and towing is hardly feasible if the iceberg is yawing.

4

The problem becomes significantly more complicated when the towing vessel is considered. In addition to the ship motion in broken ice, one must simulate the towing line, the ship wake and the jet stream from the propellers. Then, the whole towing operation can be simulated. A number of studies have been conducted to determine the influence of surface waves (Marchenko and Gudoshnikov 2005) and the rotation of an iceberg (Marchenko and Ulrich 2008) on the towing force. The numerical modelling results have been compared to model-scale experiments in the Hamburg Ship Model Basin (HSVA) by Marchenko and Eik (2012a). For the towing vessel, an optimal guidance and control algorithm has been developed and tested in a model-scale experiment (Orsten 2014). The presented model is not coupled with any ship model; however, if the former is available, it can be coupled without significant effort.

This doctoral study concentrates on drift data collection and analysis, and on the numerical modelling of iceberg towing in broken ice. The field experience drove several important assumptions for numerical modelling, and provided characteristic drift velocities for ice and icebergs. In addition, the yawing of drifting icebergs was measured for the first time and reproduced by modelling. Several more interesting conclusions were made based on the drift data analysis. Then, an attempt to develop a new model of iceberg motion through broken sea ice based on the non-smooth DEM has been made. In addition to continuous forces acting on an iceberg in open water, the model considers the contact forces between the bodies. The hydrodynamics is improved by a potential flow in the iceberg's vicinity, which allows one to reproduce closing wakes and accelerate ice flow on the sides. As a result, the towing force might be obtained for different parameters — towing speed, ice concentration, and ice thickness. The analysis of the simulations might help to plan towing operations in ice.

1.3   Research approach and time plan

A literature survey revealed the lack of knowledge about icebergs in ice. Fairly good models exist for iceberg drift forecasting in open water (Kubat et al. 2005; Kegouche 2010; Turnbull et al. 2015) or separately for sea ice drift forecasting (Blunt et al. 2013). In the first half year of the present doctoral study, a simple model considering ocean drag forces, wind and the Coriolis forcing was been developed and applied to the Research Vessel (RV) Lance moored to a drifting ice floe (CP2). RV Lance was considered as an iceberg drifting in broken sea ice. Ocean current and wind were measured precisely at

the ship position and used as input to the model. The ice forces were identified as one of the reasons for the deviation between the modelling results and the actual drift.

Next, a number of surveys in the Barents Sea and in the Greenland Sea were conducted to observe and track icebergs and sea ice (CP3, CP4 and CP5). First, the drift data analysis was performed. It considered absolute drift velocities of ice features, relative drift velocities of ice floes in the vicinity of icebergs, drift velocity spectra, curvatures of drift trajectories and yawing of icebergs. The yawing of drifting icebergs was measured for the first time and revealed interesting consistency in angular velocities. It was explained by gradual adjustment of iceberg orientation under slowly rotating tidal currents. The theory of a body motion in an unbounded fluid was employed to simulate the yawing. The field data analysis and the modelling of rotation have been published in JP3.

During the field campaigns, it was also observed that no ridging occurred around the icebergs. Considering the low relative velocities and low confinement, breaking of ice floes is unlikely and can be excluded from the considerations. Moreover, analysis of the Comprehensive Iceberg Management Database (Rudkin et al. 2005) by Canadian Program of Energy Research and Development (PERD) reveals that the average towing speed-made-good in open water does not differ significantly from the average free drift velocity (Figure 3). This speed difference for towing in open water is only 0.17 m/s; even less is expected in pack ice. Therefore, no large failure is expected during iceberg management in ice either. These assumptions allowed a planar geometry to be used for the model.

Further considerations were the following: Iceberg towing in ice is challenging; therefore, full-scale towing operations will not occur in highly concentrated ice and at high velocity. Towing is usually performed in the small ice management zone around the offshore structure. On such scales, the behaviour of each ice floe is important, and the broken sea ice should be considered as a discontinuous material. The non-smooth DEM was chosen to model the behaviour of the ice. The method treats every ice floe as a distinct body and detects and resolves contacts if they appear between the floes. Contacts are treated as almost inelastic; thus, the iceberg typically pushes the floes in front and on the sides.

The continuous forces in the model are presented by ocean and air quadratic drag, the Coriolis force, the added mass force, the hydrodynamic force acting if the ocean current is changing, and the towing force. In addition, the potential flow solution was applied within a short distance around the iceberg to increase the accuracy. The flow is characterised with up to twice the current velocity on the sides of an iceberg, resulting
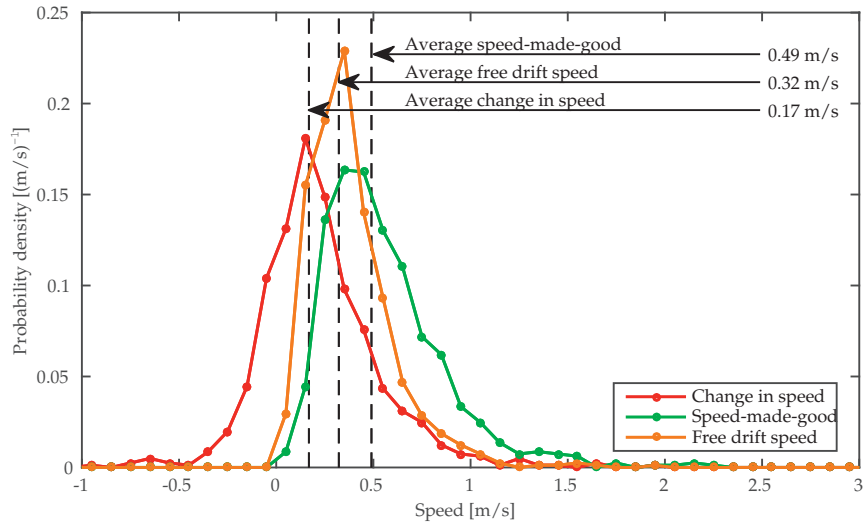
Figure 3: Distribution of velocities for towing operations in open water obtained from the PERD database.

in up to four-times higher drag forces acting on small ice floes. Besides, there appear components of the current that push the floes into the wake area. The yawing of iceberg as in JP3 has not been implemented in the non-smooth discrete element model so far.

Ice floes and icebergs are polygon shaped, and their density, defined as the mass per square meter, is assigned to every ice feature. It was found through a literature review that the ice floe size distribution in nature follows a power law (see JP1 and CP6 for references). Simultaneously, an ice field may be characterized by the ice concentration. A special algorithm was developed to generate initial set of polygonal ice floes that fill the simulation domain up to a given ice concentration (JP1 and CP6). In the newly generated ice field, all the ice floes are randomly shaped, and their sizes are distributed according to the power law.

Contacts between the bodies in the model are resolved by applying separation impulses found using the non-smooth discrete element method. The conversion of the impulses into contact forces is not always straightforward because the force evolution during each time step is unknown. Initially, it was proposed to use the relation between the kinetic energy before collision and the collision force to calculate the force magnitude. The model performance was first studied under single-floe collisions with a massive stationary object (JP1). Then, a collision impulse-force relation was found to be more robust, but it had to be downscaled for the validation study (JP2). Further, it was realized that crushing must be correctly represented when simulating towing in

ice concentrations above 70%; thus, the crushing constrain was introduced (JP2).

At the next stage, the model was validated by comparing numerical results with towing tests conducted in HSVA and several analytical approximations (JP2). The validation demonstrated that boundary conditions, concentration and towing velocity are very important. Average forces measured in the experiment were reproduced fairly well.

The present thesis is organized as a collection of papers, with a short overview of the work that has been performed. The overview part is structured in the following way: Current experience related to IM, both icebreaking and iceberg towing is presented in Chapter 2. That chapter covers full-scale experience, small-scale towing tests and state-of-the-art numerical modelling. Chapter 3 presents observations and drift data collected during sea ice and iceberg tracking in the Barents Sea and the Greenland Sea in 2011–2014. Chapter 4 presents the traditional drift modelling approach and a model of iceberg drift incorporating rotation. Chapter 5 describes the numerical model of an iceberg in broken ice and its main assumptions. Then, the model is validated in Chapter 6 using the model-scale tests in HSVA, and the results of the modelling are compared with some analytical estimates. This is followed by a discussion of the modelling process and model limitations. Finally, the overall conclusions and recommendations are made in Chapter 7.

The evolution of the present doctoral study is shown in Table 1.1.

Table 1.1: Schedule of the major activities.

	2012				2013				2014				2015			2016	
Courses				■	■		■		■								
Field activity		■	■			■	■		■								
Data analysis	■	■	■			■	■			■				■			
Literature review	■	■	■														
Model formulation					■	■	■	■	■	■							
Validation study						■	■	■	■	■	■	■	■	■			
Conferences		■				■											
Thesis													■	■	■	■	■

2 Overview of the ice management: full-scale experience, small-scale tests and numerical modelling

In this chapter, the operational experience and small-scale tests related to icebreaking and iceberg towing are reviewed. The simulation of icebergs in ice requires the coupling of models both for broken ice and icebergs. With this in mind, the state of the art in the numerical modelling of sea ice and iceberg drift is also presented.

2.1 Physical ice management

In the last few decades, IM has become a powerful technique that has significantly reduced average and peak loads on Arctic offshore structures, both fixed and floating (Hamilton et al. 2011). The set of IM activities depends on the local metocean conditions, and it is unique for every large offshore field.

Currently, physical IM can be roughly divided into icebreaking and iceberg towing. IM has been applied at the areas where only sea ice or only icebergs exist. Most sea ice management practices come from the Beaufort Sea, Sakhalin and the Arctic Coring EXpedition (ACEX) in the Arctic Basin. Iceberg management has been performed on the Grand Banks and to the West of Greenland for more than 40 years, where normally no sea ice is present simultaneously with icebergs.

2.1.1 Icebreaking

The effect of sea ice will have to be reduced as much as possible if an iceberg towing operation is planned in broken ice. The effect of ice may be reduced by performing icebreaking and, thus, reducing effective floe size. Icebreaking activities are usually performed upstream from the protected structure. But they are an important part of IM and have to be considered. A brief description of the major sources of icebreaking experience is presented below.

Historically, successful icebreaking operations supporting floaters on DP started in the Beaufort Sea in 1976 (Wright 1999; Hamilton et al. 2011). The CANMAR drillships were deployed with eight-point mooring systems and up to four icebreakers working upstream. Gradually improving the fleet, operational experience and IM strategies the feasibility of operations in ice and the operating season were significantly extended. Later, when the floater Kulluk was designed, operations in much heavier ice conditions became possible (Wright 1999, 2000). Kulluk had a strong circular hull to resist multiyear ice, a submerged twelve-line mooring system and a more sophisticated ice management plan.

IM has been performed at Sakhalin 2 to extend the season beyond the open water conditions in the springs of 1999–2001 and prior to the winter of 2000 (Keinonen et al. 2000). The IM system proved to be a success in a very dynamic ice environment consisting of 1-m-thick ice and ridges drifting with velocities of up to 40 nm/day.

Another example of IM is a station-keeping in ice performed by Vidar Viking with the support of IB Oden and IB Sovetsky Soyuz in 2004 (Keinonen et al. 2006). Vidar Viking managed to spend nine days on manual DP control in the highly concentrated multiyear ice in the Arctic Basin. IB Sovetsky Soyuz reduced the ice floe size from kilometres down to a few hundred metres, and IB Oden reduced the floe size further down to tens of metres.

Finally, various ice management trials were performed recently during a number of expeditions in the Greenland Sea and around Svalbard (Farid et al. 2014). Icebreaker performance for different breaking patterns and ice observation systems were the focus of these tests.

2.1.2 Iceberg towing

Most of the iceberg management experience comes from the Grand Banks, Newfoundland and Fylla at the West Coast of Greenland (Figure 5a). A large

(a) CANMAR drillship in managed sea ice

(b) Kulluk in managed sea ice

(c) SALM buoy and Molikpaq in managed ice at Sakhalin, Spring 2002

(d) Satellite image of Vidar Viking during station-keeping and two assisting icebreakers upstream

Figure 4: Examples of sea ice management to support offshore operations in Arctic

iceberg towing database has been collected starting from 1973. The data set covers icebergs' physical parameters, metocean data, types of management, technical details, etc. for most of the records. Several interesting conclusions can be made according to the analysis provided by Rudkin et al. (2005) and the report by McClintock et al. (2007).

The conventional method to tow an iceberg is single-vessel towing when an iceberg is encircled with a floating synthetic tow line, connected to a steel hawser afterwards, and pulled away from the protected structure by the vessel (Figure 5b). The synthetic tow line or net is deployed in 400 m segments, and the number of segments depends on the iceberg size (C-CORE 2004). Shorter lines require shorter deployment times, however, on the other hand, chasing the free end when encircling the iceberg should be avoided. To improve iceberg pitching stability, the towing force vector must produce a lower overturning moment (Figure 6). To achieve this, the moment arm can be reduced using a catenary underwater. This also helps to reduce the line stiffness. Deeper positions of the catenary require longer rope, which improves stability; however, this reduces the

(a) Siem Aquamarine tows an iceberg in Greenland, August 2011 (Johnson 2011)

(b) Single vessel iceberg towing scheme (McClintock et al. 2007)
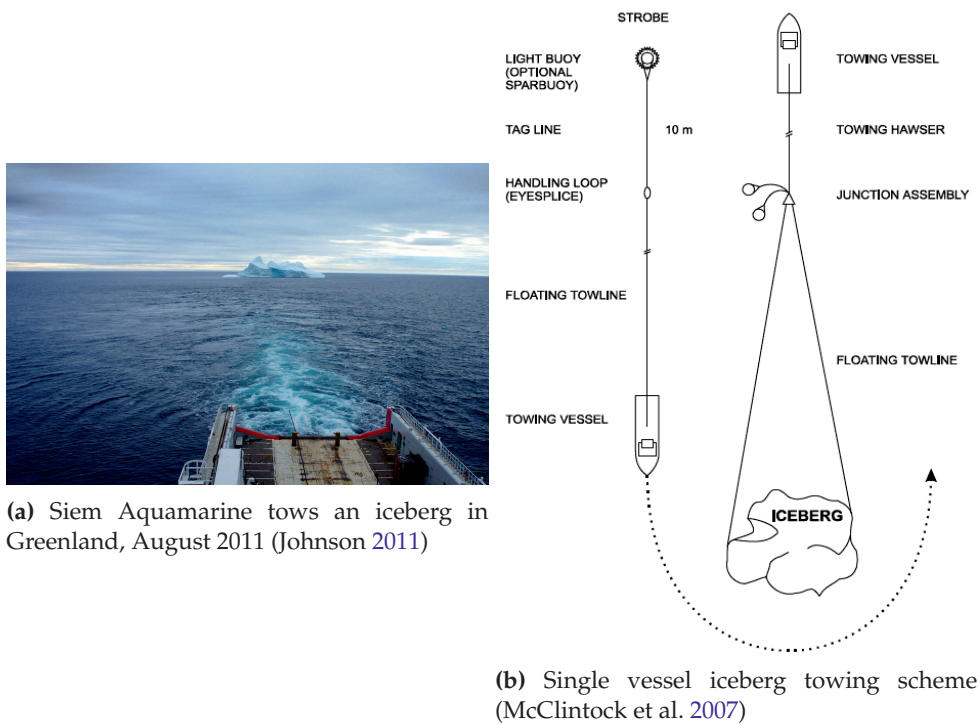
Figure 5: Examples of iceberg towing in open water

applied towing force (C-CORE 2004). This becomes one of the reasons for the weak dependence of the towing force on the iceberg mass.

Other types of towing are the two-vessel towing, water cannon deflection, and propeller washing. The last two methods are applied to icebergs that are difficult to tow with a tow line due to their irregular shape or small size.
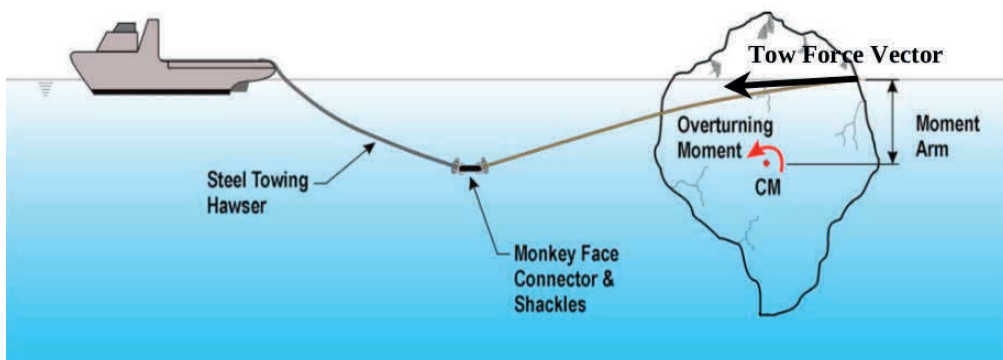
Figure 6: An operational set-up employing the towing line catenary results in improved pitching stability of icebergs (C-CORE 2004)

12

The success rate of iceberg towing in open water is quite high. There are two definitions of successful towing:

- Operational success is reached when downtime is avoided
- Technical success is reached if a) demonstrated change in course was achieved and b) the towed iceberg achieved a course made good with one or multiple attempts

In the first case, the success rate is 99%, while in the second case it is 85.5% (Rudkin et al. 2005). Among the unsuccessful tows, the most common end reason was towing line slippage and iceberg rolling.

Despite the experience in icebreaking and open water iceberg towing, the success and feasibility of iceberg towing in broken ice is still under question. There have been few attempts to tow an iceberg under icy conditions in the Barents Sea and on the Grand Banks. In April 2004, a bergy bit (or possibly remains of a large ice ridge) approximately 50 m in diameter was towed in the Barents Sea when the sea ice was present (Marchenko and Gudoshnikov 2005; Stepanov et al. 2005). The ice thickness was less than 10 cm and the concentration was approximately 90%. Later, in April 2005 a larger iceberg having a diameter of approximately 80 m was been towed in thicker, but fragmented ice cover (Marchenko and Ulrich 2008). It was been observed that the iceberg started to rotate when the towing vessel encountered an ice floe and decelerated. The rotation caused increased tension in one of the rope branches; thus, when the vessel accelerated, the rope was broken. Finally, Randel et al. (2009) mentioned a case of towing on the Grand Banks but did not provide any details on the operation.

Worthy of note, the detection of small icebergs in ice is also problematic. In addition, the performance of coupled iceberg–sea ice drift models that can be used to forecast on tactical scales is still under question.

The mentioned operational experience highlights the following aspects that have to be considered when modelling the towing of icebergs:

- the towing set-up that defines the reaction in the towing line
- realistic iceberg shape which is important when modelling hydrodynamics, contacts with ice floes and assessing the stability
- the ice will likely be managed, and towing will occur at low velocity relatively ice

13

2.2 Experimental studies

A comprehensive review of experimental studies related to ships in discontinuous ice can be found in Metrikin (2015). On the other hand, the experiments on iceberg towing are very limited. Open water tests and towing in ice have been conducted in HSVA and analysed by Eik and Marchenko (2010) and Marchenko and Eik (2012a). In short, model icebergs were towed according to different scenarios in open water and in broken ice of various concentrations. Due to complex hydrodynamic effects and insufficient ice field documentation, these test results are difficult to interpret. However, it is the only source of relevant data that can be used to validate a numerical model of iceberg towing in broken ice. These towing tests are used for the validation of the numerical model in the present study and will be described in Chapter 6.

2.3 Numerical modelling

The numerical modelling of iceberg towing in ice requires models for both ice and icebergs in open water. Sea ice and managed ice have been treated on different scales in terms of the continuous approach and the discrete element methods. Icebergs drifting in open water have been modelled using statistical approaches, where previous drift characteristics were used to make a prediction, or more often as point masses drifting under the action of different applied forces.

2.3.1 Continuum mechanics models

A sea ice floe is defined as "*any continuous piece of sea ice*" (WMO 2014). A large number of floes can be treated as a continuum. The characteristic length scale in this case is usually much larger than the size of an offshore structure and much larger than ice floe sizes. Continuous models have been used extensively on global and regional scales: the Baltic Sea, the Bohai Sea, the Beaufort Sea, the Kara Sea, the Greenland Sea, etc. (Leppäranta 2011). These models require input from large-scale atmospheric and ocean models to simulate the dynamics and thermodynamics of the sea ice. In addition, more complex, fully coupled atmospheric-ocean-ice models

are used for climate modelling (Zhang and Hunke 2001); however, they are hardly applicable for short time limits required by the offshore industry. In relation to IM, continuous models can be used when the presence of ice and its estimated thickness and concentration must be predicted in a particular area, for example in the vicinity of a protected offshore structure.

More than 40 years ago Coon et al. (1974) proposed, on large scales, the sea ice can be described as an elasto-plastic material. In his model the kinetic energy of the sea ice dissipates through plastic deformations affecting the ice thickness. Later, the model of Hibler (1979) treated the ice as a non-linear viscous compressible fluid. He introduced the relationship between the ice thickness, concentration and pressure to model dissipation:

$$P = P^* h \exp[-20(1-c)] \tag{2.1}$$

where P is the pressure in the ice, $P*$ is a constant on the order of $10^4 \mathrm{N/m}$, h is the ice thickness, and c is the ice concentration. Another model based on an elastic-viscous-plastic representation of sea ice was proposed by Hunke and Dukowicz (1997); now, the model is known as CICE (Hunke et al. 2015). There exist several other sea ice forecasting models, basically governed by similar equations (see for example (Campin et al. 2008; Notz et al. 2013)).

In addition to the Eulerian representation, the Lagrangian approach can be applied on large scales. For example, the recent model of Rampal et al. (2016) provides 10 km in spatial resolution and 200 s simulation time steps and reproduces ice drift velocity with a root mean square error of approximately 2.5 km/day. The approach utilizes unstructured meshes that preserve localized effects, such as ridges or open water leads, and provides improved numerical stability. The meshes are deformed as the ice deforms, and remeshing is performed when deformations become too excessive.

Tactical sea ice forecasting is based on similar principles of free ice drift but on much smaller spatial and temporal scales. Such models have been used for decision support during IM operations. Sea ice hindcasting in the Beaufort Sea has been performed with high accuracy (Turnbull and Pilkington 2012; Blunt et al. 2013). Using measured, but not forecasted wind data, the drift forecasting error was reduced to less than 2 km/day.

Worthy of note, a particle-in-cell (PIC) sea ice model was developed that advected ice floes between grid cells, while ocean currents, winds, ice concentration and thickness were recalculated using the Eulerean approach. An attempt was made to simulate sea ice in the Beaufort Sea (Flato 1993) and to the East of Labrador (Sayed et al. 2002); however, the discrepancies with observations were found due to uncertainties introduced by ocean input data. On much smaller scales, PIC has been successfully

applied to calculate ice forces on ships and offshore structures in ice, both in two dimensions (Sayed et al. 1999; Sayed and Kubat 2011) and three dimensions (Barker et al. 2014).

Icebergs drifting in open water have been modelled as material points drifting under a number of environmental forces. The major driving forces are the ocean and wind drag forces, the Coriolis force, the added mass force, the hydrodynamic force due to unsteady current, the sea slope force and the wave force. Existing approximations for the forces allow icebergs to be forecasted in open water or allow prediction of optimal towing direction (Orsten 2014). A large number of models have been published for the Grand Banks (Kubat et al. 2005; Allison et al. 2014), West Greenland (Turnbull et al. 2015), East Greenland (Skarbø et al. 2016), the Barents Sea (Eik 2009; Keghouche et al. 2009) and Antarctica (Lichey and Hellmer 2001).

Different techniques have been applied to understand the uncertainties and sensitivity of the prediction to different input data and coefficients. A common approach is to manually choose optimal drag coefficients that result in minimal forecasting errors (Kubat et al. 2005; Turnbull et al. 2015). Kegouche (2010) applied a Kalman filter to find optimal values for the drag coefficients for a number of icebergs in the Barents Sea. In addition to improved prediction accuracy, the evolution of optimal values for the drag coefficients was linked to the processes that were not captured by the model, e.g. shape deformation during the drift. Ensemble hindcasting has been performed by Allison et al. (2014), where a large number of simulated trajectories were obtained for the same iceberg but for various initial conditions and input data. However, in comparison to Kegouche (2010) no accuracy improvement has been found for the ensemble mean trajectory. The very recent study of Andersson et al. 2016 suggests a method that finds an ancillary current using an estimator similar to Kalman filter. The ancillary current corrects direction and magnitude of the input current and significantly improves short-term forecast.

Despite the variability of techniques, the ice and iceberg drift prediction relies on the metocean input data. Therefore, the forecasting performance fully relies on the accuracy of the currents and wind prediction. Current large-scale atmospheric and circulation models do not provide sufficient quality, especially where the current speed is low (north-east Greenland offshore) or the bottom topography is complicated (Grand Banks or to the west of Greenland). Winds and ocean currents measured *in situ* result in better hindcasting accuracy (Sodhi and El-Tahan 1980; Kubat et al. 2005), but such data are difficult to obtain.

In relation to the towing operations, several studies have analysed oscillations

appearing between icebergs and towing vessels (Marchenko and Ulrich 2008; Marchenko and Eik 2012b, 2012a). The analytical model demonstrated that, for steady-state towing, the oscillations of the system including the vessel, towing line and iceberg, would disappear. For towing in waves, the model is able to estimate towing force oscillations. Modelling these oscillations, however, is beyond the scope of the current thesis.

2.3.2 Discrete element method

On scales where the continuum hypothesis is not applicable, continuum mechanics fails to describe material behaviours. The DEM may be applied to describe a discontinuous material, i.e. one consisting of discrete particles or bodies. Originally the method was used in rock mechanics to treat large deformations in rock masses (Cundall 1971). One of the first applications in relation to sea ice was based on disc-shaped ice floes experiencing viscous forces at contacts (Hopkins and Hibler 1991). Progress in computational resources increased the number of ice floes in simulations, improved the geometry and enabled coupling with the Finite Element Method (FEM). Recently the DEM has been used to model rubble ice (Polojärvi and Tuhkuri 2013), ships in ice (Richard and McKenna 2013; Ji et al. 2013), sea ice drift (Herman 2016), ice-structure interaction (Shunying et al. 2015) and glacial ice fracture (Riikilä et al. 2015).

In the method each body is acted upon by external forces (for example, the gravitational force or drag forces) and contact forces that appear when bodies are in contact. The contact forces reflect material properties and may consist of elastic, viscous and plastic terms acting along the contact normal or tangent. The sliding friction force or rolling friction resistance for circular or spherical particles is added in the tangential direction. The force constituents are calculated using the contact geometry and the relative velocity at the contact. Contact detection is performed by checking if the shapes of advancing bodies overlap geometrically at a current time step. Detection algorithms are well established for a variety of shapes (Munjiza et al. 2011).

The forces are integrated to find velocities and positions of the bodies at every time step. Accurate integration requires small time steps, especially for stiff bodies. The choice of time step may also depend on the particle size and relative velocities in the simulation. The resulting velocity evolution and force evolution are continuous in time. This is why the conventional DEM is sometimes called "*smooth*". More details on smooth DEM algorithms can be found in Munjiza et al. (2011).

Lattice models are based on principles similar to DEM — ice floes are represented by lattices consisting of point masses linked by visco-elastic units (Berg 2016). The ice floes are possible to crush and split by breaking connections between the point masses.

Worthy of note, exact expressions for contact forces exist only for a narrow class of shapes and under the assumption of frictionless elastic contact. E.g. the contact force between elastic spheres is proportional to the penetration depth to the power of 3/2, or the contact force between infinite elastic cylinders with parallel is proportional to the penetration depth to the power of 1, and interestingly it does not depend on their radii (Landau and Lifshitz 2003). In addition, the time step needed for stability of the method must be very small. Thus, for a large number of arbitrary-shaped bodies (such as ice floes) the simulation may require large computational resources while providing an approximate solution.

As an alternative to the smooth DEM, the non-smooth DEM or contact dynamics has been widely used to simulate granular materials. Recently, it has been applied to simulate ships in ice during station-keeping (Metrikin 2014; Kjerstad et al. 2015) and manoeuvring (Lubbad and Løset 2011; Konno et al. 2013; Alanweh et al. 2015).

Instead of integrating the forces during contacts, the non-smooth DEM considers contact impulses that are calculated based on the relative velocities of the interacting bodies. The normal component of the contact impulse has to keep contacting bodies apart and therefore it must never be negative. The time step in the non-smooth DEM is chosen to be on the order of the collision time, which results in much faster calculations than in the conventional DEM. The price to pay is the accuracy of the force calculation which is the time derivative of the impulse.

In general, it is impossible in the non-smooth DEM to determine the evolution of the force during a collision (Radjai and Richefeu 2009) and only its time-average can be found. However, in the current study, it has been proposed to estimate the magnitude of the force based on the known relation between the peak force magnitude and the collision impulse (Timco 2011). As in smooth DEM, variability in shapes and mechanical properties of sea ice results in an approximate, yet much faster solution. This approach is implemented in the current version of the model of iceberg towing in ice (JP2). For more details on the non-smooth DEM and rigid body dynamics, see Featherstone (2008).

As a separate method, but still consisting of interacting particles, Smoothed Particle Hydrodynamics (SPH) has been applied to sea ice (Gutfraind and Savage 1997). This approach is similar to the DEM; however, the particle characteristics are spatially smoothed using a kernel function. The particles interact with each other and respond

18

to external force fields, and thus, their velocities and positions can be found for each advancing time step. SPH has been applied to simulate the motion of 4–10-wide km disc-shaped ice floes in the coastal zone, the marginal ice zone and narrow channels.

3 Observations

Little is known about sea ice influence on the drift of icebergs. To approach the problems of towing or forecasting in ice, the drift of icebergs and ice must be studied *in situ*. Several tracking campaigns were conducted in the Barents Sea and in the Greenland Sea between 2011 and 2014. Drift characteristics of icebergs and sea ice have been obtained and analyzed. They can be used for numerical modelling or for designing and preparing offshore operations in ice. Some oceanographic conclusions have been made as well. Detailed analysis can be found in JP3 and in CP1–CP5. In this chapter the major conclusions are presented.

3.1 Kinematics

A total of 8 ice floes were tracked in the Barents Sea in 2012–2013, and 9 icebergs and 10 ice floes were tracked in the Greenland Sea; their tracks are presented in Figure 7. These two locations were chosen as relevant to the current study — icebergs up to 3.7 million tons have been observed in the Shtokman area (Zubakin et al. 2004); Kanumas at the Greenland Sea is a promising offshore area but is under extremely hard ice and iceberg conditions.

The sea ice to the east of Svalbard, arriving from the Arctic Basin or formed locally, meets warm southern currents, causing fast melting of the ice. In April/May, when the tracking occurred, the ice cover is usually fragmented, and ice floes are relatively small, especially if broken by heavy waves. For example, in 2014, the only ice floe larger than 1 km across was found deep into Storfjorden; it was possibly part of landfast ice before. The lifetime of such ice floes below 78°N in spring is usually very short.

The waters to the south-east of Svalbard are relatively shallow, reaching depths of less
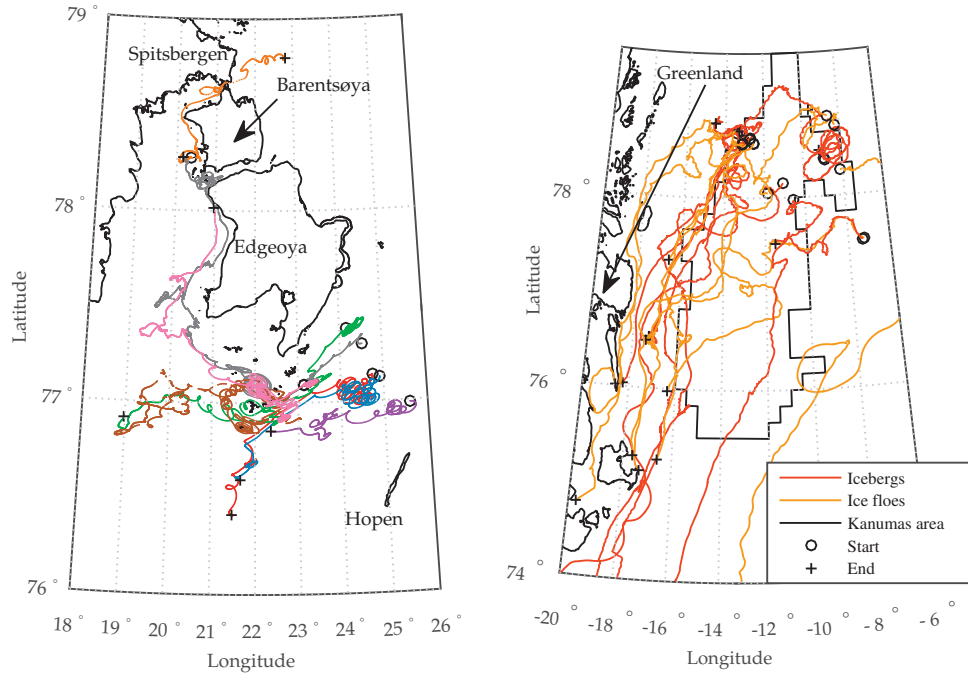
(a) Barents Sea. Each color corresponds to a different ice floe.

(b) Greenland Sea. Red denotes icebergs trajectories, and orange is used for ice floes.

Figure 7: Ice and iceberg tracks obtained during the 2012–2013 tracking campaigns

than 50 m in some areas. This causes strong tidal currents, resulting in very distinct loops on ice trajectories (Figure 7a). Tidal motion is enhanced in the vicinity of small islands, as is possible to see to the south of Edgeøya. These tidal currents accelerate ice floes to high velocities, up to 1.26 m/s. In addition, one of the trackers was deployed on the landfast ice in Storfjorden on the 2nd of May, 2013; the landfast ice breakup occurred on the 21st of June, 2013.

The average shelf depth in the Greenland Sea is approximately 300 m; consequently, the tidal currents are weak, and the ocean currents have a persistent direction along the strait coastline. Thus, the drift trajectories contain fewer loops, and the relative role of winds is greater. Ice tends to become landfast closer to the land, and a number of icebergs were captured during the winter season.

Characteristic drift velocities are required to make rough estimates of a time to potential collision for an offshore structure. They also indicate how massive a collision with an iceberg might be. Finally, they can be used when planning an iceberg towing operation. The following velocity data have been obtained from ice floes and icebergs

in the Barents Sea and in the Greenland Sea (Tables 3.1, 3.2, 3.3). The instantaneous drift velocity is denoted by $\vec{U}$, the mean drift speed is $\langle U \rangle$, its standard deviation is $\sigma(U)$, and the maximum value is U_{max}.

Table 3.1: Velocity statistics obtained from tracking ice floes in the Barents Sea

ID	Deployment date	Tracking duration [days]	$\langle U \rangle$ [m/s]	$\sigma(U)$ [m/s]	U_{max} [m/s]
BS1	18.04.2012	11	0.41	0.18	1.06
BS2	18.04.2012	9	0.43	0.18	1.08
BS3	20.04.2012	19	0.33	0.20	1.44
BS4	22.04.2012	8	0.37	0.18	1.05
BS5	30.04.2013	52	0.23	0.23	1.25
BS6	03.05.2013	34	0.32	0.20	1.25
BS7	03.05.2013	33	0.28	0.20	1.26
BS8	02.05.2013	9	0.30	0.35	3.87

Table 3.2: Velocity statistics obtained from tracking icebergs in the Greenland Sea

ID	Deployment date	Tracking duration [days]	$\langle U \rangle$ [m/s]	$\sigma(U)$ [m/s]	U_{max} [m/s]
117	21.09.2012	280	0.08	0.09	0.47
118	21.09.2012	269	0.08	0.09	0.47
120	21.09.2012	213	0.11	0.10	1.63
121	21.09.2012	228	0.11	0.10	1.10
6550	18.09.2012	102	0.28	0.27	1.66
127	24.08.2013	15	0.19	0.08	0.43
128	28.08.2013	259	0.15	0.08	0.54
129	24.08.2013	264	0.20	0.09	0.51
130	28.08.2013	259	0.15	0.08	0.54
131	29.08.2013	259	0.19	0.14	0.91
132	29.08.2013	259	0.19	0.14	0.93
1	30.08.2012	300	0.25	0.20	1.04
6	31.08.2012	17	0.15	0.08	0.41

Table 3.3: Velocity statistics obtained from tracking ice floes in the Greenland Sea

ID	Deployment date	Tracking duration [days]	$\langle U \rangle$ [m/s]	$\sigma(U)$ [m/s]	U_{max} [m/s]
119	21.09.2012	255	0.08	0.10	0.47
4560	22.09.2012	41	0.06	0.08	0.45
5390	23.09.2012	52	0.34	0.21	1.14
8660	22.09.2012	158	0.06	0.07	0.44
2	25.08.2013	8	0.19	0.09	0.40
3	28.08.2013	28	0.27	0.22	1.12
4	25.08.2013	32	0.32	0.22	1.21
5	29.08.2013	287	0.37	0.22	1.16
6	31.08.2013	36	0.21	0.14	1.02
9	30.08.2013	18	0.32	0.21	0.98

From the table, it follows that the drift velocities over Spitsbergenbanken are very high, mainly due to shallow depths and strong tidal currents. Tides are one of the reasons for such a looped drift pattern. South-east of Spitsbergen is a meeting point of warm remains of the North Atlantic Current and cold polar waters; therefore, the lifetime of ice floes here is relatively short. Due to this reason the trackers with dead weight attached were on the surface no longer than 20 days. In 2013, the trackers did not have any dead weight attached so they were tracked for much longer periods, and latter parts of their data may correspond to floating in sea water. The case of the tracker BS8 is special; the tracker was deployed on the landfast ice in Storfjorden. The tracker started to move in the end of June 2013, and its velocity reached an extreme of 3.9 m/s when the tracker went into a narrow strait called Heleysundet.

In the Greenland Sea, the average velocities are in general lower, but depend on the drift area. It was noted in JP3 that drift speed statistics are determined by whether the drift occurs in the central pack or in the shear zone. For the shear zone, lower velocities with distinct drift direction were observed.

3.2 Relative motion

The drift of sea ice and icebergs is coupled because sea ice provides additional forces that affect icebergs. Several pairs consisting of an iceberg and an adjacent ice floe were tracked to study differential drift and to understand how it correlates with the ice concentration and wind. The measured velocities were found to vary between the four different pairs. A recent study simulating the relative drift (CP1) concluded that the iceberg size and ice concentration are the most influential quantities affecting the relative velocity. Smaller icebergs drift together with ice, following the surface currents. They are also more influenced by the ice force because of their lower mass, while large icebergs are much less affected by the sea ice due to the greater influence of deeper currents.

The evolution of the measured relative distances between the ice floes and icebergs is shown in Figure 8. IB1 drifting in very close pack ice was captured and demonstrated almost no relative drift, as can be expected. This is in agreement with Lichey and Hellmer (2001), who suggested no relative motion for sea ice concentrations above 90%. Another three icebergs were drifting in very open pack ice and had much higher relative velocities, the largest iceberg having the highest relative velocity of 0.27 m/s.

24

Thus, the sea ice has its strongest effect on medium and small icebergs, but it can also affect large icebergs in the case of high concentrations. Based on simulations from JP2, it is expected that broken ice will influence the iceberg drift at concentrations above 70%.
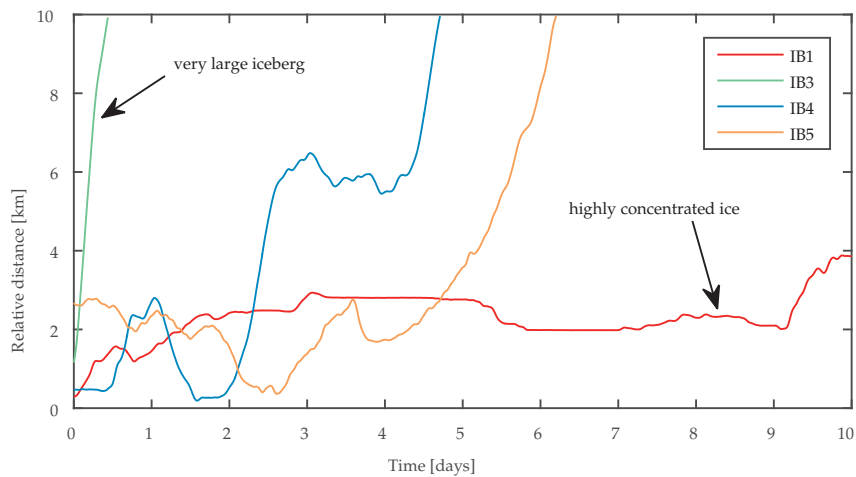
Figure 8: Evolution of relative distance between icebergs and ice floes

These four cases provide representative values of relative velocity between ice and icebergs. This information should be taken into account during towing operations in ice, because optimal towing direction becomes dependent not only on the relative ocean current, but also on the relative drift of ice.

3.3   Curvature of the drift trajectory

Being able to anticipate changes in drift direction is valuable for IM. For example, a protected vessel on DP needs assistance of icebreakers upstream in a narrow sector, which may be called an *ice corridor*. The shape of the sector can be narrowed, reducing the amount of icebreaking needed, if the local drift trajectory curvature and drift velocity are known. In addition, for a drifting iceberg, knowing how the drift trajectory is going to evolve in the near future is a helpful indicator for showing if the protected offshore structure lies in the way (Figure 9a).

As stated previously, the drift trajectory depends on local physical conditions influencing the drift, including the velocities of ocean currents, tides, wind, ice and

iceberg geometrical characteristics. All these data are required to make an accurate forecast. Statistical data on drift curvature in the area of interest may help to define ice drift corridors without actual forecasting. It will simply provide the information about the directions from which the ice and icebergs are most-likely to arrive.

(a) The drift corridor and the curvature radius

(b) Trajectory curvatures obtained for the different ice objects
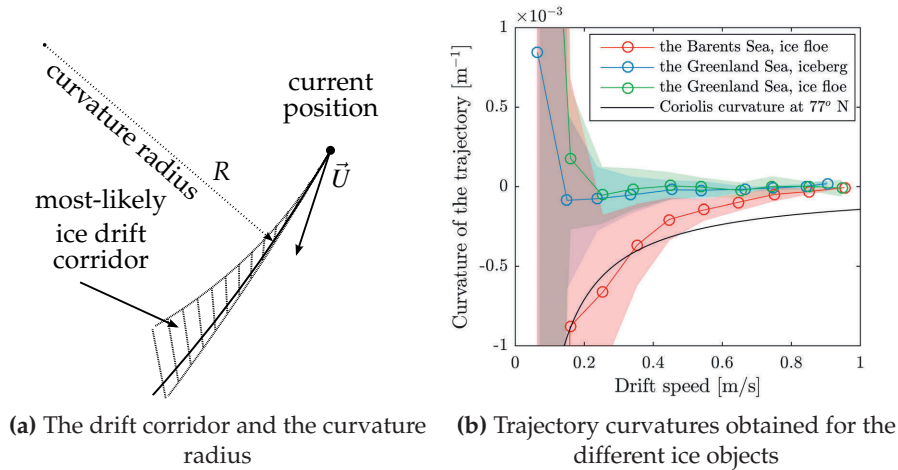
Figure 9: Statistical data on drift trajectory curvatures may help to optimize IM.

Trajectory curvature can be found using instantaneous acceleration and velocity, and its absolute values have been analysed for drifting icebergs and ice in CP3–CP5. The signed curvature is the reciprocal of the local curvature radius R, where a negative value corresponds to clockwise turn and a positive value corresponds to counterclockwise turn. It is obvious that, for a fast-drifting object, the magnitude of the curvature is small because it is more difficult for the object to change its drift direction due to its relatively high momenta. For a slow-drifting object, however, the trajectory curvature varies much more — the object can make a sharp turn or it can continue drifting in the same direction.

Typical relations between the curvature and the drift speed are shown in Figure 9b. The bounds of one standard deviation bounds are shown by color. For example, an ice floe in the Barents Sea having a drift speed of approximately 0.25 m/s is likely to make a turn with a curvature value of -0.66km^{-1} with a standard deviation of 0.48km^{-1} (Figure 9b). This defines a curved wedge having 0.9 km and 5.7 km radii that can be used for planning IM operations.

As seen from Figure 9b, the data confirms larger curvature radius for fast objects. For slow velocities, the curvature estimates are prone to large errors due to limited GPS accuracy and low frequency of the position updates. The trajectory curvature corresponding to the Coriolis radius is denoted by the black line. It demonstrates the

effect of the drift speed, but deviates from the data at high velocities. This occurred because the objects had to be accelerated by winds or currents, that tended to reduce the curvature.

3.4 Rotation of icebergs

The stability of icebergs in tow strongly affects the results of physical ice management operations. The rolling of icebergs is reported to be the second-most common reason for operational failure after rope slipping (Rudkin et al. 2005). Rolling stability can be estimated using the metacentric height position and is not covered in the present study. In addition to rolling stability, the yawing of icebergs can cause a 100% increase in towing line tension in the worst case for a single rope or net towing. Friction between the towing line and iceberg surface will lead to reduced tension on one end of the line and increased tension on another end. It might also occur in the case of net towing that the surface of the iceberg is rough, and the towing net will hook onto it. Again, this leads to a significant increase in towing line tension.

The yawing of free drifting icebergs has been measured for the first time using trackers deployed on icebergs in pairs. This is reported in JP3, CP3 and CP5. The evolution of the yaw angle of four icebergs has been obtained during the tracking campaigns in 2012 and 2013. The large tabular iceberg IB1 drifting in multi-year ice of high concentration in 2012 completed three full revolutions during the first three weeks of tracking. Afterwards, the rotation was almost absent because the iceberg was captured by the landfast ice. In 2013, the ice conditions were lighter, and the rotation of the icebergs was more consistent (Figure 10).

Notice that the yawing frequency is close to semi-diurnal or diurnal on certain intervals. It was suggested that tidal currents are responsible for the rotation, as their directions rotate with similar frequencies. An arbitrary-shaped body moving in a current will eventually become oriented with its blunt side against the flow. If the current direction rotates, a drifting iceberg will gradually change its orientation with it. The tidal current velocity to the north-east of Greenland rotated clockwise most of the time, therefore the icebergs demonstrated similar yawing. The dominant tidal constituents were M2 and K1, and the interplay between them likely resulted in yawing with close frequencies. An attempt to model the rotation of icebergs has been made in JP3, as is going to be described in the next chapter.
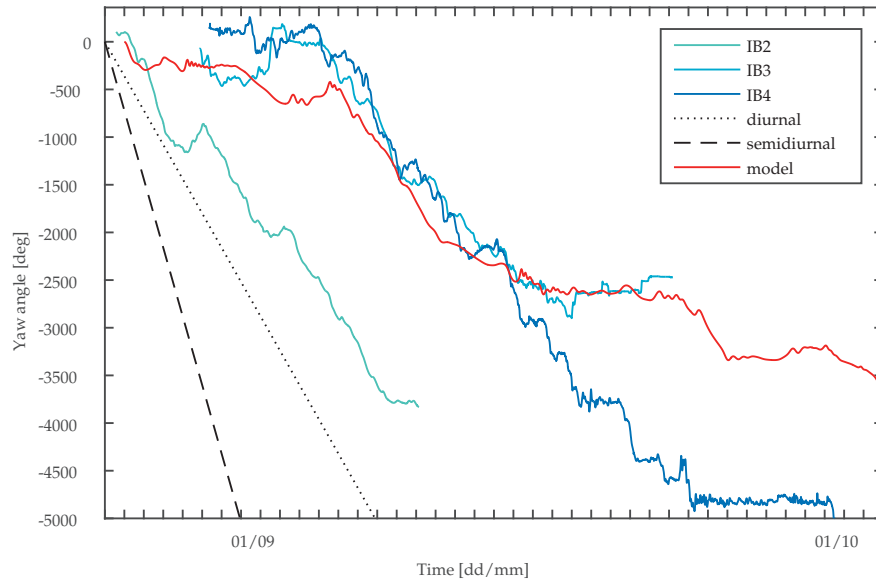
Figure 10: Measured rotation of three icebergs in 2013 and modelled (see Chapter 4) rotation of an elliptical iceberg.

Worthy of note, the instantaneous value of the angular velocity reached 0.001 rad/s at a few peaks. If this were to persist, the rotation with such an angular velocity would result in one full iceberg revolution in less than two hours. This is no doubt a remarkable value that is good to keep in mind before a towing operation.

4 Model of iceberg drift and rotation in open water

Traditional drift models have been considering an iceberg as a point mass with two translational degrees of freedom. Unfortunately, these models do not predict the rotation of icebergs. Equations for a solid body moving in an ideal liquid, resting at infinity can be used to find the yawing of icebergs. This chapter reviews a conventional model of iceberg drift in open water and presents the model of a rotating iceberg. The performance of the latter is going to be demonstrated using the measured iceberg rotation.

4.1 Traditional drift equations

First, the conventional drift model has to be formulated. It will be compared to the new model, including rotation, and this model is going to be used later when modelling icebergs in broken ice in Chapter 5.

Let us consider an iceberg that is circular in any horizontal cross section. For such an iceberg the drift equations are usually formulated in the East, North, Up (ENU) system fixed to the Earth's surface (Figure 11), the ENU system is non-inertial. Since the iceberg drifts on the water surface, the position of the iceberg in this system is defined by two coordinates: the easting x and the northing y.

The major forces acting on the iceberg are ocean and wind drag forces ($\vec{F}_w, \vec{F}_a$); the Coriolis force ($\vec{F}_C$); the hydrodynamic force ($\vec{F}_h$), including the added mass force and the force acting in a non-stationary current; the wave force ($\vec{F}_{wave}$); and the sea slope force ($\vec{F}_{ss}$). The towing force ($\vec{F}_{tow}$) is artificial and acts on the iceberg during the towing
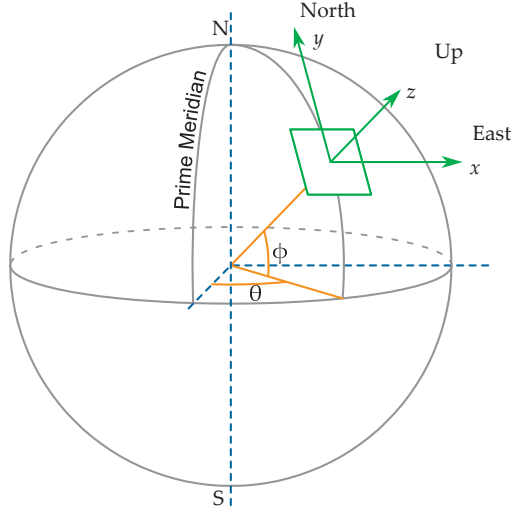
Figure 11: The East, North, Up (ENU) system fixed to the Earth's surface at the latitude φ and the longitude θ

operations. Thus, the equation of motion can be written as

$$M\frac{d\vec{U}}{dt} = \vec{F}_w + \vec{F}_a + \vec{F}_h + \vec{F}_C + \vec{F}_{wave} + \vec{F}_{ss} + \vec{F}_{tow} \tag{4.1}$$

where M is the mass of the iceberg and $\vec{U}$ is the velocity, whose components are the time derivatives of the coordinates x and y.

The flow around the iceberg is highly turbulent and is characterized by a large Reynolds number. The estimate for a 100-m-wide iceberg in a relative ocean current speed of 0.1 m/s gives

$$Re_f = \frac{UD}{\nu} = \frac{0.1 \cdot 100}{1.8 \cdot 10^{-6}} = 5.6 \cdot 10^6 \tag{4.2}$$

For the air, which has a much lower viscosity, the Reynolds number is even higher. Thus, the drag forces acting on the iceberg are calculated as the quadratic forms

$$\vec{F}_w^{IB} = \frac{1}{2}C_w^{IB}A_{keel}\rho_w|\vec{V}_w - \vec{U}|(\vec{V}_w - \vec{U}) \tag{4.3}$$

$$\vec{F}_a^{IB} = \frac{1}{2}C_a^{IB}A_{sail}\rho_a|\vec{V}_a - \vec{U}|(\vec{V}_a - \vec{U}) \tag{4.4}$$

The lower indices w and a denote water and air, respectively; C_w^{IB} and C_a^{IB} are the drag coefficients, usually on the order of 1 (Kubat et al. 2005; Keghouche et al. 2009; Turnbull et al. 2015); and A_{keel} and A_{sail} are the iceberg's keel and sail vertical cross-section areas.

The densities and velocities of water and air are denoted as ρ_w, ρ_a and $\vec{V}_w, \vec{V}_a$. In the situation where the iceberg shape, ocean current or wind profile is known, the drag forces may be calculated as the sum of the drags over the layers of depth or height using corresponding velocities and cross-section areas.

An additional hydrodynamic force $\vec{F}_h$ acts on an iceberg moving in an ocean current that varies in time. According to Newman (1977) one can write

$$\vec{F}_h = -m \frac{d(\vec{U} - \vec{V}_w)}{dt} + \rho_w V_{keel} \frac{d\vec{V}_w}{dt} \tag{4.5}$$

where V_{keel} is the volume of the keel. The first term is responsible for the added mass effect; an iceberg accelerating relative to water also has to accelerate a certain amount of it. The added mass m is usually a constant on the order of 0.5–1 of the mass M (Bass and Sen 1986; Kubat et al. 2005). The second term is a Froude-Krylov force accelerating the iceberg when the ocean current accelerates.

The Coriolis force is an inertial force acting on the bodies moving relative to the ENU system that rotates with the Earth. The effect of the Coriolis force becomes significant at time scales over several hours; therefore, the force can be neglected at the model scale. However, it must be considered for full-scale towing operations or when forecasting the drift for several hours.

$$\vec{F}_C = -M f \vec{k} \times \vec{U} \tag{4.6}$$

where $f = 2\Omega_{Earth} \sin \varphi$ is the Coriolis frequency, Ω_{Earth} is angular velocity of the Earth, $\vec{k}$ is the outer normal to the Earth's surface.

Objects floating on an inclined sea surface experience sea slope force that is approximated by

$$\vec{F}_{ss} = -Mg \nabla \zeta \tag{4.7}$$

where $\nabla \zeta$ is the sea surface gradient and g is the gravity acceleration (Lichey and Hellmer 2001). This force is important on large scales and the elevation can be extracted from large-scale ocean models.

Ocean waves exert additional force on floating bodies. Assuming short wavelengths compared to the iceberg characteristic size, vertical walls of the iceberg and no wave radiation effects, the following approximation might be used for the force magnitude

$$|\vec{F}_{wave}| = \frac{1}{2} C_{wave} \rho_w g l a^2 \tag{4.8}$$

where C_{wave} is the wave force coefficient, on the order of $0 - 1.16$, depending on the body shape and wave amplitudes (Isaacson and McTaggart 1990; Eik et al. 2009); l is

the waterline length; and *a* is the wave amplitude. The wave force is acting in the direction of wave propagation. The wave force is omitted in the model under the assumption of low sea states in sea ice.

The towing force $\vec{F}_{tow}$ is acting on the iceberg in tow, and it is actually the force of interest. This shows how much pull a tug-vessel must produce to tow the iceberg according to a certain plan. The towing force is limited by the ship power and by the net resistance produced by the water, air and ice. The limiting scenario is going to depend on the towing set-up and met/ocean/ice conditions. Obtaining characteristic towing force values for given ice conditions and towing velocities is one of the goals of the current study.

This traditional model has only two degrees of freedom and does not capture the rotation of the icebergs. Similar planar models have been tested in CP1 and CP2, and similar equations are used in the multibody model of an iceberg motion in broken ice JP1 and JP2.

4.2   Modelling of iceberg rotation

Equations for a body in an unbounded ideal fluid have been employed to model the rotation of icebergs (Lamb 1975; Marchenko 2014). A cylindrical iceberg with a symmetrical horizontal cross-section is considered. Original equations of motion have been formulated in a fluid which had to be at rest at infinity. Therefore, the equations of motion for a rotating iceberg are formulated in a non-inertial system which moves with the ocean current. The equations of motion are written using iceberg velocity projections onto a so-called *comoving* system (ξ, η) attached rigidly to the iceberg, and having its axes ξ and η parallel to the major axes of the horizontal iceberg cross-section (Figure 12).

$$\begin{cases} (M+m_{11})\dot{u} = (M+m_{22})\omega v + F_\xi \\ (M+m_{22})\dot{v} = -(M+m_{11})\omega u + F_\eta \\ (I+m_{66})\dot{\omega} = (m_{11}-m_{22})uv + M_\zeta \end{cases} \tag{4.9}$$

Here, u and v are the iceberg velocity projections in the comoving system, ω is the angular velocity, F_ξ and F_η are projections of the external forces (4.3)–(4.8) on the comoving system, and M_ζ is the external momentum of the force producing yaw. M is the mass of the iceberg, as defined earlier; I is the moment of inertia of the iceberg; m_{11} and m_{22} are the added masses for the principle axes of the iceberg; and m_{66} is the

added moment of inertia.

The external forces have been described above. Note that the Froude-Krylov force from (4.5) is excluded because of the choice of the reference system that moves with the fluid. In a non-inertial system, $-M\frac{d\vec{V}_w}{dt}$ must be projected on (ξ, η) and added to the right-hand sides of the first two equations in (4.9). This will eliminate the Froude-Krylov force, which is directed oppositely, because $\rho_w V_{keel} = M$ due to buoyancy.
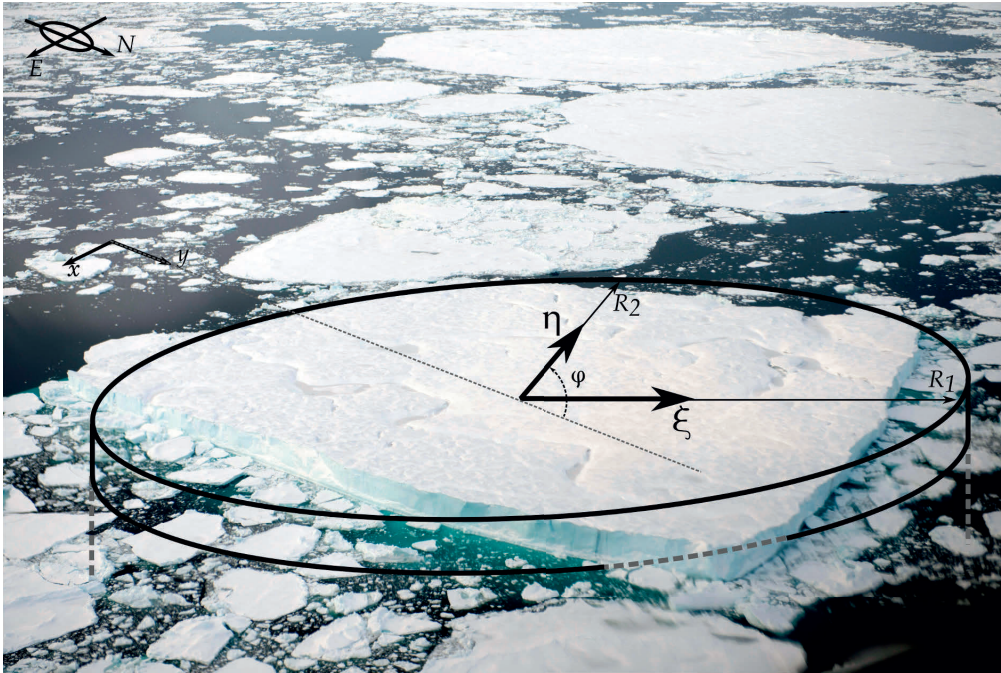
Figure 12: Drifting IB1 is approximated with an elliptical cylinder. The comoving system axes are directed along the major axes of the elliptical cross section.

For a perfectly circular cylinder, $m_{11} = m_{22}$, and no external angular momentum applied, the third equation from (4.9) can be discarded. The choice of the major axes has no importance for an iceberg with axial symmetry and thus, the axes of the system drifting with water can be chosen as the northing and the easting. The obtained system describes the traditional drift model formulated in a frame of reference that drifts with water. In addition, for ice floes, m_{11} and m_{22} are much smaller than the mass; thus, the rotational term in (4.9) can be neglected.

To find the drift and rotation of the iceberg, the external forces have to be projected onto the comoving system, and then, when the system is solved, the velocities u and v have to be projected back onto the ENU system. JP3 elaborates on the solution to the

system (4.9). The solution to the system for an elliptical cylinder is shown in Figure 10. Clearly, the simulated rotation is very similar to the measured rotations of the icebergs drifting to the north-east off Greenland. An iceberg with rectangular horizontal cross section has also been also simulated and demonstrated similar rotation features. The model of rotation is suggested to be used before towing operations to estimate possible yawing.

5 Model of iceberg motion in broken ice

The model simulating icebergs in ice is based on the conventional open water drift model described in the previous chapter and on the non-smooth discrete element model for interaction with the broken ice. In the model, discrete bodies, such as ice floes, and an iceberg are drifting under the action of environmental forces and the towing force applied to the iceberg, which are continuous in time. On the other hand, the interaction between these bodies is discontinuous. The forces appearing at contacts are calculated using the non-smooth DEM. A review of the model basics is given below; more details can be found in JP1 and JP2.

5.1 Continuous forces

When an iceberg moves through broken ice during natural drift or towing operations, it experiences additional resistance from the ice. Floe size and thickness affect the resistance because they define the effective interaction area. In addition, the resistance is expected to increase significantly in concentrated ice. Since there is a lack of experience for towing in ice, conservative scenarios are expected to be used for the first towing attempts in ice. Therefore, support of icebreakers reducing the effective ice floe size must be considered. In addition, iceberg towing is expected to be performed under moderate ice conditions with a low velocity relative to the ice.

Thus, no global-scale failure in bending, splitting, extensive crushing or ridging is expected. Therefore, the planar model is sufficient unless off-plane effects start to appear, for instance, at high ice concentrations. The motion of each body is described by continuous drift equations augmented with additional contact forces calculated in a special manner and with a towing force for the iceberg.

The equations of motion for the iceberg and ice floes are very similar and basically repeat equations (4.1).

$$\begin{cases} M\frac{d\vec{U}}{dt} = \vec{F}_w + \vec{F}_a + \vec{F}_h + \vec{F}_C + \vec{F}_{wave} + \vec{F}_{ss} + \vec{F}_{tow} + \vec{F}_{cont} \\ (I + m_{66})\frac{d\omega}{dt} = M_\zeta + M_{cont} \end{cases} \tag{5.1}$$

Here, $\vec{F}_{cont}$ and M_{cont} are the forces and angular momenta that appear at mechanical contacts between the bodies, and they are discontinuous in time. The non-smooth formulation of the DEM is applied to find these quantities. The remaining forces were defined earlier for an iceberg. The rotational terms, as in system (4.9), are omitted for the current model, but the model can potentially be customized.

A few differences in the drag force formulation exist for ice floes because of their geometrical characteristics. The drag force acting on an arbitrary object can be separated into the frictional drag and the pressure drag (Newman 1977). The first type appears due to the tangential shear stresses, and the second type is due to the normal pressure stresses acting on the object. The iceberg is a large bluff body; therefore, the effect of frictional drag is much smaller than the effect of pressure drag. In contrast, the ice floes can be treated as flat plates having large surface areas. The tangential stresses integrated over the area in this case produce a stronger drag than the integrated pressure. With this in mind, the drag forces acting on the ice floes are calculated as

$$\begin{aligned} \vec{F}_w^{IF} &= C_w^{IF} A \rho_w |\vec{V}_w - \vec{U}|(\vec{V}_w - \vec{U}) \\ \vec{F}_a^{IF} &= C_a^{IF} A \rho_a |\vec{V}_a - \vec{U}|(\vec{V}_a - \vec{U}) \end{aligned} \tag{5.2}$$

where C_w^{IF} and C_a^{IF} are the friction drag coefficients on the order of 10^{-3}, in contrast to the form drag coefficients, on the order of 1 for an iceberg; A is the horizontal surface area of the ice floe. The drag coefficients for ice may be parameterized with the ice thickness, floe sizes and ice concentration (Lu et al. 2011).

As it was shown by Tsarau and Løset (2015), ice floes approaching a floater may loose up to 20% of their kinetic energy before the impact. Moreover, according to Tchieu et al. (2010), two cylinders in an ideal liquid will never reach contact unless they are forced to. However, in the first case, the lateral dimension of ice floes was comparable to their thickness, and in the second case the two cylinders were infinitely deep. When ice floe size is large in comparison to its thickness, the flat plate approximation can be used. Thus, the added mass effect for ice floes may be neglected if the floe size in the simulations is kept large enough, such as it is done in the current study. It is also assumed that, the ice floes are acted upon by much larger forces than the added mass force, thus it can be neglected when considering contact problems.

At the same time, the flow in the vicinity of the iceberg is improved by using a potential flow solution for a cylinder of equivalent radius $R_{eq} = l/2\pi$, where l is the waterline length. The components of velocity $\widehat{V}_w^x, \widehat{V}_w^y$ of the flow at the point with coordinates ξ, η in local system can be expressed as

$$
\begin{aligned}
\widehat{V}_w^x &= V_w^x \left(1 - \frac{R_{eq}^2(\xi^2 - \eta^2)}{(\xi^2 + \eta^2)^2} \right) - V_w^y \frac{2\xi\eta R_{eq}^2}{(\xi^2 + \eta^2)^2} \\
\widehat{V}_w^y &= V_w^y \left(1 + \frac{R_{eq}^2(\xi^2 - \eta^2)}{(\xi^2 + \eta^2)^2} \right) - V_w^x \frac{2\xi\eta R_{eq}^2}{(\xi^2 + \eta^2)^2}
\end{aligned}
\tag{5.3}
$$

where V_w^x and V_w^y are the components of the undisturbed flow velocity. Then, the water drag force acting on an ice floe that drifts close to the iceberg is calculated according to (5.2) using the flow velocity (5.3) at the centre of mass of the ice floe. According to the solution and confirmed by the simulations, the ice floes on the sides of the iceberg experience higher drag forces contributing to faster removal of the floes and pushing them into the wake (JP1 and JP2). Note, that the yawing of iceberg that can be described by (4.9) is not yet implemented in the current version of the discrete element model. However, it was not necessary for the validation study involving a cylindrical iceberg, having $m_{11} = m_{22}$.

5.2   Formulation of the non-smooth DEM

The interaction between the iceberg and the ice floes is discontinuous in time. This results in discontinuous ice resistance, which does not allow simple integration of (5.1). The non-smooth discrete element method can be applied to find forces appearing during contacts between the iceberg and an ice floe or between two ice floes. Let us consider N_b bodies participating in N_c contacts. The position of each body is determined by the coordinates of the centre of mass x_i, y_i and the angle of rotation φ_i. The positions of the bodies can be stored in a $3N_b$-component vector

$$
\mathbf{x} = \left| x_1, y_1, \varphi_1, ..., x_{N_b}, y_{N_b}, \varphi_{N_b} \right|^T
\tag{5.4}
$$

The distances between pairs of separated bodies can be defined as the greatest lower bound of distances between two points belonging to each body in a pair (Figure 13):

$$
\delta_j = \inf(\|x_A - x_B\|), x_A \in A, x_B \in B, \quad j = \overline{1, N_c}
$$

If the bodies are already in contact, δ_j becomes the penetration depth. Ice floes are assumed to be rigid; therefore, their geometrical representations are not allowed to interpenetrate each other. The separation distances δ_j are enforced to be non-negative:

$$\delta_j \geq 0, \quad j = \overline{1, N_c} \tag{5.5}$$

Such inequality constraints must be fulfilled for every contact by applying normal
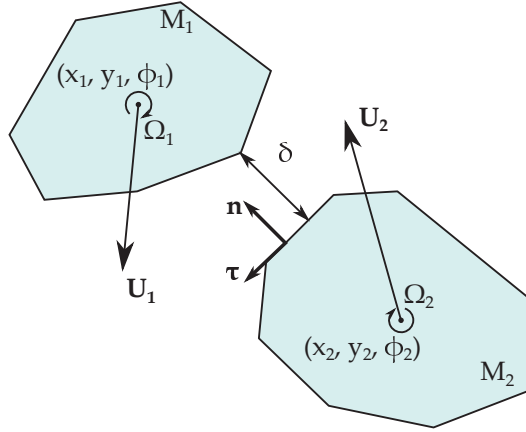

Figure 13: Geometry of a single contact between two polygons

contact impulses, which tend to separate bodies. The contact impulses must be equal to zero when there is no contact, i.e., $\delta_j > 0$; contact impulses must never produce attraction. These are the Signorini conditions, which can be formulated as

$$\begin{cases} \delta_j > 0 & \Rightarrow F^n_{cont} = 0 \\ \delta_j = 0 & \Rightarrow F^n_{cont} \geq 0 \end{cases} \tag{5.6}$$

where F^n_{cont} is the normal contact force acting on the j-th contact.

To hold a pair of bodies without overlapping, we must keep $\delta_j \geq 0$. For all the contacts, the first derivative of the separation distances δ with respect to time is a vector consisting of contact velocities.

$$\mathbf{w} = \frac{d\delta}{dt} = \frac{\partial \delta}{\partial \mathbf{x}} \cdot \mathbf{U} + \frac{\partial \delta}{\partial t} = \mathbf{J} \cdot \mathbf{U} + \mathbf{b} \tag{5.7}$$

where $\mathbf{w}$ are N_c normal contact velocities, $\mathbf{U}$ is a vector consisting of $3N_b$ body velocities, $\mathbf{J}$ is a Jacobian matrix having $N_c \times 3N_b$ components, and $\mathbf{b}$ is an N_c-component bias velocity vector. The Jacobian $\mathbf{J}$ transforms velocities in the ENU-system into the normal contact velocities, and the bias term determines the evolution of the separation distance

when it is not constant in time, e.g. when new contacts appear.

Due to the principle of virtual work, the constraint forces produce no work. It can be shown that, in the ENU-system, the contact forces can be expressed as a product of the transposed Jacobian and the normal contact impulse λ. Then, the system of equations of motion (5.1) can be projected for all the bodies

$$\mathbf{M}\Delta\mathbf{U} = \mathbf{F}_{ext}\Delta t + \mathbf{J}^T\lambda \tag{5.8}$$

where $\mathbf{M}$ is the inertia matrix of the system, $\mathbf{M}$ is diagonal and $3N_b \times 3N_b$ in size, and $\mathbf{F}_{ext}$ is a vector of $3N_b$ components containing all the continuous forces and angular momenta from (5.1).

Combining (5.7) and (5.8) yields

$$\mathbf{w} = \mathbf{J}\mathbf{M}^{-1}\mathbf{J}^T\lambda + \mathbf{J}\mathbf{M}^{-1}\mathbf{F}_{ext}\Delta t + \mathbf{b} + \mathbf{J}\mathbf{U}_1 \tag{5.9}$$

where $\mathbf{U}_1$ are the body velocities at the current time step. The constraints require no attraction at contacts when $\mathbf{w} = 0$, or zero contact forces when the relative velocity at contact is non-negative $\mathbf{w} \geq 0$. Thus, this equation is used to find the normal contact impulse components λ fulfilling the constraints posed on the physical system. It is transformed into a Linear Complementarity Problem (LCP) introduced by Cottle and Dantzig (1968), which can be formulated as

$$\mathbf{w} = \mathbf{A}\lambda + \mathbf{B} \tag{5.10}$$

$$\mathbf{w}^T\lambda = 0 \tag{5.11}$$

$$\lambda_j = 0 \leftrightarrow w_j \geq 0, \forall j \in 1, \bar{N}_c \tag{5.12}$$

$$w_j = 0 \leftrightarrow \lambda_j \geq 0, \forall j \in 1, \bar{N}_c \tag{5.13}$$

where

$$\mathbf{A} = \mathbf{J}\mathbf{M}^{-1}\mathbf{J}^T \tag{5.14}$$

$$\mathbf{B} = \mathbf{J}\mathbf{M}^{-1}\mathbf{F}_{ext}\Delta t + \mathbf{b} + \mathbf{J}\mathbf{U}_1 \tag{5.15}$$

The LCP is solved using the Projected Gauss-Seidel (PGS) method. To improve the convergence, so-called warm starting is implemented; the solver uses a solution extrapolated from the previous time step as an initial guess for the PGS. In the tangential direction, the relative velocities are projected onto the contact tangent to find the corresponding impulse. The only difference is that the tangential impulse magnitude must be limited by $\mu\lambda$, representing the friction constraint. The friction

coefficient μ for the sea ice is chosen to be 0.3 based on the experiments of Sukhorukov and Løset (2013).

Finally, once the λ are found, the equations of motion (5.8) are integrated, and new body velocities are found and used in turn to find new positions according to the semi-implicit Euler. Position drift and overlaps occurring as a result of non-exact solutions or inaccurate contact detection might be prevented using Baumgarte stabilization (Baumgarte 1972) or velocity projection stabilization (Ascher et al. 1995).

5.3   Collision force estimation

The normal contact impulse λ calculated from (5.10)–(5.15) must be considered as the time integral of the normal contact force over the time interval Δt.

$$\lambda = \int_{t_0}^{t_0+\Delta t} F_{cont}^n(t)dt \tag{5.16}$$

where t_0 is the time moment when the contact appeared. In general, for a calculated λ the evolution of the contact force $F_{cont}(t)$ during the time interval Δt is unknown and cannot be found. One can only find the average force during the time interval. In addition to the average force, the method of the peak force magnitude estimation is suggested.

In the simplest case, when the force can be assumed constant on Δt it is estimated as

$$F_{cont}^n = \frac{\lambda}{\Delta t} \tag{5.17}$$

This situation occurs when the contact forces do not undergo significant changes in magnitude, as, for example, when an iceberg slowly pushes an ice floe. Such contacts are called *resting contacts*, and they are characterized by very low relative velocities.

When the contact force is changing rapidly during *collisions*, (5.17) is no longer valid. It is proposed to use experimental data to obtain a rough estimate for the peak values of the force. In JP1 it was proposed to use the relationship between the kinetic energy before a collision and the peak force magnitude that was derived from a number of small-scale and full-scale collision events (Timco 2011). In JP2 it was realized that the relation between the momentum before a collision and the peak force magnitude from Timco (2011) is easier to implement.

Since the numerical model finds contact impulses that are in fact the momenta exchanged between the bodies, the peak force is estimated in the following way. The most-likely (the average obtained by the regression analysis) magnitude of the force during an isolated impact F_l depends on the momentum before the impact λ_0 as

$$F_l = 0.641 \cdot \lambda_0^{0.584} \tag{5.18}$$

The force is expressed in MN and the impulse λ_0 is expressed in MN·s. For example, as seen from Figure 14, during an impact with a 100-m-wide and 1-m-thick ice floe having a velocity of 0.1 m/s, the magnitude of the force will likely reach 530 kN.

Note that, for small-scale towing experiments (Eik and Marchenko 2010), the material properties of ice were modified to achieve the target flexural strength that would be in agreement with the Froude scaling. Therefore, for numerical simulations of the basin tests, (5.18) must be scaled accordingly, as was done in JP2.
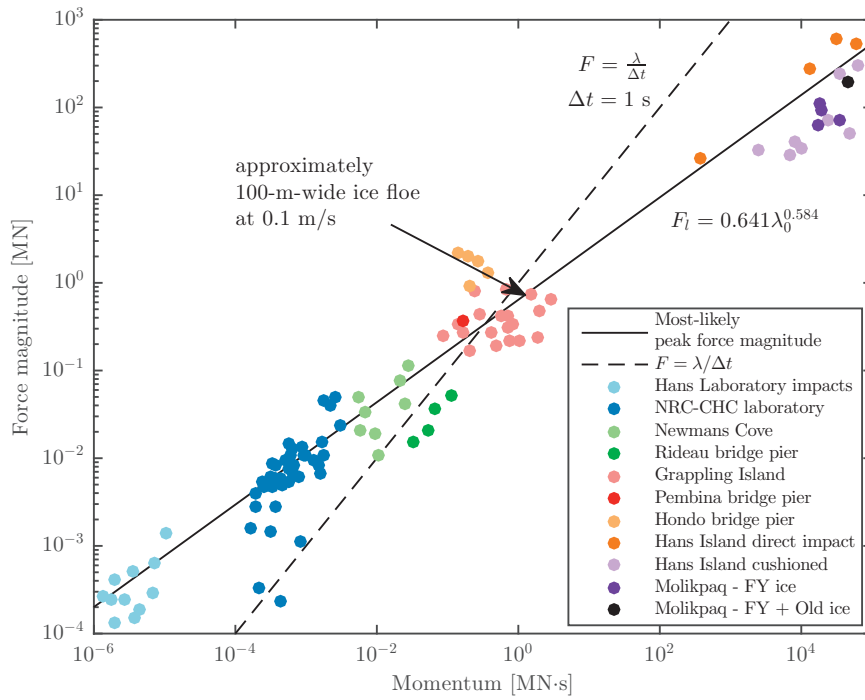

Figure 14: Model-scale and full-scale data are used to estimate the peak collision force using collision impulses. Here, F_l is the most-likely peak force magnitude.

In case when crushing occurs due to high confinement, the contacts are softened by constraining the contact impulses' magnitudes from above. The pressure-area relation

is used to calculate the limiting value based on the nominal contact area which is found as the ice thickness multiplied by the contact length. When simulating the model-scale experiment in HSVA, the contact impulse was limited by (see JP2)

$$\lambda_{crushing} = 36.6 \cdot l_{cont}^{0.3} \tag{5.19}$$

where $\lambda_{crushing}$ is the crushing impulse constraint and l_{cont} is the length of contact.

Another possibility for estimating contact forces is to soften constraints by introducing visco-elastic rheology at contacts. In this case (not implemented in the current study), the normal contact impulse may be limited by

$$\lambda_{ve} = \left[K(\frac{\partial E}{\partial \vec{x}}, \mathbf{n}) + \gamma w\right] \Delta t \tag{5.20}$$

where K is the contact stiffness; E is the energy of elastic deformation, proportional to the overlap area between two contacting features; $\vec{x}$ is the position of the body; $\mathbf{n}$ is the contact normal; γ is the damping coefficient; and w is the normal contact velocity. This form of the elastic component of the force is required to conserve kinetic energy (Pöschel and Schwager 2005), while expressions proportional to the penetration depth or overlap area are not able to guarantee it. Using (5.20), it is necessary to keep the time step much shorter than the characteristic contact time. The method becomes very similar to the classic DEM, where contacts with visco-elastic rheology are time integrated.

5.4   Choice of parameters

The normal contact response is defined by the restitution coefficient e. The restitution coefficient is chosen to be close to zero to reproduce significant kinetic energy dissipation occurring at contacts. The major losses occur due to local material plastic deformation and crushing at the contact interface. A greater discussion on the restitution coefficient can be found in JP1.

The time step is chosen as a compromise between accuracy considerations and correct collision duration. To resolve collisions in one time step, the collision duration should be less than or equal to the time step. On the other hand, the accuracy of contact detection is higher for smaller time steps. Geometrical overlaps at contacts between the bodies appearing at the beginning of each time step have to be much less than the

bodies' sizes. Therefore,

$$\Delta t \ll \frac{D}{w} \tag{5.21}$$

where D is the characteristic body size, and w is the normal contact velocity.

For example, in the small-scale towing experiment (Eik and Marchenko 2010), the ice floes are approximately 1 m wide and the largest contact velocity may reach 0.13 m/s. The collision duration for small-scale experiments is on the order of 0.1 s (Timco 2011). Therefore, a time step of no less than the collision duration and producing minimal overlap is 0.1 s. Similarly, for the full-scale towing simulation with ice floes of 30 m and a relative velocity of 0.5 m/s, the acceptable time step is defined by the collision duration, which is approximately 1 s (Timco 2011).

Such time steps are several orders of magnitude larger than the time steps used in the smooth DEM, where contact forces are integrated. This allows for much faster calculations, thereby providing close to real-time performance, as, for instance, in Lubbad and Løset (2011).

Finally, the drag coefficient parameterization from Lu et al. (2011) has been used in JP1. The drag coefficients for ice were functions of local ice concentration, ice thickness and floe size. In JP2, however, it has been realised that fine-tuning of the drag coefficients was not a priority when there existed sources of larger errors such as the failure of confined ice. Thus, the surface drag coefficient C_w^{IF} was assumed to be constant and equal to $5 \cdot 10^{-3}$.

5.5   Broken ice generation

Ice floes were represented by circles, spheres, clumps of spheres, and regular polygons in the early generations of the DEM. A method of generating randomly shaped polygonal ice floes has been developed for the present study. It is presented in one conference paper (CP6) and partly in one journal paper (JP1). The major advantage of this approach over conventional methods is the ability to produce numerical ice fields with a given floe size distribution.

Floe size is determined by the mean caliper diameter (MCD), which is defined as the average of the caliper diameter measured along all directions of the floe. The most recent version of the method generates several sets of ice floes having the same MCD D_i within a set. The generated polygonal ice floes have random shapes, formed by

creating a convex hull over N_v points randomly distributed on a unit circle and then scaled accordingly. D_i forms a partition on $[D_{min}, D_{max}]$, where D_{min} and D_{max} are the minimum and maximum floe size, respectively. The total area taken by N ice floes having MCDs distributed with a cumulative density function f_D is approximately equal to

$$A_{ice} = N \int_{D_{min}}^{D_{max}} A f_D dD \tag{5.22}$$

where A is the horizontal surface area of an ice floe. From the definition of the ice concentration N can be found as

$$N = \frac{c A_{total}}{\int_{D_{min}}^{D_{max}} A f_D dD} \tag{5.23}$$

where A_{total} is total domain area. Thus, the number of ice floes that should be in each set can be determined.

It is known that, for unmanaged sea ice, the MCD is distributed according to a power law (see JP1 and CP6 for references). Truncated above because of the upper limit on image aerial coverage and below because of the lower limit on the minimal ice floe that is able to be recognized, the cumulative distribution function can be expressed as

$$F_D = \frac{D^{-\beta} - D_{min}^{-\beta}}{D_{max}^{-\beta} - D_{min}^{-\beta}}, \quad D \in [D_{min}, D_{max}] \tag{5.24}$$

where F_D gives the probability of a floe diameter to be no larger than D. Then, f_D can be found by differentiation and substituted into (5.23) to obtain the number of floes N.

The shape of the ice floes can also be characterised by the roundness, defined as $r = \pi D^2 / 4A$; note that this gives a relation between the area A and the diameter D. The average roundness of the ice floes can also be controlled, allowing one to switch between managed and unmanaged ice. The roundness of a convex ice floe depends on N_v; a larger N_v results in more vertices and a roundness close to 1. A lower N_v results in ice floes having sharp, pointy corners such as after newly broken ice formed after icebreaking.

The average roundness for a large number of generated ice floes is shown in Figure 15 as a function of N_v. According to Lu et al. (2008), the average roundness of ice floes in the marginal ice zone is found to be between 1.3 and 1.5; therefore, for unmanaged ice floes, N_v can be chosen between 9 and 14 (Figure 15).

Two generated ice fields representing managed and unmanaged conditions are shown in Figure 16. The labels *managed* and *unmanaged* are conditional, and they only
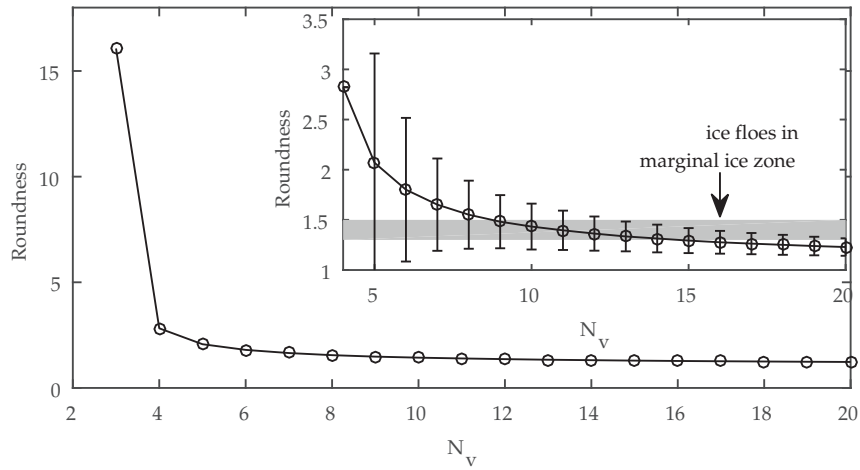
Figure 15: Roundness might be controlled by choosing a number of random points N_v needed to generate a polygon. Unmanaged ice floes in the marginal ice zone have a roundness of between 1.3 and 1.5 (grey area).

characterize the ice floe shapes. The difference in ice resistance that may exist between such conditions should be studied.

A variable ice thickness randomly distributed between the floes is straightforward to implement if needed. Ice thickness statistical distributions can be taken from, for example, Haas et al. (2008). Isolated ice ridges can be implemented as ice floes having a large equivalent thickness.
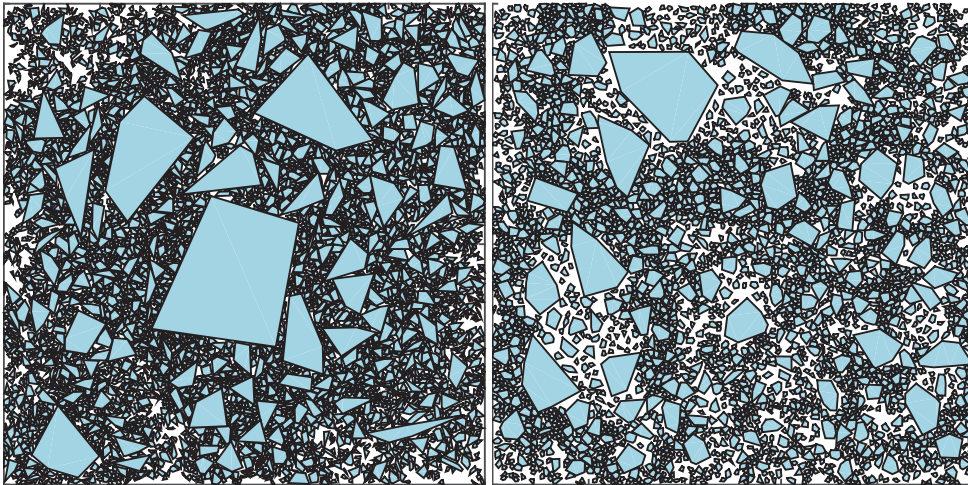
(a) $N_v = 6$ represents managed ice   (b) $N_v = 12$ represents unmanaged ice

Figure 16: Examples of generated broken ice fields on a 1 km² squared domain. The ice concentration is approximately 65%, $\beta = 2.5$, $D_{min} = 10m$, $D_{max} = 500m$, approximately 3500 ice floes.

6 Validation of the model of iceberg in broken ice

The numerical model of iceberg towing in broken ice described in Chapter 5 must be validated. However, the amount of data that can be used for the validation is very limited. Basically, the only relevant experiment is a towing experiment conducted in HSVA (Eik and Marchenko 2010). In addition to the experiment, a number of analytical approximations for ice resistance to icebergs may be considered.

6.1 Towing test in HSVA

6.1.1 Experimental set-up and reanalysis

Eik and Marchenko (2010) performed iceberg towing tests in broken ice in HSVA. These tests were conducted on 1:40 geometrical scale. Froude scaling was applied to obtain the dynamic similarity between inertia forces and gravity forces [1]. Iceberg models were towed through a 2880-m-long and 400-m-wide towing tank (Figure 17). The real towing distance was approximately 1600 m because of the melt-pit and trim-tank at the end of the basin.

The towing set-up consisted of a 920-m-long synthetic towing line looped around the iceberg and connected to a 80-m-long steel hawser attached to a towing carriage. The towing load was measured at both ends of the towing line and at the steel hawser. Cylindrical and cubic-shaped iceberg models were tested. Unfortunately, for the

---

[1]all quantities are going to be referred to full scale

cubic-shaped iceberg, load measurements were found to be unreliable; therefore, the results of these tests were not used to validate the numerical model.
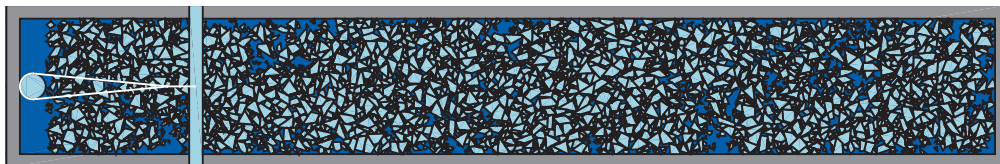

Figure 17: Schematic top view of the towing tank prior to the test in 71% concentrated ice

According to Eik and Marchenko (2010), the towing tests were performed in open water and in 20%, 50% and 80% concentrated broken ice. The ice thickness was approximately 1.16 m thick. The cylindrical iceberg was 76.36 m in diameter and 25.80 m in total height. The density was estimated as 887 kg/m^3. At full scale, it would be a 0.1 million ton iceberg, which is a medium size. Broken ice in the experiment was cut into 800 m^2 triangular pieces from an initial level ice sheet produced according to Evers and Jochmann (1993). When the initial ice sheet was cut, some ice remained on the basin walls; therefore, the wall–ice friction coefficient was assumed to be the same as the ice–ice friction coefficient $\mu = 0.3$ (Table 6.1).

Table 6.1: Parameters from the experiment used in the model

Parameter	Notation	Model-scale	Full-scale
Basin size			
Length	L	72 m	2880 m
Width	W	10 m	400 m
Iceberg			
Diameter	D	1.909 m	76.36 m
Total height	H	0.645 m	25.8 m
Density	ρ_{IB}	887 kg/m^3	887 kg/m^3
Ice field			
Ice thickness	h	29 mm	1.16 m
Average floe area	A	0.5 m^2	800 m^2
Density	ρ_{IF}	930 kg/m^3	930 kg/m^3
Friction coefficient	μ	0.3	0.3

The ice concentration prior to the tests was estimated visually in the original experimental study. Available photos of the towing tank filled with ice allowed better estimates of the ice concentration to be made in the experiment. The perspective on the digital images was adjusted to be the top view, and the area occupied by the ice was estimated. Ice floes consisted of brighter pixels than the water surface and walls of the ice tank, allowing the ice concentration to be determined. Significant adjustments were made to the ice concentrations reported previously (Figure 18). Thus, for example, the

most interesting test in 50% concentrated ice turned out to be performed for the 71% ice concentration. This reanalysis enabled a better interpretation of the experimental results.
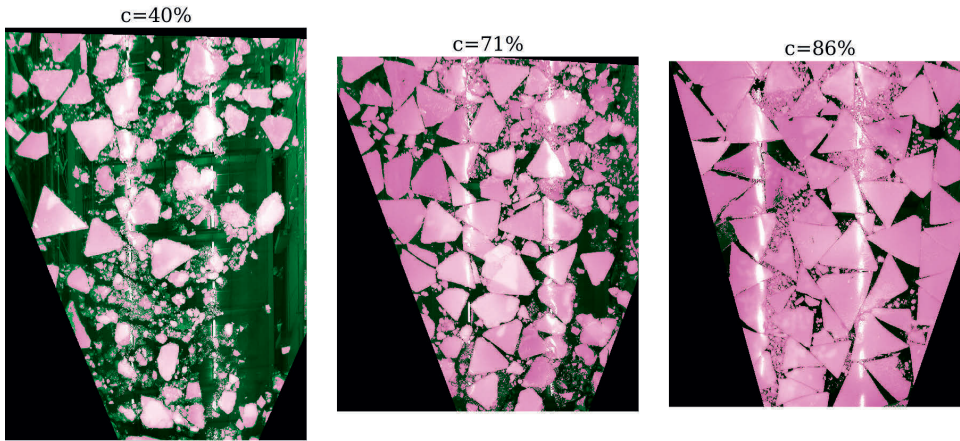

Figure 18: Photographs of the towing tank filled with broken ice prior to the tests, which were used to reanalyse the ice concentration.

A straight-line towing scenario has been used for the validation. The towing has been performed in five stages, for which the carriage motion was the following:

0. Acceleration with 0.001 m/s^2 up to 0.70 m/s
1. Constant speed of 0.70 m/s during 13.7 minutes
2. Acceleration with 0.001 m/s^2 up to 0.82 m/s
3. Constant speed of 0.82 m/s during 13.7 minutes
4. Deceleration with 0.002 m/s^2 until a full stop

The drag coefficient for the iceberg was calculated from the test in open water in Stages 1 and 3. Assuming the magnitude of the drag force F_w to be proportional to the square of the relative water velocity magnitude, which was the iceberg speed U in the test, the drag coefficient C_w^{IB} can be found as the average

$$C_w^{IB} = \frac{2}{\rho_w A_{keel}} \left\langle \frac{F_w}{U^2} \right\rangle \tag{6.1}$$

where F_w is equal to the towing force in the case of a constant towing speed and A_{keel} is the vertical cross-section area of the iceberg keel. For Stages 1 and 3, the drag coefficients were found to be 0.33 and 0.40, respectively.

Note that the Reynolds numbers for the model scale and full scale are

$$Re_m = \frac{UD}{\nu} = \frac{0.13 \cdot 1.909}{1.8 \cdot 10^{-6}} = 1.4 \cdot 10^5, \quad Re_f = 3.5 \cdot 10^7 \tag{6.2}$$

These Reynolds numbers correspond to the subcritical flow regime at the model scale and the supercritical regime at full scale, indicating that the drag coefficient of a real iceberg is likely to be different.

6.1.2 Numerical simulation

The numerical set-up is similar to the experiment: a carriage moving with a prescribed velocity pulls a cylindrical iceberg attached by a joint, producing an equivalent elastic response in tension and no response in compression. Ice floes are generated as random triangles for the test in the 86% ice concentration and as polygons having 3 or more vertices for the tests in lower ice concentrations. The potential flow solution around a cylinder (5.3) is used in the vicinity of the iceberg, therein affecting the flow of ice.

The averaged ice resistance obtained from the model-scale experiment is compared to the average resistance calculated in the numerical simulation. The ice resistances averaged during Stages 1 and 3, when the towing velocity were constant, were chosen for comparison. The results of both the experiment and the simulation are shown in Figure 19. The model is able to reproduce average forces in the experiment; however, it is difficult to match the evolution of the resistance because of the inexact replica of the broken ice in the towing tank and only three degrees of freedom disallowing the simulation of rafting and bending occurring at high confinement.
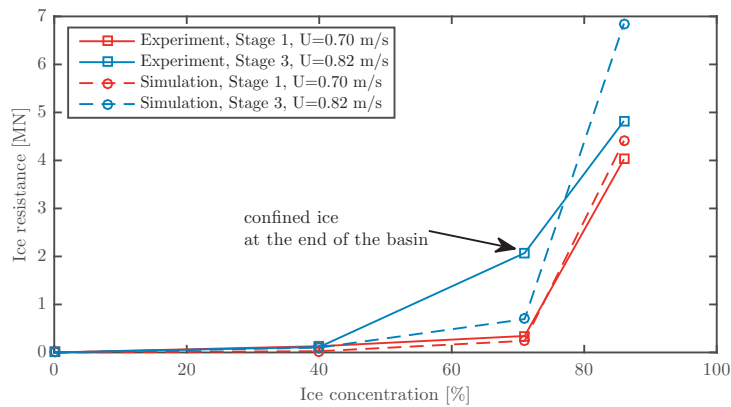

Figure 19: Average ice resistance obtained from the experiment compared to the resistance calculated by the numerical model.

The towing force undergoes a dramatic increase starting from a concentration of approximately 70%, when the flow of ice changes from rapid granular flow, driven by collisions to dense granular flow where persisting contacts are important. In addition, a higher value for the average ice resistance has been measured during Stage 3 in 71% ice concentration because of ice compaction at the end of the towing tank. Therefore, the point may actually correspond to certain higher concentration values.

The evolution of the towing force in 71% ice concentration is shown in Figure 20a. To illustrate the effect of ice confinement at the end of the basin, a snapshot extracted from the video taken during the test is shown in Figure 20b. The ice was not confined so much in the numerical test, likely due to different ice matrix in the towing tank.
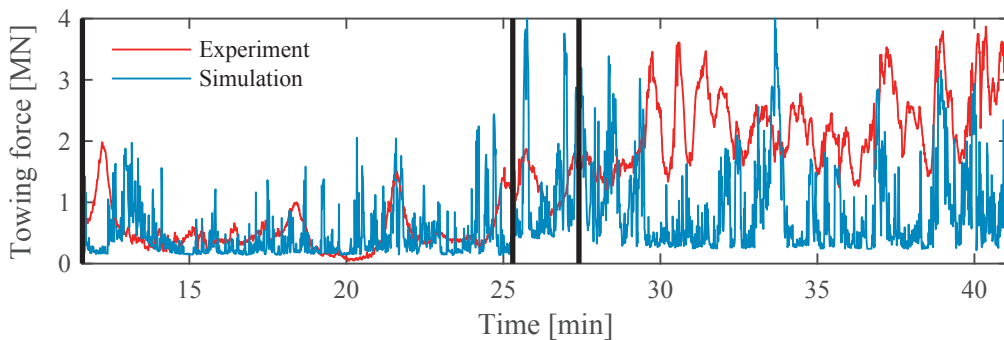
(a) Evolution of measured and simulated towing force in the test in 71% ice concentration
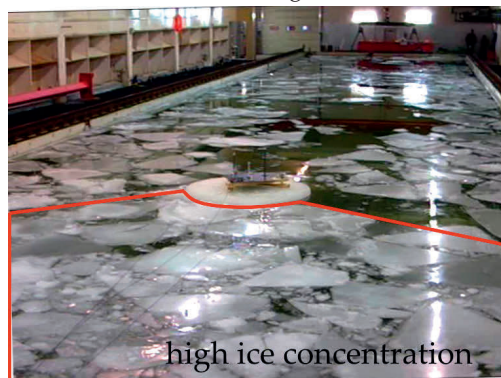
(b) A snapshot of the ice tank showing highly compacted ice in front of the iceberg during Stage 3 in 71% ice concentration (related to all ice over the total basin area)

Figure 20: Ice compaction causing higher resistance

A typical view of the towing tank after simulation in 71% ice concentration is shown in Figure 21. The ice to the right of the iceberg, at the end of the basin, is also compacted. To the left of the iceberg, there is a wake, slightly resembling the von-Karman street. The wake was closed because of the potential flow solution for the water flow applied

around the cylindrical iceberg. Otherwise, the wake area would be significantly straighter.
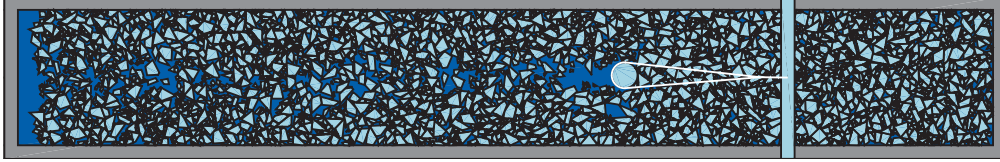

Figure 21: Numerical ice field after towing in 71% ice concentration.

6.2 Continuous approximations

In JP2, different equations for ice resistance to a cylindrical iceberg are compared. One is given for granular material and verified in a small-scale experiment (Wassgren et al. 2003). The resistance force acting on a cylindrical object is quadratic in the relative velocity; however it is only applicable when the granular material flows, e.g., under approximately 60% concentrations for spherical particles.

The other two approximations are derived for icebergs in ice with the assumption that the iceberg characteristic length is large in comparison to the ice floe size. Lichey and Hellmer (2001) introduced an expression for the ice force acting on large Antarctic icebergs drifting in ice. The ice force was neglected for ice concentrations below 15%; then, it was similar to the quadratic viscous drag up to 90% concentration. Finally, it was assumed that, in high concentrations, icebergs were captured by the ice unless the interaction force exceeded the ice strength expressed by Hibler (1979).

$$\vec{F}_{si} = \begin{cases} 0 & : & c \leq 15\% \\ 0.5\rho_i c D h_i |\vec{V}_i - \vec{U}|(\vec{V}_i - \vec{U}) & : & 15\% < c < 90\% \\ M\frac{d\vec{U}}{dt} - \vec{F}_{other} & : & c \geq 90\% \text{ and } P \geq P_s \end{cases} \tag{6.3}$$

where V_i is the ice drift velocity, D is the characteristic iceberg diameter, h_i is the ice thickness, $\vec{F}_{ext}$ is the sum of continuous forces from (5.1), P has been defined earlier in (2.1), and P_s is a certain threshold value.

Another approximation given by Marchenko et al. (2010) is derived for a cylindrical iceberg drifting in broken ice consisting of small ice floes. The resistance is associated

52

with the work performed by the iceberg during creation of a channel in ice.

$$F_{si} = \frac{D}{4} \left(\rho_i c_{crit} h_i + \frac{1}{4} C_w^{IF} \rho_w D \right) \frac{cU^2}{c_{crit} - c} \tag{6.4}$$

where F_{si} is the magnitude of the resistance force directed along the relative velocity of the iceberg and the ice field. c_{crit} is the ice concentration at the highest-density packing.

Analytical estimates and the scaled experimental and modelling results are shown in Figure 22. The numerical tests were performed for wider range of ice concentrations. The ice resistance starts to grow rapidly at approximately 70% concentration, when the ice floes must be broken or submerged by the iceberg. At high concentrations the ice resistance in the experiment and in the simulations has to be limited by the crushing and off-plane effects. While the resistance magnitude given by the analytical estimates is really not limited.
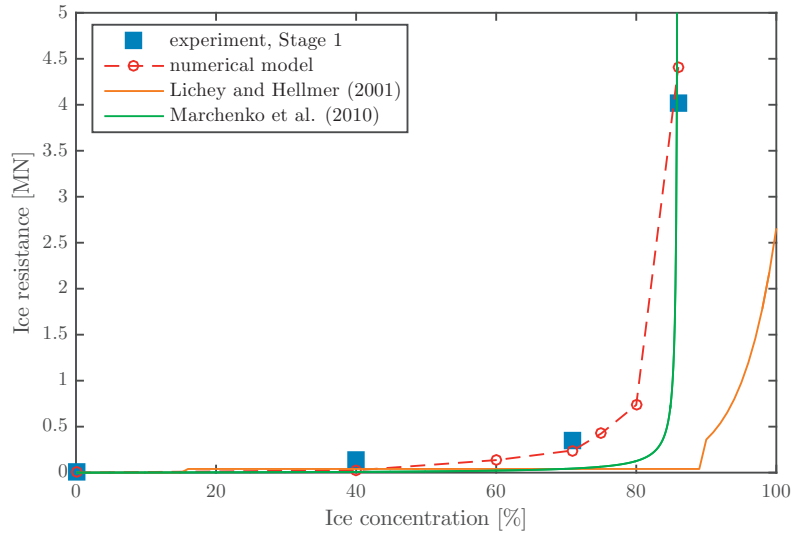
Figure 22: Ice resistance compared for analytical expressions and scaled experimental data. The towing velocity is 0.7 m/s in all cases. The upper bound resistance derived using the ice pressure (2.1) is shown for Lichey and Hellmer (2001) at concentrations above 90%. $c_{crit} = 86\%$ was used in (6.4)

The approximation given by Lichey and Hellmer (2001) demonstrates poor performance due to its week dependence on the ice concentration. The equation (6.4) performs much better, it's deviation from the scaled experimental results is due to the confinement present in the experiment. In reality, there are no walls and the ice resistance is possibly lower than that measured and simulated in the experiment.

6.3 Discussion and limitations

An attempt to model iceberg towing in pack ice using the non-smooth DEM has been made. The model has been validated using the data from the model-scale towing experiment in HSVA. It is the only relevant small-scale experiment, and no full-scale data are available. Therefore, the validity of the model at full scale is still under question. Any documented data on towing in ice are going to provide a very valuable basis for calibration. Nevertheless, considering the scaled experimental results and analytical estimates for the full-scale resistance, the model performs well. The model is able to estimate the average broken ice resistance under various ice conditions, and it provides a visualization of the process of iceberg motion through broken ice.

Ice resistance expected to be encountered in full scale towing operation may be anticipated based on the experiment and simulations. According to the data, an iceberg with the mass of 0.1 million tons in 71% ice concentration and 1.16 m ice thickness at 0.7 m/s would experience ice resistance on the order of 400 kN. Now, let us take into account that towing operations in open water were often performed at much lower velocities relatively water (Rudkin et al. 2005) and employing towing line catenary causing much more damping. In addition, for example, on the Grand Banks, the ice is only 0.3–0.7 m thick (Wright 2000). In such conditions, the ice resistance will likely be lower than 400 kN. The open-water towing forces measured at the Grand Banks were on the same order or even higher (C-CORE 2004), which allows us to conclude that towing in moderate ice conditions (similar to the above-mentioned) has to be feasible.

A number of challenges have been encountered when designing and validating the model. The first large group of challenges is associated with the experimental side, and the second group is mostly due to the limiting assumptions of the model and numerical methods.

- First of all, the resistance of highly concentrated ice in reality might not correspond to the ice resistance obtained from the experiment, even if correctly scaled. Confinement in basin-scale tests becomes an issue, when stresses transmitted through the ice cover reach walls. Higher towing loads were measured and ice failure was observed in the experiment when the ice was accumulated and jammed between the iceberg and the walls of the ice tank. Similarly, high loads were obtained in the simulations. However, due to the fact that the model was planar and the floes were not allowed to raft, there was less

opportunity to dissipate and the magnitude of the loads was significantly higher.

There are no rigid walls offshore and no jamming is possible in that sense, however, certain confinement may still appear at high concentrations and cause ice failure and consequent ridging. This is obviously not implemented in the model, but towing in such harsh ice conditions is a far-field perspective.

- Accurate simulation of large scale failure of arbitrary-shaped ice floes requires sophisticated models. Level ice failure has been implemented by Lubbad and Løset (2011) when modelling ships in level ice using the non-smooth DEM. The analytical solution is obtained for a half-space on elastic foundation, that fails by forming radial and circumferential cracks. The same solution can be applied to the ice floes, large enough in size to break. Ice floes can also be split by casting a number of rays to different directions from the contact point and choosing the shortest split edge along which the ice floe is likely to fail (Metrikin 2014). The occurrence of different failure modes has been studied by Lu (2014), and criteria for the floe size and confinement were derived. These methods may improve the performance of the model and reduce large amplitude oscillations of the towing force.

- Different dissipation mechanisms at contacts can be introduced into the model by using additional constraints. However, the position stabilization should be used carefully together with position-dependent (or holonomic) constraints. The forces obtained using holonomic constraints may be inaccurate, because position stabilization alters contacts' geometry. For example, the position stabilization reduces overlap between bodies in contact without changing their velocity, thus, altering crushing constraint, that depends on the contact length. To prevent this, the position stabilization may be activated only when overlaps become significant.

- The ice concentration is a macro parameter in common sense, it characterizes amount of ice over certain area containing many floes evenly distributed over this area. Uniform spatial distribution of the ice in the area of interest is important: 5 km^2 of ice on a satellite image covering 10 km^2 cannot be 50% concentration if ice completely covers only one half of the region with 100% concentration.

During the experiment and simulations it was observed that the amount of ice accumulated in front of the iceberg grows and the ice is pushed towards the far end of the basin. So, by the end of towing in the ice tank, the concentration of ice "in front" was significantly increased. It resulted in unexpectedly higher towing forces measured during Stage 3 in 71% ice concentration. Similar issues were

reported by Haase et al. (2012) when investigating model-scale DP in ice.

- Abnormal towing force in 71% ice concentration was initially considered as a consequence of ice floes that pushed the towing line sideways what increased the towing force. Although, the compaction of ice floes at the end of the towing tank was found to be the reason, the ice floes under the tow line still affected the results by introducing uncertainty that was hard to estimate.

- Exact shapes and positions of the ice floes were not measured when the experiment took place. It limited quantitative validation by only possibility to compare the average towing force values and magnitude variation for certain periods. The evolution of the force can be compared only qualitatively. Recent techniques allow thorough documentation of ice fields (Zhang et al. 2015), so that ice floe shapes, size distribution and accurate concentration value can be obtained.

- The hydrodynamics in the model is simplified, yet the potential flow solution introduced in the vicinity of iceberg significantly improves ice flow representation. The ice floes are now transported into the wake area, accumulated ice removal is facilitated by the flow. Further improvement of hydrodynamics in the model will likely require CFD coupled with multibody solvers. Recent studies on the subject cover ice flow around floaters and propeller wash (Tsarau and Løset 2015; Tsarau et al. 2016).

- Solution of the equations of motion provides contact forces that are averaged on the time step Δt. The actual force magnitude can not be resolved (Radjai and Richefeu 2009), but its peak value can be estimated for ice using relationship between momentum before collision and peak forces measured in a number of experiments on different scales (Timco 2011).

- Floe size distribution for sea ice affects its "macro" rheology. Polygonal broken ice floes for the simulations can be generated in a way that they follow natural power-law size distribution. Also, target total ice concentration and average roundness of the floes can be set. The choice of roundness allows to switch between natural unmanaged ice and managed ice consisting of less circular ice floes.

7 Conclusions and recommendations

The ability to perform iceberg management in broken ice could directly affect the design of offshore structures in the Arctic. Improved expertise on towing in sea ice will result in increased safety and reliability and reduced costs. This thesis has briefly presented observations and measurements related to icebergs drifting in pack ice and a numerical model of iceberg towing in ice. The major contributions of the thesis are the following:

- Unique data set containing high-quality drift data for a total of 9 icebergs and 18 ice floes drifting to the waters North-East of Greenland and to the South-East of Svalbard is collected.

- Iceberg yawing has been measured using pairs of trackers for the first time. A model of iceberg rotation has been proposed and has been validated using the measured rotations.

- A planar multibody model of iceberg motion through broken ice has been developed using non-smooth DEM.

- The model has been validated using a model-scale towing experiment, where average ice resistance was reproduced for different ice concentrations.

7.1 Observations

The following will highlight additional contributions from full-scale observations:

- Characteristic drift velocities for ice and icebergs are obtained for the mentioned regions. Moreover, velocity distributions show a clear difference between drift in the shear zone and in central pack along the east coast of Greenland.

- Relative velocities for ice floes drifting in the vicinity of icebergs are obtained. In addition to the different forcing, it is suggested that iceberg size and ice concentration are the major factors influencing the relative velocity. Given the relative drift of iceberg and broken ice it is too weak to start ridging process on the sides of the iceberg in moderate ice concentrations.

- Statistical data on drift trajectory curvature might help to define ice management corridors more accurately. It has been measured how the curvature depends on the drift speed. The obtained relation confirmed larger curvature radii for higher drift speeds.

- GPS trackers have to be used cautiously when trying to capture processes with periods shorter than 1 h (see JP3). So, one should consider position oscillations due to the GPS error. Accelerometers paired with GPS trackers should significantly improve the accuracy. Differential GPS may be an option when base stations are available close to the drift area.

7.2   Numerical modelling

The additional highlights related to the numerical modelling are as follows:

- An algorithm generating broken ice consisting of random polygonal ice blocks following target size distribution, concentration and average roundness has been developed. The algorithm is capable to produce up to 85% concentrated ice fields consisting thousands of ice floes in a short time.

- In the non-smooth DEM, the contact force magnitude during collisions is generally unknown. It is proposed to use momentum-force relation measured on different scales to estimate peak forces during collisions.

- Collisions between ice floes are assumed inelastic. Kinetic energy of the impacting ice features is assumed to dissipate into local crushing at the contact interface. This assumptions support the choice of the restitution coefficient which is set to zero.

- The flow of water around an iceberg must be taken into account, because it affects broken ice motion in the vicinity of an iceberg by accelerating it on the sides and pushing into the wake area. Potential flow solution has been utilized to calculate current velocity around the iceberg, improving broken ice motion.

- The model qualitatively reproduced the relationship between the ice concentration and time-averaged ice resistance obtained from the model-scale towing experiments. However, the validity of the method in full-scale still remains an issue and real operational data are vital.

- Towing of icebergs in broken ice can be feasible in first year ice having concentration not exceeding 70%

7.3 Recommendations for further work

The major need is calibration data: the numerical model of towing in ice will strongly benefit from basin-scale and full-scale tests. Even a qualitative observation of a full-scale towing operation in ice will provide substantial amount of valuable information. First, the validity of "slow, unconfined" interaction between the ice and iceberg in tow will be immediately established. Second, the importance of the ship wake and propeller wash on ice will be understood. If the ice accumulation in front of the iceberg is going to be washed off, the ship model has to be introduced to calculate the ice force acting on the iceberg in tow. Of course, the pull produced by the ship will be used to obtain an estimate of the ice resistance.

Once validated on the full-scale data, the model can be used for statistical analysis with random ice fields to obtain the towing resistance for the full range of towing velocities and ice conditions. Then, the analytical expression for the resistance can be obtained. Thus, the probabilistic approach can be used to assess the success rates of the towing operation and performance of IM. In addition, the relation between the ice resistance and the ice concentration and thickness for different relative velocities can be used for drift forecasting and in larger scale drift models. The overall sensitivity to the input parameters must be carefully studied, which will help to define the validity of the model more accurately.

The model can be extended to three dimensions and allow for six degrees of freedom for the bodies. Failure modes of ice floes can be implemented to provide additional force reduction mechanisms together with the buoyancy. The hydrodynamics can be improved as well, as mentioned above. All these features have to be coupled if the total accuracy of the towing model is expected to be increased.

The numerical method can be improved in different ways depending on the requirements. For example, real-time calculations are needed for control systems,

where the towing force must be estimated with high frequency to estimate optimal thruster allocation of the towing vessel.

First, an exact solution of the LCP can be performed using Lemke's method (Cottle and Dantzig 1968). This will take significantly more time than PGS but will always result in an exact solution. Second, the number of particles may be significantly increased on high-performance computers if effectively parallelized. Domain decomposition has been proved to be an effective method for the DEM (Visseq et al. 2013), therein producing a speed-up equal to the number of processors in the ideal case.

References

Alanweh, S., R. Dragt, D. Peters, C. Daley, and S. Bruneau. 2015. "Hyper-Real-Time Ice Simulation and Modeling Using GPGPU". *IEEE Transactions on Computers* 64 (12): 3475–3487. doi:10.1109/TC.2015.2409861.

Allison, K., G. Crocker, H. Tran, and T. Carrieres. 2014. "An Ensemble Forecast Model of Iceberg Drift". *Cold Regions Science and Technology* 108:1–9. ISSN: 0165-232X. doi:10.1016/j.coldregions.2014.08.007.

Andersson, L.E., F. Scibilia, and L. Imsland. 2016. "An estimation-forecast set-up for iceberg drift prediction". *Cold Regions Science and Technology* 131:88–107. doi:10.1016/j.coldregions.2016.08.001.

Ascher, U.M., C. Hongsheng, L.R. Petzold, and S. Reich. 1995. "Stabilization of Constrained Mechanical Systems with DAEs and Invariant Manifolds". *Mechanics of Structures and Machines* 23 (2): 135–157. doi:10.1080/08905459508905232.

Barker, A., D. Sudom, and M. Sayed. 2014. "Conical Structures in Ice: the Roles of Friction, Slope and Shape Play". In *Proceedings of the Arctic Technology Conference, Houston, TX, USA, February 10–12, 2014*.

Bass, D.W., and D. Sen. 1986. "Added Mass and Damping Coefficient for Certain 'Realistic' Iceberg Models". *Cold Regions Science and Technology* 12 (2): 163–174. ISSN: 0165-232X. doi:10.1016/0165-232X(86)90031-5.

Baumgarte, J. 1972. "Stabilization of Constraints and Integrals of Motion in Dynamical Systems". *Computer Methods in Applied Mechanics and Engineering* 1 (1): 1–16. doi:10.1016/0045-7825(72)90018-7.

Berg, M. van den. 2016. "A 3-D Random Lattice Model of Sea Ice". In *Proceedings of the OTC Arctic Technology Conference, St, John's, NL, Canada, October 24–26, 2016*.

Bigg, G.R., M.R. Wadley, D.P. Stevens, and J.A. Johnson. 1997. "Modelling the Dynamics and Thermodynamics of Icebergs". *Cold Regions Science and Technology* 26 (2): 113–135. ISSN: 0165–232X. doi:10.1016/S0165-232X(97)00012-8.

Blunt, J.D., D.A. Mitchell, D.G. Matskevich, T. Kokkins, A.H. Younan, and J.M. Hamilton. 2013. "A Tactical Hindcast Calibration Method for Sea Ice Drift Forecasting in the Canadian Beaufort Sea". In *Proceedings of the Twenty-third (2013) International Offshore and Polar Engineering, Anchorage, AK, USA, June 30–July 5, 2013*, 1177–1184. ISBN: 978-1-880653-99-9.

Campin, J-M., J. Marshall, and D. Ferreira. 2008. "Sea ice-ocean coupling using a rescaled vertical coordinate z*". *Ocean Modelling* 24 (1–2): 1–14. ISSN: 1463-5003. doi:10.1016/j.ocemod.2008.05.005.

C-CORE. 2004. *Stability and Drift of Icebergs Under Tow—Draft Report*. C-CORE Report R-04-072-216 v1. January 2005. Prepared for Petroleum Research Atlantic Canada (PRAC).

Coon, M.D., G.A. Maykut, R.S. Pritchard, D.A. Rothrock, and Thorndike A.S. 1974. "Modelling the Pack Ice as an Elastic-Plastic Material". *AIDJEX Bulletin: Numerical Modelling Report*, no. 24.

Cottle, R.W., and G.B. Dantzig. 1968. "Complementary Pivot Theory of Mathematical Programming". *Linear Algebra and its Applications* 1 (1): 103–125. ISSN: 0024-3795. doi:10.1016/0024-3795(68)90052-9.

Cundall, P.A. 1971. "A Computer Model for Simulating Progressive Large Scale Movements in Blocky Rock Systems". In *Proceedings of the international symposium on rock fracture, Nancy, Fracne, October, 1971*, 1:129–136.

Eik, K. 2008. "Review of Experiences within Ice and Iceberg Management". *Journal of Navigation* 61 (4): 557–572. doi:10.1017/S0373463308004839.

— . 2009. "Iceberg Drift Modelling and Validation of Applied Metocean Hindcast Data". *Cold Regions Science and Technology* 57 (2–3): 67–90. ISSN: 0165-232X. doi:10.1016/j.coldregions.2009.02.009.

Eik, K., and A. Marchenko. 2010. "Model Tests of Iceberg Towing". *Cold Regions Science and Technology* 61 (1): 13–28. ISSN: 0165-232X. doi:10.1016/j.coldregions.2009.12.002.

Eik, K., A. Marchenko, and S. Løset. 2009. "Wave Drift Force on Icebergs - Tank Model Tests". In *Proceedings of the 20th International Conference on Port and Ocean Engineering under Arctic Conditions, Luleå, Sweden, June 9–12, 2009*.

Evers, Karl-Ulrich, and Peter Jochmann. 1993. "An Advanced Technique to Improve the Mechanical Properties of Model Ice Developed at the HSVA Ice Tank". In *Proceedings of the 12th International Conference on Port and Ocean Engineering under Arctic Conditions, Hamburg, Germany, August 17–20, 1993*, 2:877–888.

Farid, F., F. Scibilia, R. Lubbad, and S. Løset. 2014. "Sea Ice Management Trials during Oden Arctic Technology Research Cruise 2013 Offshore North East Greenland". In *Proceedings of the 22nd IAHR International Symposium on Ice, Singapore, August 11–14, 2014*, 518–525. ISBN: 978-981-09-0750-1.

Featherstone, R. 2008. *Rigid Body Dynamics Algorithms*. Springer. ISBN: 978-0-387-74314-1.

Flato, G.M. 1993. "A Particle-In-Cell Sea-Ice Model". *Atmosphere-ocean* 31 (3): 339–358. doi:10.1080/07055900.1993.9649475.

Frankenstein, S., S. Løset, and H.H. Shen. 2001. "Wave-Ice Interactions in Barents Sea Marginal Ice Zone". *Journal of Cold Regions Engineering* 15 (2): 91–102. doi:10.1061/(ASCE)0887-381X(2001)15:2(91).

Gutfraind, R., and S.B. Savage. 1997. "Smoothed Particle Hydrodynamics for the Simulation of Broken-Ice Fields: Mohr-Coulomb-Type Rheology and Frictional Boundary Conditions". *Journal of Computational Physics* 134 (2): 203–215. doi:10.1029/97JC00124.

Haas, C., A. Pfaffling, S. Hendricks, L. Rabenstein, J. Etienne, and I. Rigor. 2008. "Reduced Ice Thickness in Arctic Transpolar Drift Favors Rapid Ice Retreat". *Geophysical Research Letters* 35 (17). ISSN: 1944-8007. doi:10.1029/2008GL034457.

Haase, A., S. van der Werff, and P. Jochmann. 2012. "DYPIC - Dynamic Positioning in Ice: First Phase of Model Testing". In *Proceedings of the ASME 2012 31st International Conference on Ocean, Offshore and Arctic Engineering, Rio de Janeiro, Brazil, July 1–6, 2012*, 6:487–494. doi:10.1115/OMAE2012-83455.

Hamilton, J., C. Holub, J. Blunt, D. Mitchell, and T. Kokkinis. 2011. "Ice Management for Support of Arctic Floating Operations". In *Proceedings of the OTC Arctic Technology Conference, Houston, TX, USA, February 7–9, 2011*. ISBN: 978-1-61399-172-5.

Herman, A. 2016. "Discrete-Element Bonded-Particle Sea Ice Model DESIgn, Version 1.3a — Model Description and Implementation". *Geoscientific Model Development* 9:1219–1241. doi:doi:10.5194/gmd-9-1219-2016.

Hibler, W.D. III. 1979. "A Dynamic Thermodynamic Sea Ice Model". *Journal of Physical Oceanography* 9 (4): 815–846. doi:10.1175/1520-0485(1979)009<0815:ADTSIM>2.0.CO;2.

Hopkins, M.A., and W.D. Hibler. 1991. "Numerical Simulations of a Compact Convergent System of Ice Floes". *Annals of Glaciology* 15:26–30.

Hunke, E.C., and D. Comeau. 2011. "Sea Ice and Iceberg Dynamic Interaction". *Journal of Geophysical Research: Oceans* 116 (C5): 2156–2202. doi:10.1029/2010JC006588.

Hunke, E.C., and J.K. Dukowicz. 1997. "An Elastic-Viscous-Plastic Model for Sea Ice Dynamics". *Journal of Physical Oceanography* 27 (9): 1849–1867. doi:10.1175/1520-0485(1997)027<1849:AEVPMF>2.0.CO;2.

Hunke, E.C., W.H. Lipscomb, A.K. Turner, N. Jeffery, and S. Elliott. 2015. *CICE: the Los Alamos Sea Ice Model Documentation and Software User's Manual Version 5.1.*

Isaacson, M., and K.A. McTaggart. 1990. "Modelling of Iceberg Drift Motions Near a Large Offshore Structure". *Cold Regions Science and Technology* 19 (1): 47–58. ISSN: 0165-232X. doi:10.1016/0165-232X(90)90017-Q.

ISO 19906:2010(E). 2010. *Petroleum and Natural Gas Industries—Arctic Offshore Structures*. Standard. Geneva, CH: International Organization for Standardization.

Ji, S., Z. Li, C. Li, and J. Shang. 2013. "Discrete Element Modeling of Ice Loads on Ship Hulls in Broken Ice Fields". *Acta Oceanologica Sinica* 32 (11): 50–58. ISSN: 1869-1099. doi:10.1007/s13131-013-0377-2.

Johnson, M. 2011. "Rigmover blog. Ice scale." Visited on 04/01/2015. https://rigmover.com/2013/11/26/ice-scale/.

Jongma, I.J., E. Driesschaert, T. Fichefet, H. Goosse, and H. Renssen. 2009. "The Effect of Dynamic–Thermodynamic Icebergs on the Southern Ocean Climate in a Three-Dimensional Model". *Ocean Modelling* 26 (1–2): 104–113. ISSN: 1463-5003. doi:10.1016/j.ocemod.2008.09.007.

Keghouche, I., L. Bertino, and K.A. Lisæter. 2009. "Parameterization of an Iceberg Drift Model in the Barents Sea". *Journal of Atmospheric and Oceanic Technology* 26 (10): 2216–2227. doi:10.1175/2009JTECHO678.1.

Kegouche, I. 2010. "Modeling the Dynamics and Drift of Icebergs in the Barents Sea". PhD thesis, Universtity of Bergen, Norway.

Keinonen, A., M. Shirley, G. Liljestrom, and R. Pilkington. 2006. "Transit and Stationary Coring Operations in the Central Polar Pack". In *Proceedings of the 7th International Conference and Exhibition on Performance of Ships and Structures in Ice (ICETECH), Banff, Alberta, Canada, July 16–19, 2006.*

Keinonen, A., H. Wells, P. Dunderdale, R. Pilkington, G. Miller, and A. Brovin. 2000. "Dynamic Positioning Operation in Ice, Offshore Sakhalin, May–June 1999". In *Proceedings of the Tenth (2000) International Offshore and Polar Engineering Conference, Seatle, USA, May 28–June 2, 2000*, 683–690. ISBN: 1-880653-46-X.

Kjerstad, Ø.K., I. Metrikin, S. Løset, and R. Skjetne. 2015. "Experimental and Phenomenological Investigation of Dynamic Positioning in Managed Ice". *Cold Regions Science and Technology* 111:67–79. ISSN: 0165-232X. doi:10 . 1016 / j . coldregions.2014.11.015.

Konno, A., A. Nakane, and S. Kanamori. 2013. "Validation of Numerical Estimation of Brash Ice Channel Resistance with Model Test". In *Proceedings of the 22nd International Conference on Port and Ocean Engineering under Arctic Conditions, Espoo, Finland, June 09–13, 2013.* ISBN: 978-1-63266-549-2.

Kubat, I., M. Sayed, S.B. Savage, and T. Carrieres. 2005. "An Operational Model of Iceberg Drift". *International Journal of Offshore and Polar Engineering* 15 (2). ISSN: 1053–5381.

Lamb, Horace. 1975. *Hydrodynamics*. 184–187. Cambridge University Press.

Landau, L.D., and E.M. Lifshitz. 2003. *Teoreticheskaya fizika. T.VII. Teoriya uprugosti. [Theoretical physics. Vol. VII. Theory of Elasticity]*. M.:FIZMATLIT.

Leppäranta, M. 2011. *The Drift of Sea Ice*. Berlin Heidelberg: Springer-Verlag. doi:10 . 1007/978-3-642-04683-4.

Lichey, C., and H.H. Hellmer. 2001. "Modeling Giant-Iceberg Drift Under the Influence of Sea Ice in the Weddell Sea, Antarctica". *Journal of Glaciology* 47 (158): 452–460. doi:10.3189/172756501781832133.

Lu, P., Z. Li, B. Cheng, and M. Leppäranta. 2011. "A Parameterization of the Ice-Ocean Drag Coefficient". *Journal of Geophysical Research: Oceans* 116 (C7). doi:10 . 1029 / 2010JC006878.

Lu, P., Z.J. Li, Z.H. Zhang, and Dong X.L. 2008. "Aerial Observations of Floe Size Distribution in the Marginal Ice Zone of Summer Prydz Bay". *Journal of Geophysical Research: Oceans* 113 (C2): 2156–2202. doi:10.1029/2006JC003965.

Lu, W. 2014. "Floe Ice—Sloping Structure Interactions". PhD thesis, Norwegian University of Science and Technology, NTNU.

Lubbad, R., and S. Løset. 2011. "A Numerical Model for Real-Time Simulation of Ship-Ice Interaction". *Cold Regions Science and Technology* 65 (2): 111–127. ISSN: 0165-232X. doi:10.1016/j.coldregions.2010.09.004.

Marchenko, A., and K. Eik. 2012a. "Iceberg Towing in Open Water: Mathematical Modeling and Analysis of Model Tests". *Cold Regions Science and Technology* 73:12–31. ISSN: 0165-232X. doi:10.1016/j.coldregions.2011.11.008.

— . 2012b. "Methods of Iceberg Towing". *International Journal on Marine Navigation and Sagety of Sea Transportation* 6 (4): 507–516.

Marchenko, A., and Yu. Gudoshnikov. 2005. "The Influence of Surface Waves on Rope Tension by Iceberg Towing". In *Proceedings of the 18th International Conference on Port and Ocean Engineering under Arctic Conditions, Potsdam, NY, USA, June 26–30, 2005*, 543–554.

Marchenko, A., A. Kulyakhtin, and K. Eik. 2010. "Icebergs Drift in the Barents Sea: Data Analysis of Ice Tracking Buoy and Numerical Simulations". In *Proceedings of the 20th IAHR Interntional Symposium on Ice, Lahti, Finland, June 14–18, 2010*.

Marchenko, A., and C. Ulrich. 2008. "Iceberg Towing: Analysis of Field Experiments and Numerical Simulations". In *Proceedings of the 19th IAHR International Symposium on Ice, Vancouver, BC, Canada, July 6–11, 2008*, 909–921.

Marchenko, Aleksey. 2014. "Influence of Added Mass Effect on Rotation of a Drifting Iceberg in Non-Stationary Current". In *Proceedings of the ASME 2014 33rd International Conference on Ocean, Offshore and Arctic Engineering, San Francisco, CA, USA, June 8–13, 2014*, vol. 10. doi:10.1115/OMAE2014-23868.

McClintock, J., R. McKenna, and C. Woodworth-Lynas. 2007. *Grand Banks Iceberg Management*. PERD/CHC Report 20-84. PERD/CHC, National Research Council Canada, Ottawa, ON.

Metrikin, I. 2014. "A Software Framework for Simulating Stationkeeping of a Vessel in Discontinuous Ice". *Modeling, Identification and Control* 35 (4): 211–248. ISSN: 1890-1328.

— . 2015. "Experimental and Numerical Investigations of Dynamic Positioning in Discountinuous Ice". PhD thesis, Norwegian University of Science and Technology, NTNU.

Munjiza, A.A., E.A. Knight, and E. Rougier. 2011. *Computational Mechanics of Discontinua*. John Wiley & Sons, Ltd. ISBN: 978-0-470-97080-5.

Newman, J.N. 1977. *Marine Hydrodynamics*. The MIT Press. ISBN: 978-0-262-14026-3.

Notz, D., F. A. Haumann, H. Haak, J. H. Jungclaus, and J. Marotzke. 2013. "Arctic sea-ice evolution as modeled by Max Planck Institute for Meteorology's Earth system model". *Journal of Advances in Modeling Earth Systems* 5 (2): 173–194. ISSN: 1942-2466. doi:10.1002/jame.20016.

Orsten, A. 2014. "Automatic Reliability-based Control of Iceberg Towing in Open Waters". MA thesis, Norwegian University of Science and Technology, NTNU.

Polojärvi, A., and J. Tuhkuri. 2013. "On Modeling Cohesive Ridge Keel Punch Through Tests with a Combined Finite-Discrete Element Method". *Cold Regions Science and Technology* 85:191–205. doi:10.1016/j.coldregions.2012.09.013.

Pöschel, T., and T. Schwager. 2005. *Computational Granular Dynamics. Models and algorithms.* Springer-Verlag Berlin Heidelberg.

Radjai, F., and V. Richefeu. 2009. "Contact Dynamics as a Nonsmooth Discrete Element Method". Advances in the Dynamics of Granular Materials, *Mechanics of Materials* 41 (6): 715–728. ISSN: 0167-6636. doi:10.1016/j.mechmat.2009.01.028.

Rampal, P., S. Bouillon, E. Ólason, and M. Morlighem. 2016. "neXtSIM: a New Lagrangian Sea Ice Model". *The Cryosphere* 10:1055–1073. doi:10.5194/tc-10-1055-2016.

Randel, C., F. Ralph, D. Power, and P. Stuckey. 2009. "Technological Advances to Assess, Manage and Reduce Ice Risk in Northern Developments". In *Proceedings of OTC Arctic Technology Conference, Houston, TX, USA, May 4–7, 2009*.

Richard, M., and R. McKenna. 2013. "Factors Influencing Managed Sea Ice Loads". In *Proceedings of the 22nd International Conference on Port and Ocean Engineering under Arctic Conditions, Espoo, Finland, June 09–13, 2013*. ISBN: 978-1-63266-549-2.

Riikilä, T.I., T. Tallinen, J. Åström, and J. Timonen. 2015. "A Discrete-Element Model for Viscoelastic Deformation and Fracture of Glacial Ice". *Computer Physics Communications* 195:14–22. doi:10.1016/j.cpc.2015.04.009.

Rudkin, P., C. Young, P. Barron Jr, and G. Timco. 2005. "Analysis and Results of 30 Years of Iceberg Management". In *Proceedings of the 18th International Conference on Port and Ocean Engineering under Arctic Conditions, Potsdam, NY, USA, June 26–30, 2005*, 557–572.

Sayed, M., T. Carrieres, H. Tran, and S.B. Savage. 2002. "Development of an Operational Ice Dynamics Model for the Canadian Ice Service". In *Proceedings of the Twelfth (2002) International Offshore and Polar Engineering Conference, Kitakyushu, Japan, May 26–31, 2002*. ISBN: 1-880653-58-3.

Sayed, M., R. Fredreking, and Barker A. 1999. *Numerical Simulation of Pack Ice Forces on Structures: a Parametric Study*. Techincal Report HYD-TR-041, PERD/CHC Report 9-80. National Reseach Council of Canada.

Sayed, M., and I. Kubat. 2011. "Forces on Ships Transiting Pressured Ice Covers". In *Proceedings of the Twenty-first (2011) International Offshore and Polar Engineering Conference, Maui, Hawaii, USA, June 19–24, 2011*, 1087–1092. ISBN: 978-1-880653-96-8.

Shunying, J., D. Shaocheng, and L. Shewen. 2015. "Analysis of Ice Load on Conical Structure With Discrete Element Method". *Engineering Computations* 32 (4): 1121–1134.

Sodhi, D.S., and M. El-Tahan. 1980. "Prediction of an Iceberg Drift Trajectory During a Storm". *Annals of Glaciology* 1:77–82.

Stepanov, I., Yu. Gudoshnikov, and A. Iltchuk. 2005. "Iceberg Towing Experiment in the Barents Sea". In *Proceedings of the 18th International Conference on Port and Ocean Engineering under Arctic Conditions, Potsdam, NY, USA, June 26–30, 2005*, 585–594.

Sukhorukov, S., and S. Løset. 2013. "Friction of Sea Ice on Sea Ice". *Cold Regions Science and Technology* 94:1–12. ISSN: 0165-232X. doi:10.1016/j.coldregions.2013.06.005.

Tchieu, A.A., D. Crowdy, and A. Leonard. 2010. "Fluid-Structure Interaction of Two Bodies in an Inviscid Fluid". *Physics of Fluids* 22. doi:10.1063/1.3485063.

Timco, G.W. 2011. "Isolated Ice Floe Impacts". *Cold Regions Science and Technology* 68 (1–2): 35–48. doi:10.1016/j.coldregions.2011.04.008.

Tsarau, A., and S. Løset. 2015. "Modelling the Hydrodynamic Effects Associated with Station-Keeping in Broken Ice". *Cold Regions Science and Technology* 118:76–90. doi:10.1016/j.coldregions.2015.06.019.

Tsarau, A., R. Lubbad, and S. Løset. 2016. "A Numerical Model for Simulating the Effect of Propeller Flow in Ice Management". *Cold Regions Science and Technology*. ISSN: 0165-232X. doi:10.1016/j.coldregions.2016.06.002.

Turnbull, I.D., N. Fournier, M. Stolwijk, T. Fosnaes, and D. McGonigal. 2015. "Operational Iceberg Drift Forecasting in Northwest Greenland". *Cold Regions Science and Technology* 110:1–18. ISSN: 0165-232X. doi:10.1016/j.coldregions.2014.10.006.

Turnbull, R.D., and R. Pilkington. 2012. "Beaufort Sea Ice Drift Forecasting On-Board the CCGS Amundsen". In *Proceedings of the 13th International Conference and Exhibition on Performance of Ships and Structures in Ice (ICETECH), Banff, Alberta, Canada, September 17–20, 2012*, 268–274.

Visseq, V., P. Alart, and D. Dureisseix. 2013. "High Performance Computing of Discrete Nonsmooth Contact Dynamics with Domain Decomposition". *International Journal for Numerical Methods in Engineering* 96 (9): 584–598. ISSN: 1097-0207. doi:10.1002/nme.4578.

Wassgren, C.A., J.A. Cordova, R. Zenit, and A. Karion. 2003. "Dilute granular flow around an immersed cylinder". *Physics of Fluids* 15 (11): 3318–3330.

WMO. 2014. *World Meteorological Organisation Sea Ice Nomenclature, WMO No. 259*.

Wright, B. 1999. *Evaluation of Full Scale Data for Moored Vessel Stationkeeping in Pack Ice (With Reference to Grand Banks Development)*. PERD/CHC Report 26-200. The National Reseach Council of Canada.

— . 2000. *Full Scale Experience with Kulluk Stationkeeping Operations in Pack Ice (With Reference to Grand Banks Developments)*. PERD/CHC Report 25-44. National Reseach Council of Canada.

Zhang, Q., R. Skjetne, I. Metrikin, and S. Løset. 2015. "Image Processing for Ice Floe Analyses in Broken-Ice Model Testing". *Cold Regions Science and Technology* 111:27–38. ISSN: 0165–232X. doi:10.1016/j.coldregions.2014.12.004.

Zhang, Y., and E.C. Hunke. 2001. "Recent Arctic Change Simulated With a Coupled Ice-Ocean Model". *Journal of Geophysical Research: Oceans* 106 (C3): 4369–4390. ISSN: 2156-2202. doi:10.1029/2000JC900159.

Zubakin, G., A. Naumov, and I. Buzin. 2004. "Estimates of Ice and Iceberg Spreading in the Barents Sea". In *Proceedings of the 14th International Offshore and Polar Engineering Conference, Toulon, France, May 23–28, 2004*. ISBN: 1-880653-62-1.

Appendix A:
Planar multi-body model of iceberg free drift and towing in broken ice

Numerical model of iceberg in broken ice is presented in the paper. We discuss here numerical challenges related to broken ice field generation and contact impulse to force conversion.

Planar multi-body model of iceberg free drift and towing in broken ice

Renat Yulmetov [a,b,*], Raed Lubbad [b], Sveinung Løset [a,b]

[a] The University Centre in Svalbard, P.O. Box 156, 9171 Longyearbyen, Norway
[b] Sustainable Arctic Marine and Coastal Technology (SAMCoT), Centre for Research-based Innovation (CRI), Norwegian University of Science and Technology (NTNU), Trondheim, Norway

ABSTRACT

There are no full-scale data on iceberg towing in ice. However, there is a great interest in such an operation. Simulating the interaction between icebergs and surrounding ice floes during towing may help with choosing iceberg management strategies and design criteria for icebreakers and tug vessels. Broken ice has a discontinuous nature; therefore, it is proposed to model the interaction using a discrete element method (DEM) and known approximations of wind and water drag, wave, and Coriolis forces. The DEM is used to simulate the contacts between rigid, polygon-shaped ice floes. The floes are prevented from interpenetration by applying contact impulses tending to separate the bodies. Depending on the relative velocity of the contacting bodies, the contacts can be classified into two categories: *collisions* at non-zero relative velocity and *resting contacts* where the contacting bodies have the same velocity. Converting the calculated impulses into contact forces is straightforward for resting contacts but not for collisions. First, the applied impulses for collisions depend on the choice of restitution coefficient. Second, the collision duration must be estimated in order to convert collision impulses into forces. This paper discusses the choice of the restitution coefficient for ice and proposes an approach to estimate the collision force using the collision duration, which appears to be roughly proportional to the square root of the reduced mass. Additionally, the paper presents an innovative method to generate the ice field through which the iceberg is towed. The field is represented by a domain filled with randomly shaped rigid ice floes. The algorithm is capable of creating an ice field of given concentration and size distribution of the ice floes. The power law size distribution, obtained from aerial and satellite image analysis, is reproduced with high accuracy. The new approach to estimate the collision forces is subjected to a simple test on isolated floe impacts showing a good agreement with experimental and full-scale data. Finally, the simulation of iceberg towing is demonstrated and compared to experimental data. The results of the simulation were found to be in satisfactory agreement with the experiment.

© 2015 Elsevier B.V. All rights reserved.

1. Introduction

Drifting icebergs and sea ice may be a serious threat for offshore structures in the Arctic. The waters of the Greenland Sea and the Barents Sea are of high interest for the petroleum industry. But at the same time these regions are prone to icebergs and sea ice simultaneously, which may cause extreme physical loads that need to be considered during the exploitation period or even during relatively short exploratory drilling. Ice management (IM) is performed to reduce ice actions on the structure and to secure the safety of marine operations. It involves ice and iceberg intelligence, tracking, forecasting, threat evaluation, physical ice management, and possible emergency disconnection of a structure (Eik, 2008). Correct estimation of the kinematic and dynamic parameters of sea ice and iceberg drift is important for the selection of correct IM procedures (Hamilton et al., 2011).

Drift forecasting on a strategic scale provides general information about ice conditions and the presence of icebergs in the region of interest (Blunt et al., 2013). Then, several zones may be established around the structure on a tactical scale. For example, IM plans for Shtokman gas and condensate field considered short-term forecasting starting from a general surveillance zone and ending within an emergency disconnection limit (Coche et al., 2011). Alert systems are used simultaneously with a threat-evaluation tool.

Next, physical ice management such as ice breaking or iceberg towing might be performed to reduce broken ice actions or to avoid collisions with icebergs. Ice breaking and iceberg management are usually considered separately. Iceberg towing operations in open water have been successfully performed in the Canadian Arctic since 1971. The technical success, when a planned change in course was achieved, reached 85.5% for more than 1500 towing operations in open water (Rudkin et al., 2005). But iceberg towing in broken ice still hasn't been performed and it raises a great industrial interest.

There are several Arctic offshore fields where the problem of iceberg towing in ice is relevant. For example, the ice conditions presented in the Shtokman study presume icebergs in broken ice originated from

* Corresponding author at: The University Centre in Svalbard, P.O. Box 156, 9171 Longyearbyen, Norway.. Tel.: +47 90228274.
E-mail address: RenatY@unis.no (R. Yulmetov).

Franz Josef Land, Svalbard, and Novaya Zemlya (Abramov, 1992). For those conditions, it may be necessary to move and deflect icebergs, e.g. by rope-towing. Ice forces during towing are a limiting factor here that mainly depends on the ice concentration, thickness, and floe size distribution.

The interaction between floating ice floes and an iceberg is a complex process that involves various physical phenomena (Fig. 1). Depending on confinement in the lateral direction, mechanical properties of the ice, speed, and floes' shapes, different failure processes may occur in the colliding ice floes. For example, highly concentrated and confined ice fields with internal stresses can undergo a ridging processes or crushing in the high-pressure zones between the floes. Also, large ice floes are likely to be split depending on several factors, e.g. the size, confinement, and shape (Lu et al., 2015).

On the contrary, low-energy collisions for unconfined sea ice lead only to minor local crushing without providing large deformations or sufficient change of the floes' shapes. Low relative velocities were measured in the Greenland Sea and no large-scale failure was observed in adjacent ice floes and no ridging around icebergs (Yulmetov et al., 2013a). Also, it was experimentally shown that towing in broken ice is feasible only at low velocity and in low concentrated ice (Eik and Marchenko, 2010). Therefore, free drift or towing of icebergs in broken ice may be modelled in two dimensions (2D).

When it comes to numerical modelling, sea ice is commonly treated as a continuum on global scales (Hibler, 1979; Hunke and Comeau, 2011). However, broken ice included into the towing model requires a discontinuous approach because the average size of an ice floe is comparable to the size of the zone of interest. Within the discontinuous approach, there are two alternative methods: the smooth discrete element method and the non-smooth discrete element method. The former describes ice as a set of bodies with a certain contact response. The material properties are given as elastic, viscous and plastic constants, and the friction coefficient. Forces are calculated explicitly for each time step of highly time-resolved contacts, providing a smooth velocity history. The method is used to model icebreakers in ice, dynamic positioning, and ridging processes (Hopkins, 1992; Løset, 1994a; Tuhkuri, 2005; Wilchinsky et al., 2011).

The non-smooth discrete element method (also called contact dynamics) is based on the so-called constraints. In addition to the momentum equation, the method deals with non-penetration constraints that must be fulfilled in order to correctly model the colliding bodies as separate. There are also friction constraints for the bodies in contact. The contact response in this case is described in terms of restitution and friction coefficients. The details of this method are given in a later section. The method was used to model ship motion in sea ice and dynamic positioning (see Konno et al., 2013; Lubbad and Løset, 2011; Metrikin and Løset, 2013). The waterline processes and large-scale failure in ice were incorporated into this method for the first time by Lubbad and Løset (2011). Their numerical model was able to reproduce ice breaking in bending after creating radial cracks in level ice, buoyancy and hydrodynamic drag forces.

Another approach in the sea-ice force estimation for iceberg motion through a field of relatively small ice floes was proposed by Marchenko et al. (2010). It was assumed that an iceberg spends its energy creating a channel in a broken ice field, by simply displacing ice floes on the sides. However, the approach provides only the average force value but not its evolution.

The paper presents a numerical model for the simulation of iceberg free drift and towing in a broken ice field using the non-smooth discrete element method. This method is capable of simulating contacts between icebergs and rigid ice floes of different shapes; this has never been done before in relation to iceberg free drift or towing in broken sea ice. In the non-smooth discrete element method, each contact is treated either as a *resting contact* or as a *collision* depending on the relative velocity of the contacting bodies. For the latter to be resolved accurately, a good estimation of a restitution coefficient is required. The restitution coefficient, in general, depends on the relative velocity of the colliding bodies and the contact geometry but it is usually treated as a material constant. This paper proposes numerical values for the restitution coefficients that should be used for iceberg drift and towing simulations. Moreover, the non-smooth discrete element method typically solves for impulses instead of forces. Estimating resting contact forces from the calculated impulses is straightforward, e.g. divide the calculated impulse by the time step. However, the estimation of collision forces is more complicated because the collision duration in reality is not the same as the time step used. A method for estimating the collision force from the collision duration is proposed in this paper. A simple test on isolated floe impacts is performed to validate our calculations of the collision duration and restitution coefficient.

In addition, the shapes of ice floes used for earlier studies evolved from circular disks to polygons, but the shapes were still predetermined and their size distribution was not considered. Ice floe size appears to be an important parameter as it affects possible failure mode and nominal contact area. The floe size distribution obtained from the nature and concentration of an ice field must be considered when generating a large number of polygonal ice floes. This paper also presents an effective method for generating a broken ice field with a given size distribution and ice concentration.

The paper is structured in a way that describes the equations of motion starting from known approximations of continuum forces. Then, it explains how to introduce discontinuity and contact dynamics, and how to calculate contact impulses. Next, the choice of the restitution coefficient value and the collision force estimation from the impulse history are discussed. Also, it is shown how to produce the initial set of random polygon shaped ice floes with a given power law size distribution. And finally, a couple of numerical examples are given. First, a simple numerical test of isolated floe impacts is carried out and compared with an experimental and full-scale dataset summarized by Timco (2011). Second, the iceberg towing with constant speed of 0.7 m/s in 50% concentrated 1.16 m thick broken ice is simulated. The average towing force calculated using the model is compared to the scaled values obtained in the experiment of Eik and Marchenko (2010).

2. Model description

Drift models usually refer to an iceberg as a point mass *M* (Bigg et al., 1997; Kubat et al., 2005; Lichey and Hellmer, 2001; Smith, 1993). In the current model, the iceberg is given a polygonal shape at the waterline. Further, it is given a sail and keel as needed for calculation of drag forces. The geometry of the underwater part can be studied using sonar (Smith and Donaldson, 1987), underwater vehicles (Hobson et al., 2011), or EM
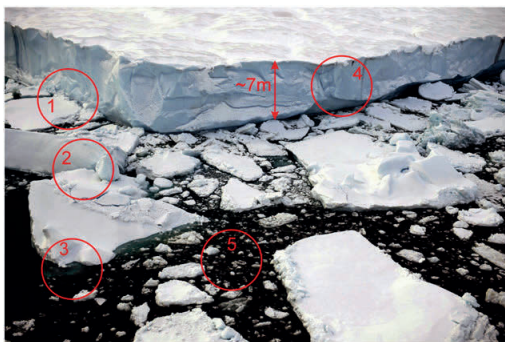

Fig. 1. An example of an iceberg drifting in broken sea ice in the Greenland Sea, 2012. Some important processes affecting the drift are: (1) ice floe–iceberg contacts, (2) floe–floe contacts, (3) water drag on floes and iceberg, (4) wind drag on floes and iceberg sail, and (5) hydrodynamic damping and brash ice.

device (Timco, 2000); the sail geometry is usually estimated optically by using a sextant, laser rangefinder (Barker et al., 2004), or stereo aerial photography (Løset and Carstens, 1996). Datasets of iceberg shapes and their analysis can be found in (McKenna, 2005; Trott and Comfort, 2007). Also, the shapes at the waterline and thickness of the ice floes in the model must be set and, thus, the mass of ice floes is defined.

The equations for the model are written in a North–East–Down (NED) coordinate system with x-, y-, and z-axes directed, respectively, towards north, east, and towards the centre of the Earth. The coordinate system has its origin fixed at the Earth's surface at a certain point associated either with the offshore structure to be protected from large ice forces by IM or with the initial position of the iceberg. We will consider only the motion in the x–y plane; the z-axis is needed only for consistency. The iceberg drifts under the action of the following physical environmental forces: water and air drag forces ($\vec{F}_w$, $\vec{F}_a$), Coriolis force ($\vec{F}_C$), wave-induced force ($\vec{F}_{waves}$), and ice-induced force or ice resistance ($\vec{F}_{si}$). In the case of towing, there are towing forces as well ($\vec{F}_{tow}$). Therefore, the momentum equation can be written in the form

$$M\frac{d\vec{U}}{dt} = \vec{F}_w + \vec{F}_a + \vec{F}_C + \vec{F}_{waves} + \vec{F}_{si} + \vec{F}_{tow} \qquad (1)$$

where $\vec{U}$ is the translational velocity of the iceberg. The angular characteristics are measured with respect to the vertical axis going through the centroid of the horizontal cross-section of the iceberg at the waterline. The angular momentum changes only because of applied torques from sea ice τ_{si} and towing τ_{tow}

$$I_z\frac{d\Omega}{dt} = \tau_{si} + \tau_{tow} \qquad (2)$$

where Ω is the angular velocity, and I_z is the moment of inertia about the vertical axis. We do not take into account torques due to hydrodynamic effects such as turbulence and assume the drift to be rotationally stable in the case of no contact with ice floes.

The mass $M = M_0 + m$ includes the real mass M_0 and the added mass m as 10%–50% of the real mass (Bass and Sen, 1986; Eik, 2009; Kubat et al., 2005). Similar equations are applied to ice floes except that no towing is applied to the floes. In the following sections, we will examine each of the forces more closely.

2.1. Continuum forces

In the general case, the total viscous drag can be separated into frictional drag and pressure (or residual) drag (Newman, 1977). Drag force approximations for icebergs and ice floes are different depending on the dominant component of the total drag. The drag force acting on icebergs and ice floes is proportional to the square of the relative fluid velocity, projected area, and the density of the fluid. The ocean current normally varies with depth; thus, the underwater part of an iceberg is often divided into layers and the drag force is calculated as a sum of the drag forces on each of these layers (Keghouche et al., 2009). Normally, the skin friction drag is neglected (Morison and Goldberg, 2012). We use the following approximations for the drag forces acting on icebergs

$$\vec{F}_w^{iceberg} = \frac{1}{2}C_w\rho_w\sum_i A_i\left|\vec{V}_{i,w} - \vec{U}\right|\left(\vec{V}_{i,w} - \vec{U}\right)$$
$$\vec{F}_a^{iceberg} = \frac{1}{2}C_a\rho_a A_{sail}\left|\vec{V}_a - \vec{U}\right|\left(\vec{V}_a - \vec{U}\right) \qquad (3)$$

where the indices w and a denote water and air, respectively. C_w, C_a are the drag coefficients for air and water, A_i is a vertical cross-section area of i-th underwater layer of the iceberg, A_{sail} is the sail vertical cross-section of the iceberg, $\vec{V}_a$ is air velocity, and $\vec{V}_{i,w}$ is current speed at the i-th layer of the water column.

According to Lu et al. (2011), the drag force on a sea ice floe is the sum of form drag, skin friction, and ridge-form drag. When excluding ridges from consideration we may use

$$\vec{F}_{a,w}^{floe} = \left(\frac{C_e}{2}\left[1 - \left(\frac{c}{1-c}\cdot\frac{h_{sail,keel}}{D}\right)^{1/2}\right]^2 h_{sail,keel}D + C_s A\right)\rho_{a,w}\left|\vec{V}_{a,w} - \vec{U}\right|$$
$$\times\left(\vec{V}_{a,w} - \vec{U}\right) \qquad (4)$$

where $h_{sail,keel}$ is the sail height or keel depth of the ice floe depending on air or water drag, D is the floe size characterized later by the mean calliper diameter, A is the horizontal surface area, c is the ice concentration, and typically $C_e = 1.0$, $C_s = 2.0 \times 10^{-3}$ (Lu et al., 2011). Approximation (4) takes into account attenuation of the form drag due to wake effects that are important in broken ice fields. In high concentrations where the spacing between ice floes is small, the form drag can be neglected. Therefore, the concentration is limited by $c < 1/(1 + h_{sail,keel}/D)$.

The water velocity may be measured in situ using an Acoustic Doppler Current Profiler (Yulmetov et al., 2012) or it can be extracted from ocean dynamics models (Keghouche et al., 2009). The same relates to the wind speed that can be measured using weather stations or extracted from large-scale wind models.

An iceberg is a relatively large object that causes disturbance in an otherwise uniform current. The flow around an iceberg is characterized by a very high Reynolds number. The estimate for a 100-m-wide iceberg in a flow with an average relative velocity of 0.1 m/s (Yulmetov et al., 2013b) gives

$$Re = \frac{V_w D}{\nu} = \frac{0.1\cdot 100}{2\cdot 10^{-6}} = 0.5\cdot 10^7 \qquad (5)$$

where V_w is the ocean current speed, D is the characteristic width of the iceberg at the waterline, and v is the kinematic viscosity of seawater. In this situation, the flow becomes turbulent and vortex shedding is observed.

The flow before the separation points can still be described by using potential flow theory. The potential flow theory is used on small distances around an iceberg (up to three times the radius of the iceberg) where sufficient difference in the current velocity exists. Because of limited computational resources and for simplicity reasons, the iceberg is approximated by a circle with the equivalent radius $R_{eq} = p/2\pi$, where p is the perimeter of the iceberg at the waterline. The following equations can be derived from the standard solution for a circular cylinder (Newman, 1977)

$$V_x = V_x^0\left(1 + \frac{R_{eq}^2(\eta^2 - \xi^2)}{(\xi^2 + \eta^2)^2}\right) - V_y^0\frac{2\xi\eta R_{eq}^2}{(\xi^2 + \eta^2)^2}$$
$$V_y = V_y^0\left(1 + \frac{R_{eq}^2(\xi^2 - \eta^2)}{(\xi^2 + \eta^2)^2}\right) - V_x^0\frac{2\xi\eta R_{eq}^2}{(\xi^2 + \eta^2)^2} \qquad (6)$$

where V_x^0, V_y^0 are the components of the undisturbed flow velocity $\vec{V}_w$ and V_x, V_y are the components of the flow velocity at the point with coordinates ξ, η measured from the centre of the iceberg. The origin of the iceberg-fixed ξ, η system is attached to the centroid of the horizontal cross-section of the iceberg at the waterline. An example of a solution for the flow directed along the y-axis is shown in Fig. 2. The black line represents the border of the domain around an iceberg where the solution given by Eq. (6) is applied. The flow provides stronger acceleration on the sides of an iceberg and pushes adjacent ice floes directly behind the iceberg, tending to close the wake.

The drag forces on an iceberg may also be calculated using computational fluid dynamics (CFD). However, it is numerically expensive and
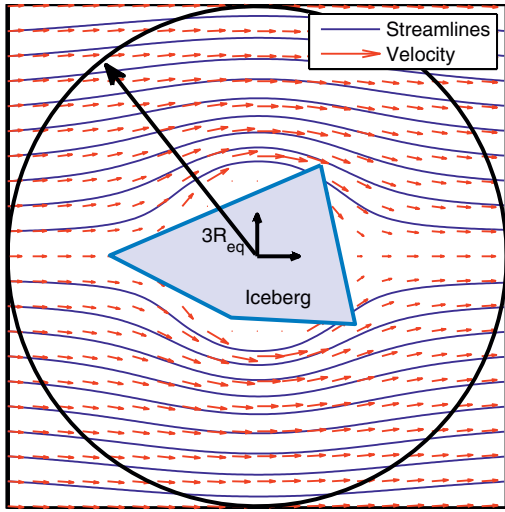
Fig. 2. The solution for potential flow around a cylinder of equivalent radius is used in a small region around an iceberg. The flow velocity is directed along the y-axis. Eq. (6) is applied within a black circle with the radius of $3R_{eq}$.

there are large uncertainties in the geometry of icebergs and the sea current properties. An approach using CFD results in uncertain drag force values for which it is not worth sacrificing the necessary computational time and complexity.

The Coriolis force is calculated for every time step as

$$\overrightarrow{F}_C = M_0 f \overrightarrow{k} \times \overrightarrow{U} \tag{7}$$

where $f = 2\Omega_{Earth} \sin \phi$ is the Coriolis parameter, $\overrightarrow{k}$ is the normal vector parallel to the z-axis and directed towards the centre of the Earth, $\Omega_{Earth} = 7.29 \cdot 10^{-5}$ rad/s is the angular velocity of the Earth, and ϕ is the latitude.

Several studies conclude that waves penetrating an ice field attenuate due to the dissipation of the wave energy in diffraction, as well as due to the floe–floe interactions. The wave amplitude is commonly considered to drop exponentially with travelled distance in the ice field (Frankenstein et al., 2001; Squire, 2007). Therefore, the wave forces are neglected in the present model.

In the case of an iceberg, or generally any kind of floating structure being towed, towing rope properties and towing setup must be considered. For example, oscillations may occur in an iceberg-towing line-tug system (Marchenko and Eik, 2012). In the model, it is possible to use simplified models of tow. For example, an elastic unit can be used between the carriage and a model of iceberg in the simulation of towing experiment in an ice tank (Eik and Marchenko, 2010). Also, assuming that the towing operation is long enough in time, two simplifications can be made: towing with a constant force $\overrightarrow{F}_{tow}$ or towing with a constant velocity. In the first case, the possible towing trajectory and velocity are of interest. In the latter case, the towing force needed to maintain the given towing velocity can be estimated. In reality, neither the towing force nor the velocity can be made constant. A ship model should be coupled with the presented iceberg model as the next step in the modelling of towing operations.

2.2. Contact forces

As mentioned previously, low relative velocity and low confinement results in almost the absence of large-scale failures in the ice. This

means that the interaction between ice floes and icebergs may be approximated as two-dimensional. In 2D, for every object, there are only three degrees of freedom—two translational and one rotational (x, y, φ). In the model, the iceberg and ice floes are represented by rigid polygons; it is also possible to represent them by discs (Fig. 3).

The contact dynamics method (Pfeiffer and Glocker, 2008) is applied for the calculation of contact response appearing in between floating bodies. An example of the calculation procedure that is used to resolve contacts in multi-body dynamics will be given below. For simplicity, we present just two bodies in contact. The basics of the method are to impose and fulfill certain constraints in addition to the momentum law for every contact. The non-penetration constraints are responsible for keeping the bodies apart and, in case of single contact, it can be written as

$$\delta \geq 0 \tag{8}$$

where δ is separation distance between the contacting bodies defined as the shortest Cartesian distance (see Fig. 3). For two polygons it can be the distance between two closest vertices belonging to different polygons, or between a vertex and an edge, or between two parallel edges. The separation distance between the bodies, contact normal, and tangent are determined according to the GJK algorithm abbreviated by the first letters of the authors' surnames (Gilbert et al., 1988).

In general, the separation distance and its derivative depend on the positions of the bodies in the form:

$$\delta = \delta(\mathbf{x}, t), \ \mathbf{x} = |x_1, y_1, \varphi_1, x_2, y_2, \varphi_2|^T \quad \frac{d\delta}{dt} = \frac{\partial \delta}{\partial \mathbf{x}} \cdot \mathbf{U} + \frac{\partial \delta}{\partial t} = \mathbf{J} \cdot \mathbf{U} + \mathbf{b} \tag{9}$$

where $\mathbf{J}$ is called Jacobian, and $\mathbf{b}$ is a bias term. They define a linear mapping between the bodies' coordinates and the normal constraints. In case of single contact, $\mathbf{J}$ is a 1×6 vector with dimensionless components and $\mathbf{b}$ is a number. For two bodies being in contact $\delta = 0$, then $\dot{\delta} = 0$, $\mathbf{b} = 0$ and therefore, $\mathbf{J} \cdot \mathbf{U} = 0$. However, small overlap between polygons is possible during the simulation. A part of the bias term $\mathbf{b}$ is responsible for position corrections preventing such overlaps, and the Baumgarte stabilization is applied (Baumgarte, 1972). Further, it will be shown that another part of the bias term is required to provide the restitution in collisions.
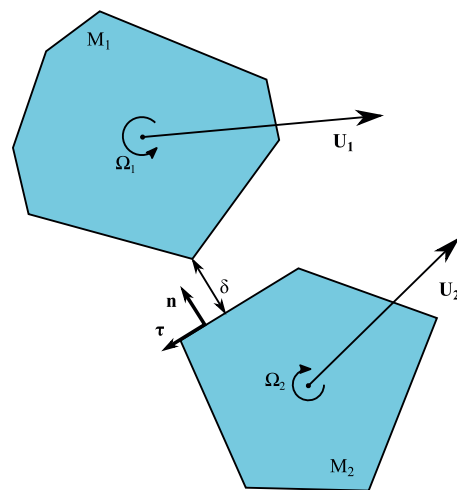

Fig. 3. Two floating bodies separated by distance δ before a contact.

The inequality (8) must be fulfilled by applying contact impulses that will tend to separate the bodies. The momentum law for the system of two bodies in contact can be written in the form

$$
\begin{aligned}
&\mathbf{M}\Delta\mathbf{U} - \mathbf{F}_{ext}\Delta t - \mathbf{P}_{cont} = 0 \\
&\mathbf{M} = diag\{M_1, M_1, I_{z1}, M_2, M_2, I_{z2}\} \\
&\mathbf{U} = \left| U_{x1} \quad U_{y1} \quad \Omega_1 \quad U_{x2} \quad U_{y2} \quad \Omega_2 \right|^T \\
&\mathbf{F}_{ext} = \left| F_{x1} \quad F_{y1} \quad \tau_1 \quad F_{x2} \quad F_{y2} \quad \tau_2 \right|^T
\end{aligned}
\tag{10}
$$

where $\mathbf{M}$ is a diagonal mass matrix of size 6×6 with the masses M and the moments of inertia I_z at the diagonal. Projections of the external forces F_x, F_y and torques τ are calculated according to Eqs. (3), (4), (6), (7). Subscripts 1 or 2 are related to the bodies in contact. Contact impulses are collected in a six-component vector $\mathbf{P}_{cont}$. Also, the normal component of the contact impulse $\mathbf{P}_{cont}$ can be expressed as $\mathbf{P}_n = \mathbf{J}^T\lambda$, where λ is normal impulse magnitude.

Eqs. (9) and (10) projected on the contact normal result in the following numerical procedure

$$
\begin{aligned}
&\mathbf{J}\mathbf{U}_+ = -\mathbf{b} \\
&\mathbf{M}(\mathbf{U}_+ - \mathbf{U}_-) = \mathbf{F}_{ext}\Delta t + \mathbf{J}^T\lambda
\end{aligned}
\tag{11}
$$

in order to find a new velocity vector $\mathbf{U}_+$ and normal impulse magnitude λ. The normal impulse must be greater than zero to be sure that the bodies are going to be separated.

The contacts are treated differently based on the relative velocity. If the relative velocity at contact is above a certain threshold value, then *collision* happens and it is treated according to Newton's impact law

$$
e = -\frac{U_+}{U_-}
\tag{12}
$$

where U_- is the normal projection of relative velocity before the collision and U_+ is the normal projection of relative velocity after the collision. The restitution coefficient e is defined by the impact law and it is an important parameter of the model. The choice of the restitution coefficient will be discussed later. The impact law (12) and condition $\dot{\delta} \geq 0$ are satisfied by $\mathbf{b} = -eU_-$. Thus, the bias term is also responsible for the restitution in collisions. Large changes of relative velocity happen in collisions, and large changes of contact force are expected.

The case of *resting contact* represents the situation where the contacting bodies move together with similar velocities. In resting contacts, the separation distance δ and normal contact velocity $\dot{\delta}$ are considered to be equal to zero for two or more consecutive time steps. The bias term in this case is used only for position corrections. A typical example of resting contact is a contact between an iceberg and an ice floe pushed by the iceberg during more than one time step.

The threshold velocity used to distinguish between the two types of contacts is chosen to be as low as possible, but it must be large enough to correctly reproduce the resting contact behaviour and to prevent numerical oscillations. We use one percent of the maximum possible velocity in the simulation as a value for the threshold velocity, assuming that relative velocities are lower than the threshold after almost inelastic impacts.

In the tangential direction, the friction constraints are introduced. At every contact, Coulomb's friction law is represented by the following constraint

$$
-\mu\lambda \leq \mathbf{P}_\tau \leq \mu\lambda
\tag{13}
$$

So, tangential impulse is applied when tangential velocity is present but its magnitude must never exceed $\mu\lambda$, where λ is found from (11). The approach doesn't distinguish between static and dynamic friction. The choice of friction coefficient μ is based on field studies carried out in the Barents Sea and in the Greenland Sea (Sukhorukov, 2013;

Sukhorukov and Løset, 2013). It was observed that there is no difference and no velocity dependence between dry ice and wet ice friction coefficients. We are also aware of surface smoothing after repeated contacts. However, we consider that regular wetting of contacting surfaces by sea water takes place and keeps surfaces in the same condition. The friction coefficient that was used in the model varies in the range of 0.3–0.5.

In case of N_c contacts between N_b bodies, matrix $\mathbf{M}$ is $3N_b \times 3N_b$ in size, $\mathbf{U}_-$, $\mathbf{U}_+$, and $\mathbf{F}_{ext}$ are $3N_b$ component vectors, the Jacobian is $N_c \times 3N_b$, $\mathbf{b}$ and λ has N_c components. The unified equations for collisions, resting contacts, and no contact can be written as a mixed linear complementarity problem and solved using a projected Gauss–Seidel iterative method (Catto, 2005; Pfeiffer and Glocker, 2008). The calculated impulses are applied to the floes and their positions and velocities are updated after the semi-explicit Euler integration. All of the calculations in relation to the contact dynamics are performed using an open source physics engine called Box2D (Catto, 2013). The engine performs contact detection and solves the constraints. We will not discuss here all of the numerical features of the engine, but a short algorithm description can be found in Catto (2005).

Finally, when the equations of motion can be solved for the iceberg and a large number of ice floes, additional boundary conditions on the domain must be set. Depending on the problem, the following conditions can be set. First, when the model is used to simulate model scale experiments in ice tank, the domain must have solid walls at the border representing the solid walls of ice tank. Second, if towing or drift of iceberg in ice is simulated in full-scale, the domain size must be chosen to be as small as possible but large enough that the ice floes at the borders of it will not be affected by the iceberg motion. Thus, in this case, the size of an ice field can be determined by the trial and error method. Also, the domain can be bordered by solid walls that are fixed or moving with constant velocity or produce certain stress on the ice field.

3. Discussions of the model

3.1. Choice of the restitution coefficient

The material properties of contacting bodies affect the forces acting on the contact. It becomes crucial in relation to the feasibility of towing in icy waters. In the model described above the collision response is determined by a restitution coefficient which is by definition a relation between the normal components of relative velocities before (U_-) and after (U_+) collision. In the present section, we will show that the restitution coefficient has a very low value for the collisions of floating ice floes.

There are several mechanical processes occurring in the colliding bodies and hydrodynamical processes in the surrounding water, both leading to energy dissipation. Large portions of kinetic energy dissipate first into local crushing in the contact zone and second into the kinetic energy of the water due to the added mass effect and viscous effects. The energy loss into elastic waves in the material is in the range of 1% of the initial kinetic energy; therefore, it might be neglected (Wu et al., 2005).

The following example illustrates the energy dissipation in crushing. Full-scale observations were made during the Oden Arctic Technology Research Cruise (OATRC'13) to the Greenland Sea in 2013 (Faridafshin et al., 2014; Scibilia et al., 2014). By using the power of the icebreaker Oden, a relatively large ice ridge was pushed with very low velocity through a broken ice field in order to observe ice behaviour in low-velocity collisions (Fig. 4). The size of the ridge with adjacent level ice was 100 m × 250 m with 2.5 m average total thickness; the pushing velocity was varied and started from 0.2 knots up to 2.5 knots, followed by the destruction of the ridge.

The observations showed full collision damping during the test with minor crushing and ridging for velocities below 1.0 knot. During the
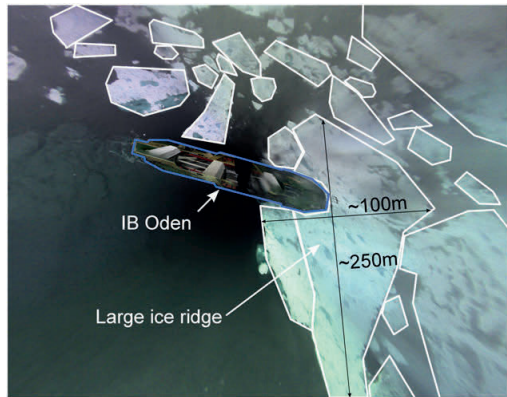
Fig. 4. A massive ice ridge was pushed by IB Oden through a broken ice field. A snapshot produced by a 360 degree camera system (Scibilia et al., 2014) during the pushing test.
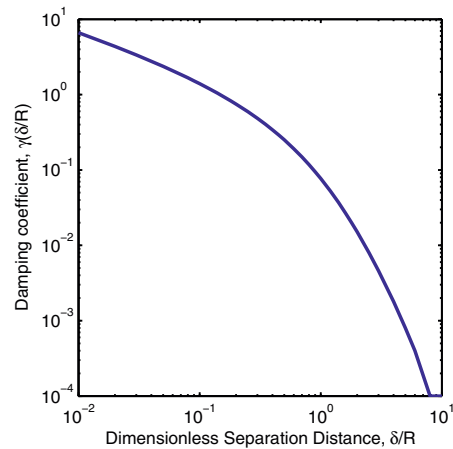

Fig. 5. Damping coefficient as a function of dimensionless separation distance between two floating cylinders as reproduced from Landweber and Shahshahan (1991).

pushing test, the ice floes that were less than 2 m in diameter acted as dampers and as lubricant in-between the larger floes.

Unfortunately, the number of studies estimating the restitution coefficient for floe–floe collisions is limited. Many of these experimental studies were carried out "on air" without taking into account the surrounding water. Experiments on colliding porous freshwater spheres were performed by Shimaki and Arakawa (2012). They found that the restitution coefficient depends negatively on porosity and was no higher than 0.3, being equal to zero in most of the experiments. Drop-ball tests on ice carried out by Likhomanov and Kheisin (1971) resulted in the restitution coefficient being within the range of 0.2–0.25 for velocities of approximately 1 m/s. Nawwar and El-Tahan (1989) developed a model for collisions of floating bodies. They referred to the work of Likhomanov and Kheisin (1971), but the restitution coefficient they used for floe–structure collisions was equal to 0.4. Finally, a large review of isolated impacts with fixed structures was made by Timco (2011). Collision damping was observed; most of the collisions, however, were followed by floe destruction in different failure modes. In the current study, it is assumed that during free drift or towing, the floe size and impact velocities remain insufficient to break ice floes in bending or to initiate splitting.

Prior to the contact, when the bodies move towards each other with a certain velocity, the kinetic energy already dissipates owing to the added mass effect, viscosity of the water, and wave generation. Slush and brash ice provide additional resistance; however, there is a lack of prior research characterizing these influences on floating bodies. Landweber and Shahshahan (1991) used potential flow theory to calculate the influence of added mass for pairs of colliding bodies with radial symmetry. Their study can be applied to the case of similar rounded ice floes advancing one another before an impact.

Assume one of the floes has an initial velocity directed along the line connecting the floes' centres, the second floe remains fixed. In this case, the velocity of the first floe will decrease because of the added-mass effect. The force acting on the incident floe can be calculated as

$$F = \gamma(\delta/R_1)\rho_w R_2 U^2 \qquad (14)$$

where γ is a known function of dimensionless separation distance δ/R_1, R_1, R_2 are the radii of the floes, and U is the velocity of the first floe. The dependency $\gamma(\delta/R_1)$ is shown in Fig. 5.

Unfortunately, the solution is applicable only for distances greater than one-tenth of the interacting bodies' radii; however, it can be shown that two cylinders of equal radius approaching each other will lose a considerable part of their velocity before their separation

becomes one-tenth of their radii. Assuming that only the mentioned force is acting on the similar floes, it can be written:

$$M\frac{dU}{dt} = \gamma(\delta/R_1)\rho_w R_2 U^2 \qquad (15)$$

or, in terms of separation distance

$$\frac{d^2\delta}{dt^2} = \frac{\gamma(\delta/R_1)\rho_w R}{M}\left(\frac{d\delta}{dt}\right)^2 \qquad (16)$$

The amount of dissipated velocity can be found after numerical integration of Eq. (16). For example, two cylinders initially separated by a distance $10R$ will lose 11% of their relative velocity. At closer distances, the viscosity of the water and radiated wave effects are expected to produce even larger damping.

Near-field hydrodynamic damping can be considered as a part of collision process together with dissipation in local crushing, resulting in a lower restitution coefficient value. Thus, in the simulations, it is chosen to be not higher than 0.1 based on the discussed observations and studies.

3.2. Collision duration and the contact force calculation

The described equations of contact dynamics are solved in terms of contact impulses resulting in non-smooth velocity and impulse history. The solution is presented by step function-like impulse history but unknown force history. However, we may confine our interest to contact force values that are derivatives of the impulse.

As prescribed by the model, there are two different contact types: when the interaction happens with large relative velocity and results in large velocity changes during short time, and when two bodies remain in contact while moving with similar velocities. The first case corresponds to a *collision* and the second case corresponds to a *resting contact*.

In contact dynamics, the collision between rigid bodies happens within one numerical time step. Since the collision duration is typically different from the time step used in the simulation, one cannot convert the collision impulse into collision force using the same method as for resting contact, i.e. divide the impulse by the numerical time step. Instead, one must calculate the collision duration first and then use this to calculate the force.

Assuming the contact force value is equal to zero anytime except for the collision duration, the mean value of the force F_{mean} can be calculated as

$$F_{mean} = \frac{\int_{t_0}^{t_0+T_{col}} F_{cont}(t)dt}{T_{col}} = \frac{\Delta P_{cont}}{T_{col}} \qquad (17)$$

where $F_{cont}(t)$ is the actual contact force, T_{col} is the collision duration and ΔP_{cont} is the impulse change during T_{col}, vector notation is taken down because the contact impulse is collinear to the contact force. Thus, in order to estimate collision force correctly, the collision duration must be estimated first.

It is possible to show that the collision duration is roughly proportional to the square root of the reduced mass of the colliding bodies. Let us consider a central collision of two floes of different mass and apply the linear contact force model complemented with a viscous term. Two bodies in contact experience a separating force that acts along the contact normal. In the very beginning of the contact the bodies demonstrate elastic behaviour, transitioning to crushing afterwards. The elastic period of the impact is often very short and it can be neglected. The linear term becomes responsible for the crushing failure (Matskevitch, 1997).

The viscous component can be added resulting in the following expression for the normal force

$$F_n = K\vartheta + Q\dot{\vartheta} \qquad (18)$$

where ϑ is the displacement of the contact surface or the indentation depth, $\dot{\vartheta}$ is the indentation velocity, K is the contact stiffness, and Q is a viscous constant.

Excluding any other force except the contact force from consideration results in

$$M_i \frac{dU_i}{dt} = K\vartheta_i + Q\dot{\vartheta}_i \qquad (19)$$

where index $i = \{1,2\}$ denotes the corresponding floe. In addition, $U_2 - U_1 = \dot{\vartheta}$ and $\vartheta_1 = -\vartheta_2 = \vartheta$, leading to the equation

$$\ddot{\vartheta} + \frac{Q}{M^*}\dot{\vartheta} + \frac{K}{M^*}\vartheta = 0$$
$$\frac{1}{M^*} = \frac{1}{M_1} + \frac{1}{M_2} \qquad (20)$$

where $\ddot{\vartheta}$ is the indentation acceleration, M_1, M_2 are masses of colliding bodies, and M^* is the so-called reduced mass. The collision duration is determined as the time interval between the beginning of the contact and the moment when the force reaches the highest value, or simply as quarter-period of oscillation described by Eq. (20)

$$T_{col} = \frac{\pi}{2\omega} = \sqrt{\frac{M^*}{K}} \frac{\pi}{2\sqrt{1 - \frac{Q^2}{4KM^*}}} \qquad (21)$$

where ω is the angular frequency of the oscillations. For the contact stiffness and viscous term values taken from Hopkins (1992) or Løset (1994b), the square root in the second multiplier is close to unity

$$\sqrt{1 - \frac{Q^2}{4KM^*}} \approx 1 \qquad (22)$$

Therefore, the collision duration becomes roughly proportional to the square root of the reduced mass. Using the contact stiffness of 10^6–10^7 Pa the collision duration can be estimated as

$$T_{col} \approx 10^{-3}\sqrt{M^*} \qquad (23)$$

In the case of eccentric collisions, the collision duration and collision force are reduced by the factor that positively depends on the impact eccentricity (Matskevitch, 1997).

The collision duration calculated for different masses is in good agreement with the time-to-fail defined similarly in Timco (2011). Eq. (23) gives an estimate that is valid for all the scales from laboratory experiments to full-scale observations. Thus, the mean collision force is estimated from the impulse values as

$$F_{mean} = \frac{\Delta P_{cont}}{T_{col}} \approx \frac{10^3 \Delta P_{cont}}{\sqrt{M^*}} \qquad (24)$$

For *resting contact*, the contact force values have moderate changes during one time step and such contact can last for many time steps. In this case, the contact force can be calculated from the change of impulse during a time step Δt

$$F_{mean} = \frac{\Delta P_{cont}}{\Delta t} \qquad (25)$$

3.3. Generation of the initial conditions

Before running the simulation of a large ice field containing many floes, the field itself must be generated. The ice field should fulfill the following given characteristics in order to resemble nature: ice concentration, floe size distribution, ice thickness, and no overlap between floes. A certain quantity that will characterize the size of an ice floe must be chosen prior to the discussion of the size distribution. We define the mean calliper diameter (MCD) of a floe as the average between calliper dimensions taken over all orientations around the floe.

The distribution of the MCD of naturally broken ice floes was found from the analysis of aerial images of broken ice fields (Table 1). The floes were identified from digital images using various recognition techniques: for example, erosion expansion (Banfield and Raftery, 1992). Then, MCD was measured for every floe's pixelated image knowing the spatial resolution. It was shown that the number of floes per unit area $N(\overline{D})$ having MCD larger than $\overline{D}$ can be approximated by a power law with a negative exponent

$$N(\overline{D}) = \alpha\overline{D}^{-\beta}, \beta > 0 \qquad (26)$$

where α and β are parameters. The values of β that were estimated from the image analysis are presented in Table 1.

Eq. (26) can be truncated at small values of MCD because of unachievable floe recognition on very small scales, and at large values of MCD because of the limited area possible to capture by photography. Thus, in accordance with Lu et al. (2008), the following cumulative distribution function $F_{\overline{D}}$ is suggested

$$F_{\overline{D}} = \alpha\left(\overline{D}^{-\beta} - \overline{D}_{\min}^{-\beta}\right) \qquad (27)$$

where $\overline{D}_{\min}$ is the lower truncated value of MCD. α can be expressed using the upper limit on MCD as

$$\alpha = \frac{1}{\overline{D}_{\max}^{-\beta} - \overline{D}_{\min}^{-\beta}} \qquad (28)$$

Table 1
Measured size distributions.

Author(s)	Period	Location	Technique	Minimum size threshold, m	β
Rothrock and Thorndike (1984)	1973–1975	Beaufort Sea	Airborne camera, Landsat image	1000	1.7–2.5
Hudson (1987)	April 1982	Beaufort Sea	Airborne camera	300	0.7–4.3
Holt and Martin (2001)	Aug 1992	Chukchi, East-Siberian, Beaufort Seas	SAR images	900	1.9–2.9
Paget et al. (2001)	Aug 1995	Antarctic	Airborne camera	1.5	1.9–3.5
Toyota and Enomoto (2002)	Feb 1997	Sea of Okhotsk	Airborne camera	30	2.1–2.5
Inoue et al. (2004)	Feb 2000	Sea of Okhotsk	Airborne camera	7	1.5–2.1
Toyota et al. (2006)	Feb 2003	Sea of Okhotsk	Landsat image, shipborne, airborne cameras	1	1.15–1.87
Lu et al. (2008)	Dec 2004–Feb 2005	Antarctic, Prydz Bay	Airborne camera	2–3	1.0–1.8
Steer et al. (2008)	Dec 2004	Wedell Sea	Airborne camera	1.2	1.91–3.36
Toyota et al. (2011)	Autumn 2006, 2007	Wedell Sea, Wilkes Land	Airborne camera, EM	2	1.0–3.0

where $\overline{D}_{\max}$ is the MCD of the largest floe. The probability density function of the MCD of a floe $f_{\overline{D}}$ can now be expressed as

$$f_{\overline{D}} = -\beta \frac{\overline{D}^{-\beta-1}}{\overline{D}_{\max}^{-\beta} - \overline{D}_{\min}^{-\beta}}, \qquad \overline{D} \in [\overline{D}_{\min}, \overline{D}_{\max}] \qquad (29)$$

The value of the exponent β depends on distance from the ice edge, mechanisms of ice breaking, and melting processes. Thus, smaller floes are harder to break and melting starts to play an important role resulting in the larger value of the exponent β.

Now the shapes of the floes can be chosen, and the floes have to be distributed across the domain without overlap. Following this, the generation algorithm basically consists of four steps:

1. Generation of random polygons
2. Scaling of the shapes in order to meet the size distribution requirements
3. Random distribution across the domain
4. Overlap elimination.

Polygonal floes are to be generated randomly; this means that the vertices of every polygon are distributed randomly in a square [0, a] × [0, a] where a is a scaling factor. A convex hull is created from the set of the vertices. In general, the shape can be characterized by roundness, length to width ratio, or perimeter to the square root of area, etc. Also, ice floes are not always convex-shaped as assumed in the algorithm. However, the mentioned characteristics are not considered in the present approach because of the lack of information on how these parameters affect the ice loads.

The floe size distribution given in Eq. (29) can be provided by controlling the polygon scaling factor a. In general, the MCD of a convex polygon depends on its perimeter p as

$$\overline{D} = \frac{p}{\pi} = a\overline{D}_1 \qquad (30)$$

where $\overline{D}_1$ is the MCD of a random polygon created in a unit square. The probability density function of a random polygon's MCD $f_{\overline{D}_1}$ can be found numerically after creating a large number of random polygons.

Assuming that the measured MCD and the MCD of a polygon before scaling are independent random quantities, one can derive the sought-after probability density function of the scaling parameter a (Fig. 6).

For a distribution function of a quotient $C = \frac{A}{B}$, the following equation is applied

$$f_C = \int_{-\infty}^{\infty} f_A(CB)f_B(B)|B|dB \qquad (31)$$

Assuming $A = \overline{D}, B = \overline{D}_1, C = A/B = a$, it can be shown that

$$f_a = -\frac{\beta a^{-\beta-1}}{\overline{D}_{\max}^{-\beta} - \overline{D}_{\min}^{-\beta}} \int_0^{\infty} f_{\overline{D}_1} \overline{D}_1^{-\beta} d\overline{D}_1 = -\frac{\beta a^{-\beta-1}}{\overline{D}_{\max}^{-\beta} - \overline{D}_{\min}^{-\beta}} \mathbf{I} \qquad (32)$$

where $\mathbf{I}$ is the value of the integral; it is constant for a given β and maximum number of polygon vertices.

At the same time, a should be made a function of a uniformly distributed variable x for simplicity: the standard random generator of MATLAB or C++ produces only a uniformly distributed variable. Thus, after the conversion one can obtain

$$a = \frac{\overline{D}_{\min}}{\mathbf{I}^{-1/\beta}} \left[1 + \left(\frac{\overline{D}_{\min}^{-\beta}}{\overline{D}_{\min}^{-\beta}} - 1 \right) x \right]^{-1/\beta} \qquad (33)$$

where x is distributed uniformly on [0, 1].

In addition to the floe size distribution, a given ice concentration is required. It can be reached either by choosing domain size or number of ice floes in the given domain. In the first case, the domain size $l \times w$ is chosen to be $l \times w = \frac{A_{ice}}{c}$, where A_{ice} is the total area occupied by the ice or the sum of the areas of the ice floes. In the second case for the
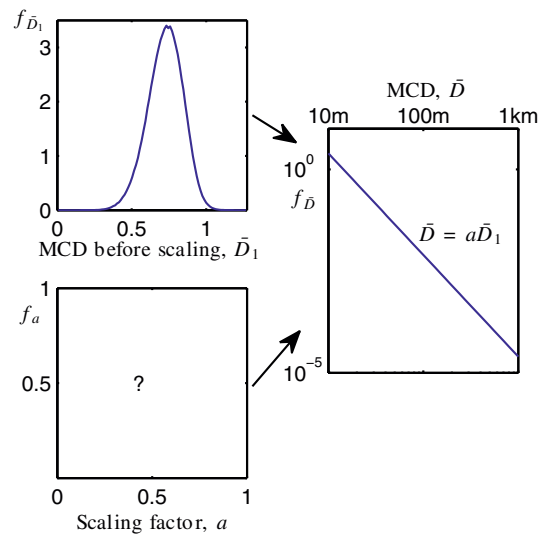

Fig. 6. The main principle of size control for the floe size distribution. The unknown distribution of the scaling parameter can be found from the distribution of ice floe's MCD and the distribution of the random polygon's MCD.

given domain size, the floes are continuously generated until they begin to occupy a given portion of the area. The domain size must be larger than the largest floe size $\overline{D}_{max}$ to fit enough floes to reproduce the distribution given by Eqs. (27) and (28).

After that, the rigid walls are "set" around the domain and the engine is run for some time until all the polygons stop to overlap. The results of the algorithm execution are presented in Fig. 7. First, a squared domain with a 100 m side and 20% concentrated ice was generated. The ice floe size ranged from 20 cm to 20 m and $\beta = 2.5$; 4250 ice floes were created in total. An example of a similar-looking ice field is shown in Fig. 7 (a1), in which a photograph was taken during the OATRC'13 expedition in the Greenland Sea. The second case is a domain with a 1000 m side, but a higher concentration of 80% ice (Fig. 7, b2). There are 1590 ice floes that are 25 to 50 m wide, creating a pattern very similar to the pattern found around Franz Josef Land as shown in Fig. 7 (a2). The numerical broken ice looks similar to the broken ice found in nature but, of course, nature brings much more variability. A number of additional characteristics of ice floes' shapes besides MCD need to be reproduced. In addition, the distributions of MCD before and after icebreaking operations are of interest for comparison and simulation using the generator.

The algorithm takes from a few seconds up to a couple of hours of execution time on an Intel® Core™ i5-2467M, 4 GB RAM. The execution time grows together with the concentration or number of floes because more contacts need to be resolved by the engine. The upper limit of the concentration appears to be approximately 0.85. For higher concentrations, the interaction goes off-plane into the third dimension. A similar limit was found in a disc-based DEM, equal to 0.79 (Hopkins and Tuhkuri, 1999). However, iceberg towing operations are likely to be performed in low concentrated ice. This requirement greatly simplifies and accelerates the generation of initial broken ice fields.

The generated floe size distribution was compared with the given distribution. A large number of polygons (10^6) were produced for the given $\beta = 2.5$, $\overline{D}_{min} = 10$ m, and $\overline{D}_{max} = 1000$ m. Then, the cumulative distribution function of the MCD was calculated. In Fig. 8, it is plotted together with the truncated distribution (27, 28). It is clear that the size distribution of the MCD of a numerical ice floe follows the given size distribution with high accuracy.

4. Numerical examples

4.1. Analysis of simulation of isolated floe impacts

A simple quality control test was performed to check the accuracy of our collision force calculations, mainly to verify our estimate of the restitution coefficient and the collision duration for single contacts. A number of random-sized and random-shaped polygonal ice floes were
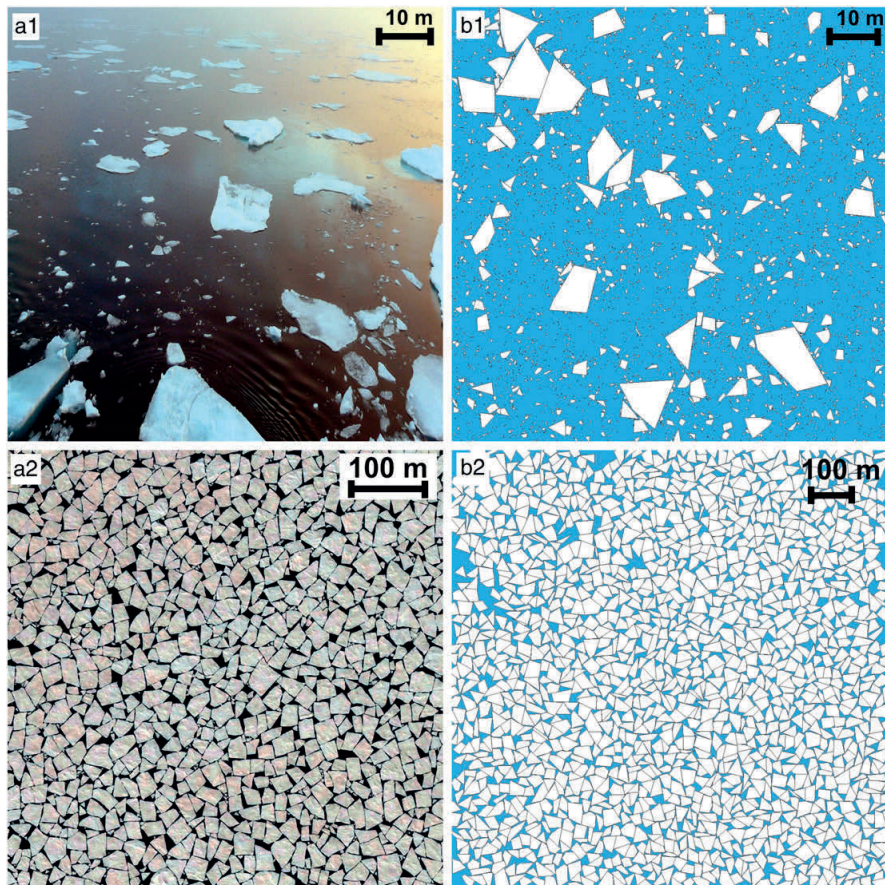

Fig. 7. Broken ice fields created numerically and broken ice found in nature. (a1) North-East Greenland, approximately 20% concentration. (a2) Franz Josef Land, approximately 80% concentration. (b1, b2) Similar domains with numerically produced broken ice. The approximate scale is given in each inset.
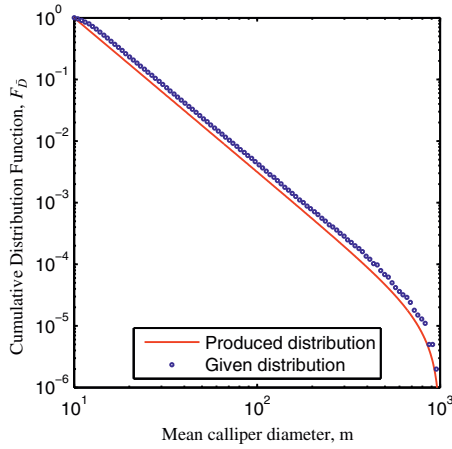
Fig. 8. In nature, the distribution of ice floes' MCD can be described by a truncated power law (solid line). MCD of the generated ice floes follows the natural distribution with high accuracy (blue circles). In the current example, the power $\beta = 2.5$.

produced using the generator as discussed earlier in the paper. The floes were made to collide with a flat stationary wall one by one. The limited momentum scenario was reproduced as the collision force was determined only by the initial momentum of the floe. No failure in the ice floes was considered following the assumptions of the numerical model. The kinetic energy before impact was varied by changing the mass and velocity of the floes. The collision force was calculated afterwards using the estimate given by Eq. (23) and then plotted against the initial kinetic energy for 1000 simulated collisions (Fig. 9).

The numerical results were compared with full-scale and small-scale studies summarized by Timco (2011). The sources of the data include impacts at Hans Island, Molikpaq, Grappling Island, Newmans Cove, Hondo bridge pier, Pembina bridge pier, Rideau bridge pier, and at the NRC-CHC laboratory. Timco (2011) also considered a limited momentum scenario for the impacts; the floes were driven only by wind, current, and Coriolis forces. In some of the impacts, ice floes failed in different modes such as splitting, bending, or crushing, but some of the floes were not damaged severely. For all of the impacts, the collision
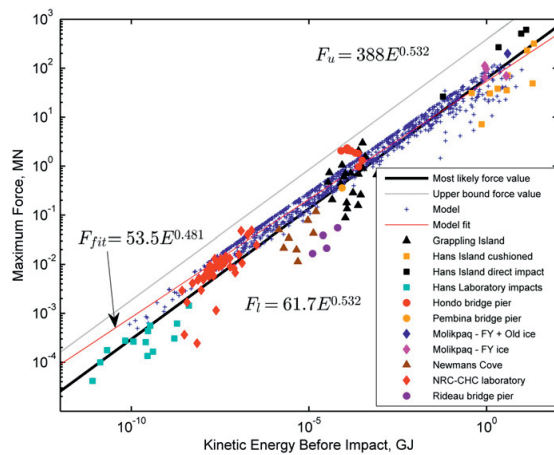

Fig. 9. Peak force during collision vs. initial kinetic energy of the floe plotted for 1000 simulated impacts together with the experimental data from Timco (2011).

forces were determined and plotted against the measured kinetic energy before the impact.

It was found from the experiments that the magnitude of the most likely impact force F_l expressed in MN depends on the kinetic energy of an ice floe E expressed in GJ as

$$F_l = 61.7E^{0.532} \tag{34}$$

The upper bound of the force value F_u is given by

$$F_u = 388E^{0.532} \tag{35}$$

At the same time, the numerical results were also fitted with the power law function resulting in a similar relation

$$F_{fit} = 53.4E^{0.481} \tag{36}$$

In Fig. 9, the numerical results demonstrate a good agreement with the experimental data on all scales. The underestimate of the value of the power law exponent is caused by the following reasons. Firstly, the value of the power in Eq. (36) is lower than 0.532 because the collision duration given in Eq. (23) is slightly overestimated for large masses. For large floes, the second multiplier in Eq. (21) should become lower, decreasing the estimated collision duration, and therefore, resulting in a higher value for the collision force.

Secondly, the underestimate and scatter in the numerical data is caused by the energy transfer from the translational motion of ice floe into rotation. Initially, the ice floe moves with no angular velocity. When it collides with the rigid wall, torque may occur, and the floe starts to rotate. The impulse and, therefore, the force that appear at the contact are less than those needed to fully stop the body as shown by Matskevitch (1997).

It can be shown that for central collisions of an ice floe with an immovable or heavy object, the collision force will be proportional to the square root of kinetic energy. A rough estimate of the collision force can be given by

$$F_{mean} = \frac{\Delta P_{cont}}{T_{col}} = \frac{M(1+e)U_-}{T_{col}} = \frac{(1+e)\sqrt{2ME}}{T_{col}} \tag{37}$$

Considering the estimate of the collision duration to be proportional to the square root of the reduced mass as given by Eq. (20), we derive a force that is proportional to the square root of the kinetic energy

$$F_{peak} \approx 1.4 \cdot 10^3 (1+e)\sqrt{E} \tag{38}$$

This result is also comparable to the power of 0.532 in Eqs. (34) and (35). Assuming that the kinetic energy is dissipated completely, the estimate (38) gives the upper limit of normal force component in a single contact. Thus, Eq. (24) gives a correct and scale-independent estimate of the collision force for the model.

4.2. Towing an iceberg in broken ice

After testing the model for isolated floe impacts, a case study of a possible full-scale iceberg towing is carried out. The main purpose of the test is to show that the actual model is capable of producing reasonable results in the case of many ice floes interacting with the iceberg and with each other. Since there are no full-scale data available for iceberg towing in ice, it was only possible to compare the mean towing force with results of a towing experiment performed by Eik and Marchenko (2010). A single case of constant velocity and concentration is presented herein. A detailed validation study is still ongoing and the results will be published in the near future.

The numerical model is setup to replicate the experiment of Eik and Marchenko (2010) as follows:

- A domain 400 m by 2880 m
- Ice concentration is 50%
- Ice thickness is 1.16 m
- MCD is ranging from 20 m to 70 m
- A cylindrical iceberg having approximately 26 m of total height and 76 m in diameter
- The iceberg moves through the domain with the constant speed of 0.7 m/s
- The walls of the domain were modelled as static objects with zero restitution that keep ice floes inside of the domain

All the presented numbers are scaled using a factor of 40 (Froude scaling). The top view of the domain is shown in Fig. 10.

The iceberg is moved with a constant speed of 0.7 m/s along the domain. We assume no surface current and no wind as in the experiment. However, Eq. (4) and water drag force are still applied to ice floes in the vicinity of the iceberg. A constant drag force acts also on the iceberg because it moves relative to the still water with a constant speed.

The ice resistance force in the numerical model is calculated as a sum of contact forces appearing where ice floes contact the iceberg. The obtained force is averaged and summed up with the water drag force to calculate the towing force. The evolution of the ice resistance force obtained from the model is shown in Fig. 11. The mean value of the ice resistance (red line in Fig. 11) is $F_{si} = 135$ kN.

The drag force acting on the iceberg is estimated according to Eq. (4) assuming a uniform current profile

$$F_w = \frac{1}{2} C_w \rho_w A_{keel} \left(\vec{V}_w - \vec{u} \right)^2 = \frac{1}{2} 0.35 \cdot 10^3 \cdot 1970 \cdot 0.5 = 153 \, \text{kN} \quad (39)$$

where the vertical crossection area A_{keel} is calculated using iceberg dimensions, the drag coefficient $C_w = 0.35$ is determined using open water test from the same experiment, the water velocity $\vec{V}_w$ has zero components. Thus, the towing force is found as

$$F_{tow} = F_w + F_{si} = 288 \, \text{kN} \quad (40)$$

In the experiment of Eik and Marchenko (2010), the average towing force in 50% ice concentration and for the towing velocity of 0.7 m/s was found to be 487 kN. The above indicates that the average force value obtained from the ice-tank experiment is twice higher than the value obtained from the numerical simulation. Different factors may have contributed to this discrepancy. First, the initial ice floes' positions and geometries are not exactly reproduced in the numerical test. This factor is hard to verify because it's impossible to exactly replicate the initial configuration of ice. Second, as reported by the authors of the experiment, there were events when the towing line was pushed sideways by the ice floes. Such events led to the increase in rope tension. Third, there were strong hydrodynamic effects which were not captured by the approximations of the drag forces in the model.

Despite the mismatch with the experimental results, the towing force values calculated by the model are of the same order of magnitude. It is an argument towards the validity of the numerical model, but a proper validation study should be carried out.
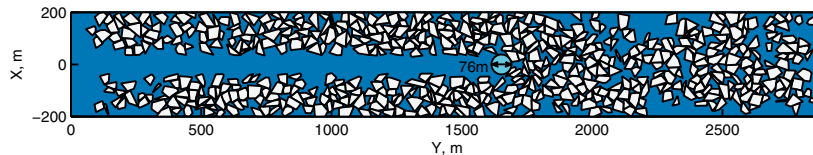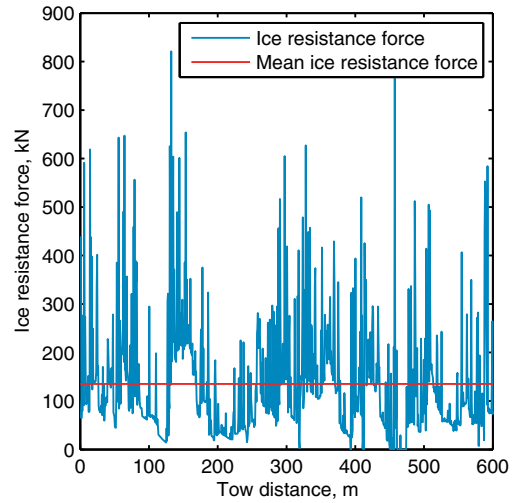

Fig. 11. The evolution of the ice resistance force calculated by the model (blue) and the mean value of the force (red).

As an example, the level of the towing force is below the bollard pull of IB Oden (Swedish Maritime Administration, 2015). Also, the towing force is below a maximum breaking force of contemporary towing lines (Phyllistran, 2015) which is 1.7 MN for a 48 mm thick line. It is possible to conclude that the towing of a medium iceberg (0.1 million tons in the presented case) in 50% concentrated 1-m-thick managed ice is feasible. In addition, the level of the ice resistance is of the same level as the water drag force. This means that the level of approximately 50% concentration for 1-m-thick ice doubles the towing force in comparison to open water towing with the given towing speed.

We have shown how the model can be applied to estimate possible towing force in icy waters. It is a simplified case, but it demonstrates the capabilities of the model. The model produces results that are comparable with the scaled experimental values. The presented case study also shows the possibility of towing a medium iceberg in 50% concentrated broken ice in full-scale.

5. Conclusions

A numerical model for the simulation of an iceberg's slow motion through broken ice is presented. The model is 2D and it neglects any large failure of ice floes, e.g. bending and splitting. Therefore, the validity of the model is expected to be limited to situations where the ice concentration is low and where the relative velocity between the ice floes and icebergs is low.

The main findings are as follows:

- In the framework of contact dynamics, each contact is treated either as *resting contact* or as *collision*. For the latter to be resolved accurately, a good estimation of restitution coefficient is required. In this paper, it

Fig. 10. The iceberg moves through the domain with a constant speed of 0.7 m/s. The ice concentration is 50%.

was shown that the restitution coefficient used to model collisions between floating ice floes should have a low value, namely, $e \in [0, 0.1]$.

- In the contact dynamics, impulses are calculated to resolve the contacts. For the *resting contacts*, the contact force is simply estimated as impulse change over a time step. In the case of *collisions*, the calculation of forces is a bit more complicated because we must first estimate the collision duration. A method for estimating collision force using the collision duration is proposed in this paper. The collision duration is shown to be roughly proportional to the square root of the reduced mass of colliding bodies.

- A simple test was presented and used to test the estimates of the collision forces. The test results showed a good agreement with full-scale and lab-scale experiments. Based on the chosen collision duration and the restitution coefficient, the relation between the kinetic energy before impact and peak impact force was fitted by a power law. The value of the exponent obtained numerically from the fit was 0.48 when the experimental value was 0.53.

- Numerical simulation of an iceberg towing with constant velocity of 0.7 m/s in 50% concentrated ice of 1.16 m thickness was performed. The average towing force in the model was found to be 288 kN. This value is comparable with the 487 kN obtained in the experiment. Such a level of the average towing force allows to conclude that towing of a medium iceberg is feasible in the given ice conditions.

- A numerical ice field generator producing specified ice conditions was developed. The created ice field is represented by a domain filled with randomly shaped polygons distributed according to a field-measured power law distribution. The generated ice field has a given concentration, and the thickness of every floe can be set. To the best of our knowledge, this is the first algorithm that simultaneously fulfils the requirements of size distribution and concentration for the polygon-based, discrete element method.

The possible applications of the model are drift forecasting and towing simulation for physical ice management operations in ice-covered waters. Future developments of the model may apply more sophisticated studies of contact response, hydrodynamics, or inclusion of failure mechanisms in the ice features.

Acknowledgements

References

Abramov, V.A., 1992. Russian iceberg observations in the Barents Sea, 1933–1990. Polar Res. 11 (2), 93–97. http://dx.doi.org/10.1111/j.1751-8369.1992.tb00415.x.

Banfield, J.D., Raftery, A.E., 1992. Ice floe identification in satellite images using mathematical morphology and clustering about principal curves. J. Am. Stat. Assoc. 87 (417), 7–16. http://dx.doi.org/10.1080/01621459.1992.10475169.

Barker, A., Sayed, M., Carrieres, T., 2004. Determination of iceberg draft, mass and cross-sectional areas. Proceedings of the 14th International Offshore and Polar Engineering Conference, Toulon, France.

Bass, D.W., Sen, D., 1986. Added mass and damping coefficient for certain realistic iceberg models. Cold Reg. Sci. Technol. 12 (2), 163–174. http://dx.doi.org/10.1016/0165-232x(86)90031-5.

Baumgarte, J., 1972. Stabilization of constraints and integrals of motion in dynamical systems. Comput. Methods Appl. Mech. Eng. 1 (1), 1–16.

Bigg, G.R., Wadley, M.R., Stevens, D.P., Johnson, J.A., 1997. Modelling the dynamics and thermodynamics of icebergs. Cold Reg. Sci. Technol. 26 (2), 113–135. http://dx.doi.org/10.1016/s0165-232x(97)00012-8.

Blunt, J.D., Mitchell, D.A., Matskevitch, D.G., Kokkinis, T., Younan, A.H., Hamilton, J.M., 2013. A tactical hindcast calibration method for sea ice drift forecasting in the Canadian Beaufort Sea. Proceedings of the 23rd International Offshore and Polar Engineering Conference, Anchorage, Alaska, USA.

Catto, E., 2005. Iterative dynamics with temporal coherence. Game Developer Conference, San Francisco, CA, USA.

Catto, E., 2013. Box2D v2.3.0 User Manual. http://box2d.org/manual.pdf (last access: 25.06.2014).

Coche, E., Liferov, P., Metge, M., 2011. Ice and iceberg management plans for Shtokman Field. OTC Arctic Technology Conference, Houston, Texas, USA.

Eik, K., 2008. Review of experiences within ice and iceberg management. J. Navig. 61 (4), 557–572. http://dx.doi.org/10.1017/S0373463308004839.

Eik, K., 2009. Iceberg drift modelling and validation of applied metocean hindcast data. Cold Reg. Sci. Technol. 57 (2-3), 67–90. http://dx.doi.org/10.1016/j.coldregions.2009.02.009.

Eik, K., Marchenko, A., 2010. Model tests of iceberg towing. Cold Reg. Sci. Technol. 61 (1), 13–28. http://dx.doi.org/10.1016/j.coldregions.2009.12.002.

Faridafshin, F., Francesco, S., Lubbad, R., Løset, S., 2014. Sea ice management trials during Oden Arctic Technology Research Cruise 2013 offshore North East Greenland. Proceedings of the 22nd IAHR International Symposium on Ice.

Frankenstein, S., Løset, S., Shen, H.H., 2001. Wave-ice interactions in Barents Sea marginal ice zone. J. Cold Reg. Eng. 15 (2), 91–102.

Gilbert, E.G., Johnson, D.W., Keerthi, S.S., 1988. A fast procedure for computing the distance between complex objects in 3-dimensional space. IEEE J. Robot. Autom. 4 (2), 193–203. http://dx.doi.org/10.1109/56.2083.

Hamilton, J., Holub, C., Blunt, J., Mitchell, D., Kokkinis, T., 2011. Ice management for support of arctic floating operations. OTC Arctic Technology Conference, Houston, Texas, USA.

Hibler, W.D., 1979. Dynamic thermodynamic sea ice model. J. Phys. Oceanogr. 9 (4), 815–846. http://dx.doi.org/10.1175/1520-0485(1979)009<0815:Adtsim>2.0.Co;2.

Hobson, B.W., Sherman, A.D., McGill, P.R., 2011. Imaging and sampling beneath free-drifting icebergs with a remotely operated vehicle. Deep-Sea Res. II Top. Stud. Oceanogr. 58 (11-12), 1311–1317. http://dx.doi.org/10.1016/j.dsr2.2010.11.006.

Holt, B., Martin, S., 2001. The effect of a storm on the 1992 summer sea ice cover of the Beaufort, Chukchi, and East Siberian Seas. J. Geophys. Res. Oceans 106 (C1), 1017–1032. http://dx.doi.org/10.1029/1999jc000110.

Hopkins, M.A., 1992. Numerical simulation of systems of multitudinous polygonal blocks. CRREL Report 99-22, U.S. Army Corps of Engineers, Cold Regions Research and Engineering Laboratory, Hanover, NH.

Hopkins, M.A., Tuhkuri, J., 1999. Compression of floating ice fields. J. Geophys. Res. Oceans 104 (C7), 15815–15825. http://dx.doi.org/10.1029/1999jc900127.

Hudson, R.D., 1987. Multiyear sea ice-floe distribution in the Canadian Arctic Ocean. J. Geophys. Res. Oceans 92 (C13), 14663–14669. http://dx.doi.org/10.1029/Jc092ic13p14663.

Hunke, E.C., Comeau, D., 2011. Sea ice and iceberg dynamic interaction. J. Geophys. Res. Oceans 116. http://dx.doi.org/10.1029/2010jc006588.

Inoue, J., Wakatsuchi, M., Fujiyoshi, Y., 2004. Ice floe distribution in the Sea of Okhotsk in the period when sea-ice extent is advancing. Geophys. Res. Lett. 31 (20). http://dx.doi.org/10.1029/2004gl020809.

Keghouche, I., Bertino, L., Lisaeter, K.A., 2009. Parameterization of an iceberg drift model in the Barents Sea. J. Atmos. Ocean. Technol. 26 (10), 2216–2227. http://dx.doi.org/10.1175/2009jtecho678.1.

Konno, A., Nakane, A., Kanamori, S., 2013. Validation of Numerical Estimation of Brash Ice Channel Resistance with Model Test, The 22nd International Conference on Port and Ocean Engineering under Arctic Conditions, June 9–13, 2013. Espoo, Finland.

Kubat, I., Sayed, M., Savage, S.B., Carrieres, T., 2005. An operational model of iceberg drift. Int. J. Offshore Polar Eng. 15 (2), 125–131.

Landweber, L., Shahshahan, A., 1991. Added masses and forces on two bodies approaching central impact in an inviscid fluid. IIHR Report No. 346. Iowa Institute of Hydraulic Research, Iowa City.

Lichey, C., Hellmer, H.H., 2001. Modeling giant-iceberg drift under the influence of sea ice in the Weddell Sea, Antarctica. J. Glaciol. 47 (158), 452–460.

Likhomanov, V., Kheisin, D., 1971. Experimental investigation of solid body impact on ice. Problemy Arktiki i Antarktiki 38 pp. 105–111.

Løset, S., 1994a. Discrete element modeling of a broken ice field - Part 1: Model development. Cold Reg. Sci. Technol. 22 (4), 339–347. http://dx.doi.org/10.1016/0165-232x(94)90019-1.

Løset, S., 1994b. Discrete element modeling of a broken ice field - Part 2: Simulation of ice loads on a boom. Cold Reg. Sci. Technol. 22 (4), 349–360. http://dx.doi.org/10.1016/0165-232x(94)90020-5.

Løset, S., Carstens, T., 1996. Sea ice and iceberg observations in the Western Barents Sea in 1987. Cold Reg. Sci. Technol. 24 (4), 323–340. http://dx.doi.org/10.1016/0165-232x(95)00029-B.

Lu, P., Li, Z.J., Zhang, Z.H., Dong, X.L., 2008. Aerial observations of floe size distribution in the marginal ice zone of Summer Prydz Bay. J. Geophys. Res. Oceans 113 (C2). http://dx.doi.org/10.1029/2006jc003965.

Lu, P., Li, Z.J., Cheng, B., Leppäranta, M., 2011. A parameterization of the ice-ocean drag coefficient. J. Geophys. Res. Oceans 116. http://dx.doi.org/10.1029/2010jc006878.

Lu, W., Lubbad, R., Løset, S., 2015. In-plane fracture of an ice floe: a theoretical study on the splitting failure mode. Cold Reg. Sci. Technol. 110 (0), 77–101. http://dx.doi.org/10.1016/j.coldregions.2014.11.007.

Lubbad, R., Løset, S., 2011. A Numerical Model for Real-Time Simulation of Ship-Ice Interaction. Cold Reg. Sci. Technol. 65 (2), 111–127. http://dx.doi.org/10.1016/j.coldregions.2010.09.004.

Marchenko, A., Eik, K., 2012. Iceberg towing in open water: mathematical modeling and analysis of model tests. Cold Reg. Sci. Technol. 73, 12–31. http://dx.doi.org/10.1016/j.coldregions.2011.11.008.

Marchenko, A., Kulyakhtin, A., Eik, K., 2010. Icebergs drift in the Barents Sea: data analysis of ice tracking buoy and numerical simulations. 20 th IAHR International Symposium on Ice, Lahti, Finland (June 14 to 18, 2010).

Matskevitch, D.G., 1997. Eccentric impact of an ice feature: non-linear model. Cold Reg. Sci. Technol. 26 (1), 55–66. http://dx.doi.org/10.1016/S0165-232X(97)00008-6.

McKenna, R.F., 2005. Refinement of iceberg shape characterization for risk to Grand Banks installations. Richard McKenna Report 04-05-01 for Canadian Hydraulics Centre. National Research Counsil, Canada (PERD/CHC Report 20-77).

Metrikin, I., Løset, S., 2013. Nonsmooth 3D Discrete Element Simulation of a Drillship in Discontinuous Ice, The 22nd International Conference on Port and Ocean Engineering under Arctic Conditions. Espoo, Finland, June 9-13.

Morison, J., Goldberg, D., 2012. A brief study of the force balance between a small iceberg, the ocean, sea ice, and atmosphere in the Weddell Sea. Cold Reg. Sci. Technol. 76–77, 69–76. http://dx.doi.org/10.1016/j.coldregions.2011.10.014.

Nawwar, A.M., El-Tahan, H., 1989. A simple model for collision of floating bodies. Proceedings of the 8th International Conference on Offshore Mechanics and Arctic Engineering.

Newman, J.N., 1977. Marine Hydrodynamics. The MIT Press, Cambridge, MA.

Paget, M.J., Worby, A.P., Michael, K.J., 2001. Determining the floe-size distribution of East Antarctic sea ice from digital aerial photographs. Ann. Glaciol. 33, 94–100. http://dx.doi.org/10.3189/172756401781818473.

Pfeiffer, F., Glocker, C., 2008. Multibody Dynamics with Unilateral Contacts. John Wiley & Sons, Inc. (329 pp.).

Phyllistran, 2015. X-Trema Line datasheet. http://phillystran.com/Resource_/PageResource/XTremaLine2015.pdf (last access: 29.07.2015).

Rothrock, D.A., Thorndike, A.S., 1984. Measuring the sea ice-floe size distribution. J. Geophys. Res. Oceans 89 (4), 6477–6486. http://dx.doi.org/10.1029/Jc089ic04p06477.

Rudkin, P., Young, C., Barron Jr., P., Timco, G., 2005. Analysis and results of 30 years of iceberg management. Proceedings of the 18th International Conference on Port and Ocean Engineering under Arctic Conditions, Potsdam, NY, USA.

Scibilia, F., Metrikin, I., Gürtner, A., Teigen, S.H., 2014. Full-scale trials and numerical modeling of sea ice management in the Greenland Sea. OTC Arctic Technology Conference, Houston, Texas, USA.

Shimaki, Y., Arakawa, M., 2012. Low-velocity collisions between centimeter-sized snowballs: porosity dependence of coefficient of restitution for ice aggregates analogues in the solar system. Icarus.

Smith, S.D., 1993. Hindcasting iceberg drift using current profiles and winds. Cold Reg. Sci. Technol. 22 (1), 33–45. http://dx.doi.org/10.1016/0165-232x(93)90044-9.

Smith, S.D., Donaldson, N.R., 1987. Dynamic Modelling of Iceberg Drift Using Current Profiles. Fisheries and Oceans, Canada.

Squire, V.A., 2007. Of ocean waves and sea-ice revisited. Cold Reg. Sci. Technol. 49 (2), 110–133. http://dx.doi.org/10.1016/j.coldregions.2007.04.007.

Steer, A., Worby, A., Heil, P., 2008. Observed changes in sea-ice floe size distribution during early summer in the Western Weddell Sea. Deep-Sea Res. II Top. Stud. Oceanogr. 55 (8-9), 933–942. http://dx.doi.org/10.1016/j.dsr2.2007.12.016.

Sukhorukov, S., 2013. Ice-Ice and Ice-Steel Friction in Field and in Laboratory. NTNU, Trondheim, Norway.

Sukhorukov, S., Løset, S., 2013. Friction of sea ice on sea ice. Cold Reg. Sci. Technol. 94, 1–12.

Swedish Maritime Administration, 2015. IB Oden Technical Data Sheet. http://www.sjofartsverket.se/pages/41381/Oden%20f%C3%B6r%20webben.pdf (last access: 29.07.2015).

Timco, G., 2000. Techniques for determining the maximum draft of an iceberg. PERD/CHC Report 20-46. Canadian Hydraulics Centre, National Research Council of Canada, Ottawa, Ontario.

Timco, G.W., 2011. Isolated ice floe impacts. Cold Reg. Sci. Technol. 68 (1-2), 35–48. http://dx.doi.org/10.1016/j.coldregions.2011.04.008.

Toyota, T., Enomoto, H., 2002. Analysis of sea ice floes in The Sea of Okhotsk using ADEOS/AVNIR images. Proceedings of the 16th IAHR International Symposium on Ice, Dunedin, New Zealand.

Toyota, T., Takatsuji, S., Nakayama, M., 2006. Characteristics of sea ice floe size distribution in the seasonal ice zone. Geophys. Res. Lett. 33 (2). http://dx.doi.org/10.1029/2005gl024556.

Toyota, T., Haas, C., Tamura, T., 2011. Size distribution and shape properties of relatively small sea-ice floes in the Antarctic marginal ice zone in late winter. Deep-Sea Res. II Top. Stud. Oceanogr. 58 (9-10), 1182–1193. http://dx.doi.org/10.1016/j.dsr2.2010.10.034.

Trott, B., Comfort, G., 2007. PERD iceberg sighting database update and quality assurance: 2006-2007. PERD/CHC Report 20-86.

Tuhkuri, J., 2005. Discrete element simulations in ice engineering. Proceedings of the 18th Nordic Seminar On Computational Mechanics, Espoo, Finland.

Wilchinsky, A.V., Feltham, D.L., Hopkins, M.A., 2011. Modelling the reorientation of sea-ice faults as the wind changes direction. Ann. Glaciol. 52 (57), 83–90.

Wu, C.-Y., Li, L.-Y., Thornton, C., 2005. Energy dissipation during normal impact of elastic and elastic–plastic spheres. Int. J. Impact Eng. 32 (1), 593–604.

Yulmetov, R., Marchenko, A., Løset, S., 2012. Characteristics of ice drift and sea currents on the Spitsbergen Bank in the Barents Sea. Proceedings of the 21st IAHR International Symposium on Ice, Dalian, China.

Yulmetov, R., Løset, S., Eik, K.J., 2013a. Analysis of drift of sea ice and icebergs in the Greenland Sea. The proceedings of the 22nd International Conference on Port and Ocean Engineering under Arctic Conditions, Espoo, Finland.

Yulmetov, R., Marchenko, A., Løset, S., 2013b. Ice drift and sea current analysis in the Northwestern Barents Sea. Proceedings of the 22nd International Conference on Port and Ocean Engineering under Arctic Conditions, Espoo, Finland.

Appendix B:

Validation of a numerical model for iceberg towing in broken ice

The paper is an attempt to validate the numerical model presented earlier having actually very limited experimental data. We also compare the numerical results with some known analytical approximations.

Full citation:

Yulmetov, R., and S. Løset. 2017. "Validation of Numerical Model of Iceberg Towing in Broken Ice (under review)". *Cold Regions Science and Technology*

Validation of a numerical model for iceberg towing in broken ice

Renat Yulmetov[a,b], Sveinung Løset[b,a]

[a] The University Centre in Svalbard, P.O.Box 156, 9171 Longyearbyen, Norway

[b] Sustainable Arctic Marine and Coastal Technology (SAMCoT), Centre for Research-based Innovation (CRI), Norwegian University of Science and Technology (NTNU), Trondheim, Norway

Abstract

The possibility of iceberg towing in broken ice is attracting considerable interest because it may help to improve the design of offshore structures to be used in regions where both sea ice and icebergs can appear simultaneously. The contribution of the broken ice resistance to the total towing force still remains uncertain. A model of iceberg towing in broken ice has been proposed and discussed (Yulmetov et al., 2016), and it requires validation. The present paper aims to validate the model and to provide an estimate of the broken ice resistance. The validation is performed using data obtained in a model-scale towing experiment in the Hamburg Ship Model Basin. The evolution of the towing force and mean towing forces calculated in the simulations are compared to the experimental results. A qualitative analysis of the broken ice field after towing is given. The numerical model reproduces the average towing forces measured in the experiment fairly well. In addition, the scaled results of the simulations are compared with the existing analytical approximations of the ice resistance to drifting icebergs and the forces acting on bodies in granular flows. The numerical model can be addressed when planning towing operations in ice; however, further testing against full-scale data would significantly improve its credibility.

1. Introduction

Ice management may be performed in close proximity to an offshore structure to reduce or avoid actions from any kind of ice features (Eik, 2008). Its major components are detection, tracking, forecasting, threat evaluation tools, physical ice management, and emergency disconnection system. Icebreaking and iceberg towing are two possible means of physical ice management that are usually considered separately. The first reduces ice actions on a structure by reducing ice floe size using icebreakers working upstream (Hamilton et al., 2011). The second attempts to reduce the possibility of collision with an iceberg by deflecting it from the structure (McClintock et al., 2007). Towing of icebergs has been successfully performed a number of times in open water, but how feasible is it when sea ice is present?

In conditions where icebergs drift together with sea ice, towing operations become challenging. Sea ice creates additional resistance to an iceberg, and the magnitude of the ice-induced force during towing still remains unknown. It is possible to make a channel in the sea ice and reduce the floe size in order to reduce resistance during towing. However, it is unrealistic to fully exclude the broken ice from the interaction process with the iceberg.

To date, only a few attempts to tow an iceberg in icy conditions have been made. Two cases are reported for the Barents Sea, where icebergs in sea ice are expected at the Shtokman field. In April, 2004, a bergy bit of approximately 15.5 thousand tons was towed in less than 10 cm thick ice of 90% ice concentration (Marchenko and Gudoshnikov, 2005). The following year, a 200 thousand tons iceberg was towed in thicker but more fragmented ice (Marchenko and Ulrich, 2008). The iceberg started to rotate when the towing vessel encountered a large ice floe and lost speed. This caused increased tension followed by the breakage in one of the towing line branches when the towing vessel accelerated again. Icebergs in pack ice at the Grand Banks may be expected approximately one out of six years. (Randell et al., 2009) mentioned a case of towing within sea ice that took place in 2008, however, no detailed

52 description was provided. Also, icebergs in sea ice are often present at the Kanumas area in

53 the Greenland Sea (Hamilton, 2011) that have been considered as a promising offshore field

54 for hydrocarbons.

55 In addition to iceberg towing in ice, there are tasks related to the towing of large structures in

56 ice. As an example, in 1983 Kulluk was towed on the drilling site through approximately 0.5

57 m thick level ice. The transit off site occurred in fragmented, 1–1.5 m thick ice of 20–70% ice

58 concentration (Loh et al., 1984). Also, a semi-submersible accommodation hull was towed in

59 the Bohai Sea in January 2013 (URL1, 2013). The ice was 10–20 cm thick, consisting of large

60 and unmanaged floes. The towing operation ended successfully after two days.

61 As stated above, there is a lack of full-scale data for towing of icebergs or large structures in

62 broken sea ice. The experimental research is limited to the experiments carried out at the

63 Hamburg Ship Model Basin (HSVA) ice basin (Eik and Marchenko, 2010). The tests were

64 performed for various ice concentrations, iceberg shapes and towing scenarios. It has been

65 found that the ice concentration had the strongest effect on the towing force after velocity,

66 acceleration and towing course changes. Towing forces measured in these few tests can be

67 used to validate the numerical model presented by the authors in the previous paper

68 (Yulmetov et al., 2016).

69 In addition to the experiment, there exist two numerical estimates of sea ice resistance to the

70 movement of icebergs. First, the sea ice resistance given by Lichey and Hellmer (2001) can be

71 calculated for large icebergs. In their study, the ice resistance force is assumed to be zero for

72 ice concentrations below 15%; for higher concentrations, the ice is treated as a viscous

73 material; and for concentrations above 90%, the iceberg is captured by ice, but the resistance

74 is limited by the sea ice strength given by Hibler (1979). The approach works well when the

75 ice can be treated as a continuum in relation to an iceberg, but its validity is questionable

76 when the ice floe size is comparable to that of the iceberg. The second estimate has been

77 given by Marchenko et al. (2010) and is based on the assumption that the ice resistance force

78 is associated with the work spent on the creation of a channel of unit length in the broken ice.

79 Our recent model of an iceberg being towed in broken sea ice was proposed and discussed in

80 (Yulmetov et al., 2016). The model is based on the non-smooth discrete element method

81 (DEM) applied to model the broken ice, and its details are presented in Section 2. In this

82 paper, we validate the model using the mentioned experiment described in Section 3. The

83 results of the simulation are presented in Section 4. We then compare the scaled experimental

84 and numerical results with known analytical approximations of the ice resistance, and discuss

85 what a potential full-scale towing of iceberg in ice may entail. With a good match between the

86 simulations and experiment, the model can be proposed for decision support in the design and

87 planning of towing operations of icebergs in broken ice or at least can be used to simulate

88 model-scale towing experiments.

89

90 ## 2. Numerical method

91 ### 2.1. General description

92 Pack ice consists of discrete floes with a size from a few metres to kilometres. When

93 icebreaking is applied, the upper limit of the floe size can be reduced to a few tens of metres.

94 On scales comparable to the floe size, the ice should be treated as a discontinuous material,

95 which means that every ice floe and iceberg should be modelled as a distinct rigid body. The

96 non-smooth DEM has been found capable of simulating ships and floaters in broken ice

97 (Kjerstad et al., 2015; Lubbad and Løset, 2011) and it has been developed to simulate iceberg

98 towing in ice (Yulmetov et al., 2016).

99 This planar model detects contacts between floating ice features and estimates forces at the

100 contacts using discretized momentum equations. In contrast to the traditional DEM

101 integrating the equations of motion on time scales much shorter than characteristic collision

102 duration, the non-smooth DEM makes time steps comparable to the collision duration

103 resulting in abrupt velocity changes between the time steps. As a consequence, the

104 accelerations and the forces are not resolved during the collision period. Instead, the non-

105 smooth DEM calculates impulses that are in fact momenta exchanged between bodies in

106 contact. So, the large time step results in much faster calculations, but at the same time it

107 complicates collision force estimations.

108 The equations of motion are formulated in a frame of reference with a fixed origin. When

109 simulating basin-scale experiments, the origin is located on the water surface, at the middle of

110 the short side of the basin, and the x-, y-axes are directed along and across the basin. For the

111 full-scale simulations, the origin is located at the water surface at the initial iceberg's position,

112 and the axes are directed northward and eastward.

113 When ice features are in contact, the contact force component that acts along the contact

114 normal pushes them apart. Following Yulmetov et al. (2016), the velocities of N_b ice features

115 participating in N_c contacts may be projected on contacts' normals

116 $$\mathbf{w} = \mathbf{J}\mathbf{U} + \mathbf{b} \tag{1}$$

117 where $\mathbf{w}$ is N_c component vector of normal contact velocities, $\mathbf{J}$ is a $3N_b \times N_c$ Jacobian of

118 transformation from Cartesian coordinates into normal separation distances between the

119 bodies participating in contacts, and $\mathbf{b}$ is the so-called bias term with N_c components that is

120 responsible for collision treatment. It is zero for inelastic collisions and for persisting contacts

121 i.e. when one ice feature pushes another.

122 The discretized system of momentum equations for the ice features can be rewritten as

123 $$\mathbf{M}\left(\mathbf{U}_2 - \mathbf{U}_1\right) = \mathbf{J}^T \lambda + \mathbf{F}_{ext}\Delta t \tag{2}$$

124 where $\mathbf{M}$ is the inertia matrix of size $3N_b \times 3N_b$ with masses and moments of inertia at the

125 diagonal, $\mathbf{U}_1$ and $\mathbf{U}_2$ are normal velocity vectors of size $3N_b$ on two consecutive time steps,

126   λ is a vector containing N_c normal projections of the contact impulses that are unknown.

127   The contact impulses are in fact momenta exchanged between bodies in contact and they must

128   never be negative. Δt is the time step, and $\mathbf{F}_{ext}$ is the external forces and torques vector with

129     $3N_b$ components. The external forces are continuous and may be represented by the drag

130   forces, the Coriolis force, the added mass force, the towing force, etc. Substituting (1) in (2)

131   will result in

132 $$\mathbf{w} = \mathbf{A}\lambda + \mathbf{B} \tag{3}$$

133   where $\mathbf{A} = \mathbf{J}\mathbf{M}^{-1}\mathbf{J}^T$ and $\mathbf{B} = \mathbf{J}\mathbf{M}^{-1}\mathbf{F}_{ext}\Delta t + \mathbf{J}\mathbf{U}_1$. When a pair of ice features is in contact the

134   normal contact velocity $\mathbf{w}$ must be zero, so their contact impulse can be determined. Then,

135   the velocities of the bodies are updated according to (2) using the newly found contact

136   impulse.

137   The tangential projection of the contact impulse is found by applying Coulomb's friction law.

138   The friction impulses are applied whenever tangential velocity exists; thus, no distinction is

139   made between static and dynamic friction. The friction coefficient for ice-ice is taken from

140   Sukhorukov and Løset (2013). For ice features that don't participate in any contact the

141   velocities are updated according to (2) with the first term on the right side omitted.

142   The choice of the time step is dictated by the following factors: since the method resolves

143   collisions in one time step, the time step should be on the order of the collision duration; on

144   the other hand, it has to be as short as possible to avoid large overlaps between the bodies

145   during their motion. So, it should be much shorter than a body size divided by the

146   characteristic relative velocity.

147   Let us consider the choice of a time step for simulation of a model-scale experiment and a

148   potential full-scale towing operation. Using data from Timco, (2011) the collision duration (or

149   time between the beginning of the contact and the moment the load reaches its maximum) for

150   the model-scale is on the order of 0.1 s. In the current paper we will attempt to simulate basin-

151 scale iceberg towing among approximately 1 m wide ice floes at 0.13 m/s, so the time step

152 must be much smaller than 8 s. Thus, it is chosen to be as short as the collision duration which

153 is 0.1 s.

154 Similarly, in full-scale the characteristic collision duration for small ice floes is under 5 s

155 (Timco, 2011). Assuming they drift as fast as 0.5 m/s and the target size for icebreaking is 30

156 m, the time step must be much less than 60 s. Therefore, a time step of 5 s is acceptable.

157

158 **2.2. Impulse-force conversion for collisions**

159 When one ice feature pushes another, as, for example, when the iceberg pushes an ice floe,

160 the contact between them persists, and the contact velocities change smoothly. In contrast,

161 when the features collide, their velocities undergo large changes. In this case, the non-smooth

162 DEM is unable to determine accelerations and, therefore, forces. However, we can roughly

163 estimate peak forces based on certain empirical data. We use the relation between the

164 magnitude of the momentum (normal impulse in our case) and peak collision force given by

165 Timco (2011) for isolated ice floe impacts analysed on a wide range of scales

166
$$F_{peak} = 0.641 \cdot P^{0.584} \tag{4}$$

167 were F_{peak} is the peak collision force expressed in MN, and P is the magnitude of the

168 momentum expressed in MN·s.

169 This equation has to be adjusted, because the sea ice used in the experiment was artificially

170 softened to provide correct mechanical properties when scaled. The experiment was

171 performed with a geometrical scale ratio of $\gamma = 40$. Froude scaling was applied to the

172 experimental results, so (4) must be adjusted accordingly. Since the force magnitude is scaled

173 as γ^3 and the momentum magnitude is scaled as $\gamma^{3.5}$, equation (4) for the model scale ice

174 becomes

175
$$F_{peak}^{m} = \gamma^{-3} \cdot 0.641 \cdot 10^{6} \cdot \left(\gamma^{3.5} \cdot P^{m} \cdot 10^{-6} \right)^{0.584} = 5.9 \cdot \left(P^{m} \right)^{0.584} \qquad (5)$$

176   where F_{peak}^{m} is the model-scale collision force magnitude expressed in N, and P^{m} is the

177   model-scale momentum magnitude expressed in N·s.

178   Then, the normal collision impulse should be limited by

179
$$\lambda_{collision} = 5.9 \cdot \lambda^{0.584} \Delta t \qquad (6)$$

180   where λ is the momentum before the collision and Δt is the time step; λ and $\lambda_{collision}$ are

181   expressed in N·s.

182   An example of the collision force estimation for a time step of 0.1 s is shown in Fig. 1. The

183   blue line estimating the force as change of momentum during one time step overestimates the

184   collision force for large contact impulses, i.e. when ice features collide. The collision force

185   estimated according to (5) is shown by the red line. These two lines intersect as certain small

186   contact impulse value. When approaching ice features have larger contact impulse they

187   collide and experience large changes in their velocities. The collision force must be estimated

188   according to (5) because of the reasons explained above. If the contact impulse is small, it is

189   assumed that one ice feature is pushing another and the force can be found as change of

190   momentum over the time step.

191
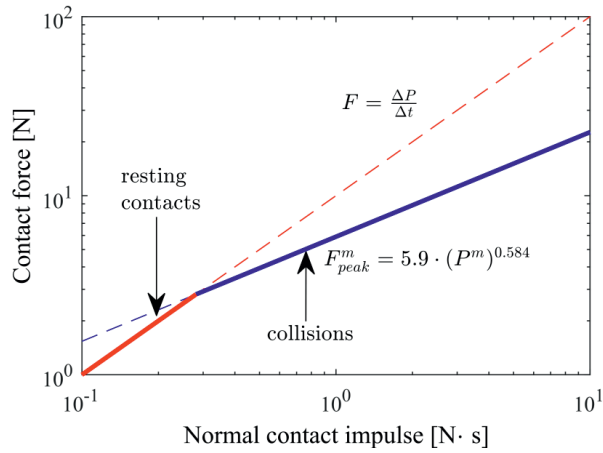
Fig. 1. Impulse-force conversion for a time step of 0.1 s. The collision force is estimated according to Timco (2011) and adjusted for the soft, model-scale ice.

2.3. Crushing constraint

For ice conditions where ice floes cannot flow around an iceberg without being crushed, the contact forces have to be limited from above by the crushing force for ice. It is difficult to tell precisely in what ice conditions the crushing of ice becomes significant. However, an ice concentration of approximately 60% can be considered by analogy to the separation between rapid and dense granular flows.

We improved our previous version of the model by introducing crushing constraints at every persisting contact. From the pressure-area relationship (Sanderson, 1988) it follows that the total contact force acting over the nominal contact area is proportional to the area to the power of 0.3. Since the nominal contact area A_{cont} is proportional to the length of the contact l_{cont} between two intersecting polygons representing contacting ice features, in the full-scale it would be equal to

$$A_{cont} = \gamma^2 h l_{cont} \tag{7}$$

209 where γ is geometrical scale factor and h is the model-scale ice thickness. The total force

210 obtained from the pressure-area relationship can be downscaled and used to find crushing

211 constraint impulse that may be used to simulate model-scale towing

$$\lambda_{crushing} = \gamma^{-3} F_{crushing} \Delta t = \gamma^{-3} 7.4 \cdot 10^6 \left(\gamma^2 h l_{cont} \right)^{0.3} \Delta t \tag{8}$$

213 where $\lambda_{crushing}$ is the constraint impulse expressed in kg·m/s, $F_{crushing}$ is the full-scale crushing

214 force.

215 In the model-scale towing experiment of Eik and Marchenko (2010), the ice floes were 29

216 mm thick and the discussed time step is chosen to be 0.1 s. The crushing constraint becomes

$$\lambda_{crushing} = 36.6 \cdot l_{cont}^{0.3} \tag{9}$$

218 So, the contact impulses are limited by

$$0 \le \lambda \le \lambda_{crushing} \tag{10}$$

220 Limiting the contact impulse from above softens the normal constraints in a similar way as it

221 has been done for viscoelastic contacts (Featherstone, 2008) or for crushing ice (Metrikin,

222 2014).

223

224 **3. Experimental setup and reanalysis**

225 Lacking full-scale measurements, the experiments of Eik and Marchenko (2010) are used to

226 validate the numerical model. Despite the necessity of scaling the experimental results, the

227 basin test benefits from the absence of the ocean currents, winds, and the Coriolis effect, that

228 can be therefore excluded. In addition, the towing was performed using a carriage moving

229 above the water. Therefore, wake, such as that behind a towing vessel, did not occur in the

230 ice. In this situation, only the hydrodynamic damping and ice resistance must to be

231 considered.

232   The towing experiments were carried out at HSVA's Large Ice Model Basin (Fig. 2); its

233   dimensions correspond to 400×2880 metres in full-scale (we will continue referring to the

234   full-scale quantities through the text). Cylindrical and cuboid icebergs were towed in broken

235   ice multiple times, in various ice concentrations, and following two different towing

236   scenarios. The case with the cylindrical iceberg has been chosen for validation because of the

237   partly unreliable force measurements for the cuboid iceberg. The radius of the iceberg was

238   38.18 m, and the total height was 25.80 m, with a measured density of 887.0 kg/m^3. The

239   iceberg was towed using a 920 m long floating Dyneema line looped around the iceberg and

240   an 80 m long piece of steel wire between the line and the towing carriage. The elastic stiffness

241   of the towing line is estimated as

$$K_e = \frac{2ES}{L_0} = \frac{2 \cdot 95 \cdot 10^9 \cdot 0.08^2 \pi}{528} \approx 7.2 \cdot 10^6 \text{ N/m} \tag{11}$$

243   where $E = 95\,\text{GPa}$ is the elastic modulus of the tow line, S is the tow line cross-sectional

244   area, and L_0 is the distance between the carriage and the centre of the iceberg. The oscillation

245   frequency is therefore estimated as $v = \frac{1}{2\pi}\sqrt{\frac{K_e}{M}} \approx 0.042\,\text{Hz}$.

246
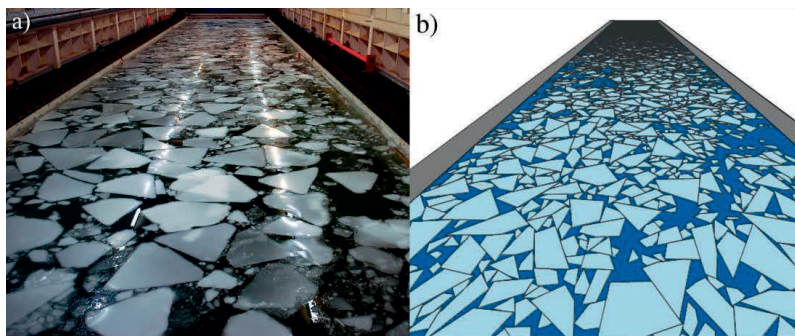
248   Fig. 2. a) The HSVA ice tank with 71% ice concentration prior to towing; b) numerical ice
249   tank filled with rigid ice floes of up to 71% ice concentration.
250

251   The carriage motion can be divided into six stages:

252   0. Linear acceleration from 0 m/s to 0.70 m/s for 11.6 minutes

253   1. Constant velocity of 0.70 m/s for 13.7 minutes;

254   2. Linear acceleration from 0.70 m/s to 0.82 m/s for 2.1 minutes;

255   3. Constant velocity of 0.82 m/s for 13.7 minutes;

256   4. Linear deceleration from 0.82 m/s to 0 m/s for 6.9 minutes;

257   5. Carriage is not moving, but the iceberg continues to move, slowly decelerating.

258   According to Eik and Marchenko (2010) the towing tests were performed in open water, and

259   in 20%, 50% and 80% ice concentration. The ice concentration prior to the tests was

260   estimated visually as a ratio between the area taken by the broken ice and total area of the

261   towing tank. We analysed photos of the parts of the towing tank filled with ice to get a better

262   estimate of the concentrations.

263   The perspective on the digital photographs was adjusted to the top view, and the area

264   occupied with broken ice was estimated. Ice floes on the photographs consisted of brighter

265   pixels than the walls of the ice tank and the water surface. So, the ice concentration was

266   estimated as the number of bright pixels divided by the total number of water and ice pixels.

267   Assuming uniform distribution of ice over the towing tank, significant adjustments were made

268   to the ice concentrations reported previously. It turned out that the towing tests were

269   performed in open water, and 40%, 71% and 86% ice concentrations (Fig. 3). This reanalysis

270   helped to make better interpretation of the experimental results.
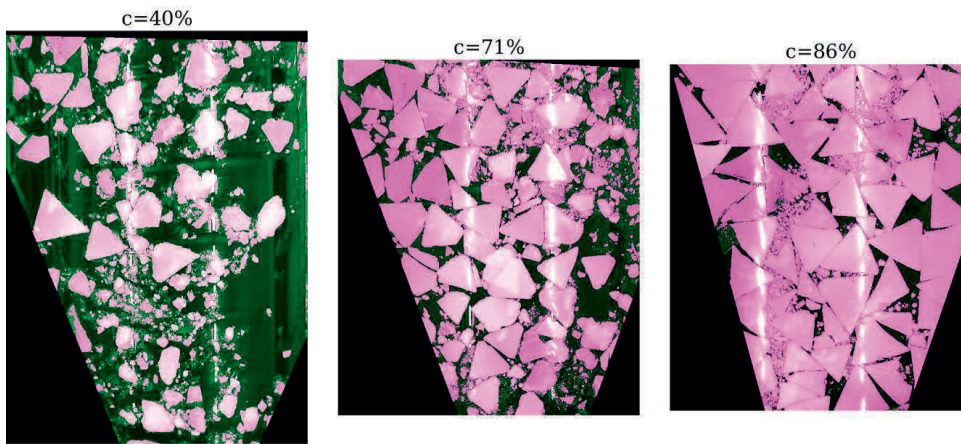
271

272　Fig. 3. Photographs of the parts of the towing tank were used to reanalyse ice concentration in

273　the towing tests.

274

275　First, the 1.16 m thick ice was broken into triangular pieces having approximate area of 800

276　m^2 in full-scale. During towing in 86% ice concentration ice often failed in crushing and ice

277　floes rafted (Fig. 4.). Then part of the ice was removed before towing in 71% concentration.

278　Since some of the ice floes were broken few small ice pieces appeared. Even more smaller

279　pieces appeared after towing in 71% concentration, but much less crushing was observed.

280

281

282　Fig. 4. Photograph taken during towing test in 86% ice concentration. Highly confined ice

283　floes are crushing in front of the iceberg.

284

285　The numerical domain has the same dimensions as the experimental one. The ice field

286　configurations could not be reproduced accurately because they were not photographed

287　properly to be analysed using the modern shape-recognition techniques (Zhang et al., 2015).

288　In 86% concentration, however, we generated only triangular floes as they were in the

289　experiment; in 71% and 40% more vertices were used for the polygons representing ice floes.

290　An example of the numerical ice tank prior to towing in the 71% ice concentration is shown in

291　Fig. 2b.

292　The coefficient of friction between the numerical towing tank walls and the ice is set equal to

293　the ice-ice coefficient of friction because of a special ice preparation method in the

294　experiment. The ice was grown at the surface of the water and then cut into floes; however,

295　some ice still remained attached to the walls. Thus, it can be assumed that the walls at the

296　waterline had the same friction coefficient as ice. The towing line was simulated by an elastic

297　connection of equivalent stiffness between the carriage and the iceberg. So the towing force

298　proportional to the change in distance between the iceberg and the carriage has been applied.

299　The parameters of the simulations are shown in Table 1.

300

301　Table 1. Parameters of simulations

Quantity	Value	Source
Friction coefficient of ice floes	0.3	Sukhorukov and Løset (2013)
Density of ice floes	930 kg/m^3	Eik and Marchenko (2010)
Density of iceberg	887 kg/m^3	Eik and Marchenko (2010)
Iceberg drag coefficient	0.33 or 0.40	Estimated from Eik and Marchenko (2010)
Surface drag coefficient for ice floes	0.005	Lu et al. (2011)
Added mass coefficient of iceberg	1	Newman (1977)
Added moment of inertia of iceberg	0	Newman (1977)
Time step	0.63 s	Approximate collision duration

302

303   The towing forces at Stages 1 and 3 measured in the experiment and obtained from the

304   simulations are compared and analysed in the next section.

305

306   **4. Numerical results**

307   **4.1. Water drag coefficient estimation**

308   First, the open water test was analysed to separate the hydrodynamic effects from the contact

309   problems. Complex flow past the cylindrical iceberg caused unpredictable drag force

310   oscillations in open water and in broken ice. Therefore, the hydrodynamic resistance could not

311   be accurately separated from the ice resistance. The estimated Reynolds numbers for the

312   model-scale and full-scale icebergs are

313
$$\mathrm{Re}_{\text{model-scale}} = \frac{UD}{\nu} = \frac{0.13 \cdot 1.909}{1.8 \cdot 10^{-6}} = 0.14 \cdot 10^{6}, \quad \mathrm{Re}_{\text{full-scale}} = \frac{UD}{\nu}\lambda^{3/2} = 34.9 \cdot 10^{6} \quad (12)$$

314   They correspond to the subcritical and supercritical flow regimes (Rodríguez et al., 2015),

315   what results in different drag coefficients for the model-scale and the full-scale once the

316   Froude scaling is applied. In the numerical model, the water action is represented only by the

317   water drag force approximation

318
$$\vec{F}_{w} = \frac{1}{2} C_{w} \rho_{w} A \left| \vec{V}_{w} - \vec{U} \right| \left(\vec{V}_{w} - \vec{U} \right) \quad (13)$$

319   where $\vec{F}_{w}$ is the force vector, C_{w} is the form drag coefficient that is usually on the order of 1,

320    $\vec{V}_{w}$ is the water velocity, and A is vertical cross-sectional area of the iceberg keel. The water

321   velocity can be set to zero because of the still water in the basin. Thus, for straight line

322   towing, the water drag force magnitude can be expressed as

323
$$F_{w} = \frac{1}{2} C_{w} \rho_{w} A U^{2} \quad (14)$$

324   where U is the towing speed. The drag coefficient is found from this equation using the

325   measured force magnitude and speed values as the time-average

326
$$C_w = \frac{2}{\rho_w A} \left\langle \frac{F_w}{U^2} \right\rangle \qquad (15)$$

327   here, the brackets $\langle \ \rangle$ mean time-averaging. The evolution of the estimated drag coefficient is

328   shown in Fig. 5. The values for the drag coefficient during Stages 1 and 3 are shown by red

329   and blue lines, respectively. For the towing velocities of 0.70 m/s and 0.82 m/s, the drag

330   coefficient is found to be 0.33 and 0.40, respectively.

331   The found drag coefficients for the iceberg are used in the numerical model to investigate the

332   towing forces in broken ice. The drag force applied to the ice floes in the numerical model is

333   proportional to the horizontal surface area of the floes, fluid density and the squared relative

334   fluid velocity. The surface drag coefficient equal to 0.005 has been chosen following Lu et al.

335   (2011).

336
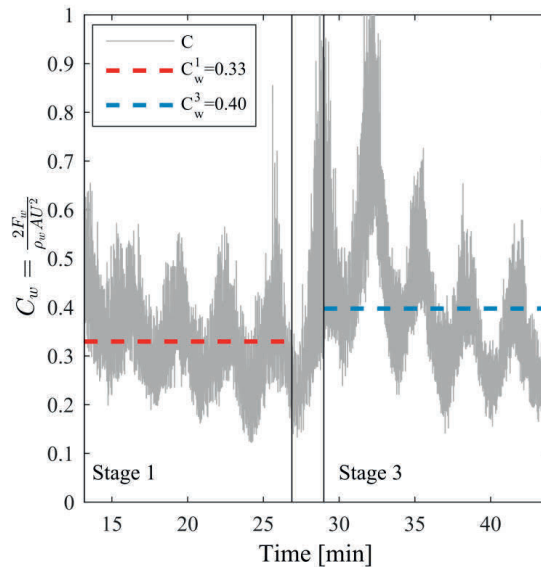
337

338   Fig. 5. Determination of the water drag coefficient for the open water test. Newly found C_w^1
339   and C_w^3 are used for Stages 1 and 3, respectively.
340

341   **4.2. Towing force evolution**

342   The evolution of the towing force magnitude F_{tow} is derived numerically, and its average

343   values during Stages 1 and 3 will be compared with the towing force magnitude measured in

344   the experiment. The force evolution for different ice concentrations is shown in Fig. 6.

345   The measured F_{tow} in 40% concentration had several distinct peaks related to collisions with

346   ice floes, as for example at 14 minutes. The magnitude of these peak forces was on the order

347   of 200 kN. At the same time F_{tow} slowly oscillated because of hydrodynamic effects. As it is

348   possible to see in Fig. 6 the water drag force is still the main source of towing resistance. The

349   force obtained numerically has higher and more frequent peaks on the order of 500 kN, they

350   occur likely, because the scaling procedure (5) overestimates the collision force.

351   Mechanical behaviour of broken ice starts to dominate during towing in 71% ice

352   concentration. The amount of ice being pushed grows, and the total surface drag force acting

353   on ice floes becomes significant. There are moments when the ice is stuck between the

354   iceberg and the walls of the basin, and high forces transmitted through long chains of contacts

355   may cause high F_{tow}. Eventually, the concentration of ice at the end of the basin grows, the ice

356   floes become confined and the scaled towing force reaches almost 4 MN.

357   In 86% ice concentration, the measured and simulated towing force oscillates with high

358   amplitude. The highest measured F_{tow} exceeded 10 MN when towing at 0.82 m/s. The

359   crushing constraint in the model allows peak force reduction and introduces necessary

360   damping into the system. As a consequence, F_{tow} obtained in the simulation behaves similarly
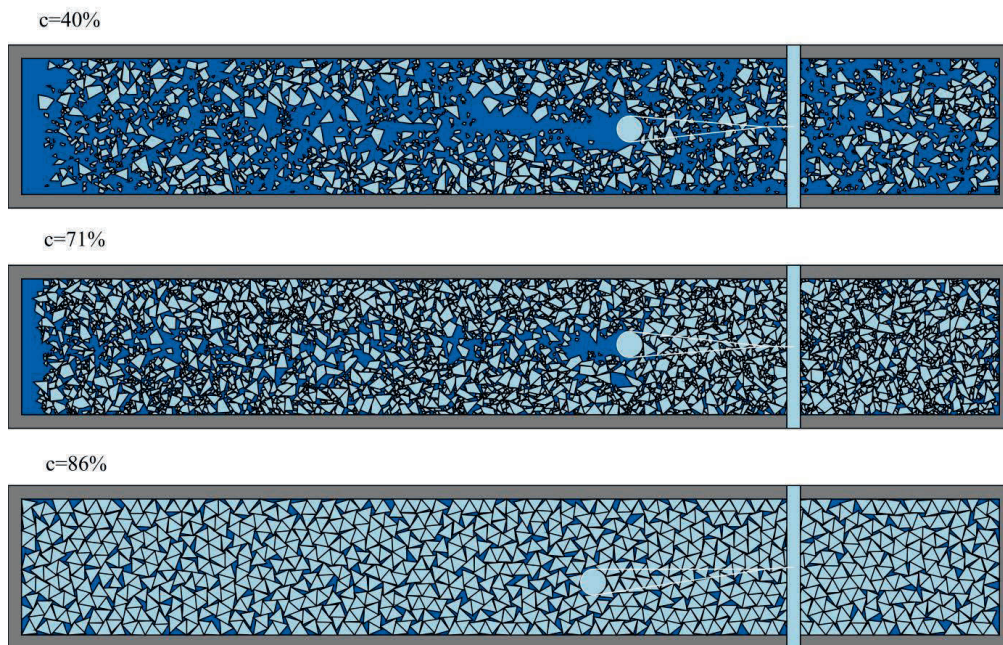
361   to the experiment.

c=40%

c=71%

c=86%
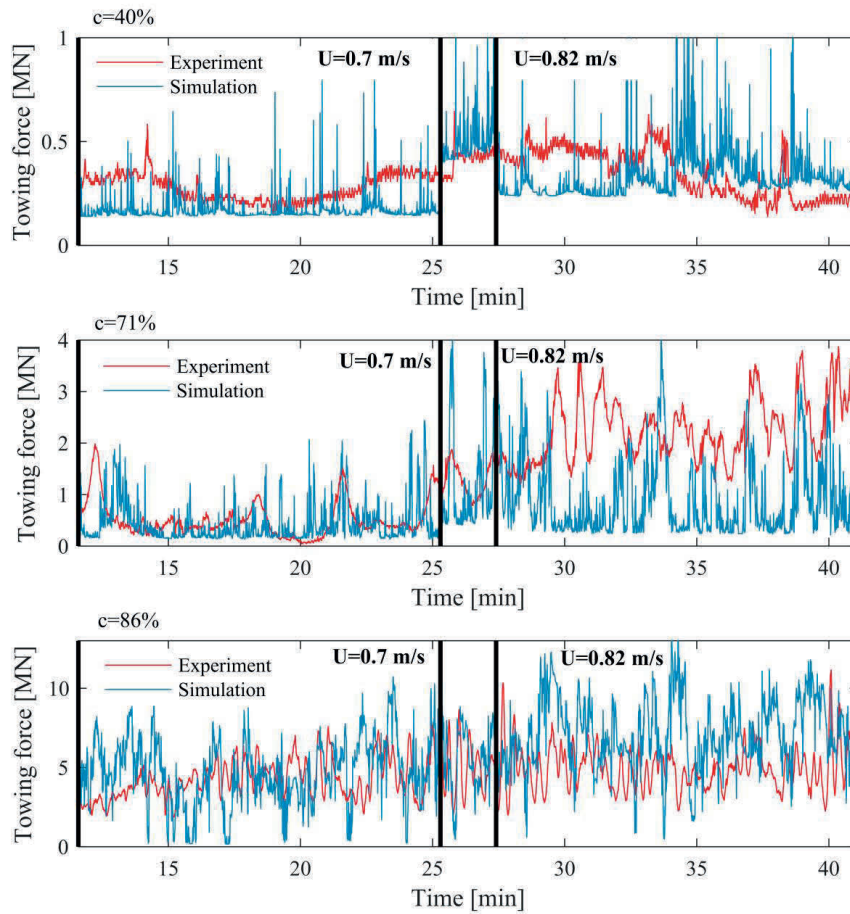
Fig. 6. Experimental and numerical towing force history for towing in 40%, 71% and 86% ice concentration.

4.3. Ice field after towing

The numerical ice field configurations after the simulation in different concentrations are shown in Fig. 7. It can be noticed that in the 40% concentration, the ice is not accumulated in the bow area. The accumulation occurs for towing in 71% ice concentration, and it confines the ice at the end of the numerical basin. As mentioned earlier, towards the end of the test, the

371 ice concentration in front of the iceberg becomes much higher than behind it. Consequently,

372 the towing force grows, as seen from a corresponding test in 71% in Fig. 6.

373 Finally in the 86% ice concentration, the ice is densely packed, and almost all ice floes are in

374 contact and have no freedom to flow. As it was observed in the experiment, the ice floes were

375 crushed and rafted. In the current implementation of the numerical model, the ice floes don't

376 change their shapes and do not raft, because the model is planar. In the last ice field in Fig. 7

377 the iceberg is just squeezed between the ice floes.

378

379 Fig. 7. End of simulations for ice fields of different concentrations. Smaller ice floes in lower
380 concentrations are used in simulations to follow the experiment. Animated simulation of
381 towing in 71%
382

383 **4.4. Mean ice resistance**

384 We compare the mean ice resistance magnitude F_{si} obtained after scaling the model results

385 with the scaled simulation results and some analytical approximations derived for ice

386 resistance to iceberg's relative motion. The mean ice resistance is determined for each of the

387   Stages 1 and 3 when the towing velocities were constant. The mean values are calculated by

388   averaging F_{tow} for each stage and then subtracting corresponding F_w calculated according to

389   (14). F_{si} is plotted against the ice concentration for Stages 1 and 3 in Fig. 8. One standard

390   deviation is shown for the experimental data using error bars.

391   F_{tow} grows dramatically between 71% and 86% concentrations. F_{si} between these two tests

392   differ by the order of 10. At the same time the velocity effect seems to be moderate and not as

393   important as the concentration.
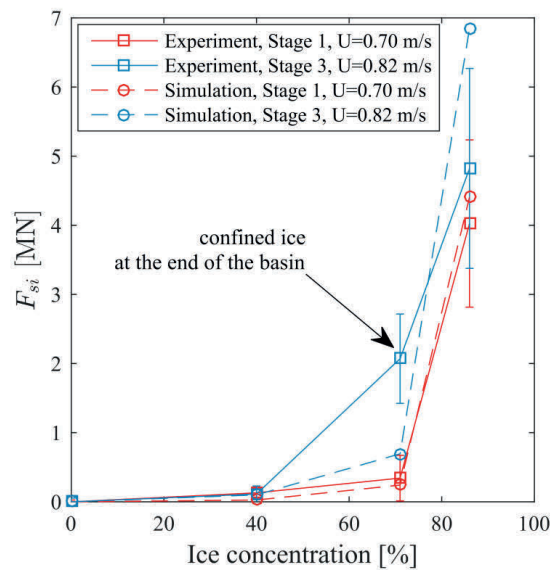
394

395   Fig. 8. Mean broken ice resistance compared between the experimental results and the

396   numerical simulations.

397

5. Discussions

5.1. General analysis

400   We have presented a numerical model that is capable to calculate towing force applied to an

401   iceberg moving through broken ice. The model takes into account continuous hydrodynamic

402 forces and contact forces discontinuous in time. Once F_{tow} is determined, the average

403 magnitude of the ice resistance is calculated as the difference between F_{tow} and the water drag

404 force.

405 The model is planar therefore its accuracy is limited when off-plane effects such as bending

406 failure of ice floes, ridging and rafting appear. These effects are seldom when iceberg drifts

407 through ice, and we expect similar behaviour for an iceberg that is going to be towed slowly

408 through managed ice of moderate concentrations. Attempting to tow an iceberg in broken ice

409 is unlikely to happen in high ice concentrations, where ice floes may accumulate in front of

410 the iceberg, stop to flow around it and significantly increase towing forces. Inability to break

411 ice in bending and submerge ice floes is one of the reasons for discrepancy between numerical

412 simulation and experiment, where some of the ice floes rafted during towing in 86% ice

413 concentration.

414 Nevertheless, the average ice resistance magnitude obtained numerically is in agreement with

415 the resistance obtained from the experiment. F_{si} undergoes dramatic increase at

416 approximately 70% because the broken ice cannot flow anymore without failing. Therefore,

417 instead of hydrodynamic surface drag of the ice floes, the friction at the contacts' interfaces

418 and compression of confined ice field become the main sources of the ice resistance. So, at

419 the concentrations higher than 70%, the iceberg has to break through confined broken ice

420 instead of pushing the ice floes out.

421 Instantaneous values of the towing forces were impossible to match obviously because of

422 randomized numerical ice fields and simplified hydrodynamics. We recommend a thorough

423 documentation of the ice field including top view photographs if similar experiments are

424 going to take place in future. This will help to identify shapes and track individual ice floes,

425 and use these data as accurate input for the model.

426 Simulated ice motion qualitatively looks correct, however, it is difficult to compare it with the

427 motion of ice in the experiment because the former was filmed under oblique angle and

428 camera moved. Potential flow solution implemented in the vicinity of the iceberg resulted in

429 closing wake that was not possible to obtain using still water approach.

430

431 **5.2. Effect of ice concentration**

432 As seen from the experiments, the ice concentration is the most influential parameter affecting

433 the mean ice resistance. The World Meteorological Organisation (WMO, 2014) defines the

434 ice concentration as the "the ratio expressed in tenths describing the amount of the sea surface

435 covered by ice as a fraction of the whole area being considered." It is obviously, an integral

436 characteristic and "the whole area" must contain a large number of ice floes, and the ice must

437 be uniformly distributed over the area. A certain ice concentration over a large domain,

438 however, does not guarantee the same concentration over a small subdomain. For example, a

439 moored floater or a vessel on station keeping may accumulate highly compacted ice upstream,

440 while the ice concentration over a larger area may be much lower.

441 For the model-scale tests, the ice concentration relates to the whole basin area. During the

442 towing, however, the ice is redistributed and some of the ice is pushed towards the end of the

443 basin. By the end of the towing in 71% ice concentration, the ice became confined causing

444 significantly higher towing forces than in the beginning of the test.

445 So, the ice concentration is a macro parameter that can be used only in relation to large

446 domains. For towing in broken ice where the motion of individual ice floes is important, the

447 ice concentration should not be used to analyse instantaneous values of dynamic or kinematic

448 quantities. The ice concentration may instead be related to spatially averaged quantities such

449 as for example the towing force magnitude averaged over 3 km long straight line towing.

450

5.3. Comparison with analytical approximations

There exist several analytical approximations for the ice resistance force acting on an iceberg in broken ice. One is given by Lichey and Hellmer (2001) for large Antarctic icebergs. The force due to the sea ice $\vec{F}_{si}$ is calculated differently for three intervals of ice concentration as

$$\vec{F}_{si} = \begin{cases} 0, & c \le 15\% \\ 0.5 C_i \rho_i A_i \left| \vec{V}_i - \vec{U} \right| (\vec{V}_i - \vec{U}), & 15\% < c < 90\% \\ M \dfrac{d\vec{V}_i}{dt} - \vec{F}_{ext}, & c \ge 90\%, P \ge P_s \end{cases} \qquad (16)$$

where $C_i = 1.0$, $A_i = Dh$ is the nominal contact area between sea ice and the iceberg, c is ice concentration, $\vec{V}_i$ is the velocity of ice and $\vec{U}$ is the velocity of the iceberg. $\vec{F}_{ext}$ are the rest of the driving forces such as the drag forces, the Coriolis force, the sea slope force, etc. $P(\text{N} \cdot \text{m}^{-1})$ is the ice strength, $P_s = P^* h \exp[-20(1-c)]$ is a threshold value calculated according to Hibler (1979), and $P^*(\text{N} \cdot \text{m}^{-2})$ is an empirical coefficient ranging from 15 to 30 kN·m^{-2}.

For low ice concentrations ($c \le 15\%$), the sea ice resistance is neglected, whereas for the concentrations between 15% and 90%, the sea ice is considered to act as a viscous material providing the drag. For concentrations above 90%, the sea ice "captures" the iceberg unless the force is so high that the sea ice begins to fail. Worth noting, we have added an additional term into the third expression in (16) because when the iceberg drifts with ice, the ice accelerations must be also considered, so $M \dfrac{d\vec{V}_i}{dt}$ must be added.

In their study Lichey and Hellmer (2001) applied (16) to hindcast more than 2 years long drift of a large Antarctic iceberg. Temporal and spatial scales of their model are much larger than corresponding scales for iceberg towing operations. At large scales, they treat sea ice as a

471 continuum and calculate certain average ice resistance. Broken ice can be treated as a

472 continuum on smaller tactical scales assuming small ice floe size in relation to the iceberg

473 characteristic diameter in the horizontal cross-section at the waterline. So, (16) can be applied

474 to calculate average ice resistance when towing, for example, a 100 m wide iceberg in well

475 managed ice consisting of ice floes having a few tens of metres in diameter. In ice

476 concentrations higher than 90% the sea ice strength P_s determined for geophysical scale is

477 likely to be inaccurate on tactical scale.

478 The second approximation is derived based on the assumption that the iceberg creates a

479 channel in the ice by pushing small compacted ice floes in the bow area and on the sides

480 (Marchenko et al., 2010). For a symmetrical flow of ice around a cylindrical iceberg, the

481 magnitude of the ice resistance can be found as

482
$$F_{si} = \frac{D}{4}\left(\rho_i c_{crit} h + \frac{1}{4}C_w \rho_w D\right)\frac{c}{c_{crit} - c}U^2 \tag{17}$$

483 where $C^{IF} \approx 0.005$ is the surface drag coefficient, and U is the absolute iceberg velocity. The

484 equation is applicable for concentrations below that of the highest-density packing c_{crit}. The

485 ice resistance can be neglected for low concentrations but grows severely as the concentration

486 approaches the critical value.

487 In addition, drag-like resistance has been measured experimentally in granular materials for

488 concentrations below the highest-density packing value (Wassgren et al., 2003). According to

489 the study, the average force acting on a cylindrical body in an initially uniform granular flow

490 can be calculated as

491
$$\vec{F}_{si} = \frac{1}{2}C_i \rho_i c(D+d)h\left|\vec{V}_i^{rel}\right|\vec{V}_i^{rel} \tag{18}$$

492 where the drag coefficient $C_i \approx 1.5$. Obviously, the equation is very similar to what has been

493 suggested by Lichey and Hellmer (2001) for intermediate concentrations. The main

494 differences are dependence on the ice concentration and wider cross section due to finite ice

495 floe size.

496 These force approximations for relative ice velocity of 0.82 m/s corresponding to Stage 3 in

497 the experiment are shown in Fig. 9 together with scaled experimental and numerical results.

498 The resistance calculated according to (18) is not shown because its magnitude is too low. For

499 the approximation (16) at concentrations above 90% we have shown the upper force limit

500 determined by the threshold pressure.

501 It can be seen that the analytical approximations result in much lower ice resistance than it

502 was numerically simulated and measured in the experiment. The major reason is confinement

503 of the ice in the towing tank during the tests in 71% and 86% concentrations. It caused higher

504 resistance than it is expected for full-scale towing where no walls exist. In spite this obvious

505 argument against such comparison, it might be useful to compare and understand the

506 uncertainties behind the model-scale experimental results.

507 The experimental results can serve as a conservative estimate of F_{si} that may be experienced

508 when, for example, the icebreaking is performed to reduce ice floe size and create a corridor

509 between larger ice floes. So the towing in ice will occur in the corridor confining smaller

510 managed ice floes, and then the scaled experimental results may be helpful.
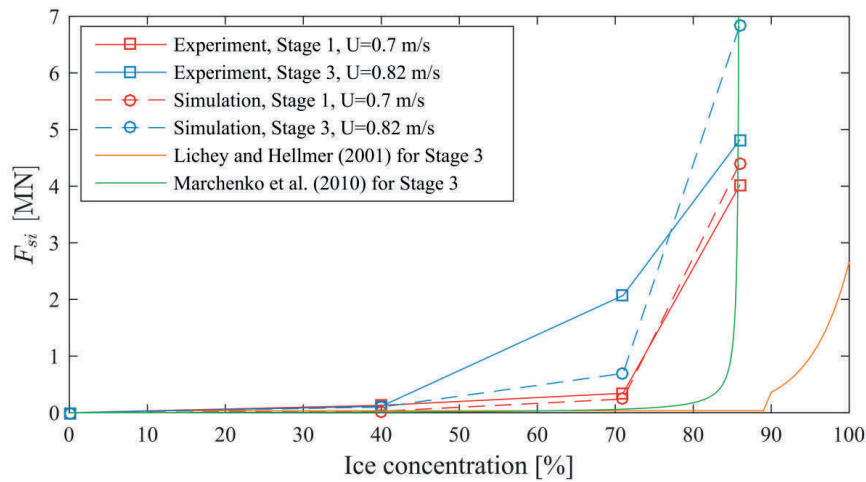
511

512 Fig. 9. Scaled experimental and numerical results for the model-scale tests are compared with
513 existing analytical approximations of ice resistance.
514

515

516 **5.4. Feasibility of a full-scale towing**

517 Now let us consider a potential full-scale towing operation. Based on the Grand Banks

518 experience the towing setup in reality is different from what was used in the experiment. To

519 ensure the iceberg's rolling stability one needs to minimize the torque produced by the towing

520 force applied at the waterline, far above the centre of gravity of the iceberg. To achieve this,

521 the iceberg has to be encircled with a floating towing line or net that is going to be attached to

522 a long steel towing hawser. Such setup causes towing line catenary which reduces the

523 overturning force moment. At the same time this kind of setup results in strong damping that

524 will potentially reduce the effect of impacts with ice floes. So, the reduced peak forces are not

525 likely to break the towing line as it happened when no towing line catenary was used (C-

526 CORE, 2004).

527 In addition, most probably, the full-scale towing velocities will be considerably less than the

528 scaled experimental velocities of 0.7 m/s and 0.82 m/s during Stages 1 and 3, respectively

529 (Mellor, 1980). Even in open water the change of iceberg speed due to towing is often below 1

530 knot. One crew member of a towing vessel operating at the Grand Banks characterized towing

531 operations by the words: "it is not us who tows icebergs, it is the opposite".

532 Again, the first attempts to tow an iceberg in ice are likely to occur in thin ice of low

533 concentration. Moreover, if the iceberg will follow into the channel of ice created by the towing

534 vessel, the amount of ice it encounters may be insignificant.

535 These reasons demonstrate that the anticipated towing force in real full-scale operation may be

536 much lower than the forces scaled from the experiment. Yet, the experimental and numerical

537 results give a conservative estimate of the ice resistance in tow.

538 Finally, let us once again review the magnitude of the towing force in ice. We consider full-scale

539 towing of the iceberg used in the experiment which was 76.4 m wide and 25.8 m in total height.

540 Then its mass is approximately equal to 0.1 million tons corresponding to a medium-sized

541 iceberg. Towing force at 0.7 m/s and 0.82 m/s in 86% concentration exceeded 10 MN with the

542 average ice resistance of approximately 4.5 MN. While in 40% and during Stage 1 in 71%

543 concentration the towing force was under 2 MN most of the time (Fig. 6), the average ice

544 resistance was under 0.5 MN. Compared to the open water towing force of approximately 147 kN

545 at 0.7 m/s, the average towing force in 40% concentration was only 173 kN, and 389 kN in 71%

546 ice concentration. These numbers are on the same order as the towing forces measured during real

547 full-scale open water towing operations (C-CORE, 2004). Thus, one must expect more than

548 doubled towing force when towing in 1.16 m thick ice in ice concentrations of 70%. Towing in

549 more severe conditions seems to be hardly feasible. As always, well-documented full-scale towing

550 trials in ice are highly needed.

551

6. Conclusions

553 We have described a numerical model of iceberg towing in broken ice and attempted to

554 validate it. The opportunities for validation were very limited: no full-scale towing in ice was

555 available, and the only model-scale experiment was difficult to reproduce numerically.

556   Moreover, we have attempted to compare existing analytical approximations of ice resistance

557   with scaled numerical results.

558   The major findings are as follows:

559   • The non-smooth discrete element method may be applied to simulate iceberg towing

560   through broken ice. The motion of ice looks realistic, the shapes of the ice features are

561   not overlapping, and the wake behind the iceberg is closing owing to potential flow

562   solution in the vicinity of the iceberg.

563   • The average towing force magnitudes measured in the experiment and calculated

564   using the model are in fair agreement. The identified sources of discrepancy are poor

565   quality input data (initial ice configuration) for the numerical model and inability of

566   the model to reproduce rafting and changing ice floes' shapes due to crushing.

567   • The ice concentration is found to be the most influential parameter determining the

568   towing force. However, the ice concentration is a macro parameter that can be applied

569   to a domain consisting of many ice floes, distributed uniformly. Only spatially

570   averaged characteristics may be discussed in terms of the ice concentration.

571   • As long as ice floes can flow or be pushed without crushing or any major failure, the

572   towing resistance will be much lower than the resistance in confined, highly

573   concentrated ice. Experimental and simulated F_{tow} for a 0.1 million ton iceberg being

574   towed at 0.82 m/s through 1.16 m thick ice floes having areas of 800 m^2 are under 0.5

575   MN for ice concentrations below 71% and under 7.5 MN for 86% ice concentration.

576   Instantaneous magnitude of the towing force exceeded 10 MN when the iceberg was

577   towed through confined 86% concentrated ice.

578   • The towing forces obtained in basin-tests are higher than the forces determined by the

579   analytical approximations. The confinement that was present in the experiments but

580   was absent from the analytical expressions is the primary source of the discrepancy.

581   Additionally, the approximations are obtained with the assumption that the ice floes

582   have a much smaller size than the iceberg's diameter. The average forces from the

583   model-scale towing may serve as conservative estimates prior to the full-scale trials.

584   • One may expect twice higher towing forces when towing in 70% ice concentrations

585   compared to the open water towing.

586 The model can be further improved by realistic towing setup including towing line catenary and

587 tug vessel, and by extending it to the full six degrees of freedom. At the current state, the model

588 can be used to simulate towing in ice prior to the full-scale tests as a decision support tool or as a

589 numerical towing facility.

590

596

597 C-CORE, 2004. Stability and Drift of Icebergs Under Tow – Draft Report. Prepared for
598   Petroleum Research NL (PRNL). C-CORE Report R-04-072-216 v1.
599 Eik, K. and Marchenko, A., 2010. Model tests of iceberg towing. Cold Regions Science and
600   Technology, 61(1): 13-28, doi: 10.1016/j.coldregions.2009.12.002.
601 Featherstone, R., 2008. Rigid Body Dynamics Algorithms. Springer US.
602 Hamilton, J., Holub, C., Blunt, J., Mitchell, D. and Kokkinis, T., 2011, Ice Management for
603   Support of Arctic Floating Operations, OTC Arctic Technology Conference, Houston,
604   Texas, USA, 7-9 February.
605 Hamilton, J.M., 2011. The Challenges of Deep-Water Arctic Development. International
606   Journal of Offshore and Polar Engineering, 21(4): 241-247,
607 Hibler, W.D., 1979. Dynamic Thermodynamic Sea Ice Model. Journal of Physical
608   Oceanography, 9(4): 815-846, doi: 10.1175/1520-
609   0485(1979)009<0815:Adtsim>2.0.Co;2.
610 Kjerstad, Ø.K., Metrikin, I., Løset, S. and Skjetne, R., 2015. Experimental and
611   phenomenological investigation of dynamic positioning in managed ice. Cold Regions
612   Science and Technology, 111(0): 67-79,
613   http://dx.doi.org/10.1016/j.coldregions.2014.11.015.

614 Lichey, C. and Hellmer, H.H., 2001. Modeling Giant-Iceberg Drift Under the Influence of Sea
615   Ice in the Weddell Sea, Antarctica. Journal of Glaciology, 47(158): 452-460,
616 Lu, P., Li, Z.J., Cheng, B. and Leppäranta, M., 2011. A Parameterization of the Ice-Ocean
617   Drag Coefficient. Journal of Geophysical Research-Oceans, 116, doi:
618   10.1029/2010jc006878.
619 Lubbad, R. and Løset, S., 2011. A Numerical Model for Real-Time Simulation of Ship-Ice
620   Interaction. Cold Regions Science and Technology, 65(2): 111-127, DOI
621   10.1016/j.coldregions.2010.09.004.
622 Marchenko, A. and Gudoshnikov, Y., 2005. The influence of surface waves on rope tension
623   by iceberg towing, Proceedings of the 18th International Conference on Port and
624   Ocean Engineering under Arctic Conditions, Postdam, NY, USA, June 26-30, 2005,
625   pp. 543-554.
626 Marchenko, A., Kulyakhtin, A. and Eik, K., 2010, Icebergs Drift in the Barents Sea: Data
627   Analysis of Ice Tracking Buoy and Numerical Simulations, Proceedings of the 20th
628   IAHR International Symposium on Ice, Lahti, Finland, 14-18 June, 2010.
629 Marchenko, A. and Ulrich, C., 2008. Iceberg towing: analysis of field experiments and
630   numerical simulations, Proceedings of the 19th IAHR International Symposium on
631   Ice, Vancouver, BC, Canada, July 6-11, 2008, pp. 909-921.
632 McClintock, J., McKenna, R. and Woodworth-Lynas, C., 2007. Grand Banks Iceberg
633   Management. PERD/CHC Report 20-84.
634 Mellor, M., 1980. High-Force Towing. Cold Regions Science and Technology, 1(3-4): 231-
635   240, Doi 10.1016/0165-232x(80)90051-8.
636 Metrikin, I., 2014. A Software Framework for Simulating Stationkeeping of a Vessel in
637   Discontinuous Ice. Modeling, Identification and Control, 35(4), 10.4173/mic.2014.4.2.
638 Newman, J.N., 1977. Marine Hydrodynamics. The MIT press, Cambridge, MA.
639 Randell, C., Ralph, F., Power, D. and Stuckey, P., 2009. Technological advances to assess,
640   manade and reduce ice risk in northern developments, Offshore Technology
641   Conference, Houston, TX, USA, 4-7 May, 2009.
642 Rodríguez, I., Lehmkuhl, O., Chiva, J., Borrell, R. and Oliva, A., 2015. On the flow past a
643   circular cylinder from critical to super-critical Reynolds numbers: Wake topology and
644   vortex shedding. International Journal of Heat and Fluid Flow, 55: 91-103,
645   http://dx.doi.org/10.1016/j.ijheatfluidflow.2015.05.009.
646 Sanderson, T.J.O., 1988. Ice Mechanics Risks to Offshore Structures. Graham and Trotman,
647   London, UK.
648 Sukhorukov, S. and Løset, S., 2013. Friction of Sea Ice on Sea Ice. Cold Regions Science and
649   Technology, 94: 1-12,
650 Timco, G.W., 2011. Isolated Ice Floe Impacts. Cold Regions Science and Technology, 68(1-
651   2): 35-48, DOI 10.1016/j.coldregions.2011.04.008.
652 Wassgren, C.R., Cordova, J.A., Zenit, R. and Karion, A., 2003. Dilute granular flow around
653   an immersed cylinder. Physics of Fluids, 15(11): 3318-3330, 10.1063/1.1608937.
654 WMO, 2014. Sea Ice Nomenclature, WMO No. 259.
655 Yulmetov, R., Lubbad, R. and Loset, S., 2016. Planar multi-body model of iceberg free drift
656   and towing in broken ice. Cold Regions Science and Technology, 121: 154-166,
657   10.1016/j.coldregions.2015.08.011.
658 Zhang, Q., Skjetne, R., Metrikin, I. and Loset, S., 2015. Image processing for ice floe analyses
659   in broken-ice model testing. Cold Regions Science and Technology, 111: 27-38,
660   10.1016/j.coldregions.2014.12.004.
661

Appendix C:
Iceberg and sea ice drift tracking and analysis off north-east Greenland

The paper analyzes the data obtained from GPS trackers deployed on drifting ice floes and icebergs in the Greenland Sea in 2012-2013. The rotation of drifting icebergs is measured and modelled.

Iceberg and sea ice drift tracking and analysis off north-east Greenland

CrossMark

Renat Yulmetov [a,b,*], Aleksey Marchenko [a,b], Sveinung Løset [a,b]

[a] *The University Centre in Svalbard, Pb. 156, 9171 Longyearbyen, Norway*
[b] *Sustainable Arctic Marine and Coastal Technology (SAMCoT), Centre for Research-Based Innovation (CRI), Norwegian University of Science and Technology (NTNU), Trondheim, Norway*

ARTICLE INFO

ABSTRACT

Drifting icebergs and sea ice floes can be serious threats to offshore structures in the Arctic; however, information about their drift is limited. We performed GPS tracking of 9 icebergs and 10 ice floes in the Kanumas area of the Greenland Sea during 2012–2014. The obtained coordinates were used to analyse the drift trajectories, derived velocities, spectra and relative drift of the icebergs and sea ice. This paper presents statistical data on the drift velocities and demonstrates the differences between drifts in the shear ice zone and the central pack or marginal ice zone. The maximum drift speed reached by an iceberg was 1.66 m/s, which happened during strong southerly wind at 66°N. The relative drift of icebergs and adjacent sea ice is strongly dependent on ice conditions and wind, but also it is determined by the different types of applied drag forces. Then, spectral analysis revealed that GPS errors may prevent capturing processes faster than one cycle per hour. In addition, for the first time, we measured the rotation of four icebergs around their vertical axes. Icebergs make an average of between one and two revolutions per day under the periodic tidal current. However, the instantaneous angular velocity reached 0.001 rad/s at some moments. Finally, this paper proposes an iceberg drift model including the rotation. The modelling results are in good agreement with the measured evolution of the icebergs' yaw angles. The drift data and the rotation model can be used when planning offshore activities in the area or as an input for numerical models involving sea ice.

© 2016 Elsevier Ltd. All rights reserved.

1. Introduction

The main challenges for Arctic offshore operations are remoteness, low temperatures and the presence of sea ice and icebergs in surrounding waters. Knowledge about ice conditions is necessary for design and operation of Arctic structures. For more fundamental scientific reasons, these interests are linked to global warming and global ice cover dynamics and kinematics. The ice cover extent and its discharge from the Arctic may serve as climate change indicators (Stroeve et al., 2012).

Traditionally, the observation of ice and iceberg drift has been performed by drifting stations, buoys and remote sensing. The famous International Arctic Buoy Program started in 1979 and has tracked more than 650 Argos-type buoys since then (Pfirman et al., 1997). Initially, the Argos buoys gave position estimation errors in the range of a few hundred metres. Such accuracy was sufficient for the gridded global scale climate models and the Arctic mass balance calculations.

Modern Lagrangian ice drift products based on synthetic aperture radar image analysis have provided velocity estimates with a precision of a few millimetres per second. However, their time resolution ranges from several hours to several days (Weiss, 2013). Such resolution has been sufficient to validate large-scale sea ice drift models (Sumata et al., 2015) but is not sufficient for the tactical scales when hourly forecasts are needed.

Finally, the ice tracking drifters (ITDs) consisting of a GPS module and an Iridium modem have been used to obtain drift patterns and drift speed of ice and icebergs (Larsen et al., 2015) to validate forecasting models (Turnbull et al., 2015; Yulmetov et al., 2012) and to study the frequency response of the ice cover (Leppäranta et al., 2012). This type of tracker benefits from relatively high spatial and time resolutions of GPS transponders and light weight (< 5 kg with battery).

Such accurate data are always needed for particular regions in the Arctic. The number of regions related to petroleum offshore development includes the Beaufort Sea, Barents Sea, the Kara Sea, the Pechora Sea, the Greenland Sea, and Sakhalin. Offshore operations in ice-infested waters are subjected to ice actions that can be reduced using ice management. Ice management is commonly defined as the sum of all activities aiming to reduce ice action on an offshore object (Eik, 2008). The success of ice management

---

* Corresponding author at: The University Centre in Svalbard, Pb. 156, 9171 Longyearbyen, Norway.
E-mail address: RenatY@unis.no (R. Yulmetov).

depends on knowledge about incoming ice and icebergs, and general environmental conditions.

Usually, physical ice management consists of the separate tasks of ice breaking and iceberg management. However, icebergs might drift together with sea ice towards an offshore structure. The role of broken ice in the iceberg drift and the differences between ice and iceberg drift must be studied for the area. Drift tracks and velocities obtained by the ITDs can be used to validate state-of-the-art numerical models of ice management operations in pack ice (Scibilia et al., 2014; Yulmetov et al., 2016).

A complex survey of ocean and ice conditions over the east Greenland offshore area and in the Fram Strait was conducted during two consecutive research surveys: Oden Arctic Technology Research Cruises (OATRC) in September 2012 and August 2013 (Lubbad et al., 2013; Scibilia et al., 2014). The studies included mechanical tests of sea ice and ice ridges, ocean current measurements and CTD-profiling, mooring deployment and retrieval, ice management trials, ice and iceberg monitoring and tracking, and marine mammal observations.

In this paper we present and analyse drift data obtained from ITDs between autumn 2012 and spring 2014. The analysis includes mostly kinematic characteristics derived from coordinates and time measurements by applying different mathematical

operations. We concentrate mostly on engineering applications, and large scale ice cover dynamics is beyond the scope of the study. Deformation characteristics, drift correlations between the trackers and wind/ocean currents are not presented.

The paper is organized as follows: Section 2 gives a brief overview of environmental conditions at the drift area and describes the equipment. Sections 3 and 4 present drift patterns and drift velocities for ice floes and icebergs that were free drifting, landfast or grounded. The relative drift of icebergs and adjacent ice floes is presented in Section 5. The next section analyses drift spectra and recommends that special care should be taken when measuring frequencies higher than one cycle per hour (cph) using GPS. A new approach for measuring iceberg rotation during drift is presented, and the rotation model is proposed in Section 7. The final section provides some conclusions and suggestions for future studies.

2. Setup

The East Greenland Shelf is well known for its heavy ice and iceberg conditions. First-year and multi-year ice together with ice ridges are discharged from the Arctic Basin southwards through
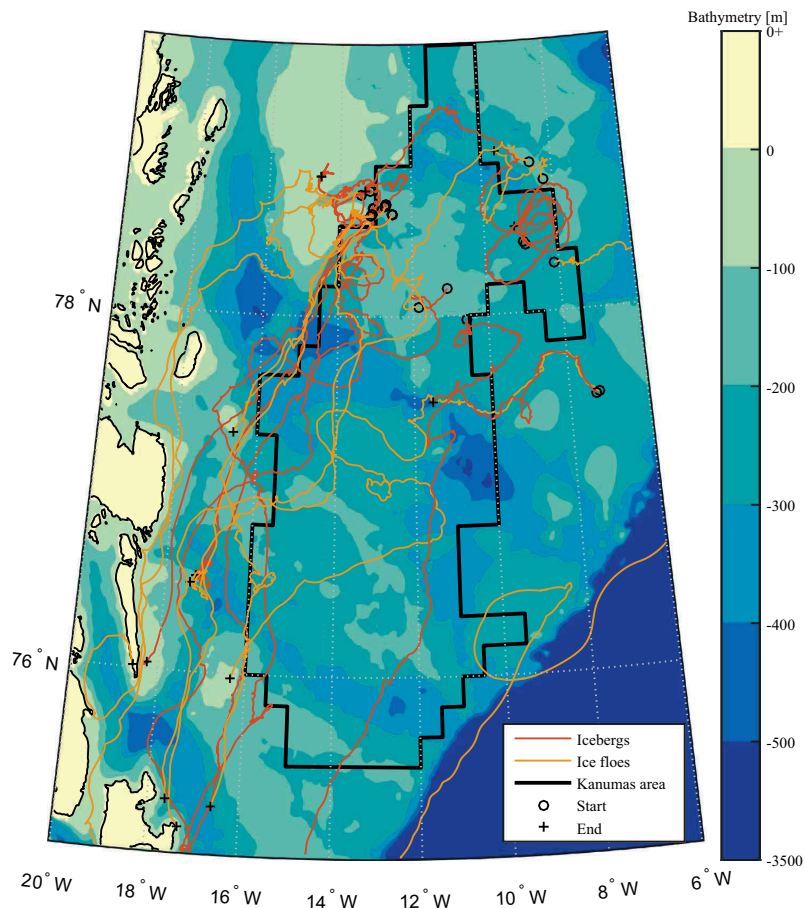

Fig. 1. Drift trajectories of 9 icebergs and 10 ice floes over the Greenland Shelf. A number of icebergs were grounded in the shallow areas of Belgica Bank and to the south-east of Store Koldewey.

the Fram Strait. The average annual ice thickness measured in 1998 by Upward Looking Sonars (ULS) was 2.54 m (Vinje et al., 1998); in 2011, the thickness was reduced to 2.00 m (Hansen et al., 2013). The amount of first-year ice in relation to multi-year ice shows an increasing trend (Comiso, 2011).

Northerly winds prevail in the area throughout the year, and they blow especially strong in winter. Strong katabatic wind blows into the sea; however, this wind appears only a short distance from the Greenland shoreline (Pedersen et al., 2011). Ocean currents on the shelf are presented by cold water masses moving from the Arctic with a relatively slow average velocity of approximately 0.1 m/s (Aagaard and Coachman, 1968). The average eastward and northward velocity projections obtained at 65–85 m depth from the moorings deployed at 78.5°N 8°W for the period between September 2003 and August 2009 were 4.1 cm/s and −6.6 cm/s, respectively (de Steur et al., 2014). The current speed increases with decreasing latitude. The average shelf depth is approximately 300 m, but it can be less than 100 m over some areas, such as at Belgica Bank or close to Store Koldewey (Fig. 1). Shallow water increases the possibility of grounded icebergs, and the ocean tides can be strongly amplified over the shallow areas.

The ice conditions in the offshore area of north-east Greenland varied substantially during the research cruises in both 2012 and 2013. The ice concentrations ranged from open water to l.0 (Fig. 2),

and the level ice thickness averaged 1.20 m as measured by drilling. Numerous ice ridges were found in the area, at up to 12.5 m of total thickness as measured by drilling. Ice floe sizes also varied, ranging from approximately a meter up to a few kilometres across. However, the mean floe size was larger in 2012 than in 2013. Additionally, the ice was warmer and therefore weaker in 2013. Larger floes, and thus less prone to deterioration, exceeding 100 metres in diameter were selected for the deployment of ice trackers.

Two types of trackers were deployed on ice floes and icebergs. The first type, produced by Oceanetic Measurements (2011) Ltd. (Spec1, 2015), had an operational frequency of 1/600 Hz. The time and GPS positions for six consecutive measurements were stored and sent as a package through the Iridium modem every hour. The accuracy of the GPS position was better than 5 m with 50% confidence and better than 8 m with 90% confidence, as stated by the manufacturer. The second type was produced by Canatec (Spec2, 2015) and obtained GPS position every 15 min. We denote the tracker's longitude and latitude as X and Y, respectively, in the text. The UTM system is used to express position in metres, x for the easting and y for the northing.

The operational frequency was chosen as high as possible to capture physical processes at all possible time scales. Three time scales has been known for drifting sea ice (Leppäranta et al., 2012):
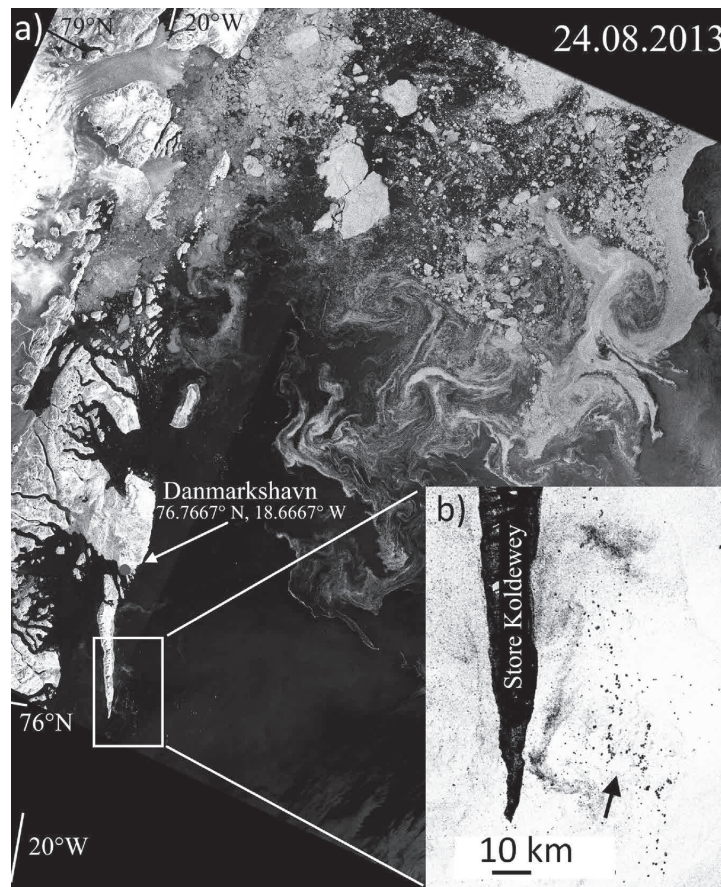

Fig. 2. Satellite image (RADARSAT-2) of the drift area. (a) The ice cover is completely fragmented after a warm summer in 2013; there are very few large ice floes. (b) Many icebergs to the south-east of Store Koldewey (set of black points) remain grounded throughout the season.

inertial ($\sim$30 min), pendulum day (12.3 h at 78°N) and deformation time scale ($\sim$10 days). For icebergs, the inertial time scale can be estimated similarly as

$$T_{IB} = \frac{M}{C_w \rho_w A_{keel} U_0} \tag{1}$$

where M is the mass of iceberg, C_w is the form drag coefficient, ρ_w is the density of water, A_{keel} is keel cross section area, and U_0 is the characteristic drift velocity. A 100 m long iceberg may have M~$0.27 \cdot 10^6$ tons and A_{keel}~$16100 m^2$ according to statistical data from Barker et al. (2004). Assuming the form drag coefficient to be in order of 0.5 and characteristic velocity U_0~0.1 m/s, the inertial time scale for an iceberg is less than 6 min. Therefore, the operational frequency was barely enough to resolve reaction of icebergs on the variations in the hydrodynamic forces. Inertial and pendulum day scales are very important for the engineering purposes, as they are in the range of the tactical time scales for iceberg management. Unfortunately, we have discovered that frequencies above 1 cycle per hour are hard to resolve using the GPS sensors we used. We used spectral analysis to demonstrate this problem in Section 6.

The inertial time scale for icebergs can be estimated in relation to the wind force by using the air density, characteristic wind speed (5 m/s) and sail cross section area in Eq. (1). The resulting characteristic response time exceeds 3 h. It shows that due to the form drag and large ratio of keel to sail cross section areas icebergs react much faster on changes in ocean currents rather than on changes in wind. This effect will be discussed further in Section 5 and in Appendix A.

The drifters were deployed by a helicopter, then activated and installed into predrilled holes in the ice. Some of the drifters were brought on ice from IB Oden while moored to ice floes during ice station work. In total, 23 ITDs were deployed during these two research cruises: 13 on icebergs and 10 on ice floes. Eight of the trackers deployed on icebergs were placed in pairs on the same iceberg to measure the rotation: one iceberg in 2012 and three icebergs in 2013. Four ITDs were initially placed on adjacent ice floes just a few hundred metres apart from the tracked icebergs. Thus, we were able to study the difference in drift between icebergs and ice floes. The trackers were placed in the approximate geometrical centre of ice floes or icebergs in case of one tracker, and on the different ends of icebergs in case of two trackers. The deployment dates, drift tracking period and dimensions of icebergs and ice floes are shown in Table 1, some of the icebergs are named for future reference. Most of the icebergs were tabular, except IB4, IB5 and the iceberg with Tracker #1. Their sail heights were estimated visually and very roughly as 5-10 m for tabular icebergs, 18 m for dome-shaped and wedge-shaped icebergs, and 23 m for the drydock-shaped IB5.

In addition to the visual observations the length was estimated as 1.5 relative distances between the trackers deployed in pairs on some of the icebergs. From Table 2 it is easy to see that the estimate is quite correct; it also provides the length estimate of IB2 that was not reported from observations.

Finally, in 2013 the Oceanetic trackers were equipped with inclination sensors; however, the measured evolution of the rolling angle of icebergs was difficult to interpret. Therefore, the rolling angle is not considered in the present study.

3. Trajectories

The trajectories of the trackers are shown in Fig. 1. The ocean depth is reproduced from the International Bathymetric Chart of the Arctic Ocean (Jakobsson et al., 2012). Red lines correspond to iceberg trajectories and orange lines correspond to ice floe trajectories. Most of the drift happened in the Kanumas area, which is believed to contain large hydrocarbon resources. The prevailing drift direction followed the East Greenland Current southwards, along the coast. The icebergs and the ice floes tend to approach the

Table 1
Information about the ITD's deployment and shape estimates.

Icebergs					
Tracker ID	Deployment date	Tracking duration, days	Length, m	Width, m	Remarks
117	21.09.2012	280	260	120	IB1
118	21.09.2012	269	260	120	IB1
120	21.09.2012	213	200	100	Reached 61.9 °N, 41.9 °W
121	21.09.2012	228	300	150	Initially grounded
127	24.08.2013	15	–	–	IB2, deteriorated in 15 days
128	28.08.2013	259	230	150	IB3
129	24.08.2013	264	–	–	IB2
130	28.08.2013	259	230	150	IB3
131	29.08.2013	259	125	60	IB4, wedged shape
132	29.08.2013	259	125	60	IB4, wedged shape
6550	18.09.2012	102	100	40	
1	30.08.2013	300	90	60	Domed shape
8	31.08.2013	17	60	50	IB5, drydocked shape
Ice floes					
Tracker ID	Deployment date	Tracking duration, days	Remarks		
119	21.09.2012	255	Adjacent to IB1		
2	25.08.2013	8			
3	28.08.2013	28	Adjacent to IB3		
4	25.08.2013	32			
5	29.08.2013	287	Adjacent to IB4		
6	31.08.2013	36	Adjacent to IB5		
9	30.08.2013	18			
4560	22.09.2012	41			
5390	23.09.2012	52			
8660	22.09.2012	158			

Table 2
Estimates of iceberg length based on observations and relative distance between the pairs of trackers deployed on the same icebergs.

ID	Observed length, m	Estimated length, m
IB1	260	260
IB2	–	390
IB3	230	308
IB4	125	119

coast despite the katabatic winds blowing away from the coast. Coriolis forcing could have deflected the drift to the west.

Approaching the coast, some of the icebergs were captured by ice that became landfast during the winter season. The landfast ice appeared in October through November and lasted until at least June of the following year. These icebergs and ice floes could not be tracked further because the trackers ran out of batteries. Short periods of sudden drift were measured between October and February for previously stationary trackers. The landfast ice experienced several breakups before it completely settled in February.

A few icebergs were grounded at shallow waters or trapped in the landfast ice. For example, one of the icebergs became landfast close to Store Koldewey and moved no further than 50 m from February to mid-June. Another iceberg became grounded to the south-east of Store Koldewey. Satellite images of the area taken at the end of August 2013 captured numerous icebergs in the area where the last signal of the iceberg was received (Fig. 2). Certain areas contain particularly large numbers of icebergs, such as the shallow waters to the east and south-east of Store Koldewey. Such icebergs remaining grounded for several consecutive seasons at the landfast zone are not affected by the summer ice breakup. Therefore, the grounding force for these icebergs might be higher than the ice strength, roughly estimated to be 100 MN using the pressure-area curve for 1.2 m thick sea ice and 100 m wide iceberg (Timco and Sudom, 2013).

Most of the ice floes deteriorated within a month of tracking. Three icebergs and one ice floe reached the 70th parallel, and one of the icebergs that drifted southernmost reached at least 61.9°N, 41.9°W, which is only 2.5° north of Cape Farewell, the southernmost point of Greenland. These observations support the idea that some of the icebergs in Baffin Bay originate from east Greenland glaciers (Hansen et al., 2004).

4. Velocities

The GPS positions of the trackers can be used to estimate velocity projections using the first derivatives of the x and y coordinates. Fourth order accuracy numerical approximation was used to calculate the velocity projections. For example, the eastwards component U_x was calculated as

$$U_x = \frac{-x_{i+2} + 8x_{i+1} - 8x_{i-1} + x_{i-2}}{12\tau} \tag{2}$$

where x_i is the easting coordinate at the i-th moment of time and τ is the time interval between two consecutive measurements. The northwards component U_y was calculated using a similar method. The velocity error can be estimated as a maximum possible error for the introduced approximation. Considering 8 m as the accuracy of the GPS-tracking, the average error is approximately $\frac{\sqrt{8}}{12} \cdot \frac{8\,[m]}{600\,[s]} \approx 0.3$ cm/s, and the largest possible error in the velocity estimate is $\frac{18}{12} \cdot \frac{8\,[m]}{600\,[s]} \approx 2$ cm/s. An example of velocity history (two weeks period) for the iceberg with Tracker #120 is shown in Fig. 3a. Periodic oscillations of the velocity projections were
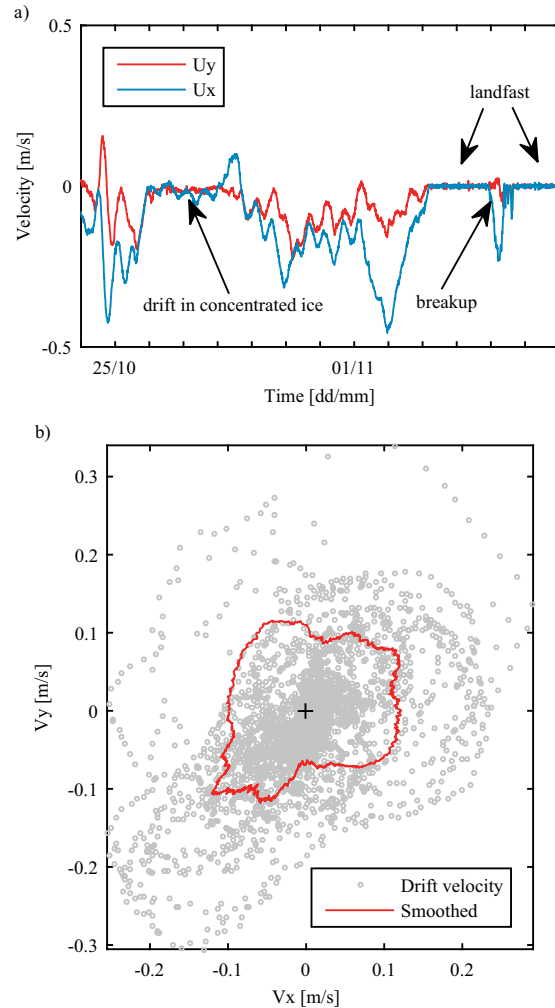

a)

b)

Fig. 3. (a) An example of velocity evolution for the iceberg with Tracker #120 during two weeks. The iceberg drifted in the shear zone, therefore its velocity was almost zero during certain periods. The iceberg became landfast in the beginning of November 2012 and was released in February 2013. (b) Velocity projections of the drift plotted against each other show the prevailing drift direction. Extreme velocity values were reached during strong wind periods. The smoothing has been performed by 100 point running average on velocity magnitude over all directions.

caused by tidal currents and the Coriolis (or inertial) effect. The velocity projections plotted in polar coordinates show that the main drift direction is along the coast and coincides with the mean current direction in the area.

The mean drift velocity, its standard deviation (SD) and the maximum velocity were calculated for each tracker. The mean velocity and its SD were found only for the period before the first grounding or landfast because intervals with zero velocity strongly affected the result. The only exception was the iceberg with Tracker #121; it was initially grounded and started to drift two weeks after the deployment. The interval between the initial grounding and the first landfast period was chosen to calculate the mean velocity. The information about the trackers is given in Table 3.

Table 3
Characteristic drift velocities.

Icebergs				
Tracker ID	Mean velocity, cm/s	SD, cm/s	Max. velocity, m/s	Remarks
117	7.6	9.4	0.47	IB1
118	7.6	9.3	0.47	IB1
120	10.6	9.6	1.63	
121	10.8	10.2	1.10	Initially grounded
127	18.7	8.3	0.43	IB2
128	14.8	8.2	0.54	IB3
129	19.6	9.3	0.51	IB2
130	14.8	8.0	0.54	IB3
131	18.6	14.4	0.91	IB4
132	18.6	14.4	0.93	IB4
6550	28.3	27.2	1.66	
1	25.4	20.0	1.04	
8	14.9	8.0	0.41	IB5

Ice floes				
Tracker ID	Mean velocity, cm/s	SD, cm/s	Max. velocity, m/s	Remarks
119	8.0	9.5	0.47	Adjacent to IB1
2	19.3	9.4	0.40	
3	26.5	22.2	1.12	Adjacent to IB3
4	31.7	22.1	1.21	
5	36.5	22.0	1.16	Adjacent to IB4
6	20.8	14.0	1.02	Adjacent to IB5
9	31.7	20.6	0.98	
4560	6.1	7.9	0.45	
5390	34.3	20.9	1.14	
8660	5.7	7.3	0.44	

The mean ice floe velocities, SDs and maximum velocities were generally higher than those of the icebergs. Different natures of the drag forces acting on icebergs and ice floes result in smaller accelerations of icebergs when the wind speed is changing (Appendix A). For example, during a storm, an iceberg takes longer to accelerate to a certain velocity than an ice floe. Therefore, the results show lower iceberg velocities, means, SDs and maxima compared to the ice floes. At the same time, the ice floes deteriorated over shorter time periods. The extremely high velocities of the icebergs with Trackers #6550 and #120 might be simply explained by longer period of observations. The highest drift speed of 1.66 m/s was reached by the iceberg with Tracker #6550 during strong winds blowing on 25.12.2012 at 66°N, 35°W.

The probability densities of the drift speed and drift direction for icebergs and ice floes are shown in Fig. 4. The density functions were calculated only for the first periods when icebergs and ice floes were drifting freely, without being captured in landfast ice or being grounded. The periods were in the range of 0.5–1.5 month long. Two groups of drifting objects can be distinguished on the drift speed distribution plots. The first group had very high probability density at drift speeds below 0.1 m/s. These were the icebergs and the ice floes that were drifting in highly concentrated ice, closer to the land. Their velocity was significantly reduced in the land proximity, but they were still moving with non-zero velocities. Such a drift speed reduction on a short distance to land or landfast ice is characteristic for the shear zone (Leppäranta, 2010).

The second group of objects had maximum probability density at approximately 0.2 m/s. This group consisted of icebergs and ice floes that drifted within the central pack or in the marginal ice zone (Leppäranta, 2010). Their mean velocities and SDs were higher than those of the first group. As expected, the ice floes from the second group had slightly higher probability densities at higher velocities than the icebergs.

The probability densities obtained for the two groups of icebergs and ice floes were approximated by the two-parameter Weibull distributions (Fig. 4a, b). The averaged Weibull scale and shape parameters were found to be (0.22, 1.64) for the icebergs and (0.31, 1.64) for the ice floes in the central pack and in the marginal zone. In the shear zone, the corresponding parameters were (0.09, 0.90) for the icebergs and (0.06, 0.76) for the ice floes. The obtained Weibull parameters can be used for the design of offshore structures and marine operation planning or as an input for numerical models involving sea ice (Kjerstad et al., 2015; Yulmetov et al., 2016).

The distribution of the drift direction had two clear maxima: a large peak corresponding to a south-west drift and one minor peak corresponding to the north-east (Fig. 4c and d). The drift velocity components shown in Fig. 3b confirm the obtained probability densities. The same two groups related to the drift in different zones can also be distinguished on the direction distribution plots. The group drifting in the vicinity of the coast had larger peaks at the south-western direction due to clockwise tidal currents that pushed sea ice towards the land before turning to the north-east. In the opposite direction, the ice diverged just before the tidal current took it to the south-west. The central pack or marginal ice was not affected by the coast; therefore, this ice drifted south-west according to the mean current flow, but its drift was not constrained. Thus, the drift of icebergs and ice floes in the shear zone is slow but has a distinct direction to the south-west. The drift in the central pack and marginal zone is characterized by higher drift speeds but more scattered drift directions. Worth noting, the borders between the shear zone and central pack are quite conditional, and they are hard to find precisely using the present array of trackers.

5. Relative drift of sea ice and icebergs

Drift of an iceberg differs from the drift of sea ice floes. Ice floes moving relative to the iceberg produce additional resistance or acceleration, depending on the conditions. For ice concentrations above 0.15, the ice force acting on an iceberg can be approximated as additional drag-type resistance limited by the ultimate resistance of the ice (Lichey and Hellmer, 2001). The resulting resistance is low for ice concentrations below 0.9 and is grows very fast for high concentrations. However, this approach is only valid for giant icebergs for which the surrounding sea ice can be treated as a continuous viscoplastic material. Recent numerical models of icebergs in pack ice based on the discrete element method require measured relative drift to be validated (Yulmetov et al., 2016).

Four sets of trackers were deployed with two (one in case of IB5) on each iceberg and one tracker on an adjacent ice floe. The distances between all three trackers within one set were a few hundred metres (Fig. 5). Therefore, the ocean current and wind velocity were assumed to be the same for the iceberg and the ice floe. Because the trackers on the iceberg were deployed approximately at the same distance from the different ends, the centre of the iceberg is roughly in the middle of the two trackers. The distance between the centre of the iceberg and the ice floe can be calculated along with the relative drift velocity.

The relative distance evolution is shown in Fig. 6 together with ice concentration and wind speed obtained from ERA-Interim reanalysis data (Dee et al., 2011). The ocean current profiles are lacking, therefore the analysis is limited by the ice concentration and wind data. All four sets demonstrated different behaviour. For the first set (IB1), the relative distance remained below 10 km during the entire 2012–2013 season including the time when the ice floe and iceberg were landfast. For the three sets (IB3, IB4 and IB5) that were drifting in 2013–2014, the relative distance increased much faster.
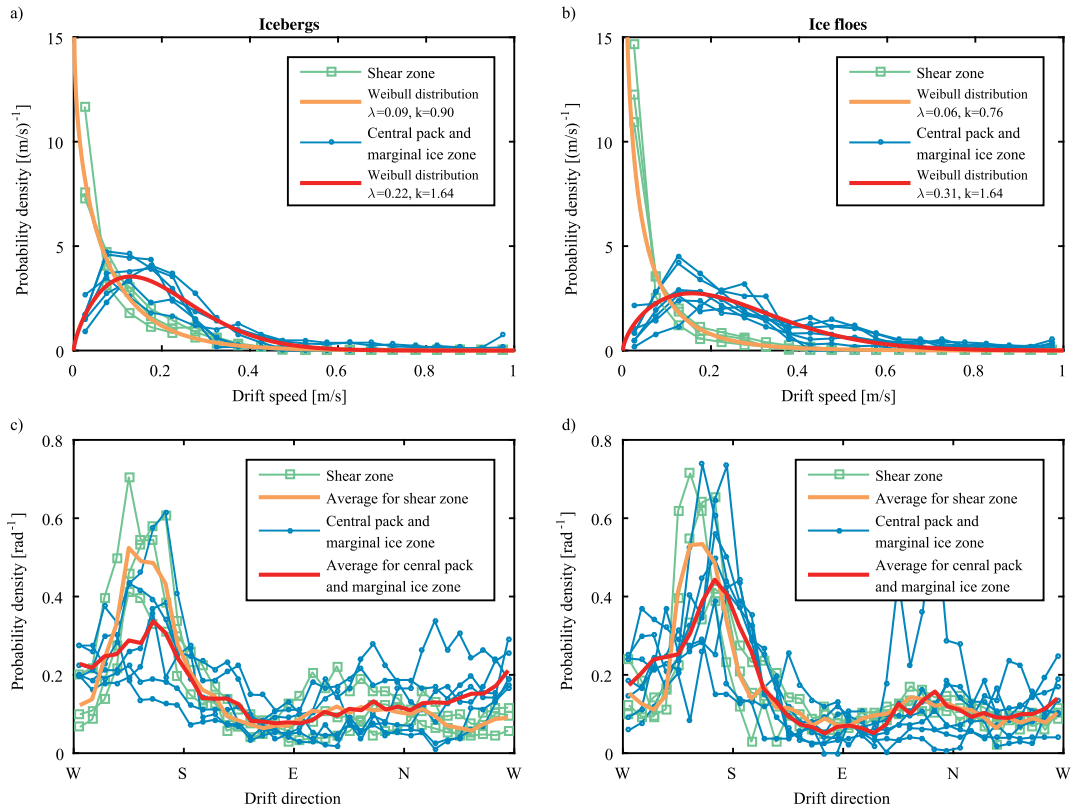
Fig. 4. Probability densities of the drift speed (a, b) and drift direction (c, d) for icebergs and ice floes. Two groups of drifting objects can be distinguished depending on the drift conditions. The first group drifted slower, but it drifted distinctly to the south-west, along the coast. The second group drifted significantly faster, but its drift direction was more scattered.
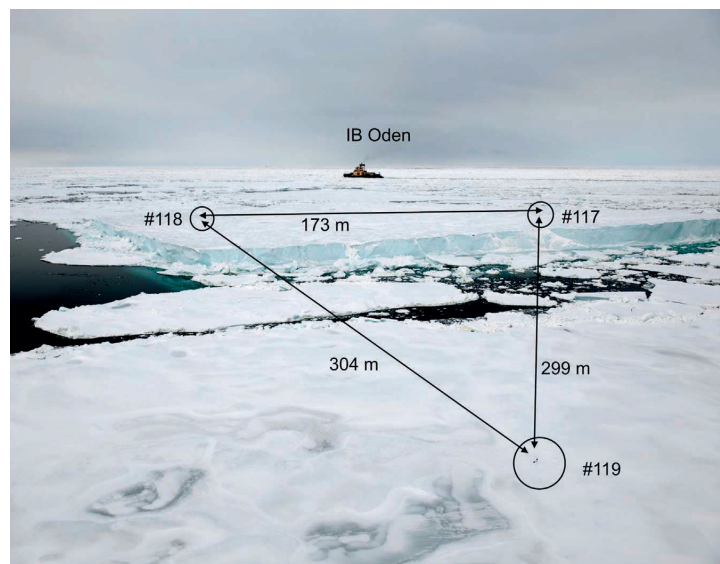

Fig. 5. Set of trackers deployed to measure rotation and relative drift. The iceberg (IB1) is tabular and approximately 250 m long.
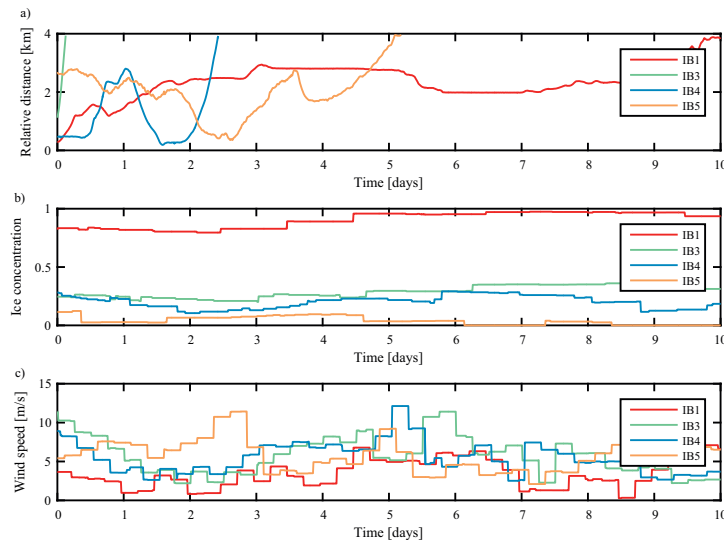
Fig. 6. (a) Evolution of the relative distance between icebergs and adjacent ice floes; (b) ice concentration in the vicinity of icebergs; (c) wind speed in the vicinity of icebergs. For the iceberg drifting together with highly concentrated ice, the relative distance remained small during the season. For the icebergs drifting in less concentrated ice, the adjacent floes diverged quicker. The fastest relative drift was demonstrated by IB3, in strong wind and ice concentration below 0.3.

Table 4
Characteristics of the relative drift of icebergs and adjacent ice floes.

ID	Initial relative distance, m	Mean relative velocity, cm/s	Mean ice concentration	Mean wind speed, m/s
IB1	289	0.24	0.91	3.7
IB3	1120	27.12	0.25	10.4
IB4	457	2.09	0.18	4.7
IB5	2680	0.29	0.06	6.6

The initial distance between the icebergs and corresponding ice floes is compared to the estimated relative drift speed, mean ice concentration and mean wind speed in Table 4. The comparison and averaging was made for distances shorter than 4 km to assess the drift of icebergs and ice floes in almost similar conditions. It can be seen from Fig. 6 and Table 4 that relative drift in high concentrations is very slow. For lower ice concentrations the wind speed controls the relative drift. So, the set with IB3 drifted as two independent objects governed by different wind and ocean drag forces. The relative velocity for this set is in order of a drift speed of the ice floe itself, and the mean wind speed is the highest among all the sets.

We have now demonstrated two important factors affecting relative drift of ice and icebergs: ice concentration and wind speed. First, highly concentrated ice is more difficult to deform; therefore, the group of trackers remained close through the season. Conversely, the trackers drifting in the weak ice among smaller ice floes diverged severely in 2013. The observed concentration effect is in qualitative agreement with the study carried out by Lichey and Hellmer (2001). Second, wind produces different accelerations on icebergs and ice floes (Appendix A). The drag forces acting on icebergs are determined mostly by the form drag, which is proportional to the vertical cross section areas of keel and sail. Therefore, the ratio between ocean and wind drag accelerations for icebergs depends on the ratio between the keel and sail cross section areas. Conversely, ice floes drift under skin friction drag, which is not dependent on the keel and sail profiles but

depends only on the horizontal surface area of ice floes, which is the same for water and wind drag forces. Therefore, the ratio between ocean and wind drag accelerations is different for ice floes and icebergs.

The obtained relative drift velocities are on the order of centimetres per second in moderate wind, however, for IB3 drifting in high wind the relative drift velocity was on the order of 30 cm/s. Conservative scenarios are likely to be used for full-scale towing of icebergs in ice, thus, strong wind conditions will be avoided and relative drift velocities of few centimetres per second are expected. Despite there were only four sets of drifting objects available, the obtained characteristic velocities might also be used to simulate ice management in broken ice.

6. Drift spectra

Periodic processes during the drift can be studied using Fourier analysis. For example, given a signal a_n consisting of N measurements, a Fourier transform can be applied

$$A_k = \sum_{n=0}^{N-1} a_n \exp\left(-i2\pi k\frac{n}{N}\right) \tag{3}$$

The values of A_k form an amplitude spectrum of signal a_n. For a complex a_n, the spectrum becomes two sided, with different amplitudes for the negative and positive frequencies. Spectral analysis of the drift velocity can be used to estimate the frequency response of drift forces, primarily Coriolis forces and tidal forces.

Drift velocity can be represented in the complex form as $U = U_x + iU_y$; after applying the Fourier transform, the result can be decomposed to clockwise (CW) and counterclockwise (CCW) components. The negative frequencies are responsible for clockwise motion, and positive for the opposite. The clockwise component always appears at the inertial frequency in the Northern hemisphere; therefore, the amplitude of the CW component must be higher than that of the CCW component. Comparing the circular components at the semidiurnal frequencies will show the roles of tidal and inertial drift.
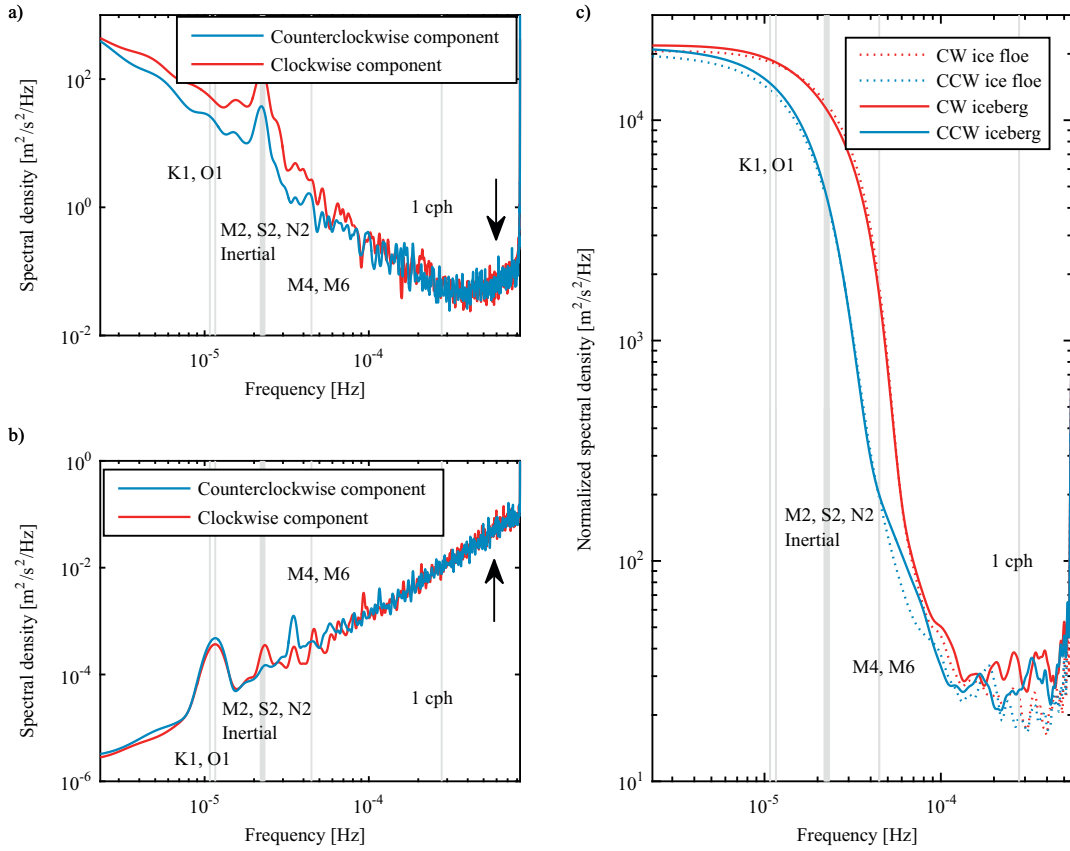
Fig. 7. Density spectrum of IB1, (a) free drifting for 42 days; (b) landfast for 102 days. Almost linear spectral density corresponds to the GPS error spectra. Normalized density spectra for IB5 and ice floe with Tracker #6 drifting in the same area for almost 17 days reveal higher densities for the iceberg at frequencies close to 1 cph.

Improved methods of spectral density estimation can be used to reduce noise in the spectrum. Welch's method was used to estimate the spectral density by analogy with Leppäranta et al. (2012). The dataset was split into 5-day long segments containing 720 points, and the segments were 75% overlapping. Additional corrections were made to the spectra because the velocity vector was obtained by numerical differentiation, which significantly reduces the high-frequency components. The correction factor α_k was calculated for the finite difference scheme (2) by substituting (3) written for the coordinates and using the Fourier transform for the derivative. Thus, every k-th component of the spectral density was multiplied by

$$\alpha_k = \left[\frac{12\pi k\tau}{\sin(4\pi k\tau) - 8\sin(2\pi k\tau)} \right]^2 \tag{4}$$

The spectrum for free drifting periods of IB1 is shown in Fig. 7a; the spectrum of the same iceberg when it was captured by landfast ice is shown in Fig. 7b.

The spectra obtained for the free drifting icebergs and ice floes are similar to those measured for sea ice in the Baltic Sea and the Sea of Okhotsk (Leppäranta et al., 2012). The spectral density has clear peaks on the semidiurnal frequencies and less visible peaks on higher frequency tidal components such as M4 and M6 (Fig. 7a). The inertial frequency in the drift area at 78.5°N is estimated as

Table 5
Tidal constituents and their periods.

Constituent	Period, h
Inertial at 78.5°N	12.31
M2	12.42
S2	12
N2	12.66
K1	23.93
O1	25.82
M4	6.21
M6	4.14

$$f = 2\Omega_{Earth} \sin \phi = 0.5131 [\text{day}^{-1}] \tag{5}$$

where Ω_{Earth} is the angular velocity of the Earth and ϕ is the latitude. Distinguishing between inertial and tidal oscillations is difficult because the inertial frequency is close to the semidiurnal tidal frequencies (Table 5).

Then, for the frequencies above semidiurnal, the spectral density follows a $-5/3$ power law that represents turbulent atmospheric and ocean forcing. The transition between continuous behaviour of ice that is driven by ocean and wind forces and granular collision-driven behaviour occurs at certain higher frequencies.
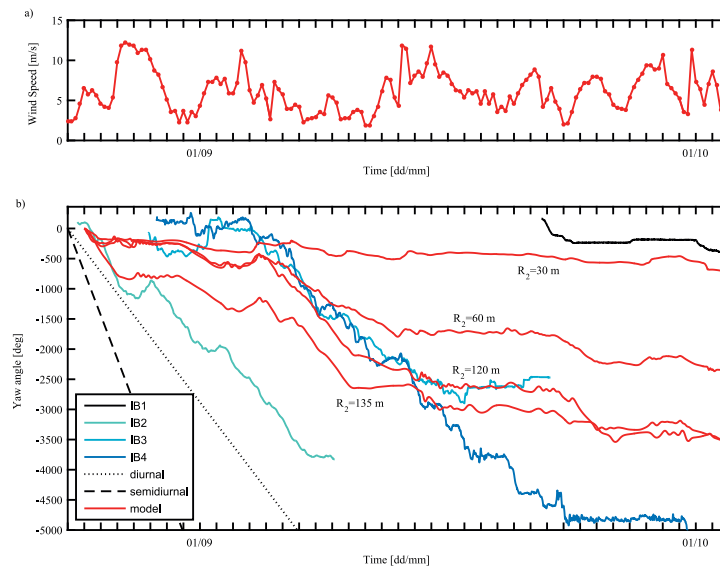
Fig. 8. (a) Wind speed obtained from ERA-Interim reanalysis; (b) Evolution of the yaw angle of icebergs. Blue lines: icebergs in 2013; black line: iceberg in 2012 plotted for the same dates in 2013; red line: modelling results; dashed and dotted lines: constant semidiurnal and diurnal angular velocities. The modelling results are presented for fixed $R_1 = 150$ m and various R_2. (For interpretation of the references to color in this figure legend, the reader is referred to the web version of this article.)

High spectral densities at the frequencies above 1 cph have been obtained by Leppäranta et al. (2012) and hold particular interest. Leppäranta et al. (2012) has suggested that three possible mechanisms might be responsible for such spectral features, e.g., non-linear ice-water interfacial stress, mechanical interaction between ice floes, or shallow water waves. Additionally, similar spectral features were found in ocean current spectra, as measured by buoy-mounted ADCP (Seim and Edwards, 2007). We compared the velocity spectrum of an iceberg (IB1) for the free drifting period to the velocity spectrum for the period when the iceberg was stationary. Spectral density during the latter period follows the power-law $\sim \nu^2$, where ν is frequency, meaning that the coordinate oscillations are basically the white noise. For the stationary iceberg, the measured coordinates oscillate mainly due to the GPS errors. Therefore, we may conclude that the high-frequency components in spectra of free drifting objects (Fig. 7a) are dominated by the "tail" of the GPS error spectra.

Therefore, this result established the requirement for the tracking equipment necessary to resolve the frequencies from 1 cph and higher: either GPS accuracy must be higher or GPS with an accelerometer correcting position estimate must be used. The DGPS could be a solution in areas where the base stations are located in the vicinity.

Spectral densities estimated by Welch's method with 5-days long segments did not reveal any significant difference in the low-frequency part for icebergs and ice floes. We used shorter segmentation to improve high frequency accuracy by sacrificing low-frequency part of the density spectra. Spectral densities compared for IB5 and ice floe with Tracker #6 show that the iceberg experienced stronger oscillations at the frequencies close to 1 cph (Fig. 7c). Comparing response time for changes in ocean currents for ice and icebergs from Section 2, and based on different drag-induced accelerations (Appendix A) it is possible to explain higher densities for the iceberg. It adjusted faster to the changing ocean currents and, therefore, oscillated with higher amplitude.

7. Rotation

7.1. Measured data

Short-term rotation of icebergs is of particular interest to the offshore industry as it affects the safety of towing operations. Unstable icebergs may cause not only the failure of the towing attempt, losing precious time, but can also damage a tug boat. The rolling stability of an iceberg can be estimated based on knowledge about its shape. The Weeks and Mellor stability criterion can assess rolling stability (Weeks and Mellor, 1978). This criterion is based on estimating the relative position of the gravitational centre and the buoyancy centre of an iceberg. In addition, the rotational stability over the vertical axis must be considered because nonzero angular momentum may significantly increase tension in the tow line. Including iceberg rotation in the drift models will result in additional terms for the drift equations, potentially increasing the forecast accuracy.

We measured the rotation around the vertical axis during free drift and estimated the angular velocity using two trackers on the same iceberg. To determine the angle of rotation, we constructed a radius vector between the two trackers on the iceberg. The angle between the radius vector and direction to the east measured CCW determines the yaw angle of the iceberg. The angular velocity of the iceberg was calculated as the first derivative of the measured yaw angle. The rotation of four icebergs was measured: one in 2012 and three in 2013. In 2013 the icebergs were drifting in different locations and were therefore subjected to different environmental forces yet showed similar behaviour.

In addition to the rotation measurement, we used the pairs of trackers to indicate GPS errors and estimate iceberg size. Because both of the trackers were fixed on the same body, the distance between them was constant. Therefore, large GPS errors were possible to detect as outliers by looking at the relative distance. When the relative distance changed significantly, those points were excluded from the analysis.

The yaw angle evolution is presented in Fig. 8b. The measured rotation angles of the three icebergs tracked in 2013 are drawn using blue solid lines. The rotation of the iceberg tracked in 2012 is shown using black at the corresponding period as if it was drifting in 2013. In 2013 the icebergs rotated clockwise with approximately the same angular velocities. Two straight lines are drawn in Fig. 8b corresponding to rotation with constant diurnal and semidiurnal cycles. During some periods, the icebergs rotated with angular velocities very close to one or two full revolutions per 24 h. Rotating tidal currents and the Coriolis effect were assumed to cause the observed rotation. The evolution of the rotation angle for the iceberg drifting in 2012 is different because it was drifting in highly concentrated ice, and the rotation was therefore heavily dampened.

Furthermore, the instantaneous values of the angular velocity were very high, sometimes reaching 0.001 rad/s. This value is extreme and was reached only at a few peaks. An iceberg with similar angular velocity for at least one hour would make more than one full revolution. Nevertheless, the extreme values of angular velocities could be used for a possible worst-case scenario for towing operations.

7.2. Numerical model of the rotation

A body moving in an unbounded fluid adjusts its position to have its blunt side forward (Steklov, 1983). The same principle was suggested to govern the rotation of icebergs subjected to tides. The tidal current velocity vector rotates following the tidal constituents; then, the icebergs should adjust their position accordingly. We attempted to reproduce the rotation numerically.

In general, the motion of a solid in an ideal liquid can be described using the approach initially proposed by Kirchhoff (1869). The planar motion of a cylinder with a symmetrical horizontal cross section in an unbounded fluid resting at infinity has been considered by Lamb (1975). This approach has been adopted to describe the drift of an iceberg in a nonstationary current by Marchenko (2014). The equations of motion are projected on a comoving system (ξ, η) corresponding to the principle axes of the cylinder at every moment in time; simultaneously, the fluid velocity at infinity must be equal to zero (Fig. 9). Thus, the system moves with the liquid velocity, and u, v are the projections of the cylinder's relative velocity $\mathbf{u}$ on the principle axes. The matrix of

rotation $\mathbf{T}$ between the global orthogonal system and the comoving system can be expressed as

$$\mathbf{T} = \begin{vmatrix} \cos\ \varphi & \sin\ \varphi \\ -\ \sin\ \varphi & \cos\ \varphi \end{vmatrix} \tag{6}$$

where φ is the angle of rotation of the cylinder. In the comoving system, the equations of motion are formulated as follows:

$$\begin{cases} \dot{u} = \dfrac{a_{22}}{a_{11}}\omega v + \dfrac{F_\xi}{a_{11}} \\[2mm] \dot{v} = -\dfrac{a_{11}}{a_{22}}\omega u + \dfrac{F_\eta}{a_{22}} \\[2mm] \dot{\omega} = \dfrac{a_{11} - a_{22}}{b}uv + \dfrac{M_w}{b} \end{cases} \tag{7}$$

where the coefficients a_{11}, a_{22} are the mass of the cylinder M plus the corresponding added mass, the coefficient b is the moment of inertia I plus the added moment of inertia, F_ξ, F_η are the projections of the external forces in the comoving system, the angular moment is dampened by M_w, and ω is the angular velocity of the cylinder.

The presented equations can be applied to the drifting iceberg to find its drift and rotation. The water and air drag forces $\mathbf{F}_w$, $\mathbf{F}_a$, respectively, together with the Coriolis force $\mathbf{F}_C$ can be substituted as external forces into the equation of motion, producing a simple open water drift model capable of capturing rotation. The model does not include the sea ice force, which is difficult to estimate, but qualitatively reproduces the rotation.

The simplified iceberg shape is assumed to be elliptical at the horizontal cross section (Fig. 9). Therefore,

$$a_{11} = \rho_i H\pi R_1^2 + M$$
$$a_{22} = \rho_i H\pi R_2^2 + M$$
$$b = \rho_i H\pi (R_1^2 - R_2^2)^2/8 + I \tag{8}$$

where ρ_i is the density of ice, H is the total height of the iceberg, and R_1, R_2 are the ellipse radii, and $R_1 > R_2$. The conventional approximations of the drag forces are used (Savage, 2001). In the comoving frame, the external forces can be expressed as
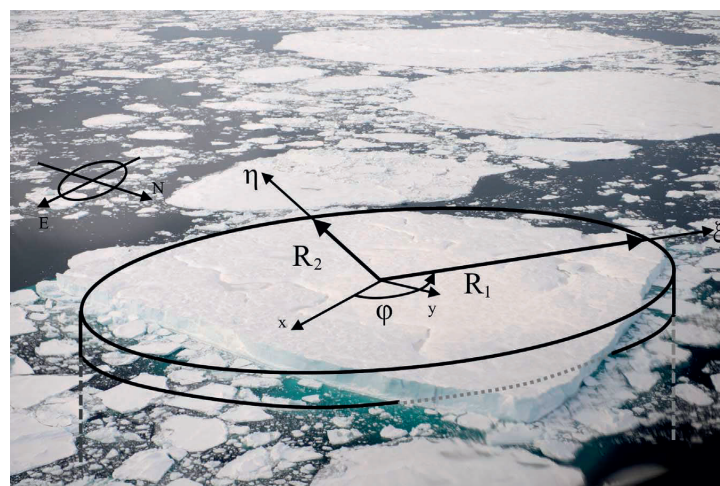

Fig. 9. Iceberg IB1 is approximated with an elliptical cylinder. The comoving system (ξ, η) corresponds to the principle axes of the cylinder.

Table 6
Simulation parameters and their values.

Parameter	Notation	Value	Unit
Major radius	R_1	150	m
Minor radius	R_2	30–135	m
Iceberg height	H	50	m
Water density	ρ_w	1000	kg/m^3
Ice density	ρ_i	920	kg/m^3
Air density	ρ_a	1.3	kg/m^3
Water drag coefficient	C_w	0.6	
Air drag coefficient	C_a	0.3	
Coriolis frequency	f	$1.43 \cdot 10^{-4}$	s^{-1}

$$\mathbf{F}_w = -\frac{1}{2}C_w \rho_w A_w^v |\mathbf{u}|\mathbf{u}$$

$$\mathbf{F}_a = \frac{1}{2}C_a \rho_a A_a^v \left|\mathbf{V}_a^{rel}\right|\mathbf{V}_a^{rel}$$

$$\mathbf{V}_a^{rel} = \mathbf{T}(\mathbf{V}_a - \mathbf{V}_w - \mathbf{Tu})$$

$$\mathbf{F}_C = -Mf\mathbf{k} \times \mathbf{u} \tag{9}$$

where C_w, C_a are the water and air drag coefficients, ρ_w, ρ_a are the water and air densities, $\mathbf{V}_w$, $\mathbf{V}_a$ are the absolute water and air velocities that inputs for the model, $\mathbf{V}_a^{rel}$ is the relative air velocity projected on the principle axes of the cylinder, $\mathbf{k}$ is the sea surface normal directed upwards, and $f = 2\Omega_{Earth} \sin \phi$ is the Coriolis frequency. The parameters of the simulation are given in Table 6. The values for the drag coefficients were selected through trial-and-error to maximize similarities between the observed and measured yaw angles. The chosen values $C_w = 0.6$, $C_a = 0.3$ are in the same range as the values used in the recent models by Hunke and Comeau (2011), and Turnbull et al. (2015).

The vertical cross section areas A_w^v, A_a^v of the iceberg's keel and sail depend on the corresponding fluid velocity as follows:

$$A_w^v = 2H\frac{\rho_i}{\rho_w}\frac{\sqrt{R_1^2 v^2 + R_2^2 u^2}}{|\mathbf{u}|}$$

$$A_a^v = 2H\left(1 - \frac{\rho_i}{\rho_w}\right)\frac{\sqrt{R_1^2(\mathbf{V}_{a,\eta}^{rel})^2 + R_2^2(\mathbf{V}_{a,\xi}^{rel})^2}}{\left|\mathbf{V}_a^{rel}\right|} \tag{10}$$

Finally, the rotation of the iceberg is dampened according to the quadratic law

$$M_\omega = -\frac{1}{4}\rho_i H(R_1^4 - R_2^4)|\omega|\omega \tag{11}$$

Ocean and wind data for the equations were extracted from the large-scale models. AOTIM5 (Padman and Erofeeva, 2004) was used to obtain tidal constituents. Eight tidal constituents (M2, S2, N2, K2, K1, O1, P1, Q1) were used in the model, among which the M2 prevailed. ERA-Interim reanalysis data (Dee et al., 2011) were used to obtain wind speed projections at 10 m above sea level. The wind velocity spatial resolution was 1° latitude and 1° longitude, and the temporal resolution was 6 h. The components of the wind velocity were recalculated for the average iceberg sail height using the 1/7-power approximation for the wind profile (Newman, 1977). Combining (6)–(11), the system can be solved to find the velocity relative to the water $\mathbf{u}$ and the yaw angle φ. The system was solved numerically using MATLAB's ode45 function.

7.3. Analysis of numerical results

The iceberg drift model taking into account rotation in the horizontal plane was presented. The equations describing motion of a solid body through an unbounded fluid were applied to iceberg drift under water and wind drag forces and the Coriolis force. The equations were solved numerically to find the yaw angle of a cylindrical iceberg.

In reality iceberg shapes deviate from the cylindrical shape, but it does not affect much numerical results. First, the drag forces acting on icebergs are proportional to the vertical cross section areas of sail and keel. So, when the air and water drag coefficients are chosen manually to produce the best result, the cross section areas are adjusted simultaneously. To be more precise one may use statistical relations between icebergs' geometrical parameters (Barker et al., 2004), but it will only result in different values for the drag coefficients. Second, the deviation from the ellipse in the horizontal cross section at the waterline does not strongly affect the performance of the model, because the ratio of the difference between the added masses to the sum of moment of inertia and added moment of inertia is approximately the same for different shapes.

We have compared the ratio for elliptical and rectangular cylinders of different semi-axes or side ratios. For the ellipse the ratio was possible to express analytically, for the rectangle it was calculated using added mass and added inertia coefficients from Veritas (2010). It is easy to see from Fig. 10a that the ratio behaves similarly for different shapes at the waterline, and, therefore, does not significantly change the solution of (7). Simulated rotation of an iceberg having elliptical horizontal cross-section with semi-axes $R_1 = 150$m and $R_2 = 120$m is compared with the rotation of an iceberg having rectangular cross-section of similar side ratio in Fig. 10b. As expected, no major differences were found. Thus, approximating iceberg shape with an elliptical cylinder does not significantly affect the results of the modelling.

Removing the rotational terms from the equations would result in well-known drift equations such as, for example, those in Bigg et al. (1997). The same effect can be reached assuming the cylinder to be perfectly round in the horizontal cross section by letting $a_{11} = a_{22}$, and thus excluding the third equation in the system (7). However, the main purpose of the model was to explain and simulate the rotation, not to reproduce the original drift trajectories.

The results of the simulation are shown in Fig. 8b using a solid red line. A clear similarity is shown between the measured angle and the angle calculated using the model. In approximately one month, the theoretical iceberg managed to rotate approximately the same amount of cycles as the real icebergs. The yaw angle evolution contains several periods with almost no rotation and periods when rotation happened in almost semidiurnal cycles. The input wind data (Fig. 8a) show that during strong wind events, the model iceberg slowed its rotation. Therefore, when the wind drag significantly exceeded the water drag, the iceberg adjusted its position to follow the wind direction.

The model must include the wind force; without the wind force, the solution of the model would eventually converge to zero relative velocity $\mathbf{u}$ and zero angular velocity ω due to the water drag force returning the system to equilibrium. The wind force maintains nonzero velocity relatively to water, thus preventing the iceberg from drifting with the water without any rotation.

Despite the satisfactory agreement between the measured and calculated rotations, a perfect match is not achieved for several reasons. The sources of the discrepancy lie within the limitations of the model and inaccurate input data. First, the icebergs drifted in sea ice, and the ice force was omitted in the presented model. Second, the ocean currents were represented only by oscillating tidal currents that we believed were important for the rotation. Moreover, the wind data were not highly resolved either spatially or in time. Nevertheless, the modelling approach seems to be a promising step forward both in rotation modelling and in drift forecasting. The model should be carefully tested for open water drift when winds, ocean currents and waves are accurately
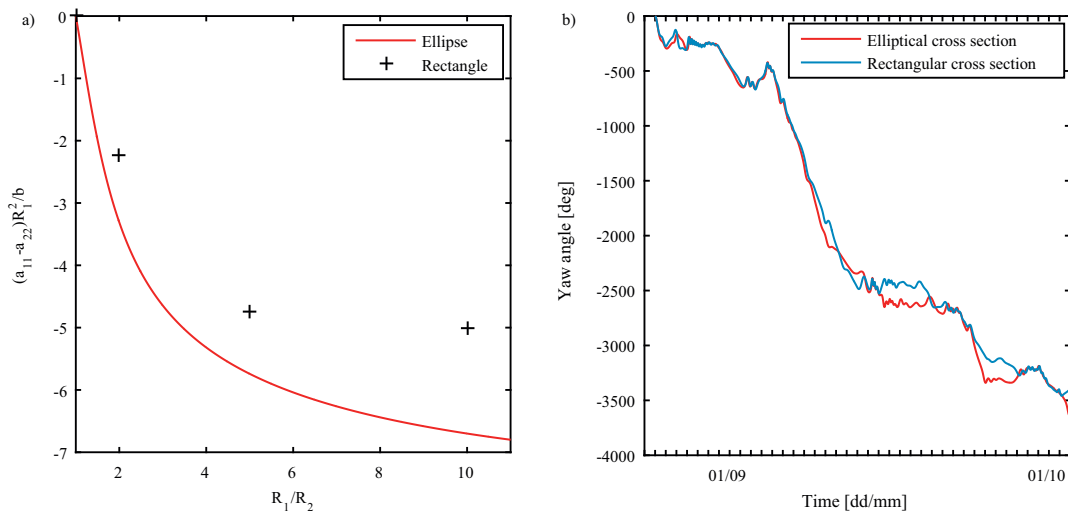
Fig. 10. (a) Dimensionless ratio of the added mass difference to the total inertia as a function of semi-axis ratio for ellipse and side ratio for rectangle. The behaviour of the solution will not be significantly affected, because there's no qualitative difference in the calculated ratio for different iceberg shapes. (b) Simulated rotation of elliptical and rectangular icebergs having semi-axes (half-length and half-width in case of rectangle) $R_1 = 150m$ and $R_2 = 120m$.

measured. After the model is verified, it can be of particular interest for simulating iceberg towing operations.

In addition, an iceberg rotating with a diurnal period may be subjected to asymmetrical melting. If an iceberg's yaw angle follows the sun, the solar radiation will act only from one side. The same can be applied to the forced convection assuming that the iceberg adjusts its angle to the rotating ocean current. Then, a significant amount of heat could be transferred to the iceberg from one side, leading to melting.

8. Conclusions

In this study, we presented and analysed the data obtained from 23 GPS ice trackers deployed on icebergs and ice floes drifting in the Greenland Sea during 2012–2014. High spatial and temporal resolution of the trackers drifting over the Greenland Shelf makes this dataset valuable both for oceanography and the petroleum industry. The analysis was limited mostly by kinematic characteristic and dynamic effects of wind, ocean currents and ice concentration were beyond the scope of the study.

The following conclusions and achievements can be stated:

- Ice and icebergs drifting south off the north-east Greenland tend to drift towards the coast due to the Coriolis force. This force brings them into the landfast ice zone where they may be interlocked for the entire winter. The ice fastening starts in October and undergoes several breakups before the coastal ice is completely set in February.
- Characteristic mean velocities are presented. The maximum drift speed reached by an iceberg was 1.66 m/s, which happened during strong southerly wind at 66 °N. However, several ice floes exceeded 1 m/s maximum drift speed yet drifted for much shorter periods. Ice floes are accelerated by wind faster than icebergs because ice floes are subjected to skin friction drag, while for icebergs, the form drag is the most important.
- Based on the drift speed and drift direction distributions, drift in the shear zone differs from the drift in the central pack and marginal zone. The drift speed follows a two-parameter Weibull distribution.

- Depending on ice conditions and wind, ice floes and icebergs may demonstrate different drift patterns, despite initially being just a few hundred metres apart. As expected, for an iceberg drifting in concentrated sea ice, the relative velocity was small. In the opposite case, the iceberg and adjacent ice floe drifted in different directions due to different accelerations produced by the drag forces. Relative velocities in moderate winds were on the order of a few centimetres per second, for stronger winds the relative velocity was 0.3 m/s.
- Spectral analysis did not reveal any strong differences between spectra of drifting ice floes and icebergs at low frequencies. The high-frequency components are slightly higher for the icebergs due to their shorter response time to the changing ocean currents. However, the GPS sensors were responsible for the high-frequency (> 1 cph) components in the spectra. Therefore, GPS data should be used with care when studying high-frequency processes in sea ice.
- The rotation of four icebergs was measured using paired trackers deployed on each end of the icebergs. To the authors' knowledge, this experiment has never been reported before. Surprisingly, the evolution of the icebergs' yaw angle revealed a trend that was close to semidiurnal rotation cycles. However, at a few moments, the angular velocity reached very high peaks of 0.001 rad/s. The measured rotation is of particular interest for the offshore industry.
- A model of iceberg drift including rotation terms was presented. This model was capable of reproducing the yaw angle evolution trend using tidal currents and wind data as input. Because the focus of the model was on rotation, the drift trajectory prediction was not our primary goal. Nevertheless, the approach seems to be promising for iceberg forecasting, and its potential should be investigated further.

Acknowledgements

Appendix A

There is a difference in the nature of the drag forces that dominate the drift of icebergs and large ice floes. This difference results in larger accelerations of ice floes caused by changing wind speed, and therefore larger variability in ice floe drift velocities compared to icebergs. In general, the drag force can be separated into the pressure drag caused by normal stresses acting on the body surface and the frictional drag due to tangential shear stresses (Newman, 1977). The pressure drag is more important for non-streamlined bodies such as icebergs. Conversely, large ice floes can be considered flat plates and are therefore governed by the frictional drag forces. Sudden strong wind can be shown to affect icebergs less than ice floes.

Assuming icebergs and ice floes are drifting under water and air drag forces, the accelerations can be expressed as

$$\frac{d\vec{U}^{IB}}{dt} = -\frac{1}{2}\frac{C_w^{IB}\rho_w A_w^v}{M^{IB}}\left|\vec{V}_{rel}^w\right|\vec{V}_{rel}^w - \frac{1}{2}\frac{C_a^{IB}\rho_a A_a^v}{M^{IB}}\left|\vec{V}_{rel}^a\right|\vec{V}_{rel}^a$$

$$\frac{d\vec{U}^{IF}}{dt} = -\frac{C_w^{IF}\rho_w A_w^h}{M^{IF}}\left|\vec{V}_{rel}^w\right|\vec{V}_{rel}^w - \frac{C_a^{IF}\rho_a A_a^h}{M^{IF}}\left|\vec{V}_{rel}^a\right|\vec{V}_{rel}^a \tag{A.1}$$

where $\vec{U}^{IB}$ and $\vec{U}^{IF}$ are the velocities of an iceberg and an ice floe, respectively, and M^{IB} and M^{IF} are their masses, respectively, $\vec{V}_{rel}^w$ and $\vec{V}_{rel}^a$ are the velocities relative to the ocean current and wind, and C_w^{IB}, C_a^{IB}, C_w^{IF}, C_a^{IF} are the form and surface drag coefficients acting on the iceberg and the ice floe. The form drag coefficients are usually on the order of 1, and the skin friction drag coefficients are on the order of 10^{-3}. A_w^v, A_a^v, A_w^h, A_a^h are the vertical cross sections of the keel and the sail of the iceberg and the horizontal surfaces of the ice floe. Finally, ρ_w, ρ_i, ρ_a are the densities of water, ice and air, respectively. The Coriolis force is neglected for simplicity because it does not change the absolute value of the drift velocity.

Then, assuming the iceberg to be a cylinder of radius R and ice floe thickness h, the equations of motion can be rewritten as

$$\frac{d\vec{U}^{IB}}{dt} = -\frac{C_w^{IB}}{\pi R}\left|\vec{V}_{rel}^w\right|\vec{V}_{rel}^w - \frac{C_a^{IB}}{\pi R}\frac{\rho_a}{\rho_i}\frac{\rho_w-\rho_i}{\rho_w}\left|\vec{V}_{rel}^a\right|\vec{V}_{rel}^a$$

$$\frac{d\vec{U}^{IF}}{dt} = -\frac{C_w^{IF}}{h}\frac{\rho_w}{\rho_i}\left|\vec{V}_{rel}^w\right|\vec{V}_{rel}^w - \frac{C_a^{IF}}{h}\frac{\rho_a}{\rho_i}\left|\vec{V}_{rel}^a\right|\vec{V}_{rel}^a \tag{A.2}$$

Now, the relative input from wind and water drag for icebergs and ice floes can be considered by comparing the corresponding accelerations. The acceleration ratio $\frac{a_w}{a_a}$ can be estimated assuming that the form drag coefficients are of the same order and that the friction drag coefficients are of the same order for water and air.

$$\left[\frac{a_w}{a_a}\right]^{IB} \approx \frac{\rho_i}{\rho_w-\rho_i}\frac{\rho_w}{\rho_a}\frac{\left|\vec{V}_{rel}^w\right|\vec{V}_{rel}^w}{\left|\vec{V}_{rel}^a\right|\vec{V}_{rel}^a}$$

$$\left[\frac{a_w}{a_a}\right]^{IF} \approx \frac{\rho_w}{\rho_a}\frac{\left|\vec{V}_{rel}^w\right|\vec{V}_{rel}^w}{\left|\vec{V}_{rel}^a\right|\vec{V}_{rel}^a} \tag{A.3}$$

The water to air drag acceleration ratio for icebergs is nine times higher than the ratio for the ice floes. Thus, when the form drag is dominant, the accelerations caused by the atmospheric forces are less important than when the friction drag governs the drift. Therefore, it is much harder to accelerate an iceberg than an ice floe in changing wind conditions.

References

Aagaard, K., Coachman, L.K., 1968. The East Greenland Current North of Denmark Strait: Part I. Arctic 21 (4), 267–290.

Barker, A., Sayed, M., Carrieres, T., 2004. Determination of Iceberg draft, mass and cross-sectional areas. In: Proceedings of the 14th International Offshore and Polar Engineering Conference, Toulon, France, 899–904.

Bigg, G.R., Wadley, M.R., Stevens, D.P., Johnson, J.A., 1997. Modelling the dynamics and thermodynamics of icebergs. Cold Reg. Sci. Technol. 26 (2), 113–135.

Comiso, J.C., 2011. Large decadal decline of the Arctic multiyear ice cover. J. Clim. 25 (4), 1176–1193.

de Steur, L., Hansen, E., Mauritzen, C., Beszczynska-Möller, A., Fahrbach, E., 2014. Impact of recirculation on the East Greenland Current in Fram Strait: results from moored current meter measurements between 1997 and 2009. Deep Sea Res. Part I: Ocean. Res. Pap. 92, 26–40.

Dee, D.P., Uppala, S.M., Simmons, A.J., Berrisford, P., Poli, P., Kobayashi, S., Andrae, U., Balmaseda, M.A., Balsamo, G., Bauer, P., Bechtold, P., Beljaars, A.C.M., van de Berg, L., Bidlot, J., Bormann, N., Delsol, C., Dragani, R., Fuentes, M., Geer, A.J., Haimberger, L., Healy, S.B., Hersbach, H., Holm, E.V., Isaksen, L., Kallberg, P., Kohler, M., Matricardi, M., McNally, A.P., Monge-Sanz, B.M., Morcrette, J.J., Park, B.K., Peubey, C., de Rosnay, P., Tavolato, C., Thepaut, J.N., Vitart, F., 2011. The ERA-Interim reanalysis: configuration and performance of the data assimilation system. Q. J. R. Meteorol. Soc. 137 (656), 553–597.

Eik, K., 2008. Review of experiences within ice and iceberg management. J. Navig. 61 (4), 557–572.

Hansen, E., Gerland, S., Granskog, M.A., Pavlova, O., Renner, A.H.H., Haapala, J., Løyning, T.B., Tschudi, M., 2013. Thinning of Arctic sea ice observed in Fram Strait: 1990–2011. J. Geophys. Res.: Ocean. 118 (10), 5202–5221.

Hansen, K.Q., Buch, E., Gregersen, U., 2004. Weather, Sea and Ice Conditions Offshore West Greenland. Danish Meteorological Institute, Copenhagen.

Hunke, E.C., Comeau, D., 2011. Sea ice and iceberg dynamic interaction. J. Geophys. Res.-Ocean. 116, C05008.

Jakobsson, M., Mayer, L., Coakley, B., Dowdeswell, J.A., Forbes, S., Fridman, B., Hodnesdal, H., Noormets, R., Pedersen, R., Rebesco, M., Schenke, H.W., Zarayskaya, Y., Accettella, D., Armstrong, A., Anderson, R.M., Bienhoff, P., Camerlenghi, A., Church, I., Edwards, M., Gardner, J.V., Hall, J.K., Hell, B., Hestvik, O., Kristoffersen, Y., Marcussen, C., Mohammad, R., Mosher, D., Nghiem, S.V., Pedrosa, M.T., Travaglini, P.G., Weatherall, P., 2012. The International Bathymetric Chart of the Arctic Ocean (IBCAO) Version 3.0. Geophys. Res. Lett. 39, L12609.

Kirchhoff, G., 1869. Ueber die Bewegung eines Rotationskörpers in einer Flüssigkeit. J. Angew. Math. 71, 237–262.

Kjerstad, Ø.K., Metrikin, I., Løset, S., Skjetne, R., 2015. Experimental and phenomenological investigation of dynamic positioning in managed ice. Cold Reg. Sci. Technol. 111, 67–79.

Lamb, H., 1975. Hydrodynamics, sixth edition. Cambridge University Press.

Larsen, P.-H., Overgaard Hansen, M., Buus-Hinkler, J., Harnvig Krane, K., Sønderskov, C., 2015. Field tracking (GPS) of ten icebergs in eastern Baffin Bay, offshore Upernavik, northwest Greenland. J. Glaciol. 61 (227), 421–437.

Leppäranta, M., 2010. The Drift of Sea Ice. Springer.

Leppäranta, M., Oikkonen, A., Shirasawa, K., Fukamachi, Y., 2012. A treatise on frequency spectrum of drift ice velocity. Cold Reg. Sci. Technol. 76–77, 83–91.

Lichey, C., Hellmer, H.H., 2001. Modeling Giant-Iceberg Drift Under the Influence of Sea Ice in the Weddell Sea, Antarctica. J. Glaciol. 47 (158), 452–460.

Lubbad, R., Raaij, Ev, Sveinung, L., Eik, K.J., 2013. Oden Arctic Technology Research Cruise 2012. Port and Ocean Engineering under Arctic Conditions, Espoo, Finland.

Marchenko, A., 2014. Influence of added mass effect on rotation of a drifting iceberg in non-stationary current. In: Proceedings of the ASME 2014 33rd International Conference on Ocean, Offshore and Arctic Engineering, OMAE2014, San Francisco, CA, USA.

Newman, J.N., 1977. Marine Hydrodynamics. The MIT Press, Cambridge, MA.

Padman, L., Erofeeva, S., 2004. A barotropic inverse tidal model for the Arctic Ocean. Geophys. Res. Lett. 31 (2).

Pedersen, L.T., Tonboe, R.T., Jensen, M.B., Dybkjær, G., Nissen, M., Rasmussen, J., Olsen, S.M., Skourup, H., Saldo, R., Forsberg, R., 2011. KANUMAS MET/ICE/OCEAN Overview Report 2011-East Greenland. Greenland Bureau of Minerals and Petroleum, Nuuk, Greenland.

Pfirman, S.L., Colony, R., Nürnberg, D., Eicken, H., Rigor, I., 1997. Reconstructing the origin and trajectory of drifting Arctic sea ice. J. Geophys. Res.: Ocean. 102 (C6), 12575–12586.

Savage, S., 2001. Aspects of iceberg deterioration and drift, Geomorphological Fluid Mechanics. Springer, pp. 279–318.

Scibilia, F., Metrikin, I., Gürtner, A., Teigen, S.H., 2014. Full-Scale Trials and Numerical Modeling of Sea Ice Management in the Greenland Sea, OTC Arctic Technology Conference, Houston, Texas, USA.

Seim, H.E., Edwards, C.R., 2007. Comparison of buoy-mounted and bottom-moored ADCP performance at Gray's Reef. J. Atmos. Ocean. Technol. 24 (2), 270–284.

Spec1, 2015. IceDrift Standart. Drifter Specification. Oceanetic Measurement (2011) Ltd, http://www.oceanetic.com/uploads/3/9/0/4/39044987/2014-oceanetic_ice driftstandardspec.pdf.

Spec2, 2015. Ice Drift Beacons. Catnatec Associates International Ltd, http://www.canatec.ca/index.php/ice-instruments/.

Steklov, V.A., 1983. O dvizhenii tvyordogo tela v zhidkosti (in Russian). Zapiski Kharkovskogo Universiteta, p. 234.

Stroeve, J.C., Serreze, M.C., Holland, M.M., Kay, J.E., Malanik, J., Barrett, A.P., 2012. The Arctic's rapidly shrinking sea ice cover: a research synthesis. Clim. Change 110 (3–4), 1005–1027.

Sumata, H., Kwok, R., Gerdes, R., Kauker, F., Karcher, M., 2015. Uncertainty of Arctic summer ice drift assessed by high-resolution SAR data. J. Geophys. Res. Oceans 120, 5285–5301. http://dx.doi.org/10.1002/2015JC010810.

Timco, G.W., Sudom, D., 2013. Revisiting the Sanderson pressure-area curve: Defining parameters that influence ice pressure. Cold Reg. Sci. Technol. 95, 53–66.

Turnbull, I.D., Fournier, N., Stolwijk, M., Fosnaes, T., McGonigal, D., 2015. Operational iceberg drift forecasting in Northwest Greenland. Cold Reg. Sci. Technol. 110, 1–18.

Veritas, D.N., 2010. DNV Recommended Practice DNV-RP-C205, Norway.

Vinje, T., Nordlund, N., Kvambekk, Å., 1998. Monitoring ice thickness in Fram Strait. J. Geophys. Res.: Ocean. 103 (C5), 10437–10449.

Weeks, W.F., Mellor, M., 1978. Some Elements of Iceberg Technology, CRREL Report. U.S. Army Cold Regions Research and Engineering Laboratory, Hanover, NH.

Weiss, J., 2013. Drift, Deformation, and Fracture of Sea Ice: A Perspective Across Scales.

Yulmetov, R., Løset, S., Lubbad, R., 2016. Planar multi-body model of iceberg free drift and towing in broken ice. Cold Reg. Sci. Technol. 121, 154–166.

Yulmetov, R., Marchenko, A., Løset, S., 2012. Characteristics of Sea Ice and Iceberg Drift Simulations in the Northwestern Barents Sea, The 21st IAHR International Symposium On Ice. Dalian University of Technology Press, Dalian, China, pp. 639–650.

Appendix D:
Modelling drift of icebergs in pack ice off the north-east Greenland

The paper discusses relative drift of icebergs and sea ice in the Greenland Sea. The drift hindcasting is performed and the effect of sea ice on icebergs is demonstrated.

Modelling iceberg drift in pack ice off North-East Greenland

Runa A. Skarbø[1], Renat Yulmetov[1, 2], Sveinung Løset[1]
[1]*The Norwegian University of Science and Technology, Trondheim, Norway*
[2]*The University Centre in Svalbard, Longyearbyen, Norway*
runa.skarbo@ntnu.no

Collisions with icebergs are a hazard for ships and offshore structures in the Arctic. Precise iceberg drift forecasting is thus required to assess the probabilities of possible collisions and damage. The conventional methods of forecasting in open water account for the wind and ocean current velocities, sea surface gradients and waves. Forecasting of icebergs in sea ice is challenging, mainly because there is little knowledge about the additional resistance associated with the surrounding ice. In this paper, we study the relative drift of icebergs and sea ice. We investigate two cases in which icebergs and adjacent ice floes were tracked by using GPS in the Greenland Sea in 2013. The icebergs differ greatly in size: the larger iceberg has a mass exceeding 16 times that of the smaller iceberg. Characteristic relative drift velocities are obtained and appear to vary between the cases. The variation is caused by differences in both the iceberg mass and local ice concentrations. A drift forecasting model is proposed and tested by hindcasting and comparing against the measured drift. The model demonstrates an acceptable level of accuracy for short-term forecasting in this region, where knowledge about winds and ocean current profiles is insufficient. In addition, we compare simulations of the model, both with and without the sea ice forcing. Results indicate that sea ice forcing significantly affects the drift of the small iceberg but that it hardly influences the large iceberg. Finally, the presented model provides accurate estimates of the relative drift. The model can be further developed to create an operational model, which would require further testing with more accurate input data and for more case studies.

1. Introduction

Marine offshore activities in waters prone to icebergs always represent a hazard to humans and infrastructure assets due to potential collisions. Even bergy bits as small as 3 to 5 m across colliding with a floating structure can cause significant damage (Savage 2001). Therefore, the forecasting of drift trajectories of icebergs is important to ensure safe marine operations in the Arctic.

Forecasting drift trajectories of icebergs is challenging, mostly because there is scarce information on winds, currents, waves and sea ice (if present) in the Arctic. Additionally, information on iceberg geometry is important to produce good forecasts. For an operational scenario, none or few of these factors may be known. However, even relatively inaccurate models may be used for operational planning purposes, given the large threat that icebergs pose (Hughes et al. 2014). Several forecasting models have been developed in recent decades, some of which have been used operationally with success. Institutions that have developed iceberg forecasting models include the Canadian Hydraulics Centre (Kubat et al. 2005), the Nansen Environmental and Remote Sensing Centre (Keghouche et al. 2009) and MET Norway (Broström et al. 2009).

Forecasting iceberg drift is more challenging than forecasting the drift of sea ice. The drift of icebergs is heavily influenced by the ocean currents in the water column, and relatively little is known about Arctic Ocean currents. The drift of ice floes depends on surface current and wind, for which we have more accurate data.

This paper presents a model for forecasting ice and iceberg drift under the influence of winds, currents and sea ice off the coast of East Greenland. The aim of the work is to find and study how icebergs move relative to sea ice. The modelling includes the impact of sea ice forcing on icebergs. The model results are verified by hindcasting and comparisons with observations of the drift trajectories of icebergs and initially adjacent ice floes off the coast of East Greenland in the autumn of 2013.

In this paper, Section 2 presents the basis of iceberg trajectory forecasting, the equations that describe iceberg dynamics and the ocean and atmosphere models used. Section 3 describes the actual observations from the tracked icebergs and ice floes in 2013. Section 4 presents the modelling results and compares them with the observations. Section 5 discusses the results, and finally, Section 6 presents the conclusions and outlines the implications and potential for further work.

2. The model system

Ice drift model

The major forces acting on icebergs and ice floes are the air drag ($\vec{F}_A$), water drag ($\vec{F}_W$), Coriolis force ($\vec{F}_C$), sea surface slope force ($\vec{F}_{SS}$) and force from interaction with the sea ice ($\vec{F}_{SI}$). According to Newton's second law, the equation of motion can be written as

$$M\frac{d\vec{U}}{dt} = \vec{F}_A + \vec{F}_W + \vec{F}_C + \vec{F}_{SS} + \vec{F}_{SI}, \qquad\qquad [1]$$

where $M = M_0(1 + C_M)$, M_0 is the mass of the object, C_M is the added mass coefficient, and $\vec{U}$ is the velocity of the object. The added mass coefficients used in the model were $C_M = 0.5$ for icebergs and $C_M = 0$ for the ice floes.

The drag forces ($\vec{F}_A$ and $\vec{F}_W$) acting on the iceberg and the ice floe are calculated differently because of their different geometry. The drag force acting on an arbitrary object can be separated as the frictional drag and the pressure drag. The frictional drag appears because of the tangential shear stresses. The pressure drag comes from the pressure stresses acting on the object. The iceberg is a large, bluff body, and therefore, the effect of pressure drag is the dominating drag force component. Ice floes can be treated as flat plates with a large surface area. Integration of the friction drag over the horizontal surface of the ice floe yields substantially higher drag forces than does integration of pressure forces over the (marginal) vertical area. Thus, for ice floes, the frictional drag component is dominant. As in Smith (1993), the air and water drag forces for icebergs (IB) and ice floes (IF) are calculated as

$$\vec{F}_x^{IB} = \frac{1}{2}\rho_x C_x^{IB} A_{vx}^{IB} |\vec{V}_x - \vec{U}|(\vec{V}_x - \vec{U}),$$ [2]

$$\vec{F}_x^{IF} = \rho_x C_x^{IF} A_{hx}^{IF} |\vec{V}_x - \vec{U}|(\vec{V}_x - \vec{U}),$$ [3]

where x refers to the fluid (air (A) or water (W)), ρ_x is the density of the fluid, C_x is the dimensionless drag coefficient, A_{vx} is the vertical area facing the air or water flow (sail and keel, respectively), A_{hx} is the horizontal surface area in contact with the air (top) and water (bottom) flow and $\vec{V}_x$ is the velocity of the flow of the fluid. The densities of air and water are assumed to be $\rho_A = 1.3$ kg m^{-3} and $\rho_W = 1.023$ kg m^{-3}, respectively. The drag coefficient C_x^{IB} for the pressure force on the iceberg is of the order of 1, while, for ice floes, the frictional drag coefficient C_x^{IF} is of the magnitude of 2×10^{-3}. The water velocity $\vec{V}_W$ is set to the mean value of the top 70 m of the vertical water column of the ocean model for the icebergs, and it is set to the surface current velocity for the ice floes.

The Coriolis force leads, on the Northern hemisphere, to a deflection to the right. Smith (1993) calculate the force according to

$$\vec{F}_C = -M_0 f_C \vec{k} \times \vec{U},$$ [4]

where $f_C = 2\Omega \sin\phi$, Ω is the rotational velocity of Earth ($\Omega = 7.272 \cdot 10^{-5}$ rad s^{-1}), ϕ is the latitude, $\vec{k}$ is the unit vector perpendicular to the Earth surface pointing out and $\vec{U}$ is the velocity of the object. The Coriolis inertial period at high latitudes is approximately 12 hours and can therefore be difficult to distinguish from the semidiurnal tidal periods.

Blunt et al. (2013) give the force acting on a floating body due to the slope of the sea surface as

$$\vec{F}_{SS} = -M_0 \vec{g} \nabla H,$$ [5]

where H is the sea surface elevation above the mean surface and $\vec{g}$ is the gravity acceleration.

The force on an iceberg from sea ice varies with the sea ice concentration. Therefore, the force from sea ice is split for three categories of sea ice concentration A (%). Lichey & Hellmer (2001) originally presented the equations for sea ice forcing. The presented model uses a modified version, which includes the acceleration of the ice in the case of $A > 90$ %:

$$\vec{F}_{SI} = \begin{cases} 0 & A \leq 15\text{ \%} \\ \frac{1}{2}\rho_{SI}C_{SI}A_{SI}|\vec{V}_{SI} - \vec{U}|(\vec{V}_{SI} - \vec{U}) & \text{for} \quad 15\text{ \%} < A \leq 90\text{ \%} \\ M\,d\vec{V}_{SI}/dt - (\vec{F}_A + \vec{F}_W + \vec{F}_C + \vec{F}_{SS}) & A > 90\text{ \% and } P \geq P_S \end{cases} \qquad [6]$$

Sea ice concentrations lower than 15 % are considered open water, and no force from sea ice is assumed to act on the iceberg. For sea ice concentrations between 15 and 90 %, sea ice acts as an additional drag force with a coefficient of resistance C_{SI}. In this study we consider $C_{SI} = 1.0$, according to Lichey & Hellmer (2001). A_{SI} is the product of the sea ice thickness and the iceberg width. The density of sea ice ρ_{SI} is set to 920 kg m^{-3}.

Lichey & Hellmer (2001) stated that for sea ice concentrations exceeding 90 % the iceberg and sea ice will form a solid block and will drift with the sea ice with a constant velocity $\vec{V}_{SI}$. Therefore, they set the sum of forces to zero. However, in reality the sea ice velocity is not constant, and an inertia term must be included to account for the acceleration of the ice. Equation [1] can be rewritten for an iceberg as

$$M_{IB}\frac{d\vec{U}}{dt} = \sum \vec{F}_{other}^{IB} + \vec{F}_{SI}^{IB}, \qquad [7]$$

where M_{IB} is the mass of the iceberg, $\vec{U}$ is the iceberg's velocity, $\sum \vec{F}_{other}^{IB}$ is the sum of all other forces acting on the iceberg except the sea ice force and $\vec{F}_{SI}^{IB}$ is the force acting on the iceberg from the sea ice. Equation [6] for ice concentration above 90 % is found from Equation [7] when the iceberg velocity $\vec{U}$ is equal to the velocity of the sea ice $\vec{V}_{SI}$.

For the observation time period in August to October 2013, the sea ice concentration in the areas studied never exceeded 90 %. Therefore, the sea ice forcing was calculated using only the first and second term of Equation [6]. The sea ice strength P and the threshold value P_S are not treated further in this paper. For more information regarding these terms, readers are referred to Lichey & Hellmer (2001).

Ocean and atmosphere model
The drift model requires velocity vector fields for wind, sea ice, sea surface gradient, ocean and tidal currents, and information about sea ice concentration and thickness.

Input data for the ocean current and sea surface elevation are obtained from the Norwegian Meteorological Institute's operational ocean model "ROMS Nordic4km" (MET Norway 2014). These data represent the current velocity as the mean over 24 hours, and have a spatial resolution of 4 km. The vertical variation in ocean current is modelled as the mean water velocity over the top 100 m of the water column. Hourly tidal currents are obtained from AOTIM5 (Padman &

Erofeeva 2004). Further, the 10-m wind velocity and sea ice concentration and thickness used in the model are retrieved from ERA-Interim reanalysis (Dee et al. 2011). These data have a temporal resolution of 6 hours and a spatial resolution of 80 km, interpolated on a 0.125 degree by 0.125 degree grid. The sea ice drift velocity are assumed to be equal to the observed drift velocity of the ice floes.

3. Iceberg and ice floe observations

Observation setup

Several icebergs and initially adjacent ice floes were tracked using GPS during the autumn of 2013. Two different types of trackers were used; the "IceDrift Standard" tracking drifter produced by Oceanetic Measurement Ltd and a tracker produced by Canatec Associates International Ltd. Both tracker types transmit their GPS coordinates through the Iridium satellite.

The Oceanetic tracking drifter is a white PVC cylinder, with attached dead weights so the tracker sink if the tracked object capsize or sink. The lower limit operating temperature of the tracker is −40°C. Its positional accuracy are given as less than 5 m with 50 % confidence and less than 8 m with 90 % confidence. This tracking drifter measured the position every 10 minutes.

The Canatec trackers were contained in boxes, pre-drilled with holes so the trackers would sink should the tracked object capsize or sink. These beacons operates at temperatures as low as −55°C; however, the accuracy decreases somewhat below −35°C. The GPS accuracy of the tracker is 1.8 m circular error probability (CEP). This tracker obtained the position every 15 minutes.

Table 1 presents information about trackers and deployment dates.

Table 1. Tracker IDs, types and deployment dates.

	Tracker ID	Tracker type	Deployment date	Comment
IB3	128 & 130	Oceanetic	28 Aug 2013	
IF3	28	Canatec	28 Aug 2013	Initially adjacent to IB3
IB8	8	Canatec	31 Aug 2013	
IF6	36	Canatec	31 Aug 2013	Initially adjacent to IB8

The dimensions of the observed icebergs (IB) and ice floes (IF) are listed in Table 2.

Table 2. Approximate dimensions of the icebergs and ice floes. The iceberg heights indicate the total vertical dimension. For the ice floes, the heights indicate approximate total ice thickness.

	L, m	W, m	H, m	Mass, 10^6 metric tons*	Comment
IB3	230	150	70	1.7	Tabular iceberg
IF3			1.2		
IB8	60	50	50	0.1	Tabular iceberg
IF6			1.2		

* The mass is estimated for an idealised cylindrical iceberg with the density of ice of 920 kg m^{-3}.

Observed drift trajectories

Figure 1 presents the observed drift trajectories for the icebergs and ice floes. The sea ice concentration for the current time and location of the body is plotted along the drift trajectory.
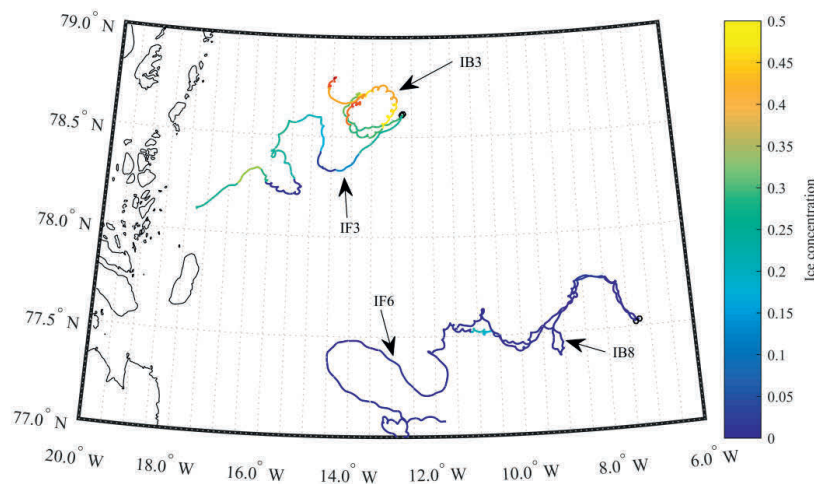
Figure 1. Sea ice concentration along the observed drift trajectories for the icebergs and ice floes. Sea ice concentrations are retrieved from Dee et al. (2011).

IB3 and IF3 were initially drifting approximately 85 nautical miles from the East Greenland coast. The trajectory of IB3 consists of a number of loops, which indicates the influence of inertial forces. Because IB3 is a large iceberg, the Coriolis acceleration is on the same order of magnitude as the acceleration produced by the drag forces. Winds and currents drove IF3 towards land, and it ended up landfast in ice later in the winter. IF3 drifted in much lower concentrations of ice than IB3, even though it was closer to land where higher ice concentrations are expected. The reason for the lower ice concentration is unknown; it might be a consequence of an inaccurate ice chart or just a coincidental polynya in the ice cover.

IB8 and IF6 drifted in almost open water, initially approximately 200 nautical mile from the coast. The drift trajectories for the first 5 days of drift were almost identical, but they later diverged due to strong winds. The similarity of the drift trajectories of IB8 and IF6 are caused by the relatively small size of IB8 and the low ice concentration. After 17 days of drift, the tracker on IB8 stopped transmitting its position. Because IB8 was a small iceberg, it most likely rolled or capsized.

Observed drift velocities

Table 3 gives the mean and maximum drift velocities for the icebergs and ice floes, along with the standard deviation of the mean velocities.

Table 3. Observed mean velocities <V>, standard deviation σ_v and maximum drift velocities for the icebergs and ice floes.

	<V>, cm s^{-1}	σ_v, cm s^{-1}	Period of averaging, days	Max(V), cm s^{-1}
IB3	15	8	19	54
IF3	15	8	19	41
IB8	27	22	17	112
IF6	21	14	36	102

The larger iceberg IB3 and IF3 demonstrated lower mean and maximum drift velocities than did the smaller iceberg IB8 and IF6. IB3 and IF3 were drifting closer to land than IB8 and IF6, as seen in Figure 1. Closer to land, ocean currents are known to be weaker and ice conditions more severe. Thus, weaker currents and more sea ice caused significantly slower drift for IB3 and IF3 compared to IB8 and IF6.

Furthermore, the standard deviations of the drift velocities of IB8 and IF6 are substantially higher than for IB3 and IF3. Open water conditions allow drift velocities of IB8 and IF6 to vary with the ocean current and winds. IB3 and IF3 would be restrained from accelerating faster than the drift ice surrounding them, causing less fluctuation in drift velocities.

Both icebergs had higher maximum drift velocities than their ice floes. The maximum drift velocity of IB3 was 54 cm s^{-1}, 32 % higher than that of IF3. IB8 had a maximum drift velocity of 112 cm s^{-1}, 10 % higher than IF6.

4. Results of drift modelling

The drift equations given in Equations [1]-[6] are solved using the **ode45** solver in MATLAB. The **ode45** solver is based on an explicit Runge-Kutta formula, the Dormand-Prince (4,5) pair (Dormand & Prince 1980). It is a single-step solver – in computing $y(t_n)$ it needs only the solution at the immediately preceding time point, $y(t_{n-1})$ (Dormand & Prince 1980, Shampine & Reichelt 1997). The function is called with time intervals equal to a time step until the specified simulation time is reached. The output time step is 1 hour.

A trial-and-error approach for best fit was used to determine the drag coefficients of Equations [2] and [3]. During this approach, it was observed that even minor changes in the drag coefficients would lead to large deviations in the modelled drift trajectories. Keghouche et al. (2009) studied the estimation of drag coefficients for iceberg drift in the Barents Sea. They found that the relation between C_w and C_a for icebergs was commonly between 0.29 and 0.35 and increased with mass. However, for this study, the relationship C_w/C_a between the coefficients used for the icebergs was found to be lower than that obtained by Keghouche et al. (2009).

The values used for the drag coefficients of Equations [2] and [3] are listed in Table 4.

Table 4. Drag coefficients used in Equations [2] and [3] for the simulations.

	C_w	C_a	C_w/C_a
IB3	0.100	1.000	0.10
IF3	0.009	0.009	1.00
IB8	0.200	0.900	0.22
IF6	0.008	0.008	1.00

The simulation time period is 10 days. As this model aims to be an operational model to be used for short-term forecasting, simulation time periods of 24 to 48 hours is of most relevance. However, to simulate for more days is interesting, in order to see how the model performs over a longer time span. Furthermore, the simulation time period was determined by observing the time before the icebergs and ice floes reach the maximum correlation distance. The maximum correlation distance is the distance between the icebergs and ice floes for which their relative velocities still correspond. For the observations, this was found to be 60 km.

Simulated drift trajectories
The observed and modelled drift trajectories of the icebergs and ice floes are presented in Figure 2.

Simulations both with and without forcing from sea ice are included in Figure 2a) and b). It can be seen that including the sea ice force in the simulations affects the drift trajectory but does not alter the overall shape of the drift trajectory to a large degree. This result indicates that the forcing from sea ice is less strong than the other forces influencing the iceberg drift, such as the ocean current.

The shape of the simulated drift trajectories of IB3, depicted as a red dashed line in Figure 2a), differs from the observed drift trajectory. The observed drift trajectory appears almost as a complete circle, with the iceberg returning to a location less than 10 km from the initial position. The simulated drift trajectories also begin drifting in a circle, with the form of the trajectory partially imitating the observations. However, after approximately five days, the drift direction changes dramatically. The simulated iceberg starts drifting southeast, with an approximately 180° difference in drift direction from the observed iceberg. It continues drifting in this direction until the end of the simulation time period.
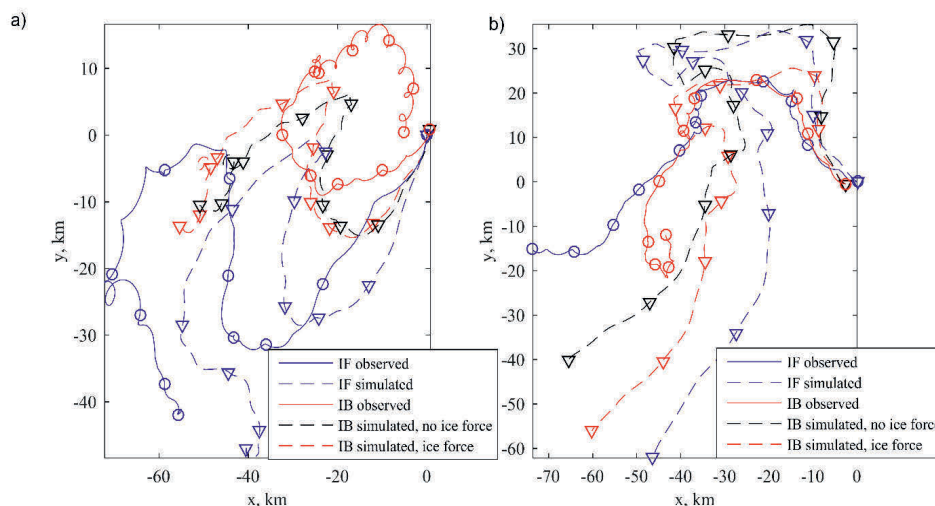
Figure 2. Drift trajectories of observed and modelled icebergs and ice floes. a) illustrates IB3 and IF3, b) illustrates IB8 and IF6. Markers indicate every 24 hours. The different simulations, both including and excluding the forcing from sea ice on the iceberg, are shown.

For IF3, presented in blue in Figure 2a), the shape of the simulated drift trajectory follows the shape of the observed drift trajectory. However, the velocity of the ice floe is probably underestimated, thus leading to the drift distance for the simulated ice floe to be underestimated, especially in the east/west direction.

The simulated drift trajectory of IB8 without ice forcing, shown as the black dotted line in Figure 2b), resembles the actual drift trajectory more closely than the trajectory including ice forcing. However, after the first five days, the simulation that does not include ice forcing diverges somewhat from the observations, drifting further east than the observation, which drifted south. Still, the general drift direction is mostly to the south, similar to the observations. However, the observed iceberg made a 180° turn and drifted northwards over the last three days of observations. Neither of the simulations reproduce this dramatic change in direction. The simulation for IB8 including sea ice forcing overestimates the drift in the northern direction in the initial two days.

The simulated drift of IF6, as presented in Figure 2b), is also overestimated in the northwards direction for the initial two days. In fact, the drift trajectory of the simulated IF6 and the simulated IB8 with no ice forcing are very similar for the first four days, and even after diverging somewhat, they remain similar over the simulation period. For the last seven days of the simulation period, the simulated IF6 drift west-south west, whereas the observed IF6 drifted east-south east.

The model does not reproduce the small loops and other small-scale behaviours of the observed drift trajectories of the icebergs and ice floes. The coarse temporal resolution of the ocean and atmosphere input data is the cause of this. The lack of looping behaviour in the model is especially

evident in Figure 2a). The observations IB3 and IF3 have the drift trajectories with most looping behaviour, but this is not reflected in the simulated trajectories. Still, the results illustrate an acceptable level of accuracy, despite the low-resolution input data for the ocean and atmosphere modelling.

The distances between the observed objects and the simulated objects over the simulation period of 10 days are presented in Figure 3.
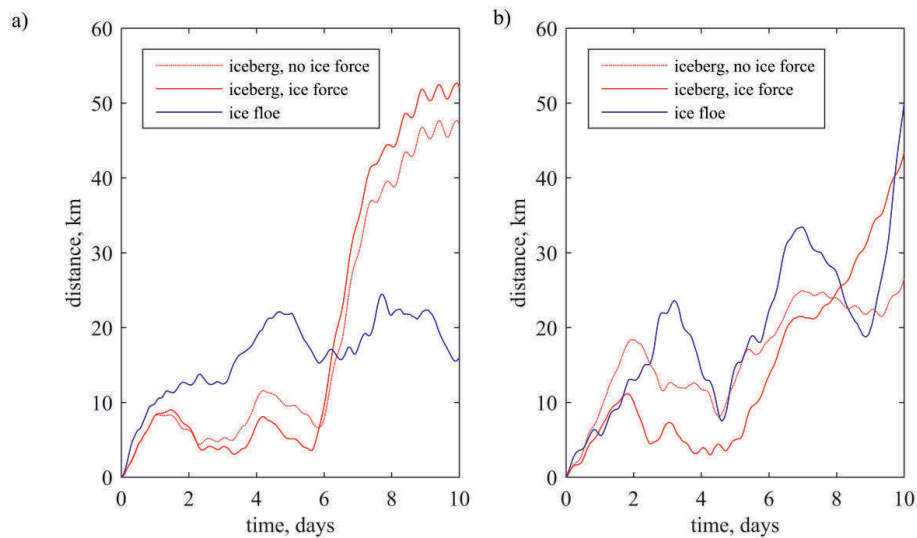

Figure 3. Distances between the simulated icebergs and ice floes and the observations over the simulation period of 10 days. a) illustrates IB3 and IF3, b) illustrates IB8 and IF6. The different simulations, both including and excluding the forcing from sea ice on the iceberg, are shown.

For both cases, in the beginning of the simulation period, the distances between the icebergs modelled with ice forcing and the observations are shorter than or approximately equal to the distances between the icebergs modelled without ice forcing and the observations. However, after approximately six and eight days for IB3 and IB8 respectively the simulations with no ice force are closer to the observed locations. The results indicate that for shorter simulation periods the inclusion of sea ice forcing produces more position accurate results for predicting the drift of icebergs.

The distances between the observed and simulated icebergs including ice force are less than 10 km for the first six days. After day 5, a steep increase in the distance between the observations and the simulations is seen for both cases. For IB3, this is explained by the previously described sharp deviation in heading of 180° for the simulated IB3 after the fifth day of drift, as seen in Figure 2a). The drift trajectories of the simulated and observed IB8 are also diverging after day five, seen from Figure 2b). However, the deviation is not as rapid as for IB3.

Distances between the observed and simulated ice floes are in both cases longer than for the icebergs for the first six and eight days for each case respectively. However, the sudden increase in distance as seen for IB3 is not reproduced for IF3.

Simulated drift velocities

Table 5 gives the mean and maximum drift velocities for the simulated icebergs and ice floes, along with the standard deviation.

Table 5. Simulated mean velocities <V>, standard deviation σ_v and maximum drift velocities for the icebergs and ice floes for the 10-day simulation period. The table also lists deviation between the simulated and observed values, as given in Table 3.

	<V>, cm s^{-1}		σ_v, cm s^{-1}		Max(V), cm s^{-1}	
IB3, no ice force	12	−20 %	7	−13 %	30	−44 %
IB3, with ice force	13	−13 %	7	−13 %	33	−38 %
IF3	18	+20 %	9	+13 %	41	0 %
IB8, no ice force	21	−22 %	7	−68 %	43	−61 %
IB8, with ice force	19	−30 %	7	−68 %	39	−65 %
IF6	24	+14 %	10	−28 %	48	−53 %

The mean drift velocities of the simulations are similar to the observed mean velocities, with deviations in the range of ±30 %. The mean drift velocities are underestimated for the icebergs, both with and without ice force, and overestimated for the ice floes.

The inclusion of ice force on the icebergs has different effects on the mean velocities; IB3 has a higher mean velocity with ice force than without, while for IB8 the mean velocity is higher without ice force. This indicates that the ice around IB3 has a higher velocity than the slower ocean currents near land, and force the iceberg to drift faster. On the contrary, for IB8, drifting further out from land and in currents with higher velocities, the inclusion of sea ice in the model cause the iceberg to slow down.

The standard deviations of the mean velocities are underestimated for all objects, except for IF3. Including the ice force does not make a difference for the prediction of the standard deviations. For IB8, the standard deviation of the mean velocity is underestimated severely by −68 %. The underestimations are lower for IB3 and IF6, with −13 % and −28 % respectively.

The maximum velocities are clearly underestimated for all objects, except IF3 which has a perfect prediction. The maximum velocities are underestimated less for IB3 than for IB8 and IF6. For IB3, the maximum velocity is less underestimated when including the ice force (−38 % with ice force vs. −44 % without ice force). The maximum velocity of IB8 is underestimated by more when including ice forcing than not (−65 % and −61 % respectively). For IF6, the maximum velocity is underestimated by −53 %.

The underestimation of velocity variations (standard deviation) and maximum velocities is most likely caused by low temporal and spatial resolution of the input data for wind and ocean current. The input data does not capture local maxima of ocean current and wind. Furthermore, the differences between the two pairs of icebergs and ice floes may indicate differences in accuracy of metocean data between the geographic regions or it may be coincidental.

The velocity predictions for the ice floes are in general better than for the icebergs. However, from Figure 3 it is seen that the trajectory predictions for the ice floes are worse than for the icebergs. This may indicate that the wind speeds in the input data are more accurate than the directions. Furthermore, the directions of the ocean current may be precise, but its magnitude may be less accurate.

The most accurate velocity prediction for all objects occur for IF6. However, the drift trajectory for IF3 is not the best predicted, as seen in Figure 3. Thus, the best prediction of velocities may be coincidental.

Relative distances and speeds of the icebergs and ice floes

The evolution in relative distance between the icebergs and ice floes for both observations and simulations are illustrated in Figure 4. The observed average relative drift speed for 10 days was 6 km/day for IB3 and 3 km/day for IB8. The latter demonstrated very slow motion relative to the ice, with the relative speed being approximately 1 km/day.
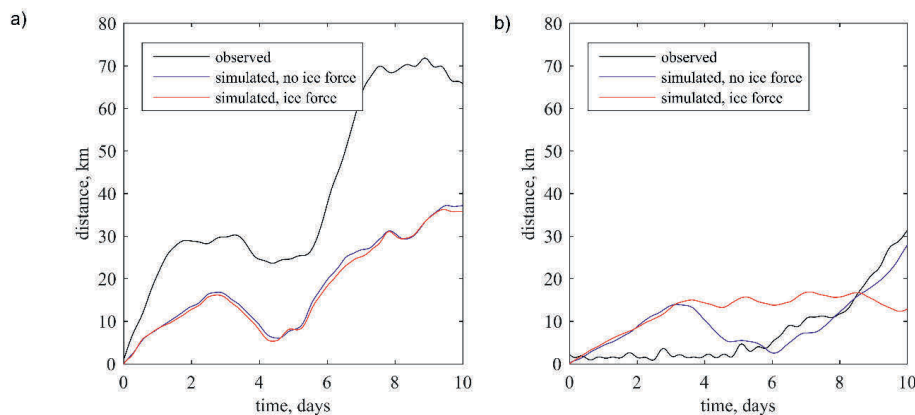
Figure 4. Evolution in relative distance between icebergs and ice floes for both observations and modelled trajectories. For the modelled results, simulations are depicted both with and without ice forcing. a) Illustrates the relative distance between IB3 and IF3; b) illustrates the relative distance between IB8 and IF6.

The relative distance between IB3 and IF3 is underestimated by approximately a factor of two. The forcing from sea ice makes little difference in the relative distance for this simulation. However, the shapes of the curves of the modelled results appear similar to those of the observations.

As seen in Figure 4b), for IB8 and IF6, the modelled relative distance between the iceberg and ice floe is larger than that of the observations for most of the simulation time period. However, for these simulations, the inclusion of sea ice forcing affects the relative distance significantly after day 3. The relative distance for the simulation with no ice forcing starts to approach the observations, and its predictions match from day 5 onwards. Nevertheless, as seen from the trajectory plot in Figure 2b), the relative position of the simulated iceberg and ice floe are not close to the observations. Thus, the concurrence of the relative distances from day 5 and thereafter may be merely coincidental.

5. Discussion

The sea ice forcing affects the modelled drift trajectories of the two icebergs differently. For IB3, the impact make only a small difference, whereas the impact is significant for IB8. IB3 has a mass of over 16 times that of IB8, which lead to the drag forces on IB3 to be much greater than those of IB8. Thus, the ratio between the ice force and the drag force is larger for IB3 than for IB8, and the sea ice will consequently have a likely greater effect on the drift trajectory. This is further evident in the simulation including sea ice forcing for IB8, which overestimates the drift in the north direction in the initial two days compared to the simulation with no sea ice forcing. From Figure 1, it can be seen that IB8 only drifts in low ice concentrations. The overestimation may indicate either that the modelled sea ice forcing is greater than the actual force or that the model input data for sea ice concentration does not accurately represent the actual conditions. In retrospect, verification of the actual sea ice conditions is not possible.

Forecasting the drift of icebergs is challenging for a number of reasons. The accuracy of the forecasting model depends on the description of the physical phenomena, as does the accuracy of the applied metocean variables, the most important of which are wind, currents and sea ice drift.

The mass and shape of the iceberg play a large role in modelling the drift. There are large uncertainties related to estimating the mass and dimensions of the icebergs, because all of the dimensions are estimated based on visual observation. A simplifying assumption that the geometry of the iceberg, can be represented as a cylinder, both above and below the waterline, is made. Additionally, the geometry and mass of the iceberg may have changed during the drifting period because of melting, freezing and wave erosion. Thus, even if the geometric modelling is initially correct, it may not remain so over the entire drifting period. However, in this study, we consider such short drifting periods that any change in geometry is assumed to be negligible.

Because the ocean current varies with depth, the representation of the underwater geometry, namely the cross-sectional area at different depths, is important for the drift prediction. In the model, the iceberg is represented by a cylinder, and the ocean current is modelled as the mean water velocity over a 70-m-deep layer. This may be a source of error in the model.

In this study, the velocity of the ice floe is used to represent the velocity of the whole level ice field. A single point vector cannot fully represent the velocity of a non-uniform 2D ice field. However, for short distances, this assumption is considered valid. Hence, the error in estimating the sea ice drift velocity near the iceberg will increase with increasing distance between the iceberg and ice floe.

Inaccuracies and the low temporal and spatial resolution of the ocean and atmosphere datasets affects the quality of the drifting forecasts. In the Arctic Ocean, the observational densities are low, which make the forecasts more uncertain than those in areas closer to populated land areas. The available datasets have a resolution of 4 km, and the velocity is only provided as a daily mean. In addition, the polar low phenomena are difficult to forecast.

6. Conclusions

The paper describes the study of the movements of two icebergs and adjacent ice floes that were tracked using GPS trackers in the Greenland Sea in 2013. The icebergs differ greatly in size: the larger iceberg IB3 has a mass exceeding 16 times that of the smaller iceberg IB8. Characteristic relative drift velocities are obtained. The drift of the two icebergs and two ice floes adjacent to each of the icebergs are simulated using a numerical model. Drift prediction of the icebergs are compared with and without inclusion of sea ice forcing. The numerical results are compared with the actual drift history provided by the trackers. A complex analysis of the data provided by trackers is carried out. The major findings are as follows:

- The iceberg and ice floe pair drifting in higher ice concentrations, IB3 and IF3, have mean drift velocities of 15 cm/s. This is lower than for the pair drifting in near open water conditions, IB8 and IF6, which has mean drift velocities of 27 cm/s and 21 cm/s, respectively.
- The standard deviations of the mean drift velocities are significantly lower for IB3 and IF3 (8 cm/s) than for IB8 (22 cm/s) and IF6 (14 cm/s). This indicate more fluctuating velocities for objects drifting in lower ice concentrations than for objects in higher ice concentrations.
- For both cases observed, the iceberg has a higher maximum drift velocity than the ice floe. The larger iceberg IB3 has a maximum velocity of 54 cm/s, 32 % higher than IF3's maximum velocity of 41 cm/s. IB8 has a maximum drift velocity of 112 cm/s, 10 % higher than IF3's maximum drift velocity of 102 cm/s.
- The relationship between the drag coefficients C_w and C_a of best fit are found to be 0.1 for IB3 and 0.22 for IB8. This is lower than found by Keghouche et al. (2009).
- The simulation results indicates that the modelled influence of forcing from sea ice on icebergs seems to be large for small icebergs and negligible for large icebergs. This is as expected, as the ratio of the sea ice force to the drag force is larger for small icebergs than for large icebergs.
- The model predicts the drift trajectories of both icebergs with an accuracy of less than 10 km for simulation periods shorter than 6 days when including sea ice forcing. Results of iceberg simulations not including sea ice forcing have larger deviations in drift trajectories.
- Short-term forecasting (less than 6 days) is two times more accurate for the icebergs than for the ice floes. However, the position forecasting accuracy for icebergs declines rapidly after 6 days.
- The simulation model underestimates the mean drift velocities of the icebergs and overestimate those of ice floes. The deviations of the mean velocities are in the range of ±30 %.
- The standard deviations of the mean velocities in the simulations are underestimated for all objects except for IF3. The underestimations range from −13 % for IB3 (drifting in higher ice concentrations) to −68 % for IB8 (drifting in near open water). Thus, the model does not reproduce rapid accelerations and velocity fluctuations. This is due to the coarse temporal and spatial resolution of the input data for ocean current and wind.

- The simulation model underestimates the maximum drift velocities of all objects except for ice floe IF3. The maximum drift velocities of the other icebergs and ice floes are dramatically underestimated, in the range of 38 % to 68 %.
- The predictions of velocities are better for the ice floes then for the icebergs, whereas the accuracy of location predictions are better for the icebergs. This may indicate that wind speeds are more accurately represented than wind directions, and furthermore that the current directions are satisfactory but that the accuracy of the speeds are less good.

The results of this study are based on a small sample of data. More studies should be performed with a larger dataset of observations and metocean data with higher temporal and spatial resolution.

Acknowledgements

References

Blunt, J. D., Mitchell, D. A., Matskevitch, D. G., Kokkinis, T., Younan, A. H., Hamilton, J. M. et al. (2013), A tactical hindcast calibration method for sea ice drift forecasting in the Canadian Beaufort Sea, *in* 'The Twenty-third International Offshore and Polar Engineering Conference', International Society of Offshore and Polar Engineers.

Broström, G., Melsom, A., Sayed, M. & Kubat, I. (2009), 'Iceberg modeling at met.no: Validation of iceberg model', *Journal of Geophysical Research* **99**(17), 3337–3350.

Dee, D., Uppala, S., Simmons, A., Berrisford, P., Poli, P., Kobayashi, S., Andrae, U., Balmaseda, M., Balsamo, G., Bauer, P. et al. (2011), 'The ERA-Interim reanalysis: Configuration and performance of the data assimilation system', *Quarterly Journal of the Royal Meteorological Society* **137**(656), 553–597.

Dormand, J. R. & Prince, P. J. (1980), 'A family of embedded Runge-Kutta formulae', *Journal of Computational and Applied Mathematics* **6**(1), 19–26.

Hughes, N., Broström, G. & Melsom, A. (2014), Iceberg remote detection, trajectory forecasting, and tracking, Technical Report Project no. 265863, Arctic Climate Change, Economy and Society (ACCESS).

Keghouche, I., Bertino, L. & Lisæter, K. A. (2009), 'Parameterization of an iceberg drift model in the Barents Sea', *Journal of Atmospheric and Oceanic Technology* **26**(10), 2216–2227.

Kubat, I., Sayed, M., Savage, S. B., Carrieres, T. et al. (2005), 'An operational model of iceberg drift', *International Journal of Offshore and Polar Engineering* **15**(02).

Lichey, C. & Hellmer, H. H. (2001), 'Modeling giant-iceberg drift under the influence of sea ice in the Weddell Sea, Antarctica', *Journal of Glaciology* **47**(158), 452–460.

Norwegian Meteorological Institute (MET Norway) (2014), 'ROMS Nordic4km Project, Ocean and Sea Ice Dataset'. http://thredds.met.no/thredds/catalog/fou-hi/nordic4km/catalog.html

Padman, L. & Erofeeva, S. (2004), 'A barotropic inverse tidal model for the Arctic Ocean', *Geophysical Research Letters* **31**(2).

Savage, S. B. (2001), *Aspects of Iceberg Deterioration and Drift*, Vol. 582 of *Lecture Notes in Physics*, Springer Berlin Heidelberg, pp. 279–318.

Shampine, L. F. & Reichelt, M. W. (1997), 'The MATLAB ODE suite', *SIAM Journal on Scientific Computing* **18**(1), 1–22.

Smith, S. D. (1993), 'Hindcasting iceberg drift using current profiles and winds', *Cold Regions Science and Technology* **22**(1), 33–4

Appendix E:
Characteristics of Sea Ice and Iceberg Drift Simulations in the Northwestern Barents Sea

The paper tests the performance of a conventional drift forecasting models applied to sea ice drifting in the Barents Sea. In addition it reports some characteristic oceanographic data.

Characteristics of Sea Ice and Iceberg Drift Simulations in the Northwestern Barents Sea

Renat Yulmetov[1,2*], Aleksey Marchenko[1,2], and Sveinung Løset[1,2,3]
1. Sustainable Arctic Marine and Coastal Technology (SAMCoT), Centre for Research-based Innovation (CRI), Norwegian University of Science and Technology, Trondheim, Norway
2. The University Centre in Svalbard, Longyearbyen, Norway
3. Department of Civil and Transport Engineering, Norwegian University of Science and Technology, Trondheim, Norway
[*] renaty@unis.no

Ice drift data collected during cruises of the RV Lance in the North-West Barents Sea (region to the North-East from the Hopen Island and Spitsbergenbanken) are analyzed and compared. All measurements were performed when the RV Lance was moored to the drifting floe. The ship's navigational system provided GPS data and data on the pitch, roll, heading and heave of the ship with a sampling interval of 1 sec. Furthermore, the speed of the sea currents was measured with an ADCP mounted on the ship bottom, and CTD profiles were measured from the drifting ice and the ship board. Numerical simulations are performed to study the dependence of iceberg drift trajectories from the iceberg drafts and wind drag coefficients when the sea current velocities coincide with measured currents. The influence of the water eddy viscosity on the iceberg drift is analyzed using explicit solution describing the Ekman current.

1. Introduction

Since 1968 when the first well opened in Prudhoe Bay, petroleum exploration in Arctic waters has moved further north, encountering harder environmental conditions and higher loads. In addition to wind, waves and current loads, environmental actions in the Arctic include ice actions and potential collisions with icebergs. All load combinations and their effects should be estimated for a structure planned in a particular geographical location. It is important to detect potential ice hazards in a timely manner such that the movement of ice features can be predicted and the situation can be handled in a manner that reduces the effects of the ice. This detection is the purpose of ice management, which has been developed extensively over recent years.

Loads induced by drift ice depend strongly on the drift speed and concentration and the thickness and properties of the ice; thus, these loads also depend on the weather conditions and sea current structure in the region of interest. Several papers have been written about the wind and sea current analysis in Spitsbergen Bank (Loeng, 1991; Kowalik and Proshutinsky, 1995). Strong tidal currents can occur north of Bjørnøya due to the relatively shallow water in the area. The mean annual temperatures are lower than those at the Great Bank or Central Bank, making the sea more prone to ice formation. However, the semidiurnal tides increase the open water fraction and amount of heat loss (Harris et al., 1998; Årthun et al., 2011). According to ice charts, the drift ice cover varies from open water in the summer and autumn to very close drift ice in the winter and spring.

Estimating the iceberg motions in these types of ice conditions is a complex task, and many scientists use similar equations (Lichey and Hellmer, 2001). Several papers provide characteristic values for the drag coefficients in particular seas (Kegouche, 2009; Kubat et al., 2005; Eik, 2009). Some simulations have shown good results for calculating backward trajectories of drift ice (Pfirman et al., 1997). However, the prediction of iceberg motion requires accurate forecast of the sea currents and wind velocity. Ice compactness also has strong influence on iceberg drift. If the ice compactness is relatively high, icebergs drift together with the ice; otherwise, the iceberg motion is mainly steered by drag forces (Marchenko et al., 2010; Hunke and Comeau, 2011). This effect has still not been extensively studied, and emphasis should be placed on understanding these processes more carefully.

In this paper, we analyze the free drift of sea ice in the Barents Sea during two annual expeditions. The coordinates and velocities are derived from navigational data, while the sea currents were measured by ADCPs installed at the ship bottom. The wind and air temperatures were measured by an onboard weather station, and the swell waves were indirectly detected by the heave measurements. The iceberg drift trajectories under the influence of the measured sea currents are estimated for different drag coefficients and iceberg sizes. CTD profiling was performed from the ice near the ship and from the shipboard during both expeditions. All of the data collected provide information about the Barents Sea currents structure and ice conditions. In the last section, the iceberg drift guided by the Ekman current is described. The drift trajectories are calculated for different iceberg sizes and eddy viscosities.

2. Ice Drift Analysis

The ship used in both expeditions is the research vessel "Lance" with an Ice Class 1A icebreaking capability, which indicates that the ship can travel through ice-rich waters with a nonconsolidated ice thickness of 0.8 m. In both 2009 and 2011, the ship was moored to an ice floe and drifted with the ice field. The tracking equipment and weather station provided information (NMEA protocol) about the coordinates, RPY angles, sea depth, wind direction, wind magnitude, and air temperature.

The first expedition occurred in the northeast of Hopen in 2009. According to the available ice charts (Fig. 1), the sea ice concentration was approximately 0.6 and the measured ice thickness was 0.25–1 m (Marchenko et al., 2010). Parts of the free drift trajectory of the RV Lance are shown in Fig. 2, displaying wavy forms without loops. There are three wavy parts extending to approximately 10, 20 and 10 km. The ship drifted northwest by approximately 40 km in 37.5 hours, resulting in a mean drift velocity of approximately 1 km/h. In 2011, the RV Lance drifted southwest of Hopen, moored to an ice ridge with a keel of approximately 10 m. According to the ice charts and visual observations, the ice concentration was approximately 0.8. The drift trajectory represents 2 loops with diameters of approximately 6 km and 14 km and a rotation period of approximately 12.5 hours.
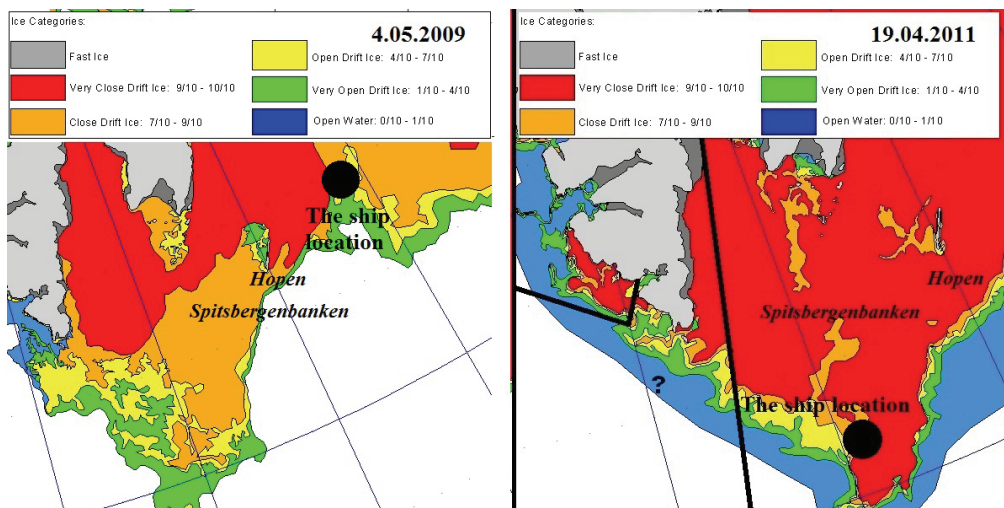
Figure 1. Ice conditions during two expeditions.

Assuming the ship drifted together with ice drift velocity was derived from the coordinate measurements; the magnitude and direction of the ship velocity are shown in Fig. 3. In 2011, the angular velocity was rather uniform, and the ship made almost two loops over 24 hours. The mean absolute velocities in 2009 and 2011 were 0.3 m/s and 0.75 m/s, respectively, due to differences in the sea bottom depths; Spitsbergenbanken had a water depth of approximately 40 m where the drift took place, and in 2009, the ship drifted above almost 200 meters of water. Deep water moves slower than shallow water. Furthermore, in 2011, the ship drifted in the waters in which the Bjørnøya Current meets the rest of the cold East Spitsbergen Current and

produces numerous dynamic vortexes (Harris et al., 1998). The velocity changes were in the range of 0 to 0.55 m/s in 2009 and 0.4 to 1.5 m/s in 2011.
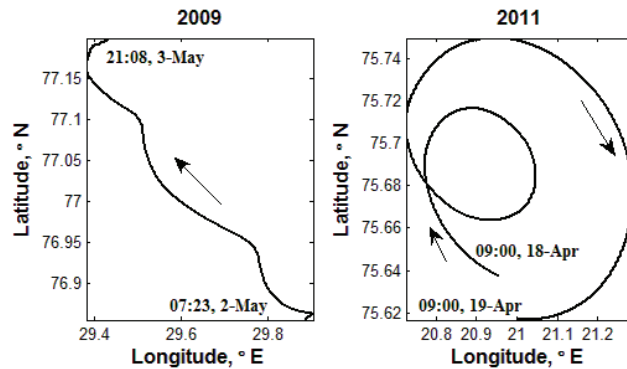

Figure 2. Free-drift trajectories in different years (drift direction is denoted by an arrow).
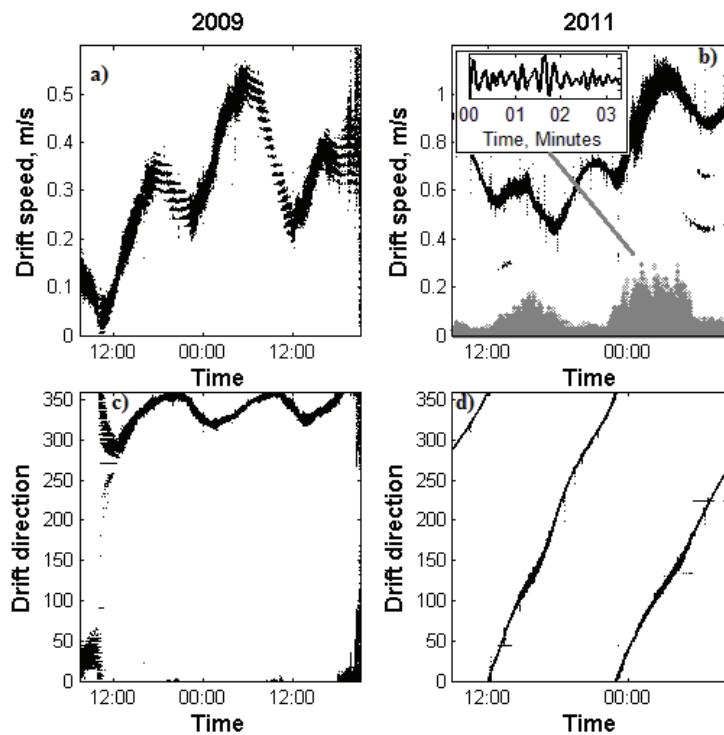

Figure 3. RV Lance drift speed a) in 2009 and b) in 2011. RV Lance drift direction c) in 2009 and d) in 2011. Inset b) Heave measurements during the semidiurnal tide.

By comparing the drift speed data with the ship heave measurements in 2011 (Fig. 3, small circle markers), the drift speed has higher values when swell waves with approximately 11 sec-period

are present (Fig. 3b, inset), possibly because diverging ice floes allows objects to be more easily penetrated though the ice field. Furthermore, the velocity values are more dispersed when waves are present due to the back and forth movement during dusting. There was no such effect in 2009 because swell waves have smaller amplitudes in deep water.

Curvature of the drift trajectory was calculated knowing velocity and acceleration components. Components of velocity were approximated with sine functions to exclude noise and increase precision of numerical derivation. Distribution of curvature value over the drift speed is in Fig. 4, showing higher curvature of trajectory during low speed drift. Having low speed the ship drift direction in 2009 changed very fast. Curvature radius (reciprocal of curvature value) is less than hundred meters for drift speed less than 0.1 m/s. The curvature radius during the drift in 2011 has mean value approximately 5.6 km and varies from 1.7 km to 9.6 km. These distribution and parameters play important role during drilling in dynamic positioning or object construction, they show how fast drift ice with certain speed can change drift direction, then it is possible to change ship bow direction fast enough to withstand ice loads.
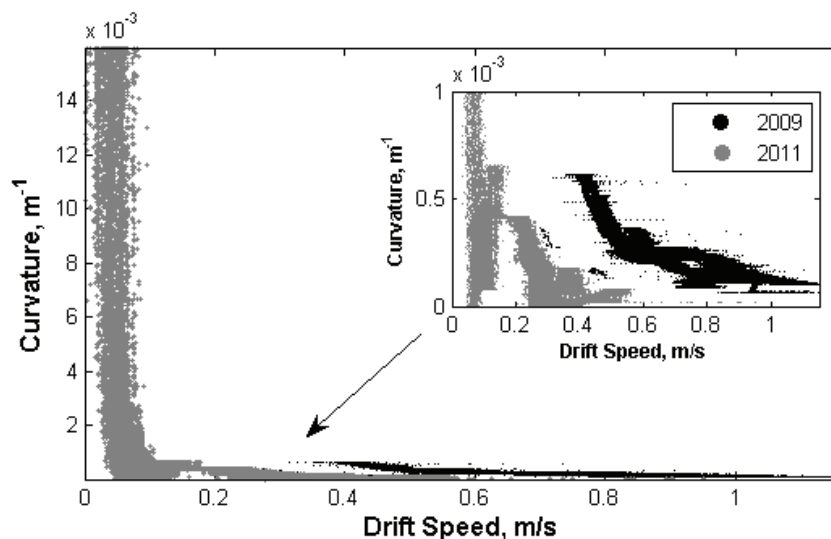
Figure 4. Curvature of trajectory vs. drift speed distribution in 2011. Drift direction can be changed strongly for low drift speeds.

3. Sea Current Analysis

The sea current was measured using Teledyne RDI ADCP (4 beams, 8 m/bin, 1st bin – 16 m). In Fig. 5, the circled points represent the relative current average magnitude and average direction for the depth ranging from 0–15.98 m (1st bin). For 2009, the sea current with a maximum magnitude has a periodicity of approximately 12 hours. The solid lines in the 2009 plots show the average velocity and direction for 20 bins (depth 0–168 m). Most of the seawater layers have similar directions but are different from the two upper layers. The top current layer changed its direction gradually and completed almost two full rounds over 24 hours, clearly indicating the presence of a semidiurnal current. In 2011, the RV Lance drifted in shallow waters on

Spitsbergenbanken, and only two sea current layers were measured. The magnitude and direction of the current velocity (circle markers) have similar values as the magnitude and direction of the drift velocity (solid line).
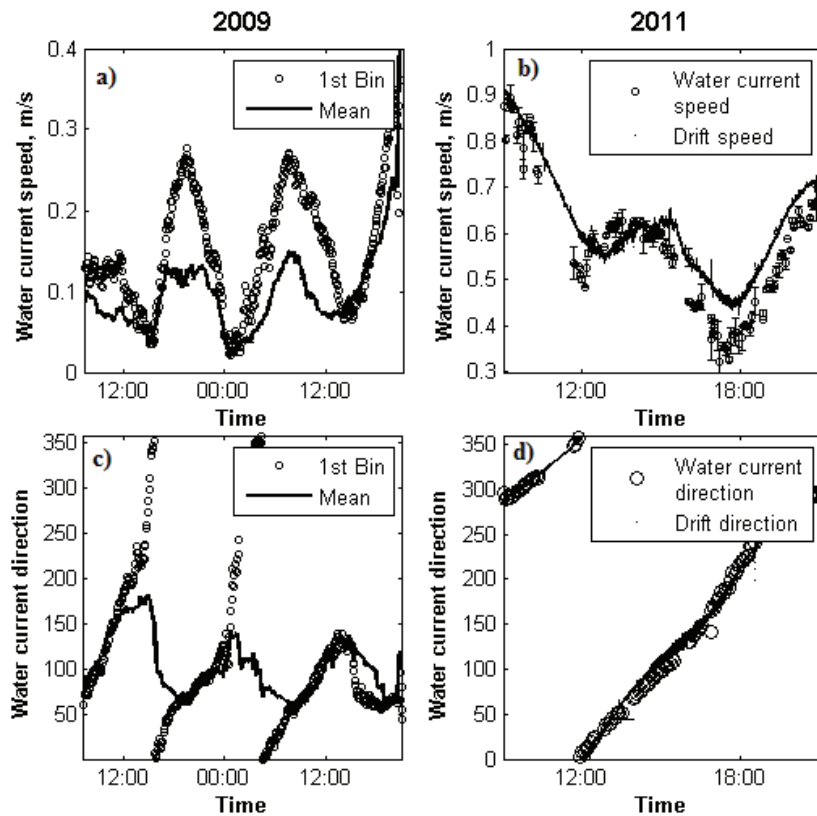

Figure 5. a) Water current speed and c) water current direction measured by ADCP in 2009 and b) water current speed measured by ADCP and drift speed, d) water current direction measured by ADCP and drift direction in 2011.

Fig. 6 shows the salinity and temperature profiles measured by the STD/CTD model SD204 in the region of the fieldwork. The first three profiles were measured from the drifting ice on May 2 and May 3, when the RV Lance was moored to the ice. The fourth profile was measured from the shipboard near the iceberg, which was 2 km away from the first three profiles. The last three profiles were measured during the last day of the fieldwork on May 5. In these days, the RV Lance drifted to the north, possibly causing the significant evolution in the temperature and salinity profiles in the period from May 2 to May 5. The vertical gradient of the water temperature reached 3°C over a 50 m depth on May 2 and May 3, causing the high heat fluxes from the sea to the ice bottom. The salinity profiles correspond well with the temperature profiles.
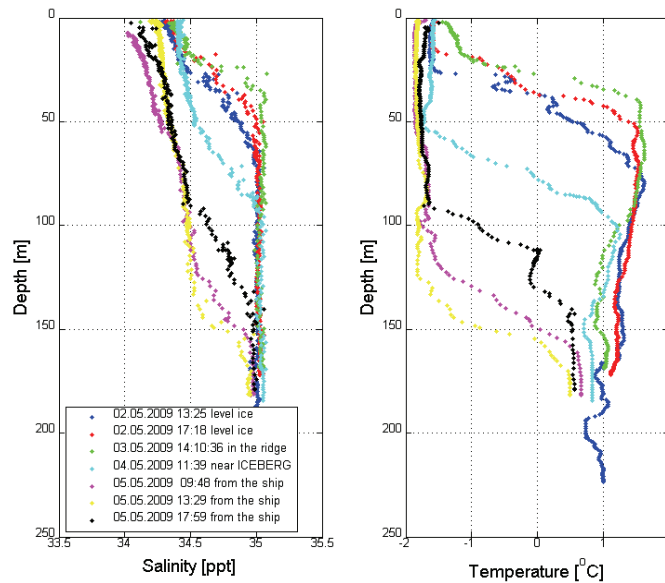
Figure 6. CTD profiles measured during the RV Lance cruise in 2009.

The CTD profiles measured in 2011 are displayed in Fig. 7. On the 18th of April, two profiles were obtained from the backside of the ship when it was moored to an ice ridge. On the 19th of April, one profile was obtained from the side, between the ship and the ridge. Another profile was measured from the edge of the ridge. In each case, we encountered a strong sea current, especially from the depths exceeding 30 m. Due to active mixing the temperature and salinity profiles have rather constant values. The CTD measurements were likely affected (high amplitude noise) by sediments in the water. Turbulent motion created by mixing the waters of the Bjørnøya Current and the East Spitsbergen Current probably lifts up sand from the bottom. However, the water masses on Spitsbergenbanken may have had a high salinity and low temperature during late April of 2011.
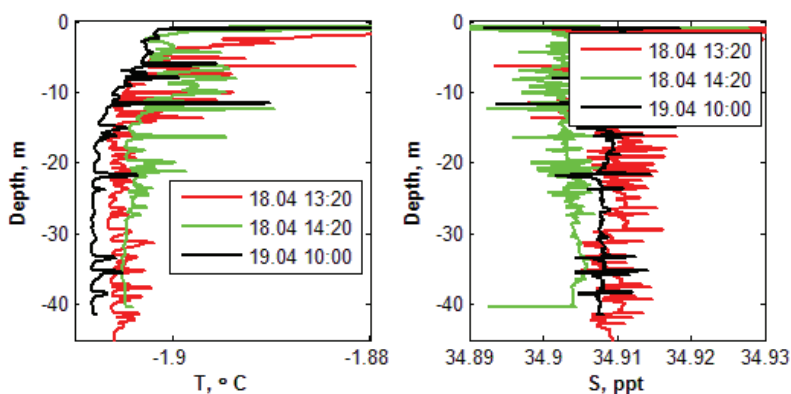
Figure 7. CTD profiles measured during the RV Lance cruise in 2011.

4. Iceberg Drift Simulations

Design of an offshore object in Arctic waters has to take into account the presence of icebergs in the region. It is important to predict further motion of an iceberg after its recognition close to the offshore object. We reproduced simple iceberg drift model that includes drag forces and Coriolis force but doesn't include interaction with surround ice. The ice drift simulation was based on a motion equation that included the water drag force ($\vec{F}_W$), air drag force ($\vec{F}_A$) and Coriolis force ($\vec{F}_C$). Let us consider an iceberg as a point mass M and velocity $\vec{u}$ in a space with wind and sea current velocity fields.

$$M\frac{d\vec{u}}{dt} = \vec{F}_W + \vec{F}_A + \vec{F}_C \tag{1}$$

The axes were chosen to be directed in the west-east and south-north directions; drift started from the zero-point with initial velocities estimated from the navigation data. The magnitudes of the drag forces are proportional to the continuum density, square of the relative velocity and depend on the vertical and horizontal surface areas.

$$\vec{F}_{A,W} = \int_{-h}^{0}\left(\frac{1}{2}C_{vA,W}A_{vA,W}(z) + C_{hA,W}A_{hA,W}(z)\right)\rho_{A,W}\left|\vec{V}_{A,W}(z)-\vec{u}\right|\left(\vec{V}_{A,W}(z)-\vec{u}\right)dz \tag{2}$$

where $C_{vA,W}, C_{hA,W}$ are the vertical and horizontal drag coefficients, respectively, $A_{vA,W}, A_{hA,W}$ are the vertical and horizontal cross-sectional areas of the iceberg on the depth z and $\rho_{A,W}$ is the continuum density; force is integrated over depth layer by layer. According to Lichey and Hellmer (2001), the representative values of the drag coefficients are $C_{vW} = 0.85$, $C_{hW} = 5\times10^{-4}$, $C_{hA} = 0.4$, and $C_{hA} = 2.5\times10^{-4}$. The speed and direction of the water and wind were taken from the ADCP and weather station measurements, respectively. ADCP data were measured and averaged over time and space from different depths, 0–16 m from ship keel in the first section and depths of every 8 m for the subsequent sections. The Coriolis force is expressed as

$$\vec{F}_C = -2M\Omega\sin\varphi\vec{k}\times\vec{u} \tag{3}$$

where Ω is the angular velocity of Earth, φ is the latitude, and $\vec{k}$ is a normal vector to the sea surface directed upward.

Icebergs are assumed to have a cylindrical shape with a radius of 50 m and different keel depths. Simulations were performed for different drag coefficients and iceberg keel depths. The forces acting on the keel were calculated for each layer using ADCP measurements for velocity values. Simulation time was equal to 37.5 hours in 2009 and 12 hours in 2011, time step was varied down to 1 second. The results of the simulations are presented in Figure 8. The simulated drift trajectories diverge significantly with the ship drift trajectory in 2009 because the influence of the internal ice stresses was not included in the momentum balance Eq. [1] (Marchenko et al., 2010). The drift of the simulated iceberg is further northwest for stronger wind forces. A variety

of trajectories for icebergs with different keels is also shown in Fig. 8. Icebergs with small keels drift in different directions than large icebergs due to the difference in the velocities of the upper and lower layers.
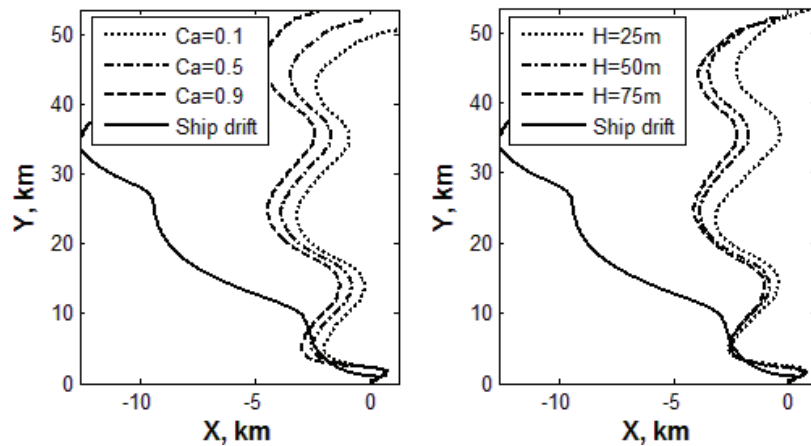

Figure 8. Trajectory of the RV Lance (solid line) and simulated trajectories for different drag coefficients and iceberg heights.

In 2011, the simulated trajectories repeat the loop but also diverge to some extent. Because the water was shallow with high sea current velocities (see Fig. 9) and the wind speed was relatively low, the sea ice cover drifted in a similar direction as the water.
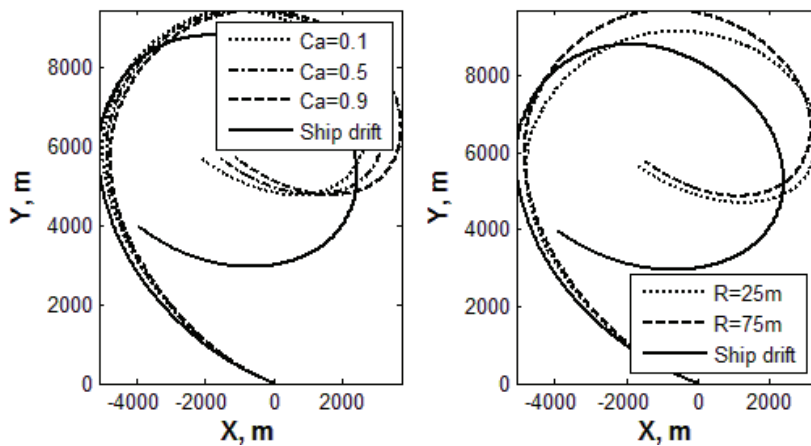
Figure 9. Trajectory of the RV Lance and simulated trajectories for different parameters in 2011.

5. Iceberg Drift in the Ekman Current

In this section, a water layer with a finite depth H and wind blowing along the x-axis with constant speed are considered at the sea bottom $z = 0$ and on the water surface $z = H$. In the

stationary case, the Coriolis force is in balance with the viscous forces in the water volume (Kundu, 1990), such that

$$-fV_y = \nu\frac{\partial^2 V_x}{\partial z^2}; \qquad fV_x = \nu\frac{\partial^2 V_y}{\partial z^2} \tag{4}$$

where $f = 2\Omega\sin\varphi$, ν is the water eddy viscosity and V_x, V_y are the water velocity projections. The boundary conditions at the water surface and water bottom are as follows:

$$V_x(z=0) = 0, V_y(z=0) = 0,$$
$$\nu\rho_w\frac{\partial V_x(z=H)}{\partial z} = \tau, \frac{\partial V_y(z=H)}{\partial z} = 0 \tag{5}$$

where τ is the wind drag stress. The Ekman solution is expressed by the following formulas:

$$V_x(z) = \text{Re}\left(\frac{\tau(1-i)}{2\rho_w\sqrt{f\nu}}\frac{sh(\omega z)}{ch(\omega H)}\right); \qquad V_y(z) = \text{Im}\left(\frac{\tau(1-i)}{2\rho_w\sqrt{f\nu}}\frac{sh(\omega z)}{ch(\omega H)}\right) \tag{6}$$

where $\omega = \sqrt{f/\nu}\,(1+i)/2$. This solution shows the reduction in the sea current velocity with depth. The top sea layer flow deflects from x-axis to the south.

The typical velocity profile is depicted in Fig. 10. The sea depth was taken to be 100 m, and the eddy viscosity of the seawater was assumed to be in range of 0.005 to 0.02 m^2/s. Depending on the eddy viscosity coefficients, icebergs can drift in different directions (Figure 10). The simulation shows that the drift direction does not depend significantly on the iceberg keel depth; however, it does depend on the iceberg width and viscosity coefficient. By knowing the potential drift trajectory, the path among the ice floes can be freed to more easily deflect icebergs.
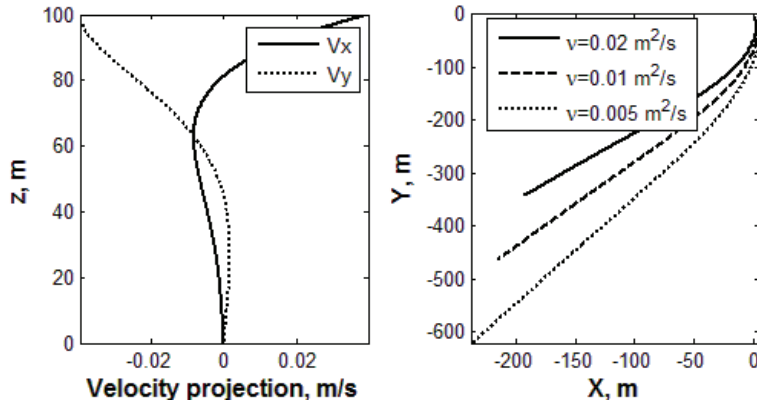

Figure 10. Velocity profile of the Ekman current and potential drift trajectories for different eddy viscosities.

6. Conclusions

During two expeditions when the RV Lance was moored to the drifting ice in the Western Barents Sea in 2009 and 2011, field data on navigation, weather and sea currents were collected and analyzed. Northeast of Hopen, the ice drift velocities were different from the velocities of the sea currents, and the floe-floe interactions influenced the ice drift characteristics significantly. The mean ice drift velocity was approximately 0.3 m/s, and the ice drift trajectories had a wavy form and were directed to the northwest. In Spitsbergenbanken, the mean drift velocity was 0.75 m/s. In this location, the ice drift velocities were similar to the velocities of the surface sea current, and the floe-floe interactions were insignificant. The ship trajectory included 2 loops with diameters of 6 km and 14 km. It was shown that sudden changes in drift direction happened on low speed drift but normally curvature radius wasn't lower than 1.5 km.

Significant differences of the sea current velocities in the 25 m-thick top layer and lower water layers were measured to the North-East from the Hopen Island. In this region vertical gradients of the water salinity (up to 1 ppt per 50 m) and the water temperature (up to $3^{o}C$ per 50 m) were revealed. The dependence of iceberg drift from the draft is stronger in this region in comparison to Spitsbergenbanken where vertical profiles of sea current velocities are uniform.

The energy of turbulent fluctuations of the water velocities can be important for the water drag force on an iceberg keel. The effect was analyzed on the example of the Ekman current, where vertical velocity profile depends on the eddy viscosity. The simulations have shown that in the Ekman current the dependence of iceberg drift trajectory on the eddy viscosity is much stronger than on the iceberg draft.

References

Eik, K., 2009. Iceberg drift modelling and validation of applied metocean hindcast data. Cold Regions Science and Technology, 57, 67–90.

Harris, C. L., Plueddemann, A. J., and Gawarkiewicz, G. G., 1998. Water mass distribution and polar front structure in the western Barents Sea. Journal of Geophysical Research, 103(C2), 2905–2917.

Hunke, E. C., and Comeau, D., 2011. Sea ice and iceberg dynamic interaction. Journal of Geophysical research, 116, C05008, doi:10.1029/2010JC006588.

Keghouche, I., Bertino, L., and Lisaeter, K. A., 2009. Parametrization of an iceberg drift model in the Barents Sea. Journal of Atmospheric and Oceanic Technology, 26, 2216–2227.

Kowalik, Z., and Proshutinsky, A. Yu., 1995. Topographic enhancement of tidal motion in the western Barents Sea. Journal of Geophysical Research, 100(C2), 2613–2637.

Kubat, I., Sayed, M., Savage, S. B., and Carrieres, T., 2005. An operational model of iceberg drift. The International Journal of Offshore and Polar Engineering, 15(2), 125–131.

Kundu, P. K., 1990. Fluid mechanics. Academic Press, California, USA, 638 pp.

Lichey, C., and Hellmer, H. H., 2001. Modeling giant-iceberg drift under the influence of sea ice in the Weddell Sea, Antarctica. Journal of Glaciology, 47(158), 452–460.

Loeng, H., 1990. Features of the physical oceanographic conditions of the Barents Sea. Proceedings of Pro Mare Symposium on Polar Marine Ecology, Trondheim, Norway, 5–18.

Marchenko, A., Kulyakhtin, A., and Eik, K., 2010. Icebergs drift in the Barents Sea: data analysis of ice tracking buoy and numerical simulations. Proceedings of the 20th IAHR Symposium on Ice, Lahti, Finland.

Pfirman, S. L., Colony, R., Nurnberg, D., Eicken, H., and Rigor, I., 1997. Reconstructing the origin and trajectory of drifting Arctic sea ice. Journal of Geophysical Research, 102(C6), 12575–12586.

Appendix F:
Ice Drift and Sea Current Analysis in the Northwestern Barents Sea

The paper presents the data obtained from the GPS tracking of four ice floes to the south-east of Svalbard. Measured current profiles, and salinity, temperature and density profiles of ocean are also presented.

Ice drift and sea current analysis in the Northwestern Barents Sea

Renat Yulmetov[1*], Aleksey Marchenko[2], Sveinung Løset[1,2,3]

[1] Sustainable Arctic Marine and Coastal Technology (SAMCoT), Centre for Research-based Innovation (CRI), Norwegian University of Science and Technology, Trondheim, Norway
[2] The University Centre in Svalbard, Longyearbyen, Norway
[3] Norwegian University of Science and Technology, Trondheim, Norway
[*] RenatY@unis.no

ABSTRACT

Drifting ice and icebergs present in the Barents Sea are a serious threat to offshore oil and gas development. The dynamic characteristics of the ice drift influence ice loads on potential offshore installations and the organisation of ice management. Ice drift characteristics were monitored using four Iridium ice tracking drifters installed on drifting ice during the survey of *RV Lance* in April 2012. A spectral analysis of the data shows the influence of semidiurnal and diurnal tides on the recorded drift characteristics. The drift speed and curvature of ice trajectories depend on the combined influence of wind and water drag forces. The measurement of vertical profiles of the sea current velocities was performed by three ADCPs with different spatial resolutions during the cruise. The structure of under-ice boundary layers was analysed during two ice stations. CTD profiling performed from the drifting ice at two ice stations and during the passage from Edgøya to the Hopen Island revealed a layer of relatively warm and salty water directly under the ice. The collected data are compared with similar data collected in earlier expeditions in the Northwestern Barents Sea.

INTRODUCTION

The exploration and exploitation of hydrocarbons in Arctic waters face challenges related to severe physical environments. Additional loads due to sea ice actions and the presence of icebergs in these waters, as well as low temperatures, lead to more complex solutions and additional costs.

The Shtokman gas and condensate field is the largest natural gas field offshore known to date. The projected environmental conditions include an annual air temperature ranging from -38ºC (100-year condition) to +30ºC, ice-rich waters in the wintertime (Le Marechal, 2011) and the presence of icebergs with a mass up to 4 million tonnes (Shtokman Development AG, 2012). Extracted gas processing and separation may be performed in these waters most like by using a moored Floating Production Unit (FPU) operating at a water depth of 320 m. Thus, it is important to estimate the sea ice loads on the FPU and the probability of collision with an iceberg to perform station keeping during production. For this reason, ice and iceberg drift driven by the sea current, wind and waves should be thoroughly studied.

Conditions similar to those at the Shtokman field can be found in the Northwestern Barents Sea. In the spring of 2012, *RV Lance* was moored to an ice floe and drifted into Storfjordbanken southeast of Spitsbergen. During the survey, we measured the sea currents, performed several CTD-tests and deployed four Ice Tracking Drifters (ITDs) on different ice floes.

Sea current profile is one of the most important input parameters in drift forecasting models because the sea ice drift is mainly governed by the drag forces (Savage, 2001; Lichey and Hellmer, 2001). Sea current is usually measured by an Acoustic Doppler Current Profiler (ADCP), where the vertical resolution depends on the frequency applied and can range from tens of metres down to a few centimetres. We had three ADCPs with different temporal and spatial resolutions that measured the relative sea current, while *RV Lance* was moored to and drifted with the ice floe. By knowing the GPS track of the ship, it was possible to estimate the influence of the sea current on the drift.

Kinematical drift characteristics for the longer period (up to 20 days) were provided by the ITDs deployed on several ice floes. We analysed the influence of tides and estimated the velocity of divergence of the ice cover. CTD profiles of the sea water were measured to obtain profiles of the salinity and temperature in the sea water column.

All data processing, manipulation and plotting were performed in MATLAB using standard fast Fourier transform, smoothing and fitting functions.

EQUIPMENT
Four drifters produced by Oceanetic Measurement (2011) were deployed on different ice floes during the survey. A hole of 150 mm diameter and approximately 30 cm deep was drilled in the ice before each deployment to fix the device. The caps of the drifters were painted white to make them less visible to polarbears. Deadweights were attached to the drifters to ensure that the trackers would sink after the deterioration of the ice floes.

Each drifter measured its position every ten minutes and sent data packages once per hour. The choice of measurement interval was determined by the consideration that the drift speed should be estimated with an accuracy of $1\,\mathrm{cm/s} \approx 8\,\mathrm{m/600\,s}$. The data transmission was performed through the Iridium channel. The horizontal accuracy in position estimation was less than 5 metres (50%) and less than 8 metres (90%).

We also used three different types of ADCP to measure the sea current velocities. The main characteristics of the devices are presented in Table 1. The onboard ADCP (BB-VM) was fixed under the ship at a depth of 4 metres and was used in the profile calculation. The two others (Nortek AWAC and RDI Workhorse Sentinel) were hung under the ice floes into predrilled holes. The different vertical resolutions of the devices allowed the current profile to be measured in the upper boundary layer under the ice.

Table 1. ADCP main characteristics.

	RDI BB-VM	AWAC	Workhorse Sentinel
# of beams	4	3	4
Transducer frequency, kHz	153.6	400	1228.8
First cell depth, m	15.98	2	0.53
Vertical resolution, m	8	1	0.3
Number of analysed cells	5	50	20
Accuracy, cm/s	---	0.5	0.3

CTD profiling was performed using an SBE 19+, which was manually lowered into the water from the ship and from the sea ice through the predrilled hole. A long wooden stick was

attached to the device to protect the pump from the sediments and mud at the sea bottom. The sampling frequency of the device was 4 Hz.

DRIFT TRAJECTORIES AND VELOCITIES

The survey started on the 16th of April, 2012, in Longyearbyen with *RV Lance*. After nearly two days of sailing, *RV Lance* reached the waters northwest of Hopen Island (Figure 1). The two first trackers (ITDs) were deployed on the sea ice, and the ADCP and CTD measurements were performed during an approximately 30-hour-long ice station. During the station, the vessel was moored to an ice floe and drifted together with the pack ice. The position of the ship was measured by GPS and compared with the position of the second ITD, which was deployed on the same ice floe the vessel was moored to. The drift trajectories of the trackers and the vessel show numerous loops that were approximately 10 km in diameter. The initial distance between the ITDs was approximately 5 km and approximately 250 m between the vessel and the second ITD. Both trackers and the ship moved in parallel.

The third tracker was deployed at the second ice station, 30 km to the north of the first one. The ice drift in that region reproduced ellipses with even more stable centres. Finally, the fourth tracker was deployed 30 km to the north of Hopen.

The ice conditions were heavy first-year ice in the region of study. Highly concentrated ice drifting from the north was pushed southwest between Hopen and Edgeøya by the strong north-eastern current. The ice concentration was 0.9 and higher (visual observations), and the ice floe size varied from tens of metres to one kilometre with an ice thickness varying from 0.3 to 0.6 metres.

The drift speed characteristics and lifetime of the different trackers are shown in Table 2. The drift velocity reaches relatively high values and exceeds 1.5 m/s for ITD #3. The mean values are also high, most likely due to strong currents and tidal motion in the shallow water. The sea depth in the region of the drift rarely exceeded 100 m. There are much lower drift velocities (0.1 m/s mean drift speed) and much deeper water (up to 500 m) in the Greenland Sea (Yulmetov et al., 2013).
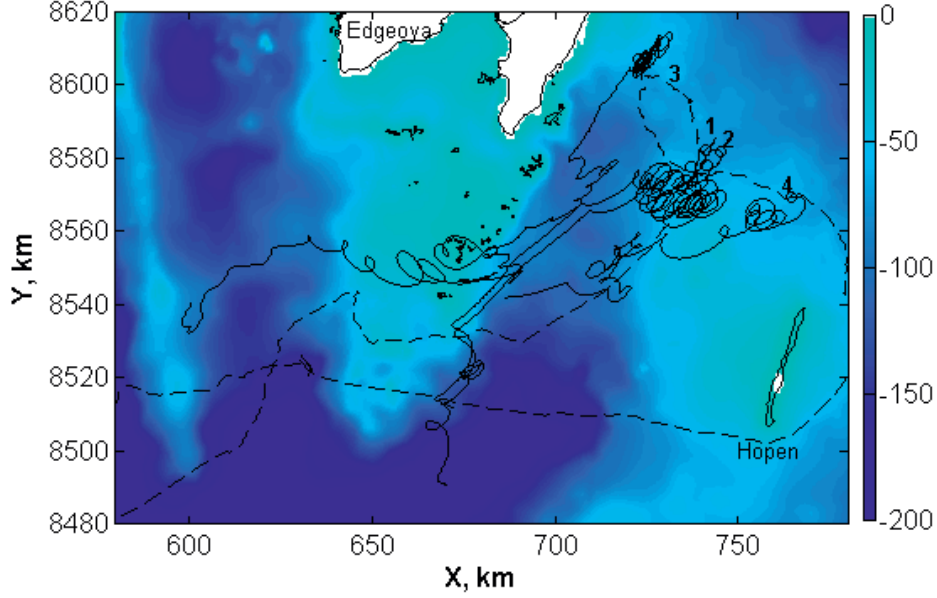
Figure 1. Trajectories of the ITDs (solid line) and the *RV Lance* track (dashed line). Deployment places are marked by numbers.

Table 2. ITD data; $\langle V \rangle$ is the mean drift speed, σ_V is the standard deviation, $\max(V)$ is the maximum drift speed.

ITD	First signal	Life time, days	$\langle V \rangle$, m/s	σ_V, m/s	$\max(V)$, m/s
#1	2012-04-18, 08:00:00	11.2	0.41	0.18	1.06
#2	2012-04-18, 14:00:00	9.8	0.43	0.18	1.08
#3	2012-04-20, 13:00:00	19.9	0.33	0.20	1.53
#4	2012-04-22, 02:00:00	8.7	0.37	0.18	1.06

The high initial concentration of ice coming from the north resulted in stresses in the ice field to the southwest of Edgeøya. The relatively thin ice cover could have been destroyed by gravity waves, explaining the short lifetime of the drifters.

The loops consisting of trajectories and cyclically changing velocities were analysed to determine how quickly the drift direction can change if the ice floe drifts with a given velocity. To provide quantitative analysis, we used the equation

$$\frac{1}{R} = \frac{\left| \vec{V} \times \vec{a} \right|}{\left| \vec{V} \right|^3} \tag{4}$$

Here, R is the radius of the curvature, $\vec{V}$ is drift velocity, and $\vec{a}$ is acceleration.

Noise and error reduction in the second derivative calculations were implemented by fitting velocity values with the sum of the harmonic functions. The entire data array was divided into equally sized blocks containing 75 points, corresponding to the semidiurnal period. On each block, we used the standard MATLAB fit function with the *"fourier8"* fit type.

The resulting data were smoothed using a *"moving average"* algorithm with a 200-point span. The smoothed curves show (Figure 2) that the fast-drifting ice is less likely to turn than the ice with low drift speeds. However, the derived dependence for Storfjordbanken is not as strong as in the Greenland Sea for the same latitude (Yulmetov et al., 2013), mostly because the ice drifting in from the Fram Straight is more massive, and its drift speed is lower.
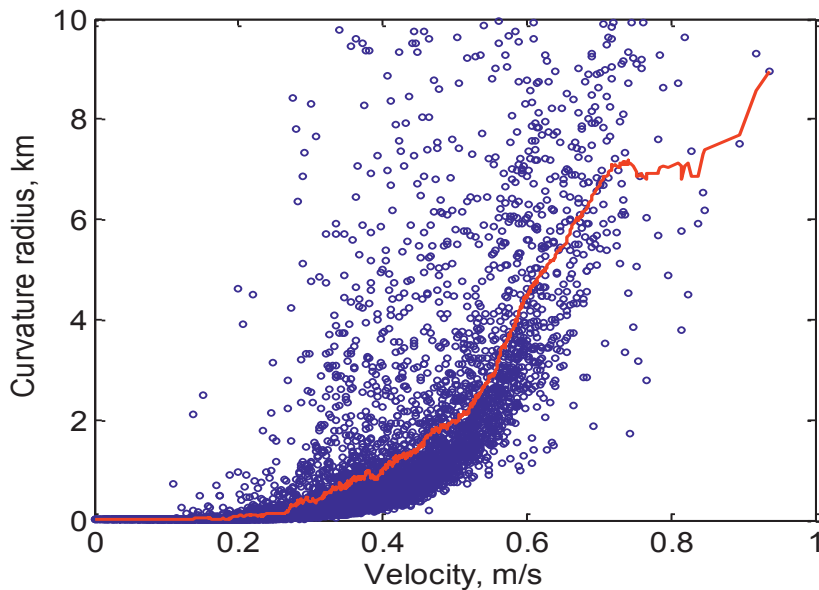
Figure 2. Curvature radius vs. drift speed. Smoothed trajectory (red).

VELOCITY SPECTRUM

To clarify the role of tidal motion and the Coriolis forcing, we analysed the velocity spectrum of the drift. The discrete Fourier transform was used to obtain the spectrum. If one has a number of measured quantities, x_n, one can use the equation

$$X_k = \sum_{n=0}^{N-1} x_n \cdot e^{-i2\pi\frac{k}{N}n} \tag{5}$$

where N is the number of measurements, and X_k are the complex numbers that reflect the amplitude and phase of a certain harmonic component in a signal. The fast Fourier transform (FFT) algorithm was used in MATLAB for the calculation of harmonic components. The amplitude-frequency spectrum is shown in Figure 3.

We cannot distinguish between the roles of the Coriolis force and semidiurnal tides because their periods are very similar. The period of the M_2 tide is 12 hours and 25 minutes, while the Coriolis force period is 12 hours and 19 minutes for 77°N. In any case, the tides and Coriolis force play an important role in the drift of the ice in these waters. Shallow waters in the region amplify the effect.
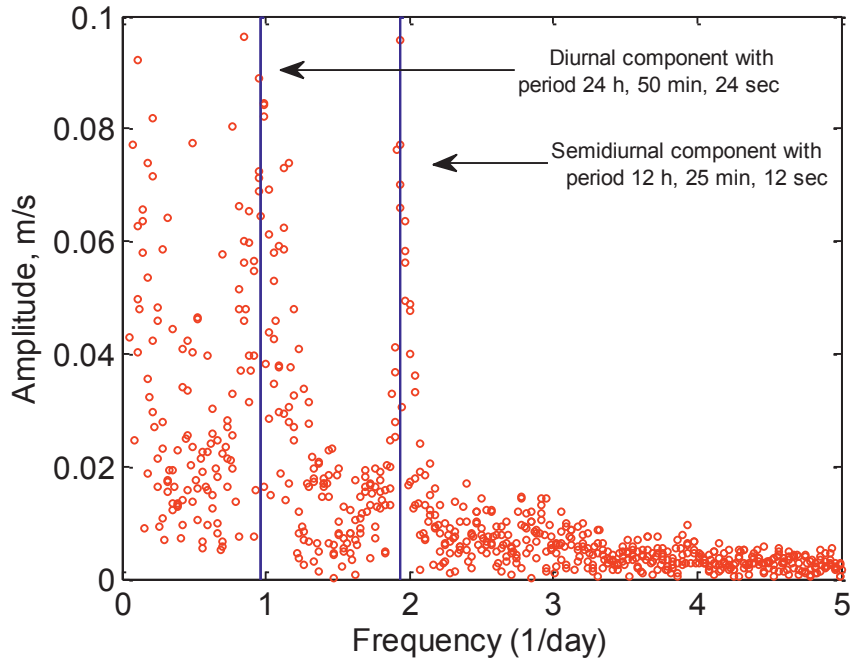
Figure 3. Velocity spectrum.

ADCP MEASUREMENTS

The measurements of the vertical profiles of the sea current velocities were performed using three ADCPs (RDI, Nortek, onboard ADCP) with different spatial resolutions at one ice station. Low-spatial-resolution onboard ADCP measurements were compared with the data provided by the high-resolution ADCPs installed on the ice adjacent to the vessel. The distance between the vessel and the deployment place on the ice was approximately 100 m (Figure 4). The ice floe contained a ridge; consequently, a turbulent wake from the geometrical irregularities and from the ship could have caused a difference in the measured values. The heading of *RV Lance* was nearly constant the entire time, and the vessel trajectory consisted of two nearly full loops during the observation period from 16:00, 18th of April, until 21:00, 19th of April.

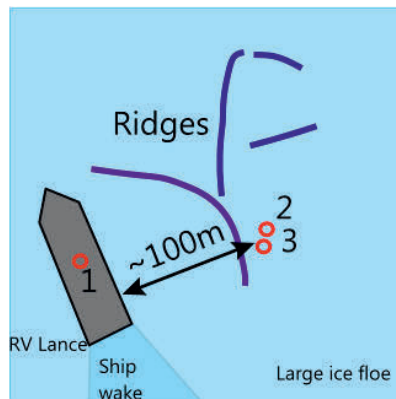
Figure 4. ADCP deployment positions. 1 – Onboard ADCP, 2 – Nortek, 3 – RDI

The devices measured current velocity relatively the ice floe. The sea current maintained direction to the south-west while the ship was making loops. The current direction was measured in degrees, clockwise, starting from direction to the North. The devices measured the sea currents in different depth ranges; thus, the values obtained were different for the devices. The measured current characteristics are plotted in Figure 5. We averaged the data among 50 (51 m) and 20 bins (6.23 m) for Nortek and RDI ADCPs, respectively. For the onboard ADCP, we took the first bin, which measured the current at a depth of 20 m.

In general, there is no sufficient difference between velocities of different water layers, but values are scattered within one layer. It can be seen that the relative velocity magnitude is lower for top layers due to viscous friction.

The relative current velocity magnitude did not exceed 0.2 m/s for all the devices, while the drift speed (black line) was up to 0.55 m/s. The magnitude has two minima during the observation period, with approximately 18 hours between them.
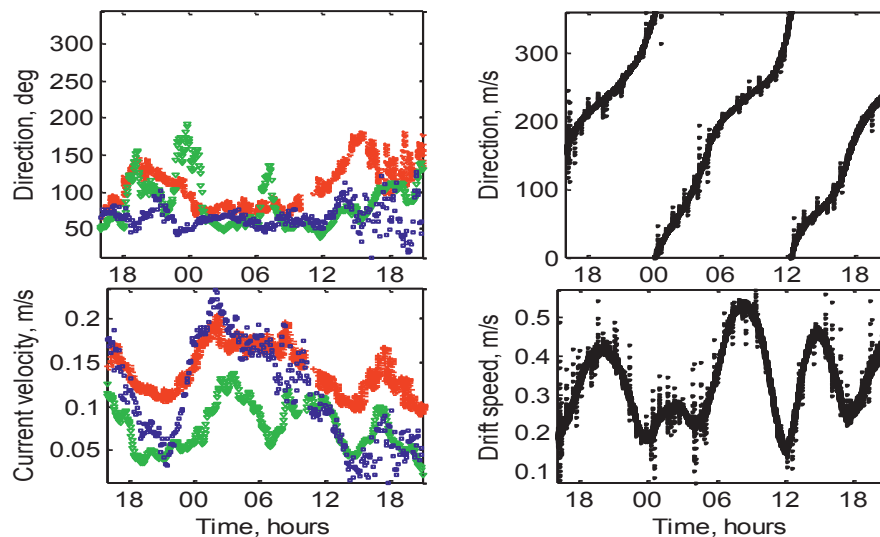

Figure 5. ADCP measurements. Nortek (red), RDI (green), onboard ADCP (blue). The drift direction and speed of RV Lance are plotted in black.

The sea current profiles measured by different devices and averaged in time for the whole observation period show that the velocity profile is mostly uniform deeper than 10 metres (Figure 6). The boundary layer has a thickness of approximately 7 metres, which can be seen clearly.
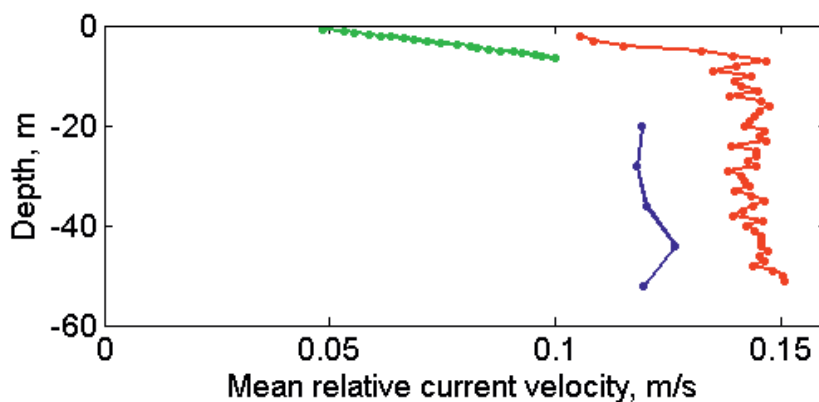
Figure 6. Current velocity profiles. Nortek (red), RDI (green), onboard ADCP (blue).

CTD PROFILES

Several CTD profiles were measured during the survey, five of which were taken at a distance of approximately 80 km starting at the northwest of Hopen (Figure 7). Data obtained with CTD were smoothed by 50 points moving average. The temperature profiles generally show warm water layers on the top and cold temperatures varying from -1.55 to -1.9°C at the bottom (Figure 8). The salinity varied from 34.3 to 34.9 ppt, with a value of approximately 34.4 ppt at the lower levels. Density profiles evidence heavier water in the top layers which are from 10 to 40 meters deep.
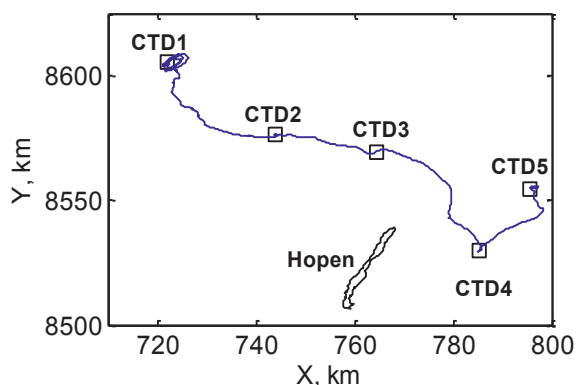

Figure 7. CTD profile positions.

Increased salinity and temperature on top in general repeats the measurements of Fer and Drinkwater (2012), that were performed to the South of Hopen in April-May, 2008. Such profile shapes are determined by warm Atlantic Water propagating from the Southwest. For the density profiles we suggest that the measurements were done in the area where warm North Atlantic current meets cold Arctic water and dense water is not yet at the bottom.
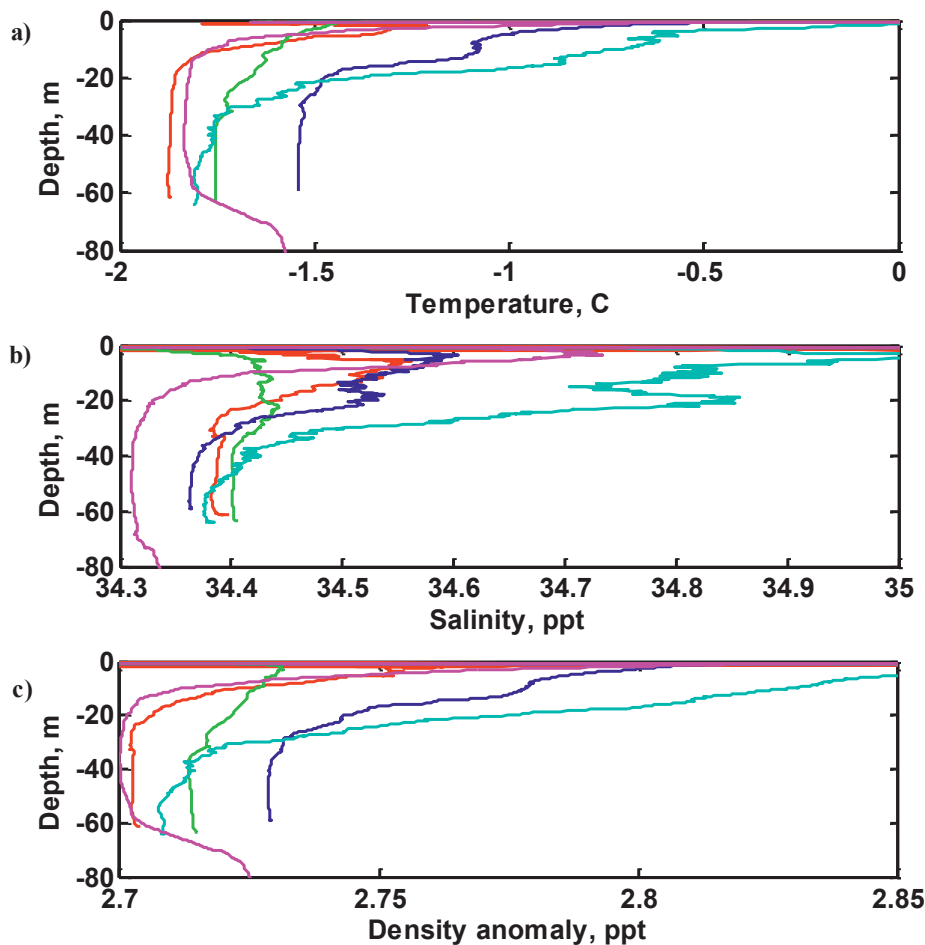
Figure 8. CTD profiles. a) temperature profiles b) salinity profiles c) density anomaly profiles.

CONCLUSIONS

Ice loads induced by drifting ice are a subject of great interest to the offshore industry. Drift characteristics are important for the validation of ice drift models. Data collected about the ice drift in a particular area can be used to predict ice motion and ice loads. These data can also be used for ice management operations.

In this paper, we carried out analyses of the data collected during a survey that took place in the waters to the southeast of Spitsbergen in April of 2012. The analysis included drift characteristics derived from the coordinates provided by Ice Tracking Drifters deployed on four different ice floes, current velocity measurements provided by three different ADCPs and, finally, CTD profiles. The major findings are the following:

- The ice drift between Hopen and Edgeøya is directed south-westwards. The drift speeds are relatively high due to the shallow water in the area. The maximum drift speed measured during a period of 20 days was 1.5 m/s, and the average drift speed was approximately 0.38 m/s.
- There was strong influence from tidal motion and Coriolis forcing. Spectral analyses of the velocity revealed two maxima corresponding to semidiurnal and diurnal cycles.

- There is a higher curvature radius for higher drift speeds.
- The mean relative current velocity was approximately 0.1 m/s. The differences in velocity measurements were caused by different spatial resolutions and slightly different positions.
- The CTD tests show high temperatures of the top layers due to warm water influx. However, the top layers have anomalously high density and salinity.

The measured current velocities and drift velocities can be used as input data for e.g. validation of drift forecasting models and oil spill drift models.

REFERENCES
Shtokman Development AG (2012): http://www.shtokman.ru/en/project/gasfield/
Guillaume Le Marechal, Philippe Anslot, Zoran Mravak, Pavel Liferov and Stephane Le Guennec (2011): "Design of a Floating Platform Hull for Arctic Conditions in the Barents Sea." Arctic Technology Conference, February 7-9, 2011, Houston, USA.
Savage, S.B. (2011): "Aspects of iceberg deterioration and drift." *Geomorphological Fluid Mechanics*, pp. 279-318.
Lichey, Christoph, and Hartmut H. Hellmer (2001): "Modelling giant-iceberg drift under the influence of sea ice in the Weddell Sea, Antarctica." *Journal of Glaciology* 47, no. 158, pp. 452-460.
Nortek (2012): http://www.nortek-as.com/lib/data-sheets/datasheet-awac
RDI (2012): http://www.rdinstruments.com/datasheets/wh_sentinel.pdf
Yulmetov, R., S. Løset and K. J. Eik (2013): "Analysis of Drift of Sea Ice and Icebergs in the Greenland Sea." Proceedings of the 22nd International Conference on Port and Ocean Engineering under Arctic Conditions, June 9-13, 2013, Espoo, Finland.
Fer, I. and K. Drinkwater (2012): "Mixing in the Barents Sea Polar front near Hopen in spring." Journal of Marine Systems.